

**FUNGUS-MEDIATED BIOSYNTHESIS OF OXIDES
NANOPARTICLES AND COMPOSITES**

VIPUL BANSAL

**BIOCHEMICAL SCIENCES DIVISION
NATIONAL CHEMICAL LABORATORY
PUNE – 411 008
INDIA**

NOVEMBER 2006

*Fungus-mediated Biosynthesis of Oxides
Nanoparticles and Composites*

THESIS SUBMITTED TO
UNIVERSITY OF PUNE

FOR THE DEGREE OF
DOCTOR OF PHILOSOPHY
IN
BIOTECHNOLOGY

BY
VIPUL BANSAL

BIOCHEMICAL SCIENCES DIVISION
NATIONAL CHEMICAL LABORATORY
PUNE – 411 008
INDIA

NOVEMBER 2006

In the sweet memories of my grandparents

Amma ji & Baba saheb...

CERTIFICATE

This is to certify that the work discussed in the thesis entitled **“FUNGUS–MEDIATED BIOSYNTHESIS OF OXIDES NANOPARTICLES AND COMPOSITES”** by **VIPUL BANSAL**, submitted for the degree of *Doctor of Philosophy in Biotechnology* was carried out under my supervision at the Biochemical Sciences and the Materials Chemistry Divisions of the National Chemical Laboratory, Pune, India. Such materials as have been obtained by other sources have been duly acknowledged in this thesis. To the best of my knowledge, the present work or any part thereof, has not been submitted to any other University for the award of any other degree or diploma.

Date:

Place: Pune

Dr. (Mrs.) Asmita Prabhune

(Research Guide)

CERTIFICATE

This is to certify that the work discussed in the thesis entitled **“FUNGUS–MEDIATED BIOSYNTHESIS OF OXIDES NANOPARTICLES AND COMPOSITES”** by **VIPUL BANSAL**, submitted for the degree of *Doctor of Philosophy in Biotechnology* was carried out under my joint supervision at the Biochemical Sciences and the Materials Chemistry Divisions of the National Chemical Laboratory, Pune, India. Such materials as have been obtained by other sources have been duly acknowledged in this thesis. To the best of my knowledge, the present work or any part thereof, has not been submitted to any other University for the award of any other degree or diploma.

Date:

Place: Pune

Dr. Murali Sastry

(Research Co-Guide)

DECLARATION

I hereby declare that the work incorporated in this thesis entitled **“FUNGUS-MEDIATED BIOSYNTHESIS OF OXIDES NANOPARTICLES AND COMPOSITES”** submitted for the degree of *Doctor of Philosophy in Biotechnology* has been carried out by me at the Biochemical Sciences and the Materials Chemistry Divisions of the National Chemical Laboratory, Pune, India under the joint supervision of Dr. (Mrs.) Asmita Prabhune and Dr. Murali Sastry. Such materials as have been obtained by other sources have been duly acknowledged in this thesis. The work is original and has not been submitted in part or full by me for award of any other degree or diploma in any other University.

Date:

Place: Pune

Vipul Bansal

(Research Student)

Acknowledgements

The work presented in this thesis would not have been possible without my close association with many people. I take this opportunity to extend my sincere gratitude and appreciation to all those who made this PhD thesis possible.

First and foremost, I would like to extend my sincere gratitude to my mentor Dr. Murali Sastry for introducing me to this exciting field of interdisciplinary science and for his dedicated help, advice, inspiration, encouragement and continuous support, throughout my PhD. His enthusiasm, integral view on research and his mission for providing only high-quality work and not less, has made a deep impression on me. During our course of interaction during the last three years, I have learnt extensively from him, including how to raise new possibilities, how to regard an old question from a new perspective, how to approach a problem by systematic thinking, data-driven decision making and exploiting serendipity. Every time, I meet him, I can feel “the fire in the belly” which he always talks about. I owe him lots of gratitude for having me shown this way of research. I am really glad to be associated with a person like Dr. Sastry in my life.

My special thanks to my research supervisor Dr. (Mrs.) Asmita Prabhune for her continuous support, guidance, cooperation, encouragement and for facilitating all the requirements, going out of her way. She was always readily available for any support, I required during my PhD. I really enjoyed being associated with her.

I express my gratitude to Dr. Absar Ahmad as an eminent collaborator for providing me accessibility to the facilities at Biochemical Sciences Division even during odd hours as well as for our fruitful discussions. My sincere thanks to Dr. B. L. V. Prasad and Prof. Satish Ogale for their continuous support, friendly nature, elderly advice and scientific interactions.

My sincere thanks to Mrs. Suguna Adhyanthaya for helping me at NCL in all the official activities and for her elderly advice, thinking about my betterment. Her help in TGA and DSC measurements used in this thesis is gratefully acknowledged. I appreciate her support in facilitating various materials characterization, going out of her way.

My heartfelt thanks to fellow labmates, Hrushikesh, Ambarish, Akhilesh, Tanushree, Amit, Atul, Sourabh, Manasi, Minakshi, Deepti, Prathap, Sanjay, Imran, Anil, Priyanka, Virginia, Umesh, Sudarshan, Baisakhi and Ramaya for always standing by my side and sharing a great relationship as compassionate friends. I will always cherish the warmth shown by them. I thank you all for your company, care and discussions. A special word of thanks to Sourabh, Manasi, Deepti and Amit for taking the great pains in proof-reading the thesis by sometimes even keeping their own priorities aside and giving me valuable suggestions to improve it.

The road to my graduate degree has been long, so I would also like to thank some people from the early days. I would like to thank my senior colleagues Dr. Debabrata, Dr. Sumant, Dr. Saikat, Dr. Anita, Dr. Senthil, Dr. Ankamwar, Kannan and Shankar, who have helped in getting me familiarized with all the lab facilities and making me feel comfortable during my initial days of PhD. A special thanks to Dr. Debabrata with whom I really enjoyed working in the initial period of my PhD. Thanks Deb.

I am thankful to Mr. Ravi Shukla and Dr. R. R. Bhonde from National Center for Cell Sciences, Pune for fruitful collaborations. I could not have wished for better collaborators. I really enjoyed working with Ravi and cherished the happy moments spent with his family.

I would like to thank Mr. R. Muthurajan, Armament Research and Development Establishment (ARDE), Pune for temperature-dependent dielectric facilities; Dr. K. Vijayamohanan and Mrs. Sneha Kulkarni, NCL, Pune for the frequency-dependent dielectric facilities; Dr. R. Ramesh, Polymer Chemistry Division, NCL for high temperature XRD facilities and Dr. P. V. Satyam, Institute of Physics (IoP), Bhubaneswar for the fruitful work done with high resolution TEM measurements.

I am grateful to many people in the Center for Materials Characterization, NCL who have assisted me in the course of this work. My sincere thanks to Dr. S. R. Sainkar, Dr. M. Bhadbhade, Mrs. R. Pasricha, Mr. A. B. Gaikwad, Dr. Patil and Dr. A. B. Mandale for making the facilities available during the research work. I would also like to acknowledge Minakshi and Manasi for their assistance with AFM measurements and Amit for providing Nikon digital camera for optical images shown in this thesis.

During my stay at NCL, several friends have gone out of their way to help me making several characterization tools accessible, which has made a positive impact on my research outcomes. Without their help, progress of the work presented in this thesis was unimaginable. Thank you friends.

I had the pleasure to work with Avinash, Meenal, Preeti, Deepshikha, Sathya, Prasanjit, Ajay and Vijaykumar who did their graduation projects in this lab and have been somehow beneficial for the work presented in this thesis.

Many thanks to the staff member of our division, who have helped me in innumerable ways. Especially thanks to Mr. Deepak and Mr. Punekar.

I am grateful to Dr. S. Sivaram, Director NCL, and Dr. S. Pal, Head, Physical Chemistry Division, NCL for giving me an opportunity to work in this institute and making the facilities available for carrying out research.

I acknowledge the Council of Scientific and Industrial Research (CSIR), Government of India for providing me with the necessary funding and fellowship to pursue research at NCL. I am also grateful to CSIR for providing me with the financial support for attending an international conference at Marburg, Germany.

I would like to thank the Almighty who always gives me strengths to strive for the best. Thank you God for always being there for me.

Last but not the least, I would like to thank the most important people in my life – my parents and my family. At this moment and always, I pay my most respectful regards to my beloved parents, who are a constant source of inspiration in every walk of my life. I express my deep gratitude and affection to my younger sisters Ritu and Chetna who have always extended their help and love whenever I needed the most.

Vipul Bansal

Table of Contents

Chapter 1: Introduction

1.1	Introduction to the Nano World	2
1.2	Nature: An Inspiration to Nanomaterials Synthesis	8
1.3	Nature: The True Habitat for Biomineralization	8
1.4	Biomimetic Nanoengineering: The Art of Imitating Nature	12
1.5	Biomineralization in the Laboratory: Nature's Way	15
1.6	Outline of the Thesis	17
1.7	References	19

Chapter 2: Characterization techniques

2.1	Introduction	36
2.2	UV-visible absorption spectroscopy	36
2.3	Fourier transform infrared spectroscopy	37
2.4	X-ray photoemission spectroscopy	38
2.5	X-ray diffraction	40
2.6	Energy dispersive X-rays analysis	42
2.7	Thermal analysis	42
2.8	Electron microscopy	43
2.9	Scanning probe microscopy	45
2.10	Polyacrylamide gel electrophoresis	48
2.11	References	49

Chapter 3: Fungus-mediated Biosynthesis of Binary and Ternary Oxide Nanoparticles using Chemical Precursors

3.1	Introduction	52
3.2	Biosynthesis of binary oxide nanoparticles <i>viz.</i> silica, titania and zirconia using the fungus <i>Fusarium oxysporum</i>	54
3.3	Biosynthesis of complex oxide nanoparticles <i>i.e.</i> barium titanate using the fungus <i>Fusarium oxysporum</i>	73
3.4	Conclusions	89
3.5	References	90

Chapter 4: Fungus-mediated Bioleaching of Silica Nanoparticles from Naturally Available Materials and Agro-industrial By-products

4.1	Introduction	95
4.2	Fungus-mediated bioleaching of white sand as a means of producing extracellular silica nanoparticles	97
4.3	Fungus-mediated bioleaching and biotransformation of amorphous silica present in rice husk into nanocrystalline silica	104
4.4	Fungus-mediated two fold approach for selective bioleaching of silica and simultaneous enrichment of zirconia in zircon sand	120
4.5	Conclusions	128
4.6	References	128

Chapter 5: Visible Light Induced Photo-oxidative Dye Degradation and Antimicrobial Applications of Non-metals Doped Biogenic Titania Nanoparticles

5.1	Introduction	133
5.2	Photo-oxidative and antimicrobial activity of biogenic NCF-TiO ₂ nanoparticles under indoor and solar light conditions	135
5.3	Conclusions	153
5.4	References	154

Chapter 6: Conclusions

6.1	Summary of the work	158
6.2	Scope for future work	159

List of Publications

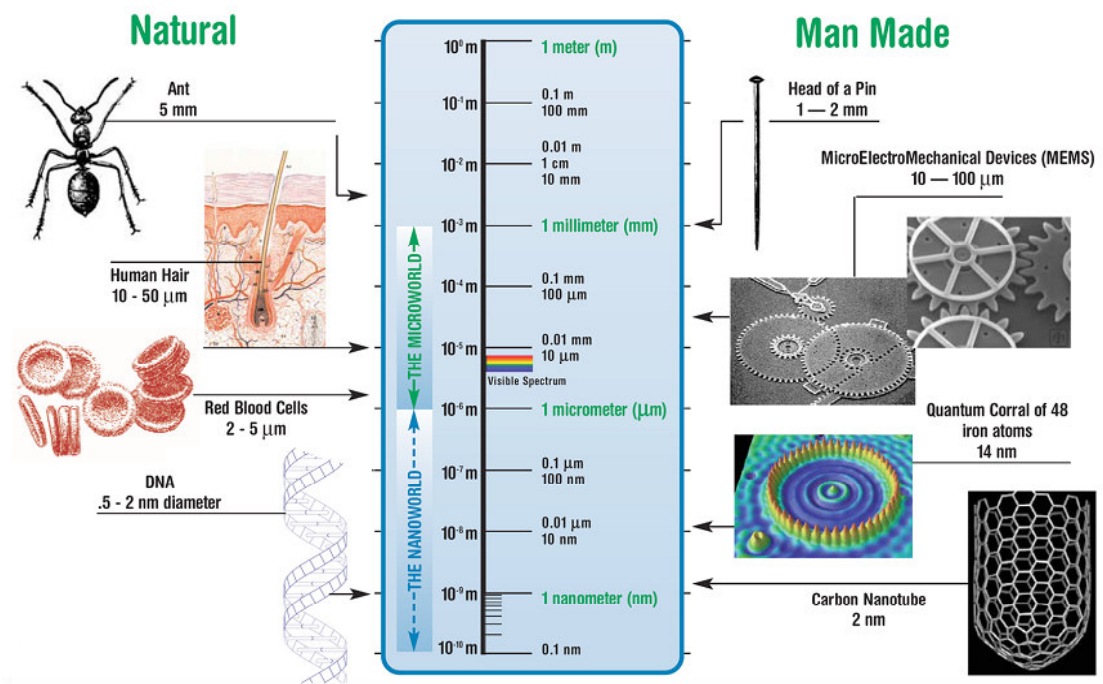
CHAPTER I

Introduction

This chapter provides an introduction to the thesis and starts with the motivation behind the work carried out in this thesis, followed by an overview of biomineralization, in particular biosilicification processes occurring in Nature. The syntheses of various biomaterials in their natural habitats and their specific biological roles have also been discussed. Further emphasis has been drawn towards various biological and biomimetic approaches currently *in vogue* for the *in silico* synthesis of nanomaterials. This chapter also briefly describes the motive behind the new biological method that we have used for the biosynthesis of oxide nanomaterials. Finally, a chapter wise outline of the protocols described in this thesis has been presented.

1.1 Introduction to the Nano World

Nature has evolved numerous incredibly functional assemblages of proteins, nucleic acids, and other macromolecules to perform complicated tasks that are still daunting for us to emulate in our laboratories. One such task, which has recently been of great interest to materials scientists, is the creation of the most efficient miniaturized functional materials by Nature through elegant and ingenious ways. The recent spur in interest towards nanoscience and nanotechnology is due to the relentless attempts to create functional miniaturized structures the Nature's way. Richard Feynman first propounded this concept in his seminal speech "There's plenty of room at the bottom" [1]. In attempts to create miniaturized structures, significant achievements have been obtained and structures of micron- and nano-dimensions can now be routinely fabricated (Figure 1.1), though the complexity manifested by Nature is yet a distant goal.



© Copyright 2002 Forbes/Wolfe Nanotech Report

Figure 1.1 Cartoon representing the relative sizes of various naturally occurring species/objects and man-made materials [Courtesy: Josh Wolfe's report on Nanotechnology; <http://www.forbeswolfe.com>].

To achieve this goal, researchers are trying to follow the "top-down" as well as "bottom-up" approaches (Figure 1.2). Among these, the top-down approach can be considered as the one with which the human race first learned to fabricate materials and in due course of time, perfected this art by being able to engineer structures at

submicron levels. Similarly, bottom–up approaches were also used for the synthesis of remarkable architectures. Exquisite illustrations of bottom–up assembly of nanomaterials can be observed in Nature, which have been discussed in the later part of this chapter.

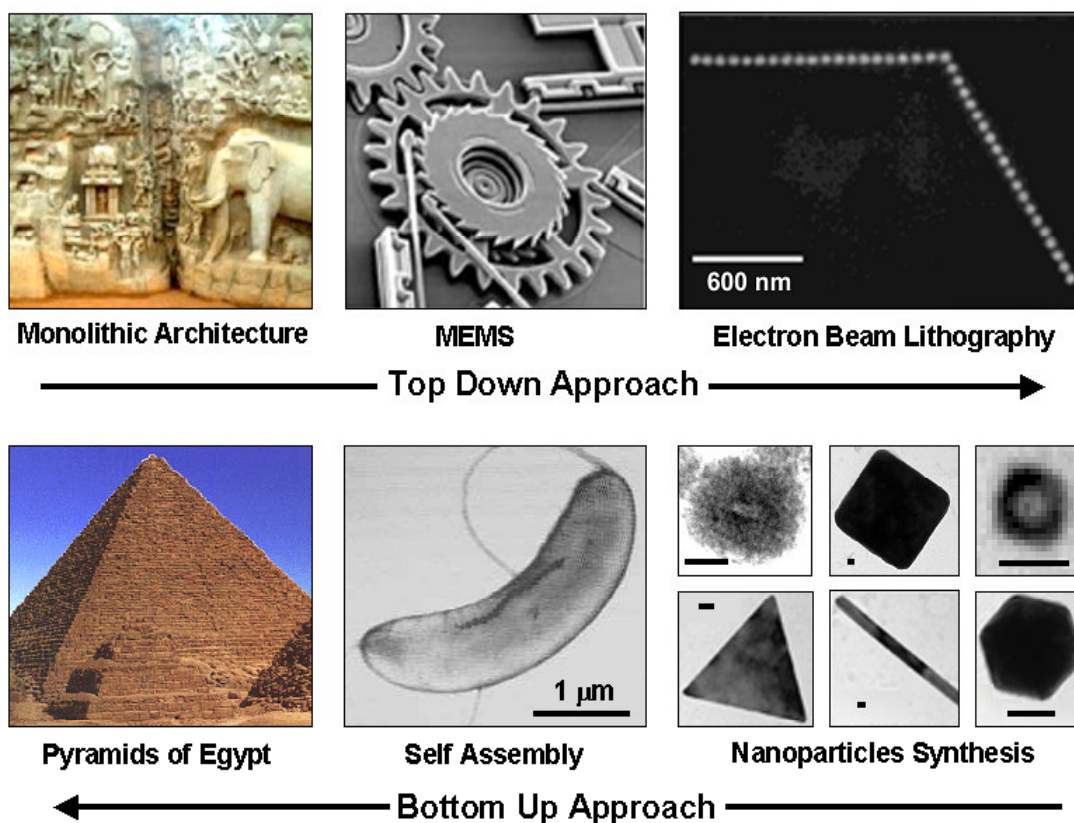


Figure 1.2 Cartoon showing the fabrication of materials by the top–down and bottom–up approaches. The monolithic architecture shown in the cartoon is a part of the rock temple at Mahabalipuram, India. The scale bars shown in “Nanoparticles Synthesis” panel correspond to 20 nm. [Courtesy: The images of MEMS, electron beam lithography, and magnetosomes self–assembly in magnetotactic bacteria *Magnetospirillum magnetotacticum* have been taken from references 2–4 respectively].

During efforts towards creation of miniaturized materials, it has been realized that materials in nano–dimensions usually exhibit properties that are very different from their bulk counterparts. Increasing knowledge about the unique properties of nanoparticles has led to renewed interest in their potential applications. Nanoparticles have been around for a long time; presumably the first nanoparticle was recognized in 1570 with aurum potable (potable gold) and luna potable (potable silver) which alchemists used as elixirs [5–8]. Unfortunately, they did not make the consumer immortal, as is evident by the fact that those alchemists are not among us today. However, one of the oldest applications of nanoparticles that we come across in literature is the use of gold nanoparticles for staining glasses; a famous example is the

Lycurgus cup that dates back to 4th century AD [9–11]. In the present age indeed, the ‘nanotechnology mania’ is sweeping through essentially all the fields of science and technology and the public is becoming aware of the quote of Nobel Laureate, Richard Smalley: “Just wait – the next century is going to be incredible. We are about to be able to build things that work on the smallest possible length scales, atom by atom. These little nanothings will revolutionize our industries and our lives” [12]. This is becoming more and more evident in the form of potential applications of nanoparticles, which extend to wide-ranging areas such as catalysis [13–14], biosensors [15–18], diagnostics [19], cell labelling [20–22], solar cells [23–24], fuel cells [25], photonic bandgap materials [26], single electron transistors [27–28], non-linear optical devices [2, 29–31], information storage [32], refrigeration [33], chemical/optical computers [34], harder metals [35], surface enhanced Raman spectroscopy [36], self cleaning paints [37], environmental clean up [38–44], and improved national security [45–46] to name a few and the list goes on [37]. The realization of their various potential applications is only limited by our imagination [47–52].

A remarkable aspect of nanomaterials is that a number of factors can influence their physical, chemical, optical, electronic and magnetic properties. The factors that can strongly modulate their properties include their size [53–58], shape [59–61], surface composition [62–65], dielectric environment [66–69] and the interparticle interactions [70–74]. Such remarkable variations in properties of nanomaterials are due to their dimensions being comparable to the de Broglie wavelength of the charge carriers, which modify their properties significantly [75–76]. One of the readily perceptible properties in case of metal nanoparticles is their colour. The colour of metal nanoparticles originates due to surface plasmons *i.e.* the coherent charge density oscillations [77]. Surface plasmon is a special phenomenon, which is observed in metal nanoparticles at nanoscale. Similarly, when the size of other nanomaterials is below certain size regime (generally few nanometers), size quantization effects become more important, leading to discrete energy levels in the conduction band and can be understood by making analogy with the case of particle-in-a-box model [78–79]. The quantum size effects have been well studied in case of semiconducting nanoparticles and the energy level spacing for a spherical particle of radius R is predicted to be inversely proportional to R^2 [80–82]. Thus, with decreasing size, the

effective bandgap increases and the relevant absorption and emission spectra blue-shifts. As a consequence, the developments, which were initially concerned with metal nanoparticles led to the realization that essentially all solid materials in nanoscale would be of interest.

The science of ceramic/oxide nanoparticles is no exception and this field of nanoscience is exciting due to the fact that many of the ceramic systems of interest have been studied extensively in the bulk form and therefore provides ready comparisons with nanoparticulate systems [83]. A beneficial consequence of the reduced size of oxide nanoparticles, and for that matter for all the nanoparticle systems, is the large increase in the surface to volume ratio of the nanomaterials in comparison with their bulk counterparts. Because of the huge number of atoms at the surface and their limited availability within the lattice, the chemistry of oxide nanoparticles is greatly affected by the defect sites present both within the lattice (point defects) as well as on the surface (planar defects). Point defects arise either due to the absence of the constituent atoms/ions on the lattice sites or their presence in interstitial positions. Even the presence of foreign atoms/ions in the lattice causes point defects. These point defects result in the displacement of neighbouring atoms/ions because of the polarization in surrounding region, and hence modify the crystal lattice. However, since the creation of point defects is generally an endothermic process, the intrinsic defect concentration in binary oxides is extremely low ($\sim 10^{-5}$ at around $0.8 T_m$). On the other hand, the surface of oxide nanocrystals constitutes considerable amount of planar two-dimensional defects in the form of grain boundaries, stacking faults and crystallographic shear planes. These extrinsic defects lead to tilt boundaries (array of period space or edge dislocations), twist boundaries (array of screw dislocations), twin boundaries (a layer with mirror plane symmetry with respect to the rotation of one part of the crystal, on a specific plane, with respect to another) and/or antiphase boundaries (across which the sublattice occupation becomes interchanged) in nanooxides. The highly ionic nature of some materials, especially TiO_2 , ZrO_2 , MgO and Al_2O_3 , further promotes the formation of many stable defect sites, including edges, corners, and anion/cation vacancies. Different morphologies of oxide nanomaterials may also alter their surface chemistry and adsorption characteristics, hence imparting important properties [44].

Additionally, phase purity is generally difficult to achieve, especially for oxides containing more than one cation [84].

Though the traditional ceramic scientists would prefer a phase pure material without any defects for fundamental studies, it is remarkable to note that the greater availability of the surface, along with these defects and phase impurities may sometimes lead to very interesting physical and chemical properties to oxide nanomaterials [85]. For instance, oxide nanoparticles can be compressed at relatively low temperature into solids that possess better flexibility and malleability than traditional ceramics [85]. In addition, defect sites in nanooxides are considered to be active sites for many interesting reactions, including methane activation [86], D₂-CH exchange [87], CO oligomerization [88] as well as oxygen exchange in CO₂ [89] and H₂O [90]. Nanocrystalline ZrO₂-SO₄ is considered to be a solid superacid catalyst which possesses acid strengths much higher than that of concentrated sulphuric acids and is capable of isomerization of *n*-alkanes to branched alkanes under mild conditions [91–92].

However, an intricate yet fascinating consequence of the size and defect dependent applicability of nanomaterials is that the properties of nanocrystals obtained by various routes cannot be generalized, since various synthesis routes may lead to altering defect conditions in these nanocrystals. The display of unique properties by the nanoparticles that can be controlled by many external and internal factors and the scope for diverse applications makes the synthesis of such nanomaterials extremely important and therefore a number of routes for synthesis of nanomaterials are evolving (Figure 1.3).

So far, synthesis of inorganic nanomaterials has been demonstrated mainly by physical and chemical means. Some of the physical routes leading to successful synthesis of nanophase materials, especially oxide powders are vapour condensation techniques [93–100], spray pyrolysis [101–106], thermochemical decomposition of metal-organic precursors in flame reactors [107–110] and other aerosol processes named after the energy sources applied to provide the high temperatures during gas-particle conversion.

The Liquid phase chemical methods for the synthesis of inorganic nanoparticles including metal oxides have received wider acceptance than physical

methods and are the most commonly followed route. This increasing interest in chemical processing of nanoscale particles of metal oxides and other materials is clearly indicated by the number of reports and reviews on this subject [111–120].

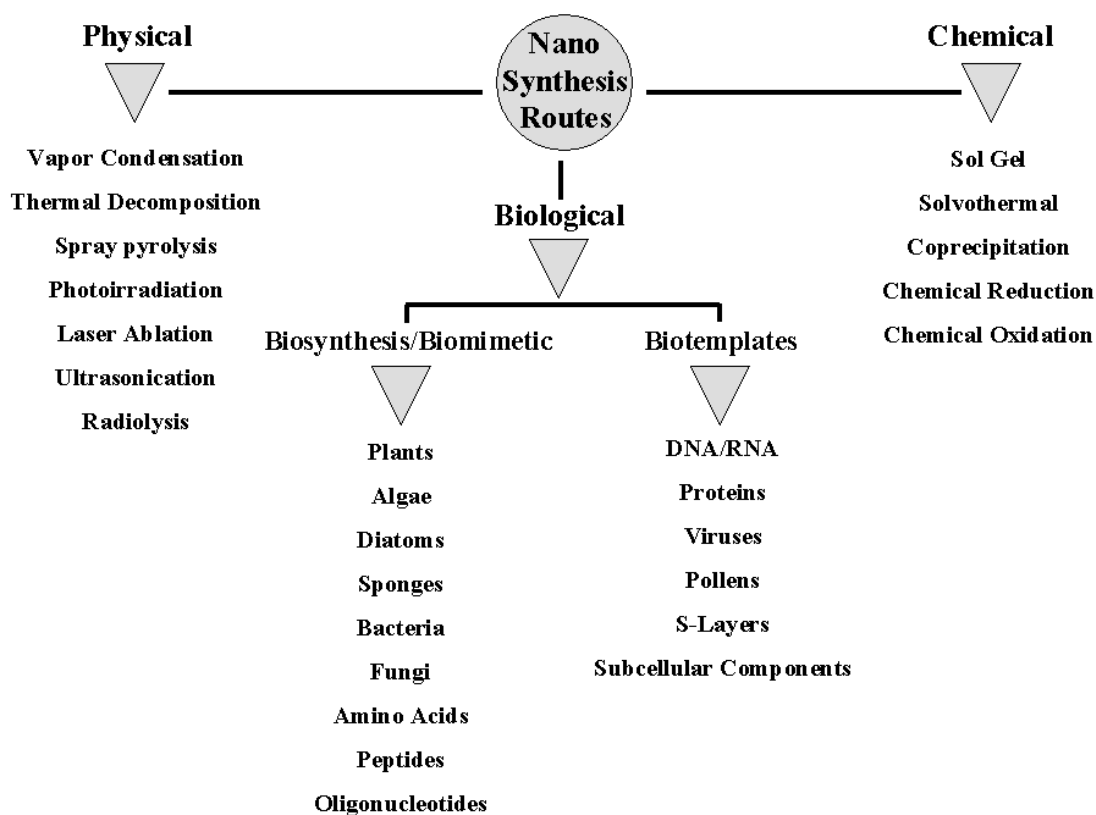


Figure 1.3 Schematic outlining the various approaches for the synthesis of nanoparticles.

Chemically, inorganic nanoparticles can be synthesized by reduction or oxidation of metal ions or by precipitation of the necessary precursor ions in solution phase. The control of size, shape, stability and the assembly of nanoparticles is achieved by incorporating different capping agents, solvents and templates. Capping agents that have been used, range from simple ions to polymeric molecules and even biomolecules [121–126]. As a solvent, though water is largely used, use of organic solvents [127–128], ionic liquids [129] and supercritical fluids [130–131] has also been demonstrated. Similarly, many soft and rigid templates such as micelles [132–134], polymeric molecules [135–136], DNA [137–138], Tobacco Mosaic Virus [3, 139–141], mesoporous materials and many more including preformed nanoparticles [142] have been employed in order to gain control over the formation and assembly of nanoparticles.

Evidently, nanoparticle synthesis has gained due focus and the scope for new synthesis methods is increasing constantly with innovative contributions. Though the

chemical and physical routes of nanomaterials synthesis have principally dominated the nanosphere, recently, there is a growing attention towards the advantageous use of biological means for nanoparticle synthesis. In the following sections of this chapter, the focus is on biological routes to nanomaterials synthesis with brief introductions to:

- 1) *Motivation behind this thesis*
- 2) *Biomineralization in natural habitats*
- 3) *Biomimetic approaches for imitating natural biomineralization*
- 4) *Nature's way of doing biomineralization in laboratory*

1.2 Nature: An Inspiration to Nanomaterials Synthesis

Mother Nature is the most efficient architect of extremely specialized materials, which are constructed, indeed engineered, by the Nature herself, in order to exert specific biological functions [143–144]. During evolution, Nature has ingeniously created an impressive variety of inorganic crystals [145–146]. Scientists and engineers have always been fascinated by the marvelous structures and functional properties of the materials formed within the living systems [147–150]. The way biological systems fabricate structural and functional inorganic materials with precise dimensions and controlled morphology in a reproducible manner and above all, in an environment nurturing manner, defies any possible description. These very basic features have lured the nanotechnologists towards biological systems to learn and improve the skills for precise fabrication of nanomaterials. While the Nature is engrossed in devising splendid biomaterials using complicated yet noble biochemical pathways, biochemists and materials scientists struggle to elucidate the complexity of Nature's artwork in their respective laboratories. Can we learn to fabricate tailor-made materials from Nature? This thesis is an attempt, a primitive step in this direction.

1.3 Nature: The True Habitat for Biomineralization

Biomineralization as a field of study involves the intersection of many scientific disciplines including biochemistry, molecular biology, geology, inorganic chemistry, crystallography, materials science and condensed matter physics [151]. The term 'biomineralization' symbolizes the formation of inorganic solids (biominerals) by organisms. Biominerals have a variety of biological functions in

these organisms, which rely on hierarchical structuring of bioorganic–inorganic composites on several length scales ranging from the Angstrom to the centimeter level [145–146]. This phenomenon is so widespread in the biological world that survival of many species depends on their ability to deposit the inorganic matrix quickly and efficiently. More than 60 biominerals are currently known, most of which incorporate silicates, iron oxides, calcium carbonates, calcium phosphates, or sulfides [142–143, 147–150, 152].

The complex nature of inorganic materials formed in association with living organisms is not only expressed at the macro-scale but also resides in the mesoscopic, microscopic and nanoscopic organization of biomineralized structures [153]. Indeed, different length scales bring into operation different controlling forces and hence the hierarchical orders of construction [153]. Despite these complicated hierarchical structures, one finds it most interesting to observe that the smallest building blocks in such materials are generally of the nanometer length scale. For instance, the bone structure consists of mineral crystal platelets of thickness around few nanometers, embedded in a collagen matrix [154–156].

Minerals, macromolecules and water are the major components of these biomaterials. The biomaterials formed under relatively controlled conditions can be classified into three major groups, based on organization of their mineral constituents [144]. Type I consists of multicrystalline arrays, in which all the individual crystals are aligned at least in one direction, and often in all the three directions. The best-known examples of such materials are bones, teeth and shells of various types. In Type II, a single crystal or a limited array of relatively larger crystals constitute the entire structure. Echinoderms are best known for forming such large single crystal skeletal structures of calcite [144, 157]. Type III consists of biological materials containing an amorphous mineral, the most common being amorphous silica synthesized by diatoms and sponges. These structures can vary enormously in size and particularly in shape. A variety of minerals are synthesized in Nature and they can be traced to various groups of organisms including plants, animals and microorganisms (Table 1.1). The component that perhaps mainly distinguishes natural materials from synthetic materials is the presence of biomacromolecules as an intimate mix with the mineral phases at all the different hierarchical levels, starting at the nanometer scale. It was recognized that many of these macromolecules have a

common chemical attribute that they are rich in carboxyl groups [143, 158]. These may be the constituents of protein and/or polysaccharide moieties. Many of these macromolecules also possess phosphate and/or sulfate groups in addition to the carboxyl groups. The presence of all these charged groups makes these macromolecules excellent candidates for interacting with the mineral ions in solution or with the surfaces of the solid phase [143, 158].

Table 1.1 Various biominerals and their roles in biological systems [159–164]

Biogenic minerals	Biological system	Biological location	Biological function
Calcium carbonate (calcite, vaterite, aragonite)	Plants, aves, mammals, many marine organisms, coccoliths	Mollusk shell, eye lens, crab cuticle, egg shells, leaves, inner ear	Exoskeleton, optical, mechanical strength, protection, gravity receptor, buoyancy device, calcium storage [165–169]
Calcium phosphate (hydroxyapatite, dahllite, octacalcium phosphate)	Mammals, fish, bivalves	Bone, teeth, scales, gills, gizzard plates, Mitochondria	Endoskeleton, ion store, cutting/grinding, protection
Calcium oxalates (whewellite, wheddellite)	Plants, fungi, mammals	Leaves, hyphae, renal stones	Protection/deterrent, calcium storage/removal, pathological
Iron oxides (magnetite, greigite, goethite, lepidocrocite, ferrihydrite)	Bacteria, algae, dinoflagellates, chitons, trouts, euglena, human brain, salmons	Intracellular, teeth, head, filaments, ferritin protein	Magnetotaxis, magnetic orientation, mechanical strength, iron storage [169–181]
Sulfates (gypsum, celestite, barite)	Jellyfish, acantharia, loxodes, chara, photosynthetic bacteria	Statoconia, cellular, intracellular, tatoliths	Gravity receptor, skeleton, gravity device/receptor [146]
Silicon oxides (amorphous silica)	Diatoms, radiolarians, sponges, plants, microbes, etc.	Cell wall, cellular, leaves	Exoskeleton, protection, mechanical support, plant nutrient, resistance against pests and predators [182]

Among various biominerals, silica in particular, is technologically one of the most important inorganic compounds. Silica is extensively used for a wide range of applications as catalyst supports, as fillers in polymeric items, as separation media as well as in biological applications like cell therapy, immunoassays, bacteria sensing, nitric oxide release, biocatalysis and biosorption [115, 183–190]. It has been estimated that the global market for silica is around two billion dollars per year [185], thus emphasizing its significant role in everyday life.

The preparation of synthetic silica, which typically occurs at extreme of temperature, pressure and pH conditions, generally results in poor control over the structure and processing of the product [115]. Biological organisms, in contrast, are able to uptake, store and process soluble silicon as well as mould it with great sophistication into ornate hierarchical patterned biosilica (Figure 1.4) [147, 151–152, 191–195]. The silica formation process in organisms is termed as biosilicification.

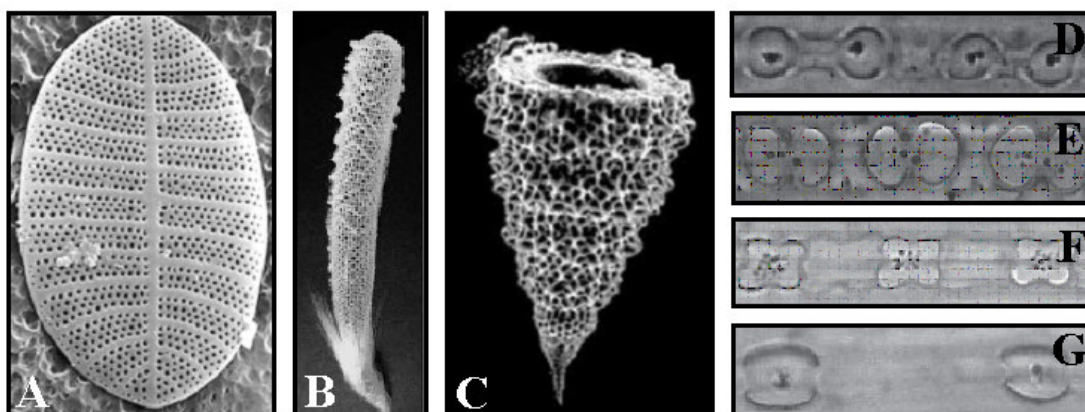


Figure 1.4 Micrographs of ornate biosilica patterns. (A) Frustule of diatom *Cocconels*, (B) spicule skeleton of sponge *Euplectella*, (C) silica skeleton of a radiolarian, (D–G) silica bodies of specific shapes found in the epidermal cells of plants viz. *Aristida setigera* (D), *Brachiaria jubata* (E), *Apochiton burttii* (F), *Astrebla squarrosa* (G) of family Poaceae (grasses) [Images courtesy: references 196–199].

In order to reveal and understand Nature’s secrets surrounding biosilicification, scientists have been systematically studying biosilica formation in diatoms, sponges and grasses [147, 191]. Several investigations have involved the selective removal of biosilica and isolation of biomolecules associated with the biosilica [200–205]. Table 1.2 summarizes the information about bioextracts obtained from various biosystems and their proposed roles in biosilicification [206].

Table 1.2 Various bioextracts from biogenic silica systems and their proposed or observed role(s) in biosilicification [206]

Biological system	Bioextracts	Proposed role in biosilicification
Diatoms	Proteins and carbohydrates	Catalysis of siloxane bond formation <i>via</i> C–O–Si between Ser/Thr and silanol [200]
	Glycoproteins	Stabilization of silica thus creating local supersaturation of silicic acid [201]
	Silaffins and long chain polyamines	Formation of spherical particles and particle networks <i>in vitro</i> [205, 207–209]
Sponges	Silicatein proteins	Catalysis of silica polymerization <i>in vitro</i> [203, 210–211]
Grasses	Proteins and carbohydrates	Increased rates of catalysis of silica polymerization, control over nucleation and growth for silica production [202, 204, 212–213]

1.4 Biomimetic Nanoengineering: The Art of Imitating Nature

The essence of today's science finds its full expression in the words of the epitome of the artist–scientist Leonardo da Vinci: “*Where Nature finishes producing its own species, man begins, using natural things and with the help of this nature, to create an infinity of species.*” Nobel laureate Jean–Marie Lehn used these words to emphasize the existence of an obvious gap between chemistry and biology and the immense possibilities that the amalgamation of these two disciplines can bring in [214]. Though the ornate hierarchical nanomaterials synthesized in Nature are of high-value, one of the major limitations with use of these materials is that their consistent harvest from natural habitats might pose a great danger to the environmental niche. Inspired by these elegant nanomaterials, coupled with the fact that it is not easy to culture marine organisms like diatoms and sponges under artificial conditions, scientists have started making efforts towards developing bioinspired/biomimetic methodologies for nanomaterials synthesis [215].

During the past several years, biomimetic synthesis approaches, which enable silicification under ambient conditions and circumneutral pH, have been developed as

a consequence of isolating bioextracts from biosilica forming organisms. Biomimetic approaches make use of organic biomolecules and their synthetic analogues, which control *in vitro* bioinspired/biomimetic silicification by catalysis, aggregation, structure direction (templating/scaffolding) or a combination thereof [206].

In the oceans, organisms take up silicic acid from the environment and then process it into biosilica (in the form of hydrated $\text{SiO}_2 \cdot n\text{H}_2\text{O}$ [216]) using specific biomolecules. A computational model was developed in order to understand the interactions between the organic biomolecules or the organic matrix and the biosilica precursors/intermediates in diatoms and these organic moieties were proposed to catalyze the condensation of silanol groups between adjacent silicic acid molecules [200, 217–218]. Proteins, named silicateins were extracted from the sponge *Tethya aurantia*, sequenced and their role in biosilicification studied [203, 210–211]. Silicatein was shown to promote hydrolysis and condensation of tetraethoxysilane (TEOS) under *in vitro* conditions and three active residues of silicateins *viz.* serine, histidine and asparagine were proposed to catalyze the hydrolysis of TEOS [210–211].

Similarly, phosphorylated native silaffin proteins isolated from the diatom *Cylindrotheca fusiformis* have been found to be active for *in vitro* silica synthesis [219]. The *in vitro* silica synthesis was also achieved using the R 5 peptide (a nineteen amino acid polypeptide derived from silaffin protein) and three genetically engineered proteins with known secondary structures (α helix rich, β sheet rich and random coil) [220–221]. In addition, extracts of higher plants like *Equisetum telmateia* were observed to promote synthesis of crystalline silica (quartz) under *in vitro* conditions, which is usually produced by high temperature/pressure procedures [204, 213].

Recently Coradin and Lopez proposed an elegant model suggesting that cationic molecules also drive silica polymerization [222]. Belton and co-workers studied the effect of a series of amino acids and lysine oligomers (monomer to pentamer) and polymer for their respective roles in bioinspired silica synthesis [223]. Subsequently, a range of peptide-based and synthetic macromolecule-based compounds have been used for *in vitro* silica synthesis and their roles in bioinspired silicification have been proposed (Table 1.3).

Table 1.3 Proposed roles of various (poly)peptides and synthetic molecules in bioinspired silicification [206]

Bioinspired molecules	Proposed role in biosilicification
Poly-L-lysine	Silica precipitation and formation of novel structures [217, 224–227]
Poly-L-arginine	Precipitation of gel like and particulate silicas [224, 226–229]
Poly-L-histidine	Formation of nearly spherical silica particles [230]
R 5 peptide	Spherical silica particles, fibre like silica structures and silica patterned polymeric hologram [205, 228, 230]
Mutants of R5 peptide	Precipitation of particulate silica only when peptide contained terminal RRIL motif [231]
Poly[(L-alanine) ₃₀ - <i>b</i> -(L-lysine) ₂₀₀]	Non-ordered silica [232]
Poly[(L-glutamine) ₃₀ - <i>b</i> -(L-lysine) ₂₀₀]	Non-ordered silica [232]
Poly[(L-serine) ₃₀ - <i>b</i> -(L-lysine) ₂₀₀]	Non-ordered silica [232]
Poly[(L-tyrosine) ₃₀ - <i>b</i> -(L-lysine) ₂₀₀]	Non-ordered silica [232]
Poly[(L-cystein) _n - <i>b</i> -(L-lysine) _m]; n = 10/30/60; m = 200/400	Spheres, elongated globules and columnar silica [232]
Poly[(L-cystein) ₃₀ - <i>b</i> -(L-glutamate) ₂₀₀]	Non-ordered silica [232]
Peptides obtained from biopanning	Sphere-like silica [233]
Genetically engineered proteins	Spherical, elongated and sheet-like silica particles [221, 234]
Poly(allylamine hydrochloride)	Spherical and elongated silica particle formation [222, 235]
Polyallylamine	Precipitation of sphere-like silica [224]
Polyethyleneimines	Formation of nearly spherical particles [224, 236]
Lysine oligomers	Controlled catalysis and aggregation
Cellulose	Stabilization of primary particles

1.5 Biomineralization in the Laboratory: Nature's Way

The conviction that Nature has evolved the best processes for synthesis of inorganic materials in natural habitats (*in situ* synthesis), coupled with the increasing pressure to develop green chemistry routes for nanomaterials' synthesis, have encouraged biomaterial scientists to imitate Nature by various biomimetic approaches (*in vitro* synthesis); however, *in vitro* approaches still have some lacunas in comparison with the *in situ* materials synthesis. For instance, the major differences between the biological and biomimetic silica formation can be understood if we compare the following aspects of mineral formation – precursor concentration, pH at which biosilica polymerization occurs, temperature, time required for biosilica deposition, control over the process and product, involvement of other molecules (ions, organic molecules, membranes, *etc.*) and reproducibility [189]. Biosilicifying organisms typically start with an undersaturated solution of silicic acid; on the other hand, the precipitation of silica *in vitro* from an undersaturated solution of silicic acid (≤ 1 mM) is yet to be demonstrated [189]. Preparation of particulate silica synthetically requires moderately high pH; biosilicification in contrast, occurs at mildly acidic to neutral pH [238]. Biological silicification imposes great control over silica formation process as well as on the form of biosilica, while there is not much control under *in vitro* synthesis conditions. Other possible regulating factors present in biological systems include microtubules, filaments and cell organelles [239], which are absent under *in vitro* conditions. Another major difference between biological and bioinspired silicification is that the former takes place in a genetically controlled environment. Under the light of these facts, it can be argued that if *in vivo* materials synthesis routes (involving whole cell or organism) could be evolved to work *in silico* (under laboratory condition), this might be able to fill in the gap between *in situ* and *in vitro* materials synthesis.

It is interesting to note that though microorganisms such as bacteria [240–241] and yeast [242] have been previously employed for remediation of toxic metals because of their inherent capability of coping with high metal ion concentration through specific resistance mechanisms [243–245], the possibility of using such microorganisms in the deliberate synthesis of nanomaterials is a relatively recent phenomenon. Some of the earliest reports on the accumulation of inorganic particles in natural habitats of microorganisms were those of gold in precambrian algal

blooms [246], gold in algal cells [247], gold in bacteria [248], CdS in bacteria [240], CdS in yeast [249–250], ZnS in sulfate reducing bacteria [251], and magnetite in bacteria [252]. Inspired by these observations, various investigators started using microbes for deliberate synthesis of various nanomaterials which include bacteria for the synthesis of gold [253–256], silver [256–259], gold–silver alloy [256], CdS [260–262], ZnS [263], iron sulfide [264–265] and magnetite [266–269]; yeast for the synthesis of PbS [250] and CdS [270]; and algae for the synthesis of gold nanoparticles [271]. In all these studies, nanoparticles are formed intracellularly and hence cannot be used directly without suitable treatment of biomass to release these particles.

During the past few years, Sastry and co-workers have screened approximately 200 genera of fungi and observed that fungi, when challenged with aqueous metal ions, lead to the formation of a range of nanomaterials, both intra–(*Verticillium* sp.) [272–273] and extracellularly (*Fusarium oxysporum*) [274–275]. Sastry's Group identified various Genera of fungi for the extracellular synthesis of gold [274], silver [275], gold–silver alloy [276], and CdS [277] nanoparticles, as well as intracellular formation of gold [272] and silver [273] nanocrystals. In an attempt to make the biological synthesis route compete with chemical routes of synthesis, Sastry and co-workers showed that fairly monodisperse gold nanoparticles could be synthesized using the extremophilic actinomycete, *Thermomonospora* sp. [278]. The *in vitro* synthesis of CdS nanoparticles using proteins from fungi, along with external cofactors was also demonstrated [276]. The development of a rational nanoparticle biosynthesis procedure using specific enzymes secreted by fungi has many attractive associated features. Fungi generally produce copious quantities of enzymes and are easily cultured in the laboratories.

It is interesting to know that even a number of plants are capable of accumulating gold in large percentage within them, one of them is *Equisetum* sp. (horsetail) [279–281]. This provides a possibility to explore plants as a means for synthesizing metal nanoparticles analogous. Indeed, Yacaman and co-workers have shown that gold and silver nanoparticles are formed within different parts of live Alfalfa plant on uptaking the corresponding metal ions from solid media [282–283]. In an attempt towards deliberate synthesis of metal nanoparticles using plants, Sastry and co-workers showed that various plant extracts like that of

Geranium sp. [284–285], neem (*Azadirachta indica*) [286], lemon grass (*Cymbopogon flexuosus*) [287–288] and aonla (*Emblica officinalis*) [289] can be used for the size and shape-directed biosynthesis of gold [286–290], silver [284, 286, 290] and gold–silver bimetallic core–shell nanoparticles [286].

It thus appears that extracellular biological synthesis of nanomaterials involving whole cell microorganisms like fungi offers an edge over other synthetic routes, as far as scale up issues and commercial implications of the technology are concerned, since fungi can be easily cultured under controlled environments. In this thesis, we have explored the potential of fungus-based biological synthesis routes for the extracellular biosynthesis of various oxide nanoparticles with interesting properties. A brief outline of the work presented in this thesis is given in the next section 1.6, with elaborate discussions in separate chapters.

1.6 Outline of the Thesis

The work presented in this thesis describes the biosynthesis of metal oxide nanoparticles using a fungus *Fusarium oxysporum*, in an attempt to extend the biological synthesis protocols towards a possibility of scale-up. An important outcome of this approach is that a vast range of oxide nanoparticles (binary as well as ternary) can be synthesized using biological route. These nanoparticles possess unusual yet interesting functional properties. An attempt has been made to harvest the silica nanoparticles from naturally available raw materials as well as agro-industrial by-products. Further, the biosynthesized titania nanoparticles have been shown to possess photocatalytic and antimicrobial activity under diffused indoor and solar light conditions. The chapter wise discussion of these studies is as follows:

Chapter 2 describes the various instrumentation techniques used in this study. The oxide nanoparticles formed by a fungus-mediated approach were observed using various microscopy tools *viz.* scanning electron microscopy (SEM), transmission electron microscopy (TEM), high-resolution transmission electron microscopy (HR-TEM), optical microscopy and atomic force microscopy (AFM). The nanoparticles formation and reaction kinetics were established using various techniques *viz.* UV-visible absorption spectroscopy (UV-vis), Fourier transform infrared spectroscopy (FTIR), X-ray photoemission spectroscopy (XPS), X-ray diffraction (XRD) studies, energy dispersive X-rays analysis (EDX),

thermogravimetric analysis (TGA) and differential scanning calorimetry (DSC). Temperature- as well frequency-dependent dielectric measurements on ferroelectric barium titanate nanoparticles were also performed. Moreover, ferroelectric behaviour of individual barium titanate nanoparticles was probed using Kelvin probe/surface potential microscopy (SPM). In addition, the biomolecules involved in the biosynthesis process were studied using polyacrylamide gel electrophoresis (PAGE).

Chapter 3 discusses the room-temperature, extracellular, fungus-mediated biosynthesis of oxide nanoparticles in aqueous environment. Oxide nanoparticles *viz.* silica (SiO₂), titania (TiO₂) zirconia (ZrO₂) and barium titanate (BaTiO₃) of sub-10 nm dimensions could be synthesized under ambient conditions by reaction of fungus *Fusarium oxysporum* with appropriate chemical precursors for 24 hours. The fungal proteins involved in the hydrolysis of precursors to yield oxide nanoparticles were investigated and involvement of low molecular weight proteins of *ca.* 20–30 kDa in the biosynthesis process was established. In addition, tetragonality could be established for the first time in sub-10 nm barium titanate nanocrystals. Temperature and frequency dependent dielectric measurements demonstrated the ferroelectric behaviour of sub-10 nm barium titanate particles. Furthermore, SPM was also utilized to show the read/write capability on individual barium titanate particles.

Chapter 4 deals with the use of naturally available raw materials as well as agro-industrial by-products for the fungus-mediated bioleaching of oxide nanoparticles of diverse morphologies. In chapter 3, we demonstrated the use of chemical precursors for the synthesis of oxide nanomaterials. We have extended the concept and tried to make the process fully biogenic and eco-friendly by substituting the chemical precursors with naturally available raw materials. White sand, which consists of complex silicates, was exposed to the fungus *Fusarium oxysporum*. The reaction results in room temperature synthesis of spherical, porous silica particles, which on further calcination at 400 °C for 2 h, form hollow silica particles. In another experiment, rice husk, which consists of huge amount of amorphous silica, was exposed to the fungus *F. oxysporum*. The reaction of rice husk with the fungus results in the extracellular bioleaching of flat, porous silica nanostructures, which, on calcination at 400 °C for 2 h, form flat plate-like silica structures. It is interesting to note that this reaction results in room-temperature biotransformation of amorphous silica in rice husk to extracellular crystalline silica particles. The proteins bound on to

the surface of silica nanoparticles were also investigated after mild dissolution of silica using ammonium fluoride treatment. In a separate experiment, zircon sand, which consists of complex zirconium silicates, was exposed to the fungus *F. oxysporum*. Interestingly, the reaction results in selective bioleaching of silica component from zircon in the form of extracellular silica nanoparticles, which in turn results in enhancement of high dielectric zirconia component in zircon sand.

Chapter 5 demonstrates the photocatalytic applications of a new class of biosynthesized anatase titania based material, which is significantly modified with nitrogen, carbon and fluorine (referred as NCF-TiO₂). The photocatalytic activity of NCF-TiO₂ has been shown in terms of its capability for degradation of environmentally toxic dyes (Congo Red, Malachite Green and Basic Fuchsin) as well as for the inhibition of potentially destructive microbes under indoor- and solar-light conditions. NCF-TiO₂ nanoparticles were found to exhibit strong antibacterial, antifungal and antispore activity against a vast range of microorganisms under indoor light conditions.

Chapter 6 includes a brief summary of the work presented in the thesis and the scope for possible further research in these areas.

1.7 References

- [1] Feynman, R. P. *Eng. Sci.* **1960**, *23*, 22.
- [2] Maier, S. A. *et al.*, *Adv. Mater.* **2001**, *13*, 1501.
- [3] Ongaro, A. *et al.*, *Chem. Mater.* **2005**, *17*, 1959.
- [4] Frankel, R. *Hyperfine Interactions* **2003**, *151–152*, 145.
- [5] Antonii, F. *Panacea Aurea–Auro Potabile*, Bibliopolio Frobeniano, Hamburg **1618**.
- [6] Kunckels, J. *Nuetliche Observationes oder Anmerkungen von Auro und Argento Potabili*, Schutzens, Hamburg **1676**.
- [7] Helcher, H. H. *Aurum Potabile oder Gold Tinstur*, J. Herbord Klossen, Breslau and Leipzig **1718**.
- [8] Ostwald, W. *Kolloid Z.* **1909**, *4*, 5.
- [9] Savage, G. *Glass and Glassware*, Octopus Book, London **1975**.

- [10] Wagner, F. E. *et al.*, *Nature* **2000**, 407, 691.
- [11] Turkevich, J. *Gold Bull.* **1985**, 18, 86.
- [12] Smalley, R. *Congressional Hearings*, **Summer 1999**.
- [13] Roucoux, A.; Schulz, J.; Patin, H. *Chem. Rev.* **2002**, 102, 3757.
- [14] Lewis, L. N. *Chem. Rev.* **1993**, 93, 2693.
- [15] Niemeyer, C. M. *Angew. Chem. Int. Ed.* **2001**, 40, 4128.
- [16] Niemeyer, C. M. *Angew. Chem. Int. Ed.* **2003**, 42, 5974.
- [17] Parak, W. J. *et al.*, *Nanotechnology* **2003**, 14, R15.
- [18] Caski, A.; Maubach, G.; Born, D.; Reichert, J.; Fritzsche, W. *Single Mol.* **2002**, 3, 275.
- [19] Rosi, N. L.; Mirkin, C. A. *Chem. Rev.* **2005**, 105, 1547.
- [20] Parak, W. J.; Pellegrino, T.; Plank, C. *Nanotechnology* **2005**, 16, R9.
- [21] Bruchez, M.; Moronne, Jr. M.; Gin, P.; Weiss, S.; Alivisatos, A. P. *Science* **1998**, 281, 2013.
- [22] Chan, W. C. W.; Nie, S. M. *Science* **1998**, 281, 2016.
- [23] Hagfeldt, A.; Graetzel, M. *Acc. Chem. Res.* **2000**, 33, 269.
- [24] Bueno, J. T.; Shchukina, N.; Ramos, A. A. *Nature* **2004**, 430, 326.
- [25] Fichtner, M. *Adv. Eng. Mater.* **2005**, 7, 443.
- [26] Moran, C. E.; Steele, J. M.; Halas, N. J. *Nano Lett.* **2004**, 4, 1497.
- [27] Simon, U. *Nanoparticles: From Theory to Application*, Schmid, G. (ed.) Wiley-VCH, Weinheim, Germany **2004**.
- [28] Edelstein, A. S.; Cammarata, R. C. (eds.) *Nanomaterials: Synthesis, Properties, and Applications*, Institute of Physics Publishing, Bristol, U.K. **1996**.
- [29] Maier, S. A.; Brongersma, M. L.; Kik, P. G.; Atwater, H. A. *Phys. Rev. B* **2002**, 65, 193408.
- [30] Wang, Y. *Acc. Chem. Res.* **1991**, 24, 133.
- [31] Yoffe, A. D. *Adv. Phys.* **1993**, 42, 173.

- [32] Matejivic, E. *Annu. Rev. Mater. Sci.* **1985**, *15*, 483.
- [33] Shull, R. D.; McMichael, R. D.; Swartzendruber, L. J.; Bennett, L. H. *Studies of Magnetic Properties of Fine Particles and Their Relevance to Materials Science*, Pormann, J. J.; Fiorani, D. (eds.) Elsevier Publishers, Amsterdam **1992**, p. 161.
- [34] Heath, J. R.; Kuekes, P. J.; Snider, G. S.; Williams, R. S. *Science* **1998**, *280*, 1716.
- [35] Andres, R. P. *et al.*, *J. Mater. Res.* **1989**, *4*, 704.
- [36] Li, X. *et al.*, *Langmuir* **2004**, *20*, 1298.
- [37] Roco, M. C.; Williams, R. S.; Alivisatos, P. (eds.) *Interagency Working Group in Nanoscience Engineering and Technology (IWGN) Workshop Report: Nanotechnology Research Directions; Vision for Nanotechnology R and D in the Next Decade*, Int. Tech. Research Institutes, WTEC Division, Loyola College **1999**.
- [38] Kiwi, J.; Gratzel, M. *Angew. Chemie. Int. Ed.* **1979**, *18*, 624.
- [39] Riegel, G.; Bolton, R. J. *J. Phys. Chem.* **1995**, *280*, 1716.
- [40] Boronina, T.; Klabunde, K. J.; Sergeev, G. B. *Environ. Sci. Technol.* **1995**, *29*, 1511.
- [41] Li, Y. X.; Klabunde, K. J. *Langmuir* **1991**, *7*, 1388.
- [42] Lucas, E.; Klabunde, K. J. *Nanostruct. Mater.* **1999**, *12*, 179.
- [43] Khaleel, A.; Kapoor, P.; Klabunde, K. J. *Nanostruct. Mater.* **1999**, *11*, 459.
- [44] Koper, O.; Lagadic, I.; Volodin, A.; Klabunde, K. J. *Chem. Mater.* **1997**, *9*, 2468.
- [45] Koper, O. B.; Lucas, E.; Klabunde, K. J. *J. Appl. Toxicol.* **1999**, *19*, 559.
- [46] Wagner, G. W.; Koper, O. B.; Lucas, E.; Decker, S.; Klabunde, K. J. *J. Phys. Chem. B* **2000**, *104*, 5118.
- [47] Rouvray, D. *Chem. Br.* **2000**, *36*, 46.
- [48] Lawton, G. *Chem. Ind. (London)* **2001**, 174.
- [49] Havancsak, K. *Mater. Sci. Forum* **2003**, *414*, 85.

- [50] Mazzola, L. *Nature Biotech.* **2003**, *21*, 1137.
- [51] Hayat, M. A. (ed.) *Colloidal Gold :Principles, Methods and Application*, Academic Press, San Diego **1989**, Vol. 1.
- [52] Alivisatos, P. *Nature Biotechnol.* **2004**, *22*, 47.
- [53] Buffat, P.; Borel, J. P. *Phys. Rev. A* **1976**, *13*, 2287.
- [54] Brust, M.; Kiely, C. J. *Colloids Surf. A: Physicochem. Eng. Asp.* **2002**, *202*, 175.
- [55] Link, S.; El-Sayed, M. A. *J. Phys. Chem. B* **1999**, *103*, 4212.
- [56] Dick, K.; Dhanasekaran, T.; Zhang, Z.; Meisel, D. *J. Am. Chem. Soc.*, **2002**, *124*, 2312.
- [57] Glinka, Y. D.; Lin, S. H.; Hwang, L. P.; Chen, Y. T.; Tolk, N. H. *Phys. Rev. B*, **2001**, *64*, 085421.
- [58] McHale, J. M.; Auroux, A.; Perotta, A. J.; Navrotsky, A. *Science* **1997**, *277*, 788.
- [59] El-Sayed, M. A. *Acc. Chem. Res.* **2001**, *34*, 257.
- [60] Link, S.; El-Sayed, M. A. *J. Phys. Chem. B* **1999**, *103*, 8410.
- [61] Burda, C.; Chen, X.; Narayanan, R.; El-Sayed, M. A. *Chem. Rev.* **2005**, *105*, 1025.
- [62] Chen, S. *et al.*, *Science* **1998**, *280*, 2098.
- [63] Chen, S.; Pei, R. *J. Am. Chem. Soc.* **2001**, *123*, 10607.
- [64] Zhang, P.; Sham, T. K. *Appl. Phys. Lett.* **2002**, *81*, 736.
- [65] Quinn, B. M.; Liljeroth, P.; Ruiz, V.; Laaksonen, T.; Kontturi, K. *J. Am. Chem. Soc.* **2003**, *125*, 6644.
- [66] Link, S.; Mohamed, M. B.; El-Sayed, M. A. *J. Phys. Chem. B* **1999**, *103*, 3073.
- [67] Templeton, A. C.; Pietron, J. J.; Murray, R. W.; Mulvaney, P. *J. Phys. Chem. B* **2000**, *104*, 564.
- [68] Itoh, T.; Asahi, T.; Masuhara, H. *Appl. Phys. Lett.* **2001**, *79*, 1667.
- [69] Yan, B.; Yang, Y.; Wang, Y. *J. Phys. Chem. B* **2003**, *107*, 9159.
- [70] Al-Rawashdeh, N.; Foss, C. A., Jr. *Nanostruct. Mater.* **1997**, *9*, 383.

- [71] Xu, H.; Bjerneld, E. J.; Kall, M.; Borjesson, L. *Phys. Rev. Lett.* **1999**, *83*, 4357.
- [72] Su, K. H. *et al.*, *Nano Lett.* **2003**, *3*, 1087.
- [73] Kelly, K. L.; Coronado, E.; Zhao, L. L.; Schatz, G. C. *J. Phys. Chem. B* **2003**, *107*, 668.
- [74] Schmid, G.; Simon, U. *Chem. Commun.* **2005**, *6*, 697.
- [75] Zhang, J. H. *Acc. Chem. Res.* **1997**, *30*, 423.
- [76] Raimondi, F.; Scherer, G. G.; Kotz, R.; Wokaun, A. *Angew. Chem. Int. Ed.* **2005**, *44*, 2190.
- [77] Kreibieg, U.; Vollmer, M. *Optical properties of metal clusters*, Springer, Berlin and New York **1995**.
- [78] Schaaf, T. G. *et al.*, *J. Phys. Chem. B* **1997**, *101*, 7885.
- [79] Melinger, J. S. *et al.*, *J. Phys. Chem. A* **2003**, *107*, 3424.
- [80] Brus, L. E. *J. Phys. Chem.* **1986**, *90*, 2555.
- [81] Heath, J. R. *Science* **1995**, *270*, 1315.
- [82] Alivisatos, A. P. *Science* **1996**, *271*, 933.
- [83] Khabibullin, A.; Richards, R. M. *Nanoscale Materials in Chemistry* Klabunde, K. J. (ed.) John Wiley & Sons, New York **2001**, pp. 85–120.
- [84] Rao, C. N. R.; Raveau, B. *Transition Metal Oxides, Structures, Properties and Synthesis of Ceramic Oxides*, 2nd edition, Wiley–VCH, New York **1998**, p. 4.
- [85] Klabunde, K. J.; Mohs, S. *Chemistry of Advanced Materials*, Interrante, L. V.; Smith, M. J. H. (eds.) Wiley-VCH, New York **1998**, p. 317.
- [86] Driscoll, D. J.; Martin, W.; Wang, J. X.; Lunsford, J. H. *J. Am. Chem. Soc.* **1985**, *107*, 58.
- [87] Hoq, M. F.; Klabunde, K. J. *J. Am. Chem. Soc.* **1986**, *108*, 2114.
- [88] Tashiro, T. *et al.*, *J. Phys. Chem.* **1995**, *99*, 6115.
- [89] Tsuji, H. *J. Chem. Soc. Faraday Trans.* **1994**, 803.
- [90] Li, Y. X.; Klabunde, K. J. *Chem. Mater.* **1992**, *4*, 611.
- [91] Knickerbein, M.; Wang, S.; Riley, S. J. *J. Chem. Phys.* **1990**, *93*, 94.

- [92] Choudary, B. M.; Kantam, K. L.; Santhi, L. P. *Catal. Today* **2000**, *57*, 17.
- [93] El-Shall, M. S.; Slack, W.; Vann, W.; Kane, D.; Hanley, D. *J. Phys. Chem.* **1994**, *98*, 3067.
- [94] Edelstein, A. S.; Hadjipanayis, G. C.; Siegel, R. W. (eds.) *Nanophase Materials*, Kluwer Academic Publishers, Dordrecht **1994**, pp. 73–80.
- [95] Edelstein, A. S.; Hadjipanayis, G. C.; Siegel, R. W. (eds.) *Nanophase Materials*, Kluwer Academic Publishers, Dordrecht **1994**, pp. 85–88.
- [96] Tan, S.; Leo, N. T. *Trans. Nanostruct. Met. Soc. China* **1995**, *2*, 58.
- [97] Baraton, M. I.; El-Shall, M. S. *Nanostruct. Mater.* **1995**, *6*, 301.
- [98] Cow, G. M.; Gonsalves, K. E. (eds.) *Nanotechnology, Molecularly Designed Materials*, American Chemical Society, Washington, D.C. **1996**, pp. 79–99.
- [99] Siegel, R. W. *et al.*, *J. Mater. Res.* **1998**, *3*, 1367.
- [100] Huh, M. Y.; Kim, S. H.; Ahn, J. P.; Park, J. K.; Kim, B. K. *Nanostruct. Mater.* **1999**, *11*, 211.
- [101] Messing, G. L.; Gardner, T. *J. Am. Ceram. Soc. Bull.* **1984**, *64*, 1498.
- [102] Kudas, T. T. *Adv. Mater.* **1989**, *6*, 180.
- [103] Jayanthi, V.; Zhang, S. C.; Messing, G. L. *J. Aerosol Sci. Technol.* **1993**, *19*, 478.
- [104] Messing, G. L.; Zhang, S. C.; Jayanthi, V. *J. Am. Ceram. Soc.* **1993**, *76*, 2707.
- [105] Edelstein, A. S.; Hadjipanayis, G. C.; Siegel, R. W. (eds.) *Nanophase Materials*, Kluwer Academic Publishers, Dordrecht **1994**, pp. 109–116.
- [106] Janackovic, D.; Jokanovic, V.; Gvozdenovic, L. K.; Uskokovic, D. *Nanostruct. Mater.* **1998**, *10*, 341.
- [107] Ulrich, G. D.; Riehl, J. W. *J. Colloid Interface Sci. Technol.* **1982**, *87*, 257.
- [108] Cow, G. M.; Gonsalves, K. E. (eds.) *Nanotechnology, Molecularly Designed Materials*, American Chemical Society, Washington, D.C. **1996**, pp. 64–78.
- [109] Lindackers, D.; Janzen, C.; Rellinghaus, B.; Wassermann, E. F.; Roth, P. *Nanostruct. Mater.* **1998**, *10*, 1247.

- [110] Palkar, V. R. *Nanostruct. Mater.* **1999**, *11*, 369.
- [111] Barringer, E. A.; Bowen, H. K. *J. Am. Ceram. Soc.* **1982**, *65*, C199.
- [112] Segal, D. *Chemical Synthesis of Advanced Ceramic Materials*, Cambridge University Press, Cambridge **1989**.
- [113] Gesser, H. D.; Gosswami, P. C. *Chem. Rev.* **1989**, *89*, 765.
- [114] West, J. K. *Chem. Rev.* **1990**, *90*, 33.
- [115] Brinker, C. J.; Scherer, G. W. *Sol–Gel Science: The Physics and Chemistry of Sol–Gel Processing*, Academic Press, Boston **1990**.
- [116] Chandler, C. D.; Roger, C.; Smith, M. J. H. *Chem. Rev.* **1993**, *93*, 1205.
- [117] Klein, L. (ed.) *Sol–Gel Optics: Processing and Applications*, Kluwer, Boston **1993**.
- [118] Hench, L. L.; Avnir, D. *Acc. Chem. Res.* **1995**, *28*, 328.
- [119] Narula, C. K. *Ceramic Precursor Technology and Its Applications*, Marcel Dekker, New York **1995**.
- [120] Interrante, L. V.; Smith, M. J. H. (eds.) *Chemistry of Advanced Materials: An Overview*, Wiley–VCH, New York **1998**.
- [121] Toshima, N.; Harada, M.; Yonezawa, T.; Kushihashi, K.; Asakura, K. *J. Phys. Chem.* **1991**, *95*, 7448.
- [122] Chaudret, B.; Bradley, J. S.; Mazel, R.; Roucau, C. *J. Am. Chem. Soc.* **1993**, *115*, 11638.
- [123] Toshima, N.; Wang, Y. *Adv. Mater.* **1994**, *6*, 245.
- [124] Naka, K.; Yaguchi, M.; Chujo, Y. *Chem. Mater.* **1999**, *11*, 849.
- [125] Warner, M. G.; Reed, S. M.; Hutchison, J. E. *Chem. Mater.* **2000**, *12*, 3316.
- [126] Tan, Y.; Dai, X.; Li, Y.; Zhu, D. *J. Mater. Chem.* **2003**, *13*, 1069.
- [127] Trivino, G. C.; Klabunde, K. J.; Dale, E. B. *Langmuir* **1987**, *3*, 986.
- [128] Brust, M.; Fink, J.; Bethell, D.; Schiffrin, D. J.; Kiely, C. J. *Chem. Commun.* **1995**, 1655.
- [129] Kim, K. S.; Demberelnyamba, D.; Lee, H. *Langmuir* **2004**, *20*, 556.

- [130] Ohde, H.; Hunt, F.; Wai, C. M. *Chem. Mater.* **2001**, *13*, 4130.
- [131] Viswanathan, R.; Lilly, G. D.; Gale, W. F.; Gupta, R. B. *Ind. Eng. Chem. Res.* **2003**, *42*, 5535.
- [132] Meyer, M.; Wallberg, C.; Kurihara, K.; Fendler, J. H. *Chem. Commun.* **1984**, 90.
- [133] Petit, C.; Jain, T. K.; Billoudet, F.; Pileni, M. P. *Langmuir* **1994**, *10*, 4446.
- [134] Forster, S.; Antonietti, M. *Adv. Mater.* **1998**, *10*, 195.
- [135] Minko, S.; Kiriya, A.; Gorodyska, G.; Stamm, M. *J. Am. Chem. Soc.* **2002**, *124*, 10192.
- [136] Zhang, M.; Drechsler, M.; Muller, A. H. E. *Chem. Mater.* **2004**, *16*, 537.
- [137] Braun, E.; Eichen, Y.; Sivan, U.; Yoseph, G. B. *Nature* **1998**, *391*, 775.
- [138] Richter, J. *et al.*, *Adv. Mater.* **2000**, *12*, 507.
- [139] Shenton, W.; Douglas, T.; Young, M.; Stubbs, G.; Mann, S. *Adv. Mater.* **1999**, *11*, 253.
- [140] Fowler, C. E.; Shenton, W.; Stubbs, G.; Mann, S. *Adv. Mater.* **2001**, *13*, 126.
- [141] Dujardin, E.; Peet, C.; Stubbs, G.; Culver, J. N.; Mann, S. *Nano Lett.* **2003**, *3*, 413.
- [142] Wiesner, J.; Wokaun, A. *Chem. Phys. Lett.* **1989**, *57*, 569.
- [143] Addadi, L.; Weiner, S. *Angew. Chem. Int. Ed.* **1992**, *31*, 153.
- [144] Weiner, S.; Addadi, L. *J. Mater. Chem.* **1997**, *7*, 689.
- [145] Ozin, G. A. *Acc. Chem. Res.* **1997**, *30*, 17.
- [146] Baurerlein, E. *Angew. Chem. Int. Ed.* **2003**, *42*, 614.
- [147] Lowenstam, H. A. *Science* **1981**, *211*, 1126.
- [148] Mann, S.; Webb, J.; William, R. J. P. *Biomaterialization; Chemical and Biochemical Perspectives*, Wiley-VCH, Weinheim, Germany **1989**.
- [149] Lowenstam, H. A.; Weiner, S. *On Biomaterialization*, Oxford University Press, Oxford **1989**.

- [150] Bommel, K. J. C. V.; Friggeri, A.; Shinkai, S. *Angew. Chem. Int. Ed.* **2003**, *42*, 980.
- [151] Baeuerlein, E. *Biomineralization*, Wiley–VCH, Weinheim, Germany **2000**.
- [152] Simkiss, K.; Wilbur, K. M. *Biomineralization*, Academic Press, San Diego **1989**.
- [153] Mann, S. *J. Chem. Soc., Dalton Trans.* **1997**, 3953.
- [154] Landis, W. J. *Bone* **1995**, *16*, 533.
- [155] Landis, W. J.; Hodgens, K. J. *J. Struct. Biol.* **1996**, *117*, 24.
- [156] Roschger, P. *et al.*, *J. Struct. Biol.* **2001**, *136*, 126.
- [157] Addadi, L.; Azenberg, J.; Beniash, E.; Weiner, S. *Crystal Engineering: From Molecules and Crystals to Materials*, Braga, D. *et al.*, (eds.) Kluwer Academic Publishers, The Netherlands **1999**.
- [158] Weiner, S.; Traub, W.; Lowenstam, H. A. *Biomineralization and Biological Metal Accumulation*, Westbroek, P.; Jong, E. W.; Dordrecht, R. (eds.) **1983**, p. 205.
- [159] Gower, L. A. *Variety of Biomineral Types and Biological Systems*, <http://www.gower.mse.ufl.edu/research.html>.
- [160] Mann, S. *Inorganic Materials*, 2nd edition, Bruce, D. W.; O'Hare, D. (eds.) John Wiley & Sons **1996**.
- [161] Cheavin, W. H. S. *Microscope* **1938**, *2*, 155.
- [162] Monje, P. V.; Baran, E. J. *J. Plant Physiol.* **2004**, *161*, 121.
- [163] Arnott, H. J. *Biological Mineralization and Demineralization*, Nancollas, G. H. (ed.) Springer Verlag, Berlin **1982**, pp. 199–218.
- [164] Monje, P. V.; Baran, E. J. *Advances in Plant Physiology*, Vol. 7, Hemantaranjan, H. (ed.) Scientific Publishers, Jodhpur **2004** pp. 403–419.
- [165] Wal, P. V. D.; Jong, E. W. D.; Westbrock, P.; Bruijn, W. C. D.; Stapel A. A. H. *J. Ultrastructure. Res.* **1983**, *85*, 139.
- [166] Rowson, J. D.; Leadbeater, B. S. C.; Green, J. C. *Br. Phycol. J.* **1986**, *21*, 359.

- [167] Young, I. R.; Didymus, I. M.; Brown, P. R.; Prins, N.; Mann, S. *Nature* **1992**, 356, 516.
- [168] Marsh, M. E. *Protoplasma* **1999**, 207, 54–66.
- [169] Marsh, M. E. *Biomineralization*, Baeuerlein, E. (ed.) Wiley–VCH, Weinheim, Germany **2000**, p. 251–268.
- [170] Frankel, R. B.; Bicudo, C. E. M. *Biophys. J.* **1986**, 50, 375.
- [171] Mann, S.; Sparks, N. H.; Walker, M. M.; Kirschvink, J. L. *J. Exp. Biol.* **1988**, 140, 35.
- [172] Kirschvink, A. K.; Woodford, B. J. *Proc. Natl. Acad. Sci. USA* **1992**, 89, 7683.
- [173] Kirschvink, J. L.; Dobson, J.; Grassi, P. P. *Brain Res. Bull.* **1996**, 39, 255.
- [174] Walker, M. M. *et al.*, *Nature* **1997**, 390, 371.
- [175] Devouard, B. *et al.*, *Am. Mineral.* **1998**, 83, 1387.
- [176] Grassi, P. P. S.; Wessiken, R.; Dobson, J. *Biochem. Biophys. Acta* **1999**, 1426, 212.
- [177] Grassi, P. P. S.; Dobson, J. *BioMetals* **1999**, 12, 67.
- [178] Araujo, F. F. T. D.; Pires, M. A.; Bazylinski, D. A.; Frankel, R. B. *Biomineralization*, Baeuerlein, E. (ed.) Wiley–VCH, Weinheim, Germany **2000**, p. 41–43.
- [179] Diebel, C. E.; Proksch, R.; Green, C. R.; Neilson, P.; Walker, M. M. *Nature* **2000**, 406, 299.
- [180] Posfai M. *et al.*, *Eur. J. Mineral.* **2001**, 13, 691.
- [181] Josifovska M. G.; McClean R. G.; Schofield M. A.; Sommer C. V.; Kean W. F. *Eur. J. Mineral.* **2001**, 13, 863.
- [182] Monje, P. V.; Baran, E. J.; *J. Plant Physiol.* **2000**, 157, 457.
- [183] Iler, R. K. *The Chemistry of Silica*, Johy Wiley & Sons, New York **1979**.
- [184] Hench, L. L. *J. Am. Ceram. Soc.* **1991**, 74, 1487.
- [185] Kendall, T. *Ind. Miner.*, **March 2000**, 49.
- [186] Perry, C. C. *Rev. Mineral. Geochem.* **2003**, 54, 291.

- [187] Zhou, C. J. *et al.*, *J. Mater. Chem.* **2004**, *14*, 2317.
- [188] Carturan, G.; Toso, R. D.; Borringsegna, S.; Monto, R. D. *J. Mater. Chem.* **2004**, *14*, 2099.
- [189] Nassif, N.; Roux, C.; Coradin, T.; Boured, O. M. M.; Livage, J. *J. Mater. Chem.* **2004**, *14*, 2264.
- [190] Pryce, R. S.; Hench, L. L. *J. Mater. Chem.* **2004**, *14*, 2303.
- [191] Bottcher, H.; Soltmann, U.; Mertig, M.; Pompe, W. *J. Mater. Chem.* **2004**, *14*, 2176.
- [192] Simpson, T. L.; Volcani, B. E. (eds.) *Silicon and Siliceous Structures in Biological Systems*, Springer–Verlag, New York **1981**.
- [193] Morse, D. E. *Trends Biotechnol.* **1999**, *17*, 230.
- [194] Tacke, R. *Angew. Chem. Int. Ed.* **1999**, *38*, 3015.
- [195] Hildebrand, M. *Prog. Org. Coat.* **2003**, *47*, 256.
- [196] Patwardhan, S. V.; Clarson, S. J. *Macromolecules Containing Metal and Metal-Like Elements*, El-Aziz, A. S. A.; Carraher Jr., C. E.; Zeldin, M. (eds.) John Wiley & Sons, Hoboken, NJ **2005**.
- [197] Lopez, P. J.; Descles, J.; Allen, A. E.; Bowler, C. *Curr. Opin. Biotechnol.* **2005**, *16*, 180.
- [198] Aizenberg, J. *et al.*, *Science* **2005**, *309*, 275.
- [199] Hamley, I. W. *Angew. Chem. Int. Ed.* **2003**, *42*, 1692.
- [200] Pyrchid, C. J.; Rudall, P. J.; Gregory, M. *The Botanical Rev.* **2004**, *69*, 377.
- [201] Hecky, R. E.; Mopper, K.; Kilham, P.; Degens, E. T. *Mar. Biol.* **1973**, *19*, 323.
- [202] Swift, D. M.; Wheeler, A. P. *J. Phycol.* **1992**, *28*, 202.
- [203] Harrison, C. C. *Phytochemistry* **1996**, *41*, 37.
- [204] Shimizu, K.; Cha, J.; Stucky, G. D.; Morse, D. E. *Proc. Natl. Acad. Sci. USA* **1998**, *95*, 6234.
- [205] Perry, C. C.; Tucker, T. K. *Colloid Polym. Sci.* **2003**, *281*, 652.
- [206] Sumper, M.; Kroger, N. *J. Mater. Chem.* **2004**, *14*, 2059.

- [207] Patwardhan, S. V.; Clarson, S. J.; Perry, C. C. *Chem. Commun.* **2005**, 1113.
- [208] Kroger, N.; Deuzmann, R.; Sumper, M. *Science* **1999**, 286, 1129.
- [209] Kroger, N.; Deuzmann, R.; Bergsdorf, C.; Sumper, M. *Proc. Natl. Acad. Sci. USA* **2000**, 97, 14133.
- [210] Kroger, N.; Deuzmann, R.; Sumper, M. *J. Biol. Chem.* **2001**, 276, 26066.
- [211] Cha, J. *et al.*, *Proc. Natl. Acad. Sci. USA* **1999**, 96, 361.
- [212] Zhou, Y.; Shimizu, K.; Cha, J.; Stucky, G. D.; Morse, D. E. *Angew. Chem. Int. Ed.* **1999**, 38, 780.
- [213] Perry, C. C.; Tucker, T. K. *J. Biol. Inorg. Chem.* **2000**, 5, 537.
- [214] Perry, C. C.; Tucker, T. K. *Chem. Commun.* **1998**, 2587.
- [215] Lehn, J-M. *Supramolecular Chemistry: Concepts and Perspectives*, Wiley-VCH, Weinheim, Germany **1995**.
- [216] Patwardhan, S. V.; Mukherjee, N.; Kannan, M. S.; Clarson, S. J. *Chem. Commun.* **2003**, 10, 1122.
- [217] Mann, S. *et al.*, *J. Chem. Soc., Chem. Commun.* **1983**, 4, 168.
- [218] Lobel, K. D.; West, J. K.; Hench, L. L. *J. Mater. Sci. Lett.* **1996**, 15, 648.
- [219] Lobel, K. D.; West, J. K.; Hench, L. L. *Mar. Biol.* **1996**, 126, 353.
- [220] Kroger, N.; Lorenz, S.; Brunner, E.; Sumper, M. *Science* **2002**, 298, 584.
- [221] Patwardhan, S. V.; Shiba, K.; Clarson, S. J. *Polym. Prepr.* **2004**, 45, 612.
- [222] Patwardhan, S. V.; Shiba, K.; Raab, C.; Husing, N.; Clarson, S. J. *Polymer Biocatalysis and Biomaterials*, Gauss, R. A. (ed.) **2005**.
- [223] Coradin, T.; Lopez, P. J. *ChemBioChem* **2003**, 4, 251.
- [224] Belton, D.; Paine, G.; Patwardhan, S. V.; Perry, C. C. *J. Mater. Chem.* **2004**, 14, 2231.
- [225] Patwardhan, S. V.; Mukherjee, N.; Clarson, C. J. *J. Inorg. Organomet. Polym.* **2001**, 11, 193.
- [226] Belton, D.; Paine, G.; Patwardhan, S. V.; Perry, C. C. *J. Mater. Chem.* **2004**, 14, 2231.

- [227] Patwardhan, S. V.; Clarson, C. J. *Silicon Chem.* **2002**, *1*, 207.
- [228] Coradin, T.; Durupthy, O.; Livage, J. *Langmuir* **2002**, *18*, 2331.
- [229] Patwardhan, S. V. PhD Dissertation, Department of Materials Science and Engineering, University of Cincinnati, **2003**.
- [230] Patwardhan, S. V.; Clarson, C. J. *J. Inorg. Organomet. Polym.* **2003**, *13*, 193.
- [231] Brott, L. L. *et al.*, *Nature* **2001**, *413*, 291.
- [232] Knecht, M. R.; Wright, D. W. *Chem. Commun.* **2003**, 3038.
- [233] Cha, J. N.; Stucky, G. D.; Morse, D. E.; Deming, T. J. *Nature* **2000**, *403*, 289.
- [234] Naik, R. R.; Brott, L. L.; Clarson, S. J.; Stone, M. O. *J. Nanosci. Nanotechnol.* **2002**, *2*, 95.
- [235] Patwardhan, S. V.; Mukherjee, N.; Clarson, C. J. *J. Inorg. Organomet. Polym.* **2001**, *11*, 117.
- [236] Patwardhan, S. V.; Mukherjee, N.; Clarson, C. J. *Silicon Chem.* **2002**, *1*, 47.
- [237] Menzel, H. *et al.*, *Chem. Commun.* **2003**, 2994.
- [238] Perry, C. C.; Lu, Y. *J. Chem. Soc. Faraday Trans.* **1992**, *88*, 2945.
- [239] Vrieling, E. G.; Gieskes, W. W. C.; Beelen, T. P. M. *J. Phycol.* **1999**, *35*, 351.
- [240] Meene van de, A. M. L.; Heaps, J. D. P. *J. Phycol.* **2002**, *38*, 351.
- [241] Aiking, H.; Kok, K.; Heerikhuizen, H. V.; Riet, J. V. *Appl. Environ. Microbiol.* **1982**, *44*, 938.
- [242] Stephen, J. R.; Meenaughton, S. J. *Curr. Opin. Biotechnol.* **1999**, *10*, 230.
- [243] Mehra, R. K.; Winge, D. R. *J. Cell. Biochem.* **1991**, *45*, 30.
- [244] Beveridge, J. T. *et al.*, *Adv. Microb. Physiol.* **1997**, *38*, 178.
- [245] Silver, S. *Gene* **1996**, *179*, 9.
- [246] Rouch, D. A.; Lee, B. T.; Morby, A. T. *J. Ind. Micro.* **1995**, *14*, 132.
- [247] Zumberg, J. E.; Sielgo, A. C.; Nagy, B. *Miner. Sci. Eng.* **1978**, *10*, 223.
- [248] Hosea, M. *et al.*, *Inorg. Chim. Acta.* **1986**, *123*, 161.

- [249] Beveridge, T. J.; Doyle, R. J. *Metal Ions and Bacteria*, John Wiley & Sons, New York **1989**.
- [250] Reese, R. N.; Winge, D. R. *J. Biol. Chem.* **1988**, 263, 12832.
- [251] Dameron, C. T. *Nature* **1989**, 338, 596.
- [252] Temple, K. L.; LeRoux, N. *Econ. Geol.* **1964**, 59, 647.
- [253] Maratea, D.; Wolfe, R. S. *J. Bacteriol.* **1979**, 140, 720.
- [254] Southam, G.; Beveridge, T. J. *Geochim. Cosmochim. Acta* **1996**, 60, 4369.
- [255] Beveridge, T. J.; Murray, R. G. E. *J. Bacteriol.* **1980**, 141, 876.
- [256] Fortin, D.; Beveridge, T. J. *Bio-mineralization. From Biology to Biotechnology and Medical Applications*, Baeuerien, E. (ed.), Wiley-VCH, Weinheim, Germany **2000**, p. 7.
- [257] Nair, B.; Pradeep, T. *Cryst. Growth Des.* **2002**, 2, 293.
- [258] Klaus, T.; Joerger, R.; Olsson, E.; Granqvist, C. G. *Proc. Natl. Acad. Sci. USA* **1999**, 96, 13611.
- [259] Joerger, T. K.; Joerger, R.; Olsson, E.; Granqvist, C. G. *Trends Biotechnol.* **2001**, 19, 15.
- [260] Joerger, R.; Klaus, T.; Granqvist, C. G. *Adv. Mater.* **2000**, 12, 407.
- [261] Cunningham, D. P.; Lundie, L. L. *Appl. Environ. Microbiol.* **1993**, 59.
- [262] Holmes, J. D. *et al.*, *Arch. Microbiol.* **1995**, 163, 143.
- [263] Smith, P. R.; Holmes, J. D.; Richardson, D. J.; Russell, D. A.; Sodeau, J. R., *J. Chem. Soc., Faraday Trans.* **1998**, 94, 1235.
- [264] Labrenz, M. *et al.*, *Science* **2000**, 290, 252.
- [265] Watson, J. H. P.; Ellwood, D. C.; Sper, A. K.; Charnock, J. M. *J. Magn. Magn. Mater.* **1999**, 203, 69.
- [266] Watson, J. H. P.; Cressey, B. A.; Roberts, A. P.; Charnock, J. M. E. *J. Magn. Magn. Mater.* **2000**, 214, 13.
- [267] Frankel, R. B.; Blakemore, R. P. (eds.) *Iron Biominerals*, Plenum Press, New York **1991**.

- [268] Philipse, A. P.; Mass, D. *Langmuir* **2002**, *18*, 9977.
- [269] Roh, Y. *et al.*, *Solid State Commun.* **2001**, *118*, 529.
- [270] Kowshik, M.; Vogel, W.; Urban, J.; Kulkarni, S. K.; Paknikar, K. M. *Adv. Mater.* **2002**, *14*, 815.
- [271] Kowshik, M. *Biotechnol. Bioeng.* **2002**, *78*, 583.
- [272] Robinson, M. G.; Brown, L. N.; Beverley, D. *Biofouling* **1997**, *11*, 59.
- [273] Mukherjee, P. *et al.*, *Angew. Chem. Int. Ed.* **2001**, *40*, 3585.
- [274] Mukherjee, P. *et al.*, *Nano Lett.* **2001**, *1*, 515.
- [275] Mukherjee, P. *et al.*, *Chem Bio Chem.* **2002**, *3*, 461.
- [276] Ahmad, A. *et al.*, *Coll. Surf. B* **2003**, *28*, 313.
- [277] Ahmad, A. *et al.*, *J. Am. Chem. Soc.* **2002**, *124*, 12108.
- [278] Chandran, S. P.; Chaudhary, M.; Pasricha, R.; Ahmad, A.; Sastry, M. *Biotech. Progress* **2006**, *22*, 577.
- [279] Ahmad, A.; Senapati, S.; Khan, M. I.; Kumar, R.; Sastry, M. *Langmuir* **2003**, *19*, 3550.
- [280] Cannon, H. L.; Shacklette, H. T.; Bastron, H. *Metal Absorption by Equisetum (horsetail)*, United States Geological Survey Bulletin 1278–A, **1968**, A1–A21.
- [281] Shacklette, H. T.; Lakin, H. W.; Hubert, A. E.; Curtin, G. C. *Absorption of Gold by Plants*, United States Geological Survey Bulletin 1314–B, **1970**, 1–23.
- [282] Lakin, H. W.; Curtin, G. C.; Hubert, A. E.; Shacklette, H. T.; Doxtader, K. G. *Geochemistry of Gold in the Weathering Cycle*, United States Geological Survey Bulletin 1330, **1974**, 1–80.
- [283] Torresdey, J. L. G. *et al.*, *Nano Lett.* **2002**, *2*, 397.
- [284] Torresdey, J. L. G. *Langmuir* **2003**, *19*, 1357.
- [285] Shankar, S. S.; Ahmad, A.; Sastry, M. *Biotech. Progress* **2003**, *19*, 1627.
- [286] Shankar, S. S.; Ahmad, A.; Pasricha, R.; Sastry, M. *J. Mater. Chem.* **2003**, *13*, 1822.

- [287] Shankar, S. S.; Rai, A.; Ahmad, A.; Sastry, M. *J. Colloid Interface Sci.* **2004**, 275, 496.
- [288] Shankar, S. S.; Rai, A.; Ankamwar, B.; Singh, A.; Ahmad, A.; Sastry, M. *Nat. Mater.* **2004**, 3, 482.
- [289] Shankar, S. S.; Rai, A.; Ahmad, A.; Sastry, M. *Chem. Mater.* **2005**, 17, 566.
- [290] Ankamwar, B.; Damle, C.; Ahmad, A.; Sastry, M. *J. Nanosci. Nanotechnol.* **2005**, 5, 1665.

CHAPTER II

Characterization Techniques

The different experimental characterization techniques used during the course of the present work are discussed in this chapter.

2.1 Introduction

Biosynthesis of a range of oxide nanoparticles under ambient conditions using a fungus-mediated approach, and their potential applications is the central idea behind this thesis. While pursuing these aspects, a range of techniques including spectroscopic and microscopic techniques such as UV–visible absorption spectroscopy (UV–vis), Fourier Transform Infrared Spectroscopy (FTIR), X–Ray photoemission spectroscopy (XPS), X–Ray diffraction (XRD) measurements, Energy dispersive X–rays analysis (EDX), Thermogravimetric Analysis (TGA), Differential Scanning Calorimetry (DSC), Transmission Electron Microscopy (TEM), Scanning Electron Microscopy (SEM), Atomic Force Microscopy (AFM), Surface Potential Microscopy and Polyacrylamide Gel Electrophoresis (PAGE) were used. This chapter is devoted to explain the basic principles of the techniques used for the characterization.

2.2 UV–visible absorption spectroscopy (UV–vis)

Energy absorbed in the UV or visible region causes changes in the electronic energy of the molecule, and hence results in corresponding change in its ability to absorb light in the UV–visible region of electromagnetic radiation, in turn leading to color transitions. The relationship between the energy absorbed in an electronic transition and the frequency (ν), wavelength (λ) and wavenumber ($\bar{\nu}$) of radiation producing the transition can be explained as:

$$\Delta E = h\nu = hc/\lambda = h\bar{\nu}c$$

where h is the Planck's constant, c is the velocity of light and ΔE is the energy absorbed in an electronic transition in a molecule from a low energy state (ground state) to a higher energy state (excited state).

The energy absorbed is dependent on the energy difference between the ground state and the excited state; smaller the difference, larger the wavelength of absorption. The principal characteristics of an absorption band are its position and intensity. The position of an absorption band corresponds to the wavelength of radiation whose energy is equal to that required for an electronic transition. The intensity of absorption is largely dependent on two factors *viz.* the probability of interaction between the radiation energy and the electronic system as well as the

difference between the ground and the excited states. The intensity of absorption may be derived from the Beer–Lambert’s law:

$$A = \varepsilon \cdot c \cdot l$$

where A is the measured absorbance, ε is the proportionality constant known as absorptivity, c is the analyte concentration and l is the path length of the cell.

UV–vis spectroscopy is also a powerful tool for the characterization of colloidal particles [1–3]. Optical absorption features are also exhibited by semiconductor nanoparticles and can be explained on the basis of excitation of the valence shell electrons to the conduction band, creating an electron–hole pair in the system. The semiconductor nanoparticles display size quantization effect. The dependence of the change in the band gap energy (ΔE_{BG}) in the semiconductor nanoparticles on their size in terms of the radius (R) of spherical particle can be expressed as:

$$\Delta E_{BG} = \frac{\hbar^2 \pi^2}{2} \left(\frac{1}{m_e} + \frac{1}{m_h} \right) \frac{1}{R^2} - \frac{1.8e^2}{\varepsilon} \cdot \frac{1}{R}$$

where m_e and m_h correspond to the effective masses of electron and hole respectively, and ε is the dielectric constant of the semiconducting material [4].

Absorption spectroscopy in the UV and visible region has long been used as an important tool for chemical analysis [5]. In the work presented in this thesis, UV–vis absorption spectroscopy has been used to monitor the band gap and absorption characteristics of biogenic titania nanoparticles. UV–vis–NIR measurements were also carried out to monitor the photooxidative degradation of organic dyes using titania photocatalyst. These measurements were performed on JASCO V–570 UV/VIS/NIR spectrophotometer operated at a resolution of 1 nm [6].

2.3 Fourier transform infrared spectroscopy (FTIR)

The atoms in a molecule do not remain in a fixed relative position and keep vibrating about their mean positions. Due to this vibrational motion, if there is a periodic alternation in the dipole moment, such modes of vibrations are infrared (IR) active. The IR region of the electromagnetic spectrum ranges from 100 μm to 1 μm wavelength. The vibrating molecules absorb energy only from those radiations, with which it can coherently interact *i.e.* the radiations of its own oscillation frequency.

This makes each functional group to have specific vibrational frequencies, which is very sensitive to its chemical environment and the neighboring species. The appearance or non-appearance of certain vibrational frequencies in IR spectra of any molecule gives valuable information about the structure of that particular molecule. The vibrational frequency:

$$\nu = \frac{1}{2\pi} \sqrt{\frac{k}{\mu}}$$

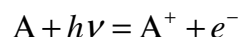
where k is the force constant and μ is the reduced mass. In FTIR spectroscopy, a mathematical operation known as Fourier transformation converts the time domain signal (intensity versus time) to the frequency domain signal (intensity versus frequency), which assists in saving the time required to obtain an IR spectrum (1 sec or less versus 10 to 15 min for a single scan). This in turn, provides an opportunity to enhance the signal-to-noise (S/N) ratio of IR spectrum by increasing the total number of sample scans, since the S/N ratio is proportional to the square root of the total number of scans. This explains the term “Fourier transform” used in infrared spectrometry. [7, 8] In FTIR spectroscopy, frequency is conventionally displayed in the form of wavenumbers.

FTIR spectroscopy has been used in this thesis for obtaining insights about the formation of oxides nanoparticles, their phase identifications and obtaining important information about biomolecules bound onto the surface of nanoparticles during the synthesis process [9–11]. All the FTIR spectra shown in this thesis have been presented as obtained, except for the baseline correction. Samples were prepared in the form of pellets by dispersing powder samples in KBr. FTIR measurements of samples were carried out on a Perkin Elmer FTIR Spectrum One spectrophotometer operated in the Diffuse Reflectance Infrared Fourier Transform (DRIFT) mode at a resolution of 2 cm^{-1} with 256 scans.

2.4 X-ray photoemission spectroscopy (XPS)

XPS is a highly surface sensitive technique, which is used to study the composition and electronic state of the surface region of a sample. Since, the technique provides a quantitative analysis of the surface composition, it is also referred by alternative acronym, ESCA (Electron Spectroscopy for Chemical Analysis) or X-ray photoelectron spectroscopy. XPS is based on well-known

photoelectric effect (a single photon in/electron out process) first explained by Einstein in 1905. Photoelectron spectroscopy uses monochromatic source of radiation (*i.e.* photons of fixed energy given by relation $E = h\nu$). In XPS, the photon of energy $h\nu$ is absorbed by an atom A in a solid, leading to the ionization and emission of a core (inner shell) electron. The kinetic energy distribution of the emitted photoelectrons is measured and a photoelectron spectrum is obtained. The overall process of photoionization can be demonstrated as:



Conservation of energy requires that:

$$E(A) + h\nu = E(A^+) + E(e^-)$$

Since the energy of electron is available solely in the form of kinetic energy (KE), the above expression can be rearranged to find the following expression for the KE of the photoelectron:

$$KE = h\nu - [E(A^+) - E(A)]$$

The final term in parentheses, representing the difference in energy between the ionized and neutral atoms is generally referred as *binding energy* (BE) of the electron. This leads to the following commonly quoted equation:

$$KE = h\nu - BE$$

The BE of electrons in various energy levels in the solids are conventionally measured with respect to the Fermi level, rather than the vacuum level. This involves a small correction to the above equation in order to account for the work function (ϕ) of the solid:

$$KE = h\nu - BE - \phi$$

Employing photons of fixed energy $h\nu$, it is obvious that if the kinetic energy (KE) and the work function (ϕ) of the sample are measured, the binding energy (BE) of the electron can be calculated. Binding energies, being characteristic of atoms, different elements present in the sample can be identified. Electrons traveling through a material have a relatively high probability of experiencing inelastic collisions with locally bound electrons as a result of which they suffer energy loss and contribute to the background of the spectrum rather than a specific peak. However, XPS signals are recorded in the form of peaks only from those photoemitted electrons, which successfully reach the surface without undergoing inelastic collisions. Since the fraction of such electrons decrease significantly with distance, XPS cannot provide

information beneath a certain distance from the surface ($< 100 \text{ \AA}$) and hence termed as a surface sensitive technique.

The exact BE of an electron depends not only upon the level from which photoemission is occurring, but also upon the formal oxidation state of the atom and the local chemical and physical environment. Change in either of these gives rise to small shifts in the peak positions in the spectrum, so-called *chemical shifts*. The ability to discriminate between different oxidation states and chemical environments is one of the major strengths of XPS [12].

Photoelectron peaks are labeled according to the quantum numbers of the level from which the electron originates. An electron originating from an orbital with principal quantum number (n), orbital quantum number (l), and spin quantum number (s) is indicated as nl_{l+s} . For a non-zero orbital quantum number ($l > 0$), spin moment is coupled with orbital moment (called L–S coupling) and it has the total momentum ($j = l + 1/2$) and ($j = l - 1/2$) [generally, $j = l \pm s$], each state being filled with $(2j + 1)$ electrons. Hence most XPS peaks appear in doublets and the intensity ratio of the components is $(l + 1)/l$.

For the work described in this thesis, the XPS spectra of various core levels were recorded and their binding energies were aligned with respect to C 1s BE of 285 eV. The samples were prepared by drop-coating the solution either on freshly etched Si (100) substrate or Cu strips. XPS measurements were carried out on a VG MicroTech ESCA 3000 instrument at a pressure better than 1×10^{-9} Torr with un-monochromatized Mg $K\alpha$ radiation (1253.6 eV energy). The measurements were made in the constant analyzer energy (CAE) mode at a pass energy of 50 eV and electron takeoff angle (angle between electron emission direction and surface plane) of 60° . This leads to an overall resolution of ~ 1 eV in the measurements. The chemically distinct components in the core level spectra were resolved by a non-linear least squares fitting algorithm after background removal by the Shirley method [13].

2.5 X-ray diffraction (XRD)

Powder XRD is one of most important techniques for determining the structure of materials [14]. The work presented in the thesis emphasizes on the synthesis of various oxide nanoparticles. Their crystalline nature and crystal type

could be identified from their XRD patterns. The sample is usually in a powder form, consisting of randomly oriented fine grains of crystalline material. When the diffraction pattern is recorded, it shows concentric rings of scattering peaks corresponding to various interplanar spacings in the crystal lattice. The positions and the intensities of peaks are used to identify the underlying crystal structure of the material.

X-rays are electromagnetic radiation with typical photon energies in the range of 100 eV – 100 keV. For diffraction applications, only short wavelength X-rays in the range of a few Angstroms to 0.1 Angstrom (1 keV – 120 keV) are used. Since the wavelength of X-rays is comparable to the size of atoms, they are ideally suited for probing the structural arrangement of atoms and molecules in a wide range of materials [15]. X-rays primarily interact with electrons in atoms. When X-ray photons collide with electrons, some photons from the incident beam deflect away from their original direction of travel. If the wavelength of these scattered X-rays does not change during this process, this is called elastic scattering (only momentum is transferred in the elastic scattering process, not the energy). These are the X-rays that are measured in diffraction experiments, as the scattered X-rays carry information about the electron distribution in materials. If the atoms are arranged in a periodic fashion, as in crystals, the diffracted waves will consist of sharp interference maxima (peaks) with the same symmetry as in the distribution of atoms. Measuring the diffraction pattern therefore allows us to deduce the distribution of atoms in a material. When certain geometric requirements are met, X-rays scattered from a crystalline solid can constructively interfere, producing a diffracted beam. In 1912, W. L. Bragg recognized the following relationship among several factors:

$$n\lambda = 2d \sin \theta$$

The above equation is called Bragg's equation, where n denotes the order of diffraction, λ represents the wavelength of the X-ray, d is the interplanar spacing and θ signifies the scattering angle.

All the room-temperature XRD data shown in this thesis was carried out on a Philips PW 1830 instrument operating at a voltage of 40 kV and a current of 30 mA with Cu K α radiation. The XRD samples were made either by drop coating the sample on a glass substrate or in the powder form. The high-temperature XRD measurements of barium titanate powder was performed at 150 °C using

Rigaku Dmax 2500 wide-angle powder diffractometer with a diffracted beam graphite monochromator on a rotating anode generator with a Cu target.

2.6 Energy dispersive X-rays analysis (EDX)

EDX is a chemical microanalysis technique, used most commonly in conjunction with scanning electron microscope (SEM) and utilizes the X-rays emitted from the sample during bombardment by an electron beam. EDX is used to characterize the elemental composition of the analyzed volume. Features or phases as small as about 1 μm can be analyzed. When the electron beam of SEM bombards the sample, electrons are ejected from the atoms comprising the sample's surface and another electron from a higher shell fills up the resulting electron vacancy. In this process, an X-ray photon is emitted in order to balance the energy difference between the two electrons. The EDX X-ray detector measures the number of emitted X-rays versus their energy. The energy of the emitted X-rays is the characteristic of the element from which the X-ray is emitted. A spectrum of the energy versus relative counts of the detected X-rays is obtained and evaluated for qualitative and quantitative determinations of the elements (atomic number ≥ 4) present in the sampled volume.

Combining the EDX system with the SEM allows the identification at microstructural level, of compositional gradients at grain boundaries, second phases, impurities and inclusions. In the scanning mode, the SEM/EDX unit can be used to produce maps of element location, their concentration, and distribution. In this thesis, we have used EDX measurements in order to determine the chemical composition (both qualitative and quantitative) of oxides, oxide-protein composites and naturally available materials used in our studies. EDX was performed using a Phoenix EDX, attached to Leica Stereoscan – 440 SEM.

2.7 Thermal analysis

Thermal analysis includes a group of techniques in which a physical property of a substance is measured as a function of temperature, while the substance is subjected to a controlled temperature program. Among several thermal analytical techniques, we have explored thermogravimetric analysis (TGA) and differential scanning calorimetry (DSC) in this thesis.

2.7.1 Thermogravimetric analysis (TGA)

The determination of changes in chemical or physical properties of material and information about its phase transformation as a function of temperature can be obtained by TGA. TGA is based on the measurement of weight loss of the material as a function of temperature. TGA curve provides information concerning the thermal stability of the initial sample, intermediate compounds that might form and of the residues, if any. In addition to thermal stability, the weight losses observed in TGA can be quantified to predict the pathway of degradation or to obtain compositional information. The experimental data offers more sophisticated understanding of reactions occurring at materials heating. This ability to obtain measurements at higher temperatures is most useful for inorganic materials such as minerals used in this thesis. In this thesis, TGA was performed to find out the contribution of proteins/biomolecules in the metal oxide–proteins hybrid nanostructures. TGA of biogenic oxide powders was performed on a TGA–7 Perkin Elmer instrument at a scan rate of 10 °C per min.

2.7.2 Differential scanning calorimetry (DSC)

DSC can be used to determine the enthalpy change associated with a thermal transition. When a particular material is either heated or cooled down, it might undergo a crystallographic phase transition, associated with an enthalpy change. DSC can pick up these phase transitions. Change in crystal lattice size due to impurity doping or some other factors might shift the phase transition temperature [16–18]. In this thesis, DSC was used to determine the shifts in Curie transition temperature of ferroelectric barium titanate nanoparticles. DSC measurements were carried out on DSC–Q10 V9.0–275 instrument under nitrogen environment from 25 to 250 °C at a heating rate of 10 °C/min.

2.8 Electron microscopy (EM)

Although some structural features can be revealed by XRD, direct imaging of particles is only possible using transmission and scanning electron microscopes. Both operate on the same basic principle as the light microscope does, however electrons are used here instead of light [19]. The development of the electron microscopes as imaging devices has enhanced the resolution power of the light microscopes by

several orders of magnitude. Since the de Broglie wavelength of electrons decrease with the increase in their kinetic energies, fast moving electrons have very short wavelength and therefore, are capable of very high resolution, if that wavelength can be used in an appropriately designed instrument. Resolving power of a microscope is given by the formula:

$$d = \frac{0.5\lambda}{\sin \alpha}$$

where λ represents the wavelength and α signifies the one-half of the angular aperture. Since the wavelength of electrons is in few Angstroms, in principle, the resolution of electron microscopes can be achieved upto few Angstroms.

2.8.1 Transmission electron microscopy (TEM)

A beam of accelerated electrons interacts with an object in a conventional TEM in one of the two ways [20]. Usually the electrons that undergo elastic scattering contributes to imaging in TEM, however the electrons that undergo inelastic scattering but do not significantly lose their energy can also participate in the imaging of an object. As a result, based on the interaction of falling electrons with different elements in the object, differences in light intensity (contrast) are created in the final image, which relates to areas in the object with different scattering potentials. This fact can be deduced from the Rutherford formula, which describes the deflection potential of an atom:

$$K = \frac{-e.eZ}{r^2}$$

where K is the deflection potential, e is the electron charge, z is the positive charge and r is the distance between electron to nucleus. As the atomic number of interacting element increases, their scattering efficiency also increases. In TEM, the great depth of focus provides the high magnification of the sample.

All the TEM images presented in the thesis were recorded on a JEOL 1200 EX instrument at an accelerating voltage of 80 kV, while high resolution TEM (HR-TEM) was performed on a JEOL JEM-2010 UHR instrument operated at an image resolution of 0.14 nm. Samples for TEM and HR-TEM were prepared by drop coating the sample on the carbon coated copper grids and allowing the solvent to evaporate.

2.8.2 Scanning electron microscopy (SEM)

SEM is able to provide 3-dimensional images of the objects, since it does not record the electrons passing through the specimen (as in TEM), but on the other hand, it records the secondary electrons that are released from the sample as a result of interaction with falling electron beam [21–22]. The broad magnification range of the SEM, coupled with the ease of shifting magnification makes its operation easy in order to zoom a gross image to a final image showing finer details.

When the electron beam strikes the sample, some of the electrons interact with the nucleus of the atom. The negatively charged electrons are attracted towards the positively charged nucleus, however if the angle is just right, instead of being captured by the nucleus, these electrons (backscattered electrons) encircle the nucleus and come back out of the sample without slowing down and form an image. In addition, beam electrons also interact with the specimen electrons, which slow down the beam electrons. Beam electrons, in turn push the specimen electrons out of the sample surface and these specimen electrons are called secondary electrons. Unlike the backscattered electrons, the secondary electrons move very slowly while they leave the sample. A positively charged detector pulls in the slow moving secondary electrons from a wide area and from around the sample corners. The ability to pull in secondary electrons from around the corners gives secondary electron image a 3-D look. The detector also counts the secondary electrons ejected from sample and hence image contrast is created based on the intensity of electrons emitted from each spot on the sample [23].

SEM images presented in the thesis were carried out on a Leica Stereoscan – 440 instrument. Powder samples were prepared either by drop coating samples on Si (100) wafers or directly on aluminium SEM substrate. Sand and rice husk samples were prepared for SEM by sticking them directly onto aluminium substrates using silver paste.

2.9 Scanning probe microscopy (SPM)

SPM is the field of microscopy, wherein images of surfaces are formed using a physical probe that scans the specimen. An image of the surface is obtained by mechanically moving the probe in a raster scan of the specimen, line by line, and

recording the probe–surface interaction as a function of position. The manner of using these interactions to obtain an image is generally called a mode.

2.9.1 Atomic force microscopy (AFM)

Atomic force microscope is a very high–resolution type of SPM, with a maximum magnification power of 5×10^6 times the regular size of an image, and an image resolution down to the size of molecules or groups of atoms. AFM is one of the foremost tools for imaging, measuring and manipulating matter at the nanoscale [24–25].

The AFM consists of a microscale cantilever with a sharp tip/probe (radius of curvature of the order of nanometers) at its end that is used to scan the specimen surface. When the tip is brought into proximity of a sample surface, forces between the tip and the sample lead to a deflection of the cantilever according to Hooke's law. Depending on the situation, forces that are measured in AFM include mechanical contact force, Van der Waals forces, capillary forces, chemical bonding, electrostatic forces, magnetic forces, solvation forces etc.

The AFM can be operated in a number of modes, depending on the application. The primary modes of operation of AFM are static (contact) mode and dynamic mode. In the static mode operation, the tip scans the sample very close to the sample surface. However, close to the sample surface, attractive forces can be quite strong, causing the tip to 'snap-in' to the surface. Thus static mode AFM is usually done in contact where the overall force is repulsive. Consequently, this technique is typically called “contact mode”. In contact mode, the force between the tip and the surface is kept constant during scanning by maintaining a constant deflection. In the dynamic mode, the cantilever is externally oscillated at or close to its resonance frequency. The oscillation amplitude, phase and resonance frequency are modified by tip–sample interaction forces; these changes in oscillation with respect to the external reference oscillation provide information about the sample. Dynamic mode operation include frequency modulation and the more common amplitude modulation. In frequency modulation, changes in the oscillation frequency provide the information about tip–sample interactions. In amplitude modulation, changes in the oscillation amplitude or phase provide the information for imaging, wherein changes in the phase of oscillation can be used to discriminate between different types of materials on the

surface. Amplitude modulation can be operated either in the non-contact or in the intermittent-contact regime. In ambient conditions, most samples develop a liquid meniscus layer. Because of this, keeping the probe tip close enough to the sample for short-range forces to become detectable, while preventing the tip from sticking to the surface presents a major hurdle for the non-contact dynamic mode. Dynamic contact mode (also called intermittent contact or tapping mode) was developed to bypass this problem [26] wherein, the cantilever is oscillated such that it comes in contact with the sample with each cycle, and then enough restoring force is provided by the cantilever spring to detach the tip from the sample.

2.9.2 Electrostatic force microscopy

Electrostatic force microscopy is a type of dynamic non-contact AFM, which can be further categorized into Electric Force Microscopy (EFM) and Surface Potential (SP) imaging, both of which characterize materials for electrical properties. A conductive AFM tip interacts with the sample through long-range Coulomb forces (of the order of 100 nm). This force arises due to the attraction or repulsion of separated charges. These interactions change the oscillation amplitude and phase of the AFM cantilever, which are detected to create EFM or SP images. In an EFM image, the phase, frequency, or amplitude of the cantilever oscillation is plotted at each in-plane (XY) coordinate. This phase, frequency, or amplitude is related to the gradient of the electric field between the tip and the sample. In a SP image, variations in the surface potential on the sample are plotted. A voltage carrying AFM tip also enables electrical modification of materials on or beneath the surface. Applications of electrostatic force microscopy include electrical failure analysis, detecting trapped charges, quantifying contact potential difference between metals and/or semiconductors, mapping relative strength and direction of electric polarization, testing electrical continuity and performing electrical read/write.

SP imaging maps the electrostatic potential on the sample surface with or without a voltage applied to the sample. SP imaging is a nulling technique. As the tip travels above the sample surface in Lift Mode, the tip and the cantilever experience a force wherever the potential on the surface is different from the potential of the tip. The force is nullified by varying the voltage of the tip so that the tip is at the same potential as the region of the sample surface underneath it. The voltage applied to the

tip in nullifying the force is plotted versus the in-plane coordinates, creating the surface 3–dimension potential image. During the Lift Mode scan, the piezoelectric element that mechanically drives the cantilever in Tapping Mode height imaging is idle. Instead, an adjustable AC electric signal at, or near, the cantilever’s fundamental resonance frequency is applied directly to the tip. In the presence of a DC potential difference between the tip and the sample, the AC signal gives rise to a periodic Coulomb force, which has the right frequency to drive the cantilever into resonant mechanical oscillation. The DC voltage of the tip is then adjusted by feedback electronics until the tip and the sample are at the same potential, where the frequency of the periodic Coulomb force on the cantilever is now twice the fundamental resonance frequency.

In this thesis, we have performed AFM imaging of nanoparticles–polymer composites as well as microbial cells in tapping mode. In addition, SP imaging (also known as Kelvin Probe Microscopy) was also performed on ferroelectric barium titanate nanoparticles for electrical read/write purposes. We have used NanoScope IV Multimode scanning probe microscope by VEECO Inc for AFM and SP imaging.

2.10 Polyacrylamide gel electrophoresis (PAGE)

The term electrophoresis describes the migration of a charged particle under the influence of an electric field. Many biological molecules including amino acids, peptides, proteins, nucleotides and nucleic acids possess ionizable groups and therefore, at any given pH, exist in solution as electrically charged cationic (+) or anionic (–) species. Under the influence of an electric field these charged particles migrate to the respective electrodes, depending on the nature of their net charge and hence can be separated by electrophoresis [27].

In this thesis, we have used polyacrylamide gel electrophoresis (PAGE) for analysis of various proteins involved in the biosynthesis of oxide nanoparticles. PAGE may be categorized into native and denaturing PAGE. In native PAGE, proteins are separated in their native form on the basis of their charge as well as molecular weight. Sodium dodecyl sulphate polyacrylamide gel electrophoresis (SDS–PAGE) is a form of denaturing PAGE, in which the anionic detergent SDS is used, which denatures the native proteins into their polypeptide units and completely swamps the original charge of the proteins while rendering an overall negative charge

to all the protein molecules analyzed. Therefore in SDS–PAGE, proteins can be separated in a protein mixture, only on the basis of their relative masses. This helps in identification of molecular weights of proteins under investigation [28].

2.11 References

- [1] Mie, G. *Ann. Phys.* **1908**, 25, 377.
- [2] Greighton, J. A.; Eadon, D. G. *J. Chem. Soc. Faraday Trans.* **1991**, 87, 3881.
- [3] Mulvaney, P. *Langmuir* **1996**, 12, 788.
- [4] Brus, L. *J. Phys. Chem.* **1986**, 90, 2555.
- [5] Denney, R. C; Sinclair, R. *Visible and Ultraviolet Spectroscopy: Analytical Chemistry by Open Learning Series*, John Wiley & Sons, USA.
- [6] Willard, H. H.; Merritt, L. L.; Dean, J. A. *Instrumental Methods of analysis*, D van Nostrad Publications, Torronto **1951**.
- [7] Hsu, C. P. S. *Handbook of Instrumental Techniques for Analytical Chemistry*, Infrared Spectroscopy, Chapter 15, Settle, F. A. (ed.) Prentice Hall, New Jersey **1997**.
- [8] George, W.O.; McIntyre, P.S. *Infrared Spectroscopy: Analytical Chemistry by Open Learning Series*, John Wiley & Sons, USA **1987**.
- [9] Marshbanks, T. L.; Ahn, D. J.; Franses, E. I. *Langmuir* **1994**, 10, 276.
- [10] Falini, G.; Albeck, S.; Weiner, S.; Addadi, L. *Science* **1996**, 271, 67.
- [11] Dong, A.; Huang, P.; Caughey, W. S. *Biochemistry* **1992**, 31, 182.
- [12] Carlson, T. A. *X–ray Photoelectron Spectroscopy*, Plenum Publishing Corporation, New York **1975**.
- [13] Shirley, D. A. *Phys. Rev. B* **1972**, 5, 4709.
- [14] Cullity, B. D. *Elements of X–Ray Diffraction*, Addison–Wesley Publishing Co. Inc. **1978**.
- [15] Azaroff, L. V. *X–Ray Diffraction*, Mc Graw Hill Co. **1974**.
- [16] Dean, John A. *The Analytical Chemistry Handbook*. New York. McGraw Hill Inc., New York **1995**.

- [17] Pungor, Erno. *A Practical Guide to Instrumental Analysis*, Boca Raton, Florida **1995**.
- [18] Skoog, D. A.; Holler, F. J.; Nieman, T. *Principles of Instrumental Analysis*, 5th edition., New York **1998**.
- [19] Rochow, T. G.; Tucker, P. A. *Introduction to Microscopy by Means of Light, Electrons, X-Rays or Acoustics*, Plenum Publishing Corporation, New York **1994**.
- [20] Williams, D. B. *Transmission Electron Microscopy: A Textbook for Material Science*, Plenum Pres, New York and London **1996**.
- [21] Everheart, T. E.; Hayes, T. L. *Sci. Am.* **1972**, 226, 55.
- [22] Reimschuessel, *J. Chem. Educ.* **1972**, 49, A 413.
- [23] Oatley, C. W. *Scanning Electron Microscope: The Instrument*, Cambridge **1972**.
- [24] Howlard, R.; Benatar, L. *A Practical Guide to Scanning Probe Microscopy*, TM Microscopes, Sunnyvale **2000**.
- [25] Miles, M. *Science* **1997**, 277, 5333.
- [26] Zhong, Q.; Innis, D.; Kjoller, K.; Elings, V. B. *Surf. Sci. Lett.* **1993**, 290, L688.
- [27] Wilson, K.; Walker, J. *Practical Biochemistry*, 5th edition, Cambridge University Press.
- [28] Laemmli, U. K. *Nature* **1970**, 227, 680.

CHAPTER III

Fungus-mediated Biosynthesis of Binary and Ternary Oxide Nanoparticles using Chemical Precursors

This chapter discusses the use of a fungus *Fusarium oxysporum* for the biosynthesis of oxide nanoparticles of technological significance. The fungus, on exposure to the aqueous solutions of complex anionic oxide precursors, results in extracellular biosynthesis of oxide nanoparticles *viz.* silica, titania, zirconia and barium titanate under ambient conditions. The formation of biogenic oxides is believed to occur *via* interaction of extracellular fungal cationic proteins with the respective anionic precursors. The existence of ferroelectricity and ferroelectric-relaxor behaviour in sub-10 nm barium titanate nanoparticles at room-temperature and the capacity to electrically write and thereafter read the information on these particles has been shown using Kelvin probe microscopy.

Part of the work presented in this chapter has been published:

1) Bansal, V.; Rautaray, D.; Ahmad, A.; Sastry, M. *J. Mater. Chem.* **2004**, *14*, 3303–3305. 2) Bansal, V.; Rautaray, D.; Bharde, A.; Ahire, K.; Sanyal, A.; Ahmad, A.; Sastry, M. *J. Mater. Chem.* **2005**, *15*, 2583–2589. 3) Bansal, V.; Poddar, P.; Ahmad, A.; Sastry, M. *J. Am. Chem. Soc.* **2006**, *128*, 11958–11963.

3.1 Introduction

Biology is replete with examples of exquisite hierarchically assembled inorganic structures. Synthesis of inorganic materials by various biological systems is characterized by processes that occur at close to ambient temperatures, pressures and neutral pH. From a materials scientist's point of view, the formation of the aligned magnetic nanoparticles synthesized by magnetotactic bacteria [1]; calcareous structures produced by haptophytes [2] as well as S-layer bacteria [3]; and the appealing siliceous structures [4] formed by organisms in the form of frustules in diatoms (a Phylum of algae, the Bacillariophyta) [5–9], spicules in sponges (a Phylum of animals, the Porifera) [10], and in various siliceous forms in Radiolarians (a group of planktonic Protists) [11] and Choanoflagellates [12] are highly inspirational, since they might assist in generation of new materials with specific form and function for industrial applications.

Biosilicification in diatoms has been studied in much detail, both from the materials point of view [6–9] and for understanding the link between global silicon and carbon cycles [9]. Diatoms are single-celled microscopic plants that are capable of accumulating silica containing molecules even from the external environment drastically undersaturated with silica, and can concentrate Si to produce an intricate external skeleton of hydrated silica protected by an organic casing, all within a matter of hours [13]. Silica formation in diatoms/sponges proceeds *via* hydrolysis of silicic acid by proteins such as silicateins [6] and polycationic peptides termed silaffins [8]. Elucidation of the biological synthesis of silica through silicatein and silaffin has resulted in the design of synthetic cationic polypeptides that mimic the behavior of silicateins [14].

While purely biological and bioinspired methods for the synthesis of silica provide environmentally benign and energy-conserving processes, to our knowledge, there have been a very few previous efforts towards the exploration of other class of microorganisms like fungi, which are not a familiar native to silicate environments for the biosynthesis of silica nanoparticles. The fact that fungi are easier to culture under laboratory conditions and have a better chance of scale up, make them prospective candidates for large-scale commercial synthesis of oxide nanomaterials. The possibility of synthesizing various oxide nanoparticles using fungi, would offer an environmentally benign alternative to the conventional chemical routes of preparation,

which generally employ extremes of pH and temperature [15]. This would also help stave off growing apprehensions related to environmental degradation and biological hazards that accompany the enthusiasm of emerging nanoscience and nanotechnology [16], apart from being a cost effective process with potential for large scale synthesis.

In this chapter, we discuss our discovery that silica nanoparticles may be produced by challenging a plant pathogenic fungus, *Fusarium oxysporum* with aqueous anionic hexafluorosilicate (SiF_6^{2-}) complex. Extracellular hydrolysis of the anionic complex by low molecular weight cationic proteins secreted by the fungus results in the room temperature synthesis of crystalline silica particles in aqueous environment. The fungus *F. oxysporum* is a plant pathogenic fungus and during its life cycle, is not exposed to such ions. That this fungus should secrete proteins capable of hydrolyzing SiF_6^{2-} complexes is unexpected but has significant potential for development. It is interesting to note that we are successful not only in extending our studies towards the biosynthesis of other binary oxide nanoparticles like titania and zirconia using hexafluorotitanate (TiF_6^{2-}) and hexafluorozirconate (ZrF_6^{2-}) anionic complexes respectively, we could also biosynthesize complex ternary oxide nanoparticles like barium titanate using the same fungus under ambient conditions. The choice of the plant pathogenic fungus *F. oxysporum* for this purpose was not random but directed towards the fact that plant pathogenic fungi produce a vast array of extracellular hydrolases to degrade their host plants in their natural habitats; these hydrolases can be explored *in silico* to hydrolyze oxide precursors to form respective oxide nanoparticles extracellularly in an aqueous environment at room temperature. The use of non-mineral forming microorganisms in advanced materials synthesis opens up exciting possibilities for commercially viable biological synthesis of technologically important oxides and semiconductors. The fact that biomolecules/proteins might get entrapped in oxide nanoparticles during biosynthesis can impart unusual properties to biogenic oxides synthesized using the fungal route. This possibility has been explored in terms of room-temperature existence of ferroelectricity and ferroelectric-relaxor behaviour in sub-10 nm biogenic barium titanate nanoparticles. Moreover, the capacity to electrically write and thereafter read the information on these barium titanate particles has also been shown using Kelvin probe microscopy, which opens up new opportunities, including the replacement of

traditional ferromagnetic memories with ultra-high density non-volatile ferroelectric memories.

This chapter describes:

- 1) *Biosynthesis of binary oxide nanoparticles viz. silica, titania and zirconia using the fungus F. oxysporum.*
- 2) *Biosynthesis of complex oxide nanoparticles i.e. barium titanate using the fungus F. oxysporum.*

3.2 Biosynthesis of binary oxide nanoparticles viz. silica, titania and zirconia using the fungus *Fusarium oxysporum*.

3.2.1 Experimental details

The plant pathogenic fungus *Fusarium oxysporum* was isolated from *Rosa* sp. and cultured as described elsewhere [17]. Briefly, the fungal mycelia was inoculated in a 500 mL Erlenmeyer flask containing 100 mL of MGYP medium composed of malt extract (0.3%), glucose (1.0%), yeast extract (0.3%) and peptone (0.5%) at 25–28 °C under shaking condition (200 rpm) for 72 h. After incubation, the fungal mycelia were harvested from the culture broth by centrifugation (5000 rpm) at 10 °C for 20 min and the settled biomass was washed thrice with sterile deionized water. Twenty grams (wet weight) of the harvested fungal biomass was then resuspended separately in 100 mL aqueous solutions of 10^{-3} M K_2SiF_6 (pH 3.1), K_2TiF_6 (pH 3.5) and K_2ZrF_6 (pH 4.5) in 500 mL Erlenmeyer flasks and kept on a shaker (200 rpm) at 25–28 °C. The reactions between the fungal biomass and the SiF_6^{2-} , TiF_6^{2-} and ZrF_6^{2-} ions were carried out for a period of 24 h. The biogenic products of the reactions were collected under sterile conditions at various time intervals during the reaction by separating the fungal mycelia from the aqueous extract through filtration. The reaction products obtained were precipitated by repeated centrifugation and washing with deionized water at 15000 rpm for 30 min. Further characterization of the purified products as well as of the calcined products (300 °C for 3 h) were carried out by Fourier transform infrared (FTIR) spectroscopy, transmission electron microscopy (TEM), selected area electron diffraction (SAED) analysis, X-ray diffraction (XRD) analysis, thermogravimetric analysis (TGA), electron dispersive X-rays (EDX) analysis and X-ray photoemission spectroscopy (XPS).

In vitro syntheses of oxide nanoparticles were also performed using extracellular fungal extract, for which 20 g of thoroughly washed sterile fungal biomass was suspended in 100 mL of sterile deionized water in 500 mL Erlenmeyer flasks under shaking condition (200 rpm) at 25–28 °C. The extracellular components (mainly proteins) secreted by the fungus in water after 24 h were collected by filtration and concentrated by lyophilization. The lyophilized extracellular fraction containing a mixture of proteins was dialyzed against deionized water (using a 12 kDa cutoff dialysis membrane) and further purified using CM sephadex cation exchange matrix. The lyophilized total extracellular proteins as well as various cationic protein fractions obtained from CM sephadex column were reacted for 24 h with 10^{-3} M aqueous solutions of K_2SiF_6 , K_2TiF_6 and K_2ZrF_6 and checked for their activity by FTIR spectroscopy and TEM.

The differential expression profile of extracellular fungal proteins secreted by the fungus in the filtrate, both in the absence as well as in presence of ZrF_6^{2-} ions was studied by concentrating both the filtrates by lyophilization and thereafter loading on 10% native and SDS–PAGE (sodium dodecyl sulphate polyacrylamide gel electrophoresis) carried out at pH 8.3. In addition, the proteins inducibly secreted by the fungus *F. oxysporum* in the presence of SiF_6^{2-} ions and involved in the biosynthesis of oxide nanoparticles were purified and characterized by ammonium sulphate precipitation, ion exchange chromatography and SDS–PAGE. Briefly, the extracellular proteins secreted by the fungus in water in the presence of SiF_6^{2-} ions were salted out overnight at 4 °C using 80% ammonium sulphate, followed by centrifugation (15000 rpm) at 4 °C for 20 min. The proteins obtained thereafter were dissolved in the minimal volume of deionized water, dialyzed (12 kDa cutoff) and loaded onto CM sephadex column. The cationic proteins bound to CM sephadex matrix were eluted in various fractions using increasing concentration of sodium chloride. Column-eluted cationic protein fractions were checked for their activity by FTIR and the cationic fraction found active for hydrolysis of oxide precursors was analyzed along with proteins precipitated using 80% ammonium sulphate on a 10% SDS–PAGE.

The proteins bound to the surface of the biogenic oxide nanoparticles were also analyzed in the following manner. The filtrate obtained after the reaction of ZrF_6^{2-} ions with the fungus *F. oxysporum* was centrifuged (15000 rpm) at 10 °C for

20 min and the precipitated zirconia particles were thoroughly washed with copious amounts of deionized water and analyzed on SDS–PAGE. Surface-bound proteins were detached from ZrO_2 particles by boiling particles at 95 °C in 1% SDS solution for 5 min. SDS-treated as well as untreated nanoparticles were analyzed on a 10% SDS–PAGE.

3.2.2 Control experiments

Various control experiments were performed to check the validity of results obtained. To nullify the possibility of leaching of silica from Erlenmeyer flasks, 20 g of fungal biomass was suspended in 100 mL deionized water in an Erlenmeyer flask in the absence of hexafluoro derivatives and the filtrates obtained thereafter were characterized by TEM and FTIR. These reactions did not result in the formation of silica nanoparticles. In another control experiment, the hydrolysis of hexafluoro derivatives in deionized water in the absence of fungal biomass at pH 3.1 (K_2SiF_6), 3.5 (K_2TiF_6) and 4.5 (K_2ZrF_6) was studied by TEM and FTIR. This control experiment was also negative and did not yield any silica, titania or zirconia particles. Moreover, a number of other genera of fungi (*Trichothecium* sp., *Phomopsis* sp., *Curvularia lunata*, *Colletotrichum gloeosporioides* and *Aspergillus niger*), when tested for extracellular hydrolytic activity, did not yield oxide nanoparticles.

3.2.3 FTIR spectroscopy measurements

FTIR spectroscopy is an appropriate tool to study the hydrolysis of anionic oxide precursors into respective oxides. FTIR measurements were carried out to monitor the time-dependent kinetics of oxides formation as well as to identify the nature of the biomolecules interacting/capping with oxides during their biosynthesis (Figure 3.1, 3.2 and 3.3). In order to monitor the kinetics of hydrolysis of SiF_6^{2-} ions into SiO_2 , FTIR analyses of the fungus– K_2SiF_6 reaction medium were performed after 1 h, 6 h, 12 h, 18 h and 24 h of reaction (curves 1–5 respectively, Figure.3.1.A). It is observed that as the reaction proceeds, there is a gradual and monotonic increase in absorbance at *ca.* 1086 cm^{-1} that is accompanied by a decrease in intensity of the resonance at *ca.* 750 cm^{-1} (Figure 3.1 A). The 1086 cm^{-1} band is attributed to excitation of the antisymmetric Si–O–Si stretching mode of vibration [18] while the absorption band at *ca.* 750 cm^{-1} is due to SiF_6^{2-} ions used as a precursor for SiO_2 formation (curve 1, Figure 3.1 B). This clearly indicates the hydrolysis of SiF_6^{2-} ions,

resulting in extracellular SiO₂ in the aqueous environment. However, FTIR analysis of SiO₂ after 24 h of reaction also showed a relatively weak absorption band at *ca.* 750 cm⁻¹, along with prominent absorbance at *ca.* 1086 cm⁻¹, which indicate the presence of some unreacted SiF₆²⁻ ions along with SiO₂ (curve 2, Figure 3.1 B).

Once the extracellular formation of SiO₂ is confirmed by FTIR studies, it suggests the role of some extracellular fungal enzymes/proteins, which are synthesized by fungi in large amounts. This speculation is in accordance with the fact that enzymes in diatoms and sponges are known to play a crucial role in formation of SiO₂ particles in these organisms [6, 8]. Proteins occluded in/bound to SiO₂ can be easily traced using FTIR spectroscopy due to the characteristic amide I and II signatures in peptides and proteins. In order to confirm our speculation, a more careful analysis of biologically synthesized SiO₂ was performed in the amide region (curve 2, Figure 3.1 C), which indicates the presence of two absorption bands at *ca.* 1650 cm⁻¹ and 1540 cm⁻¹ that may be assigned to the amide I and II signatures respectively. Presence of amide signatures in SiO₂ (curve 2, Figure 3.1 C) and their clear absence in the silica precursor K₂SiF₆ (curve 1, Figure 3.1 C) attests to the presence of proteins in SiO₂. The biogenic silica was further calcined at 300 °C for 3 h in order to degrade the protein molecules bound to SiO₂. FTIR analysis of the silica powder after calcination shows a sharpening of the Si–O–Si vibrational band (curve 3, Figure 3.1 B), accompanied by disappearance of the protein amide I and II signatures from SiO₂ powders (curve 3, Figure 3.1 C). Thus, FTIR spectroscopy studies indicate that extracellular fungal proteins may be involved in hydrolysis of SiF₆²⁻ precursors to form SiO₂.

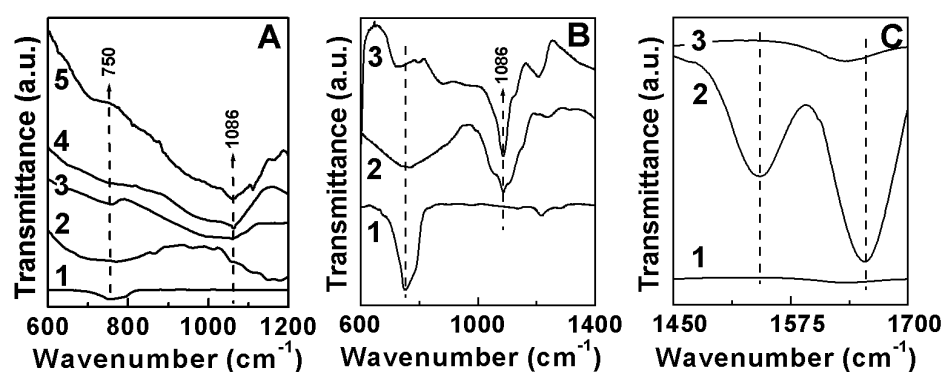


Figure 3.1 (A) FTIR kinetics recorded from biogenic silica synthesized by the reaction of K₂SiF₆ with *F. oxysporum* at reaction intervals of 1, 6, 12, 18 and 24 h (curves 1–5) respectively. (B) FTIR spectra recorded from powders of K₂SiF₆ (curve 1); biogenic silica synthesized using *F. oxysporum* before (curve 2) and after calcination at 300 °C for 3 h (curve 3). (C) An expanded view of FTIR spectra shown in (B) in the region of protein amide bands.

FTIR spectroscopy studies of the formation of TiO_2 via hydrolysis of TiF_6^{2-} precursor ions using the fungus *F. oxysporum* were also performed (Figure 3.2). The kinetics of titania formation in the fungus– TiF_6^{2-} reaction medium was followed by FTIR spectroscopy after 1 h, 6 h, 12 h, 18 h and 24 h of reaction (curves 1–5 respectively, Figure 3.2 A). It is observed that as the reaction proceeds, there is a steady increase in intensity of the resonance at *ca.* 1107 cm^{-1} , which can be attributed to Ti–O–Ti vibrational modes of TiO_2 [19], indicating hydrolysis of the TiF_6^{2-} ions into TiO_2 . Apart from intense Ti–O–Ti vibrational mode at *ca.* 1107 cm^{-1} , the FTIR spectrum recorded from TiO_2 after 24 h of reaction (curve 2, Figure 3.2 B) also showed a weak Ti–O–Ti vibrational mode at *ca.* 606 cm^{-1} and another weak Ti–O antisymmetric stretching mode at *ca.* 954 cm^{-1} [20] that are missing in the K_2TiF_6 sample (curve 1, Figure 3.2 B). In addition, the presence of proteins in titania is indicated in the form of amide I and II signatures in the FTIR spectrum (curve 2, Figure 3.2 C), which are absent in the K_2TiF_6 powder (curve 1, Figure 3.2 C). FTIR analysis of the titania powder after calcination at $300\text{ }^\circ\text{C}$ for 3 h shows a sharpening of the Ti–O–Ti vibrational bands (curve 3, Figure 3.2 B) that is accompanied by disappearance of the amide I and II bands (curve 3, Figure 3.2 C), as in the case of silica (Figure 3.1 C).

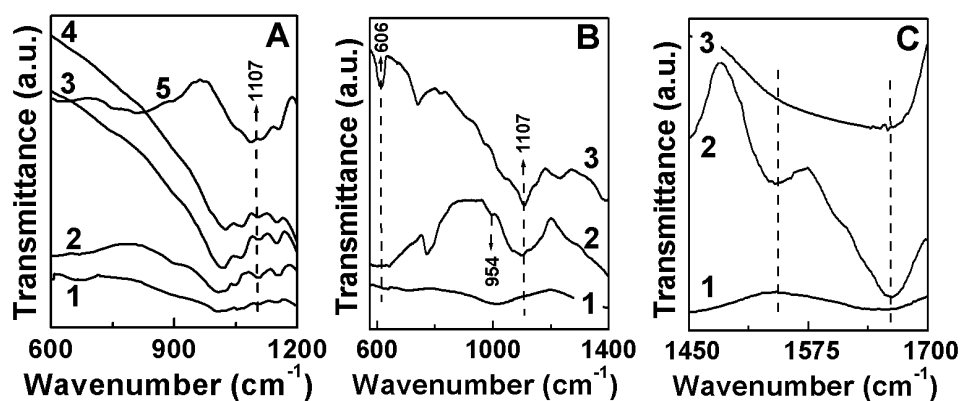


Figure 3.2 (A) FTIR kinetics recorded from biogenic titania synthesized by the reaction of K_2TiF_6 precursor with *F. oxysporum* at reaction intervals of 1, 6, 12, 18 and 24 h (curves 1–5) respectively. (B) FTIR spectra recorded from powders of K_2TiF_6 (curve 1); biogenic titania synthesized using *F. oxysporum* before (curve 2) and after calcination at $300\text{ }^\circ\text{C}$ for 3 h (curve 3). (C) An expanded view of FTIR spectra shown in (B) in the region of protein amide bands.

FTIR spectroscopy studies of the formation of ZrO_2 via hydrolysis of ZrF_6^{2-} precursor ions using the fungus *F. oxysporum* were also performed (Figure 3.3). The kinetics of zirconia formation in the fungus– ZrF_6^{2-} reaction medium was followed by FTIR spectroscopy after 1 h, 6 h, 12 h, 18 h and 24 h of reaction (curves 1–5

respectively, Figure 3.3 A). It is observed that with time, there is a steady increase in intensity of the resonance at *ca.* 613 cm^{-1} and 819 cm^{-1} , which can be attributed to Zr–O–Zr stretching mode vibrations of monoclinic ZrO_2 [21], indicating hydrolysis of ZrF_6^{2-} ions into ZrO_2 . These vibrational modes are clearly missing in the K_2ZrF_6 sample (curve 1, Figure 3.3 B). In addition, the presence of proteins in biogenic zirconia is indicated in the form of amide I and II signatures in the FTIR spectrum (curve 2, Figure 3.3 C), which are absent in K_2ZrF_6 powder (curve 1, Figure 3.3 C). FTIR analysis of zirconia powder after calcination at 300 °C for 3 h shows a sharpening of the Zr–O–Zr vibrational bands (curve 3, Figure 3.3 B) that is accompanied by disappearance of the amide I and II bands (curve 3, Figure 3.3 C), as in the case of silica (curve 3, Figure 3.1 C) and titania (curve 3, Figure 3.2 C). Thus, the FTIR spectroscopy results indicate the involvement of extracellular fungal proteins in the hydrolysis of respective anionic oxide precursors to form silica, titania and zirconia.

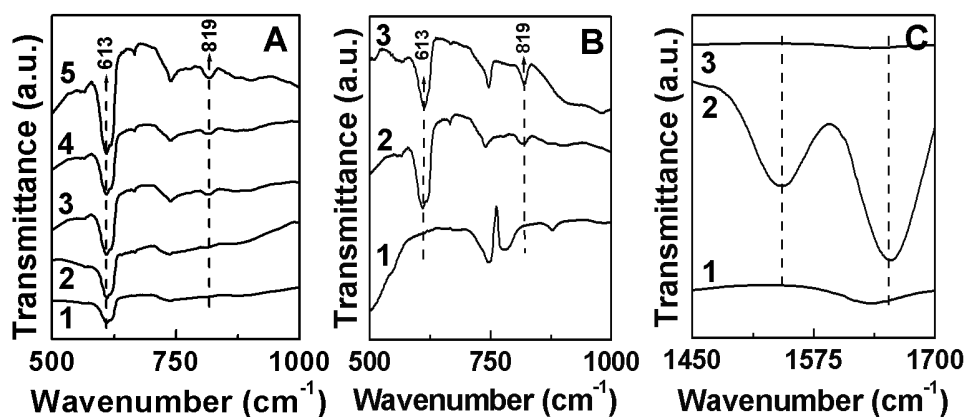


Figure 3.3 A) FTIR kinetics recorded from zirconia synthesized by the reaction of K_2ZrF_6 precursor with *F. oxysporum* at reaction intervals of 1, 6, 12, 18 and 24 h (curves 1–5) respectively. B) FTIR spectra recorded from powders of K_2ZrF_6 (curve 1); biogenic zirconia synthesized using *F. oxysporum* before (curve 2) and after calcination at 300 °C for 3 h (curve 3). C) An expanded view of FTIR spectra shown in (B) in the region of protein amide bands.

3.2.4 TEM and SAED measurements

The formation of oxide particles in the nanometer size regime can be easily monitored using TEM. A representative TEM image from the particles obtained after reacting the fungal biomass with SiF_6^{2-} ions for 24 h is shown in Figure 3.4 A. The silica nanoparticles formed are irregular in shape presenting an overall quasi-spherical morphology. The particle size histogram of the silica particles shows that the particles range in size from 5 to 15 nm and possess an average size of 9.8 nm (Figure 3.4 B).

The SAED pattern obtained from these particles clearly indicates the crystalline nature of silica particles (inset, Figure 3.4 A). The diffraction spots could be indexed based on the tridynite polymorph of SiO_2 wherein the d values obtained (3.24 Å, 3.00 Å, 2.50 Å and 2.09 Å) match well with the standard d values [3.24 Å (420), 2.98 Å (224), 2.48 Å (040) and 2.07 Å (441)] for the tridynite polymorph of SiO_2 [22]. Notably, we did not observe diffraction spots from potential impurities such as unreacted K_2SiF_6 .

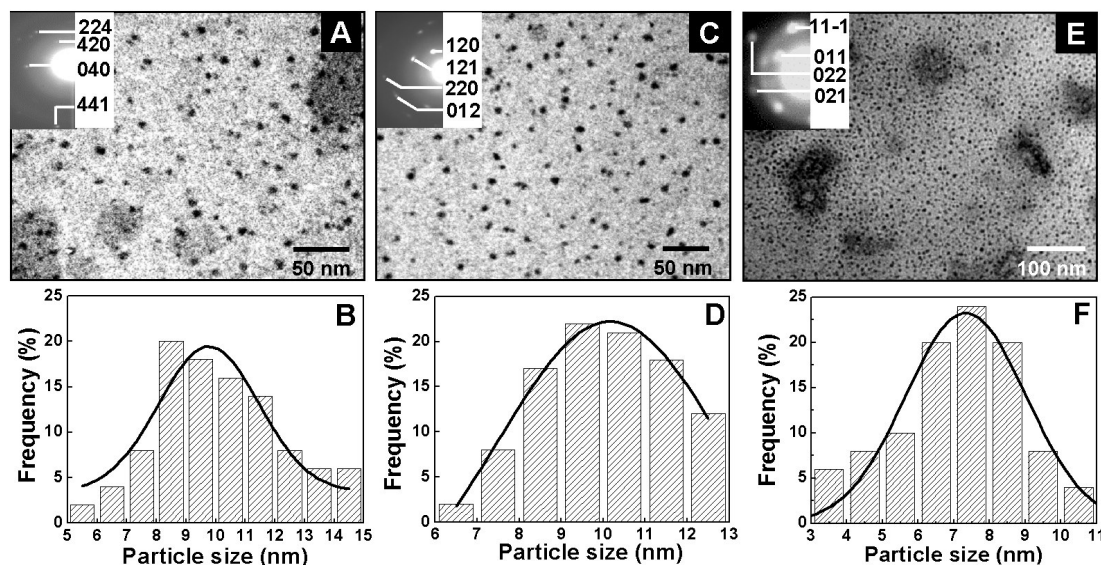


Figure 3.4 TEM micrographs of silica (A), titania (C) and zirconia (E) nanoparticles synthesized using the fungus *F. oxysporum*. The insets in A, C and E correspond to the SAED patterns recorded from the representative silica (A), titania (C) and zirconia (E) particles shown in the main part of the figure. Particle size histograms of the silica, titania and zirconia particles shown in images A, C and E are shown in (B), (D) and (F) respectively.

Similarly, TEM analysis was also performed on the particles from the fungus- TiF_6^{2-} reaction mixture after 24 h of reaction (Figure 3.4 C). A number of quasi-spherical particles ranging in size from 6 to 13 nm with an average size of 10.2 nm were seen, for which particle size histogram is shown in Figure 3.4 D. SAED analysis of the biogenic titania particles indicated that they were crystalline (inset, Figure 3.4 C). The diffraction spots could be indexed based on the brookite structure of TiO_2 wherein the d values obtained (3.53 Å, 2.90 Å, 2.47 Å and 2.34 Å) match well with the standard d values [3.51 Å (120), 2.90 Å (121), 2.47 Å (012) and 2.34 Å (220)] for the brookite polymorph of TiO_2 [22]. We did not observe diffraction spots from potential impurities such as unreacted K_2TiF_6 .

TEM analysis when performed on particles obtained from fungus- ZrF_6^{2-} reaction mixture after 24 h of reaction (Figure 3.4 E) showed that particles are fairly

regular in shape, presenting an overall quasi-spherical morphology. The particle size histogram shows that particles range in size 3 to 11 nm with an average particle size of 7.3 nm (Figure 3.4 F). SAED pattern of the biogenic zirconia particles (inset, Figure 3.4 E) indicated that they were crystalline and revealed the monoclinic phase of ZrO_2 , wherein the d values obtained (3.69 Å, 3.16 Å, 2.61 Å, 2.32 Å) match excellently with the standard d values [(3.69 Å (011), 3.16 Å (11(-1)), 2.61 Å (022), 2.32 Å (021)] for the monoclinic phase of ZrO_2 [22]. As in the previous examples, diffraction spots corresponding to potential impurities such as unreacted K_2ZrF_6 were not observed.

One of the interesting observations of the biological synthesis of oxides nanoparticles is that the particles formed are relatively small (average size 10 nm). This can be explained on the basis of our observations that the proteins involved in the biosynthesis bind to the surface of these particles during their growth and hence restrict the further growth of oxide nanoparticles. Presence of amide signatures in the FTIR spectra of oxides nanoparticles (curve 2 in Figure 3.1 C, 3.2 C and 3.3 C) is also indicative of the same. Further evidence to this observation has been shown in the section 4.3.10 of chapter 4 of this thesis. The FTIR, TEM and SAED analyses of the products of the reaction between oxide precursors with *F. oxysporum* establish the formation of crystalline oxide nanoparticles with a fair degree of proteins occluded into their structures. The biogenic oxide powders were then calcined in air at 300 °C for 3 h to remove the occluded proteins and promote further crystallization of oxide nanoparticles. The TEM images of SiO_2 (Figure 3.5 A), TiO_2 (Figure 3.5 B) and ZrO_2 (Figure 3.5 C) particles after calcination show that these particles undergo a significant change in particle morphology and form large aggregates after calcination.

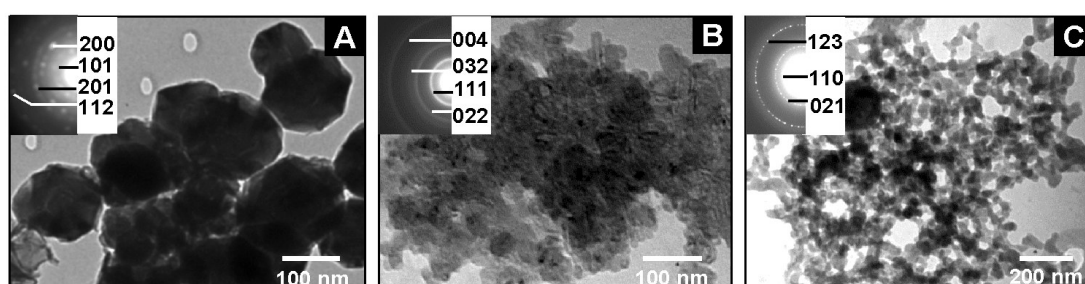


Figure 3.5 TEM micrographs of silica (A), titania (B) and zirconia (C) nanoparticles synthesized using the fungus *F. oxysporum* after calcinations at 300 °C for 3 h. The insets in A, B and C correspond to the SAED patterns recorded from the representative silica (A), titania (B) and zirconia (C) particles shown in the main part of the figure.

It is observed that the particles show greater contrast indicating sintering and formation of denser oxide particles. The discrete, individual particles observed in the as-prepared biogenic oxides (Figure 3.4 A, C and E) have given way to a more aggregated structure after calcination, in which the individual particles can barely be discerned (Figure 3.5).

The SAED analysis of the silica particles after calcination suggests that the particles have become more crystalline with a number of well-defined Bragg reflections appearing in the SAED patterns (inset, Figure 3.5.A), wherein the d values obtained (3.35 Å, 2.13 Å, 1.98 Å and 1.82 Å) match well with the standard d values [3.36 Å (101), 2.13 Å (200), 1.98 Å (201) and 1.82 Å (112)] for the tridymite polymorph of SiO_2 [22]. A sharp SAED ring pattern is observed in case of calcined titania particles (inset, Figure 3.5 B) that could be indexed based on the brookite structure of TiO_2 , wherein the d values obtained (3.47 Å, 2.24 Å, 1.97 Å and 1.28 Å) match reasonably well with the standard d values [3.46 Å (111), 2.24 Å (022), 1.97 Å (032) and 1.28 Å (004)] for the brookite polymorph of TiO_2 [22]. SAED analysis of the zirconia particles after calcination (inset, Figure 3.5 C) also shows a sharp ring patterns that could be indexed based on the monoclinic structure of ZrO_2 , wherein the d values obtained (3.63 Å, 2.32 Å and 1.34 Å) match excellently with the standard d values [d -values: 3.63 Å (110), 2.32 Å (021) and 1.34 Å (123)] for the monoclinic phase of ZrO_2 [22]. Thus, removal of the occluded proteins by calcination improves the crystallinity of the biogenic silica, titania and zirconia particles.

3.2.5 XRD measurements

The crystallinity of various oxide nanoparticles formed by reaction of appropriate precursor ions with the fungus *F. oxysporum* as well as after their calcination at 300 °C for 3 h can be further established by XRD measurements. Figure 3.6 shows the XRD patterns recorded from drop cast films of silica (Figure 3.6 A), titania (Figure 3.6 B) and zirconia (Figure 3.6 C) particles. As-prepared silica particles (curve 1, Figure 3.6 A) failed to show well-defined Bragg reflections indicating that the particles are X-ray amorphous. While the reasons for silica particles being X-ray amorphous, but crystalline under electron diffraction analysis (SAED pattern, inset Figure 3.4 A) are not clear at this point, we speculate that the particles undergo mild heating during electron irradiation in the TEM that facilitates

their crystallization under the electron beam. However, calcination of silica particles results in increase in crystallinity of silica particles, as is mirrored in the XRD pattern of calcined silica powder that shows intense Bragg reflections (curve 2, Figure 3.6 A), characteristic of crystalline silica. The d values obtained in XRD pattern of silica particles match well with the standard d values [4.26 Å (100), 3.36 Å (101), 2.46 Å (110) and 1.85 Å (112)] of the tridynite phase of silica [22].

Figure 3.6 B shows the XRD pattern obtained from drop cast films of as-synthesized TiO_2 particles (curve 1, Figure 3.6 B) as well as after their calcination (curve 2, Figure 3.6 B). A number of Bragg reflections characteristic of the brookite phase of TiO_2 with a small percentage of the rutile phase of TiO_2 (peak marked with 'R') are evident in the XRD pattern obtained from as-synthesized particles (curve 1, Figure 3.6 B). XRD analysis of the titania powder after calcination shows an increase in intensity of all the brookite peaks (curve 2, Figure 3.6 B). The d values obtained in XRD pattern of titania particles match well with the standard d values of the brookite [3.46 Å (111), 2.71 Å (200), 2.40 Å (201), 2.34 Å (220), 2.29 Å (040), 1.96 Å (032), 1.83 Å (212), 1.66 Å (241), 1.64 Å (151)] and the rutile phase [2.48 Å (101)] of TiO_2 [22–23]. These results correlate well with the SAED pattern obtained from TiO_2 particles, which show development of well defined ring patterns after calcination of particles (compare insets, Figure 3.4 C and Figure 3.5 B), indicating an increase in crystallinity of TiO_2 particles after calcination.

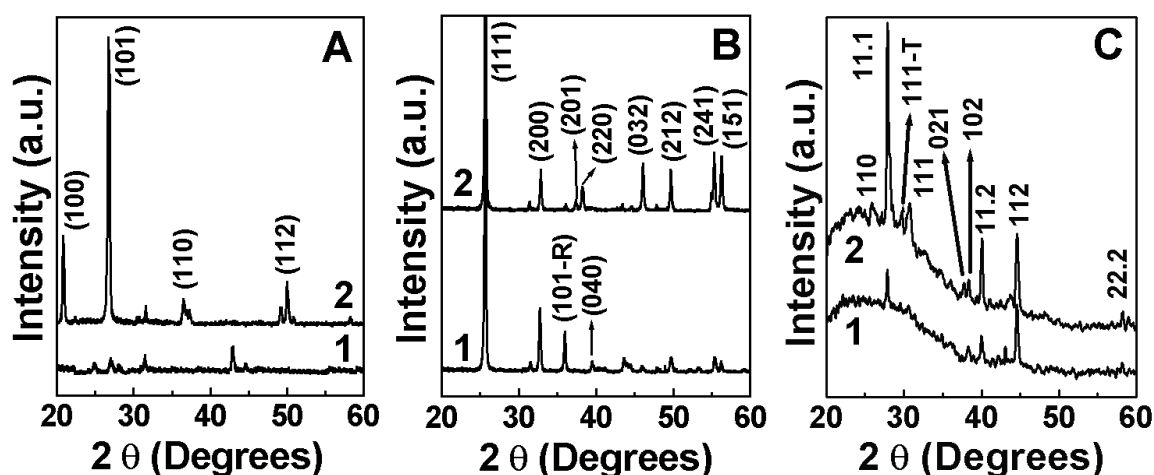


Figure 3.6 XRD patterns recorded from silica (A), titania (B) and zirconia (C) particles synthesized by the reaction of appropriate aqueous precursors with the fungus *F. oxysporum*. Curve 1 and 2 in all the figures correspond to patterns recorded from the as-prepared and calcined samples respectively. The peak marked with 'R' in (B) corresponds to the rutile phase of TiO_2 and the peak marked with 'T' in (C) corresponds to the tetragonal phase of ZrO_2 .

Similarly, XRD measurements of as-synthesized as well as calcined ZrO_2 particles were also performed (Figure 3.6 C). XRD analysis of as-synthesized particles show well-defined Bragg reflections characteristic of monoclinic phase of ZrO_2 (curve 1, Figure 3.6 C). After calcination, there is an increase in crystallinity of ZrO_2 particles as well as partial transformation of ZrO_2 particles from the monoclinic to the tetragonal phase. This is mirrored in the XRD pattern of the calcined zirconia sample that shows increase in the intensity of Bragg reflections (curve 2, Figure 3.6 C) characteristic of the monoclinic phase with the simultaneous development of a small percentage of the tetragonal phase of zirconia (peak marked with 'T') [22].

Increase in crystallinity of silica, titania and zirconia particles after calcination might be attributed to the fact that calcination at 300 °C for 3 h would result in decomposition of the proteins bound to the oxide nanoparticles, as was observed during FTIR spectroscopy studies (compare curve 2 and 3 in Figure 3.1 C, 3.2 C and 3.3 C for silica, titania and zirconia respectively). This, in turn, would lead to increased crystallinity of oxide particles.

3.2.6 TGA measurements

TGA can be used to find out the weight contribution of biomolecules/proteins in the biosynthesized oxide nanoparticles. As is evident from the FTIR data (curve 2 in Figure 3.1 C, 3.2 C and 3.3 C for silica, titania and zirconia respectively), biogenic oxide nanoparticles are capped with proteins/biomolecules that stabilize them against aggregation. TGA of air-dried biogenic oxide powders, when performed up to 650 °C, resulted in *ca.* 54%, 57% and 65% loss in weight in case of SiO_2 (curve 1, Figure 3.7; solid curve), TiO_2 (curve 2, Figure 3.7; dashed curve) and

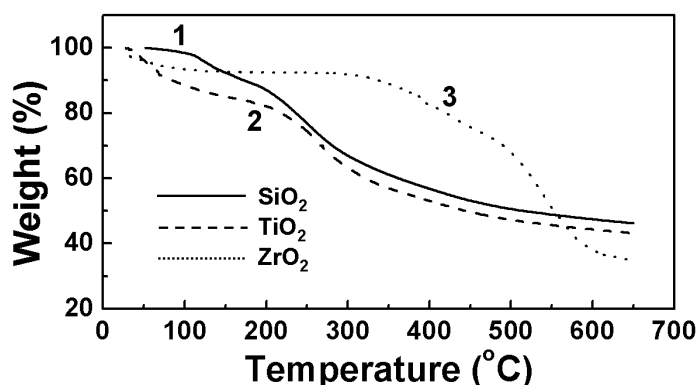


Figure 3.7 TGA spectra recorded from silica (continuous line; curve 1), titania (dashed line; curve 2) and zirconia (dotted line; curve 3) particles synthesized by the reaction of appropriate anionic precursors with the fungus *F. oxysporum*.

ZrO₂ (curve 3, Figure 3.7; dotted curve) respectively. This loss in weight can be attributed to the removal of adsorbed water and biomolecules bound to oxides nanoparticles.

3.2.7 EDX measurements

Chemical analyses of biogenic oxides were performed by EDX measurements. EDX analyses of drop-cast films of biogenic oxide nanoparticles clearly show the presence of Si signal (1.741 keV) in silica (curve 1, Figure 3.8), Ti signal (4.509 keV) in titania (curve 2, Figure 3.8) and Zr signals (2.040, 2.122 and 2.223 keV) in zirconia (curve 3, Figure 3.8) particles. In addition, presence of O signal (0.517 keV) in all the three oxides can be attributed to molecular oxygen from the respective oxides and from the bound protein molecules. Signatures of C (0.266 keV), N (0.381 keV) and S (2.307 keV) in EDX spectra of oxides arise due to the proteins bound/intercalated with in the oxide nanostructures. Additionally, weak signals of K and F were also observed in EDX spectra, indicating the presence of some unreacted oxide precursors (K₂SiF₆, K₂TiF₆ and K₂ZrF₆) in SiO₂, TiO₂ and ZrO₂ nanoparticles (Figure 3.8).

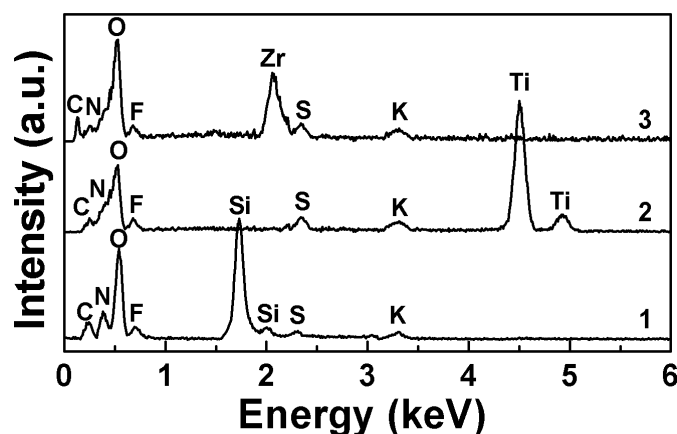


Figure 3.8 EDX spectra recorded from silica (curve 1), titania (curve 2) and zirconia (curve 3) nanoparticles synthesized by the reaction of appropriate aqueous precursors with the fungus *F. oxysporum*.

3.2.8 XPS measurements

A more refined chemical analysis of the biogenic silica nanoparticles was performed by XPS, which is known to be a highly surface sensitive technique. The Si 2p, O 1s, C 1s, N 1s and F 2p core level XPS spectra were recorded with an overall resolution of ~1 eV (Figure 3.9). The core level spectra were background

corrected using the Shirley algorithm [24] and the chemically distinct species were resolved using a nonlinear least squares fitting procedure. The core level binding energies (BEs) were aligned with the adventitious carbon binding energy of 285 eV.

The Si 2p core level spectrum (Figure 3.9 A) obtained from biogenic silica particles could be resolved into two spin-orbit pairs (spin-orbit splitting ~ 0.6 eV) [25] with $2p_{3/2}$ binding energies (BEs) of 102.7 eV (curve 1, Figure 3.9 A) and 106.2 eV (curve 2, Figure 3.9 A) respectively. The low BE component at 102.7 eV agrees excellently with values reported for SiO_2 [26], while the high BE component at 106.2 eV is assigned to unhydrolyzed SiF_6^{2-} ions [25] present on the surface of the silica nanoparticles. From the peak intensities of curve 1 (SiO_2) and curve 2 (SiF_6^{2-}), it is observed that the amount of unhydrolyzed SiF_6^{2-} ions is extremely small indicating that most of the SiF_6^{2-} ions have been hydrolyzed to form SiO_2 nanoparticles. In addition to the Si 2p spectrum, an F 2p signal (Figure 3.9 E) was also observed in the sample, supporting the presence of some amount of unhydrolyzed SiF_6^{2-} ions in the nanoparticles. The oxygen core level XPS spectrum (Figure 3.9 B) was also recorded with the O 1s BE of 532.5 eV, which matches excellently with previously reported O 1s values for SiO_2 [27].

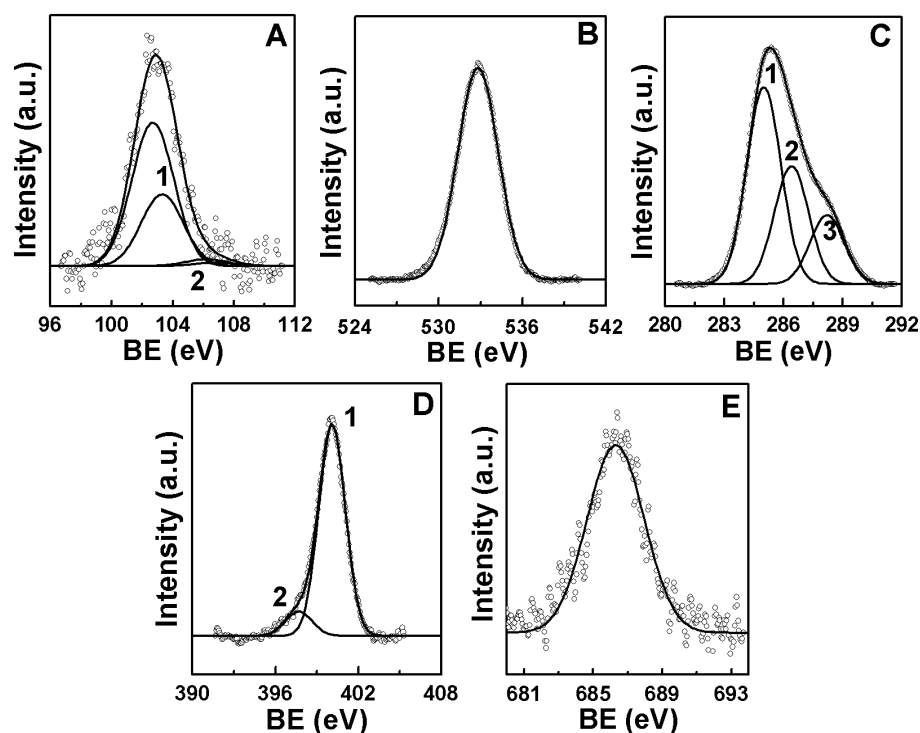


Figure 3.9 XPS data showing the Si 2p (A), O 1s (B), C 1s (C), N 1s (D) and F 2p (E) core level spectra recorded from biogenic silica nanoparticles film cast onto a Cu substrate. The raw data are shown in the form of symbols, while the chemically resolved components are shown as solid lines and are discussed in the text.

Since XPS is a highly surface sensitive technique, the presence of proteins on the surface of silica nanoparticles can easily be detected by XPS. In order to appreciate the presence of proteins on the surface of biogenic silica nanoparticles, C 1s (Figure 3.9 C) and N 1s (Figure 3.9 D) core level spectra were recorded from silica sample. In Figure 3.9 C, curves 1, 2 and 3 correspond to the chemically distinct C 1s core levels originating from the hydrocarbon chains (285 eV), α -carbon (286.6 eV) and -COOH groups (289 eV) of the proteins that are present in the protein-silica nanobiocomposite structures [25]. In addition, the N 1s core level spectrum in Figure 3.9 D could be deconvoluted into two components with BEs of 400.1 eV (curve 1, Figure 3.9 D) and 397.6 eV (curve 2, Figure 3.9 D). The high BE component at 400.1 eV (curve 1) agrees excellently with values reported for -NH amide linkage [28], while the low-intensity, low BE component at 397.6 eV (curve 2) matches closely with the values reported for Si₃N₄ [29], indicating the complexation of proteins with the surface of the silica nanoparticles. Thus, XPS data further support our belief that surface-bound proteins play an important role as capping agents to restrict the growth of oxide particles in nanometer regime.

3.2.9 *In vitro* oxides syntheses and protein analyses

In order to appreciate the role of extracellular proteins of *F. oxysporum* in the biosynthesis of oxide nanoparticles, the *in vitro* syntheses of oxides was performed in the absence of fungal biomass. The extracellular proteins secreted by the fungus in deionized water (in the absence of anionic precursor complexes), when reacted with aqueous solutions of K₂SiF₆, K₂TiF₆ and K₂ZrF₆ for 24 h, resulted in room-temperature synthesis of silica, titania and zirconia nanoparticles respectively (Figure 3.10 and 3.11). The hydrolysis of anionic oxide precursor complexes into respective oxides is evident from FTIR signals corresponding to silica (curve 2, Figure 3.10 A), titania (curve 2, Figure 3.10 B) and zirconia (curve 2, Figure 3.10 C). Silica, titania and zirconia formation in nanoparticulate form is also evident from TEM images of respective reaction products (Figure 3.11 A, B and C for silica, titania and zirconia respectively).

In addition, the extracellular proteins secreted by the fungus in the absence of anionic metal complexes were purified into various fractions using CM sephadex column. The fact that CM sephadex is a cation exchange matrix and cationic proteins

bind to this matrix with varying strength based on their isoelectric points (pI), can be utilized to separate various cationic proteins present in extracellular fungal extract. CM sephadex–purified various cationic protein fractions, when further reacted with SiF_6^{2-} , TiF_6^{2-} and ZrF_6^{2-} ions for 24 h and checked for their activity by FTIR spectroscopy and TEM, only one fraction was capable of hydrolysis of these complexes to silica (FTIR: curve 3, Figure 3.10 A; TEM: Figure 3.11 D), titania (FTIR: curve 3, Figure 3.10 B; TEM: Figure 3.11 E) and zirconia (FTIR: curve 3, Figure 3.10 C; TEM: Figure 3.11 F) respectively. Notably, the protein fraction unbound to CM–sephadex column (anionic proteins) when checked for hydrolytic activity, did not yield respective oxides, thus indicating the cationic nature of hydrolyzing proteins. This result is in corroboration with the results obtained by other groups, wherein cationic proteins and polypeptides in diatoms and sponges [6, 8] as well as synthetic cationic polypeptides [14] have been explored to play an important role in silica synthesis.

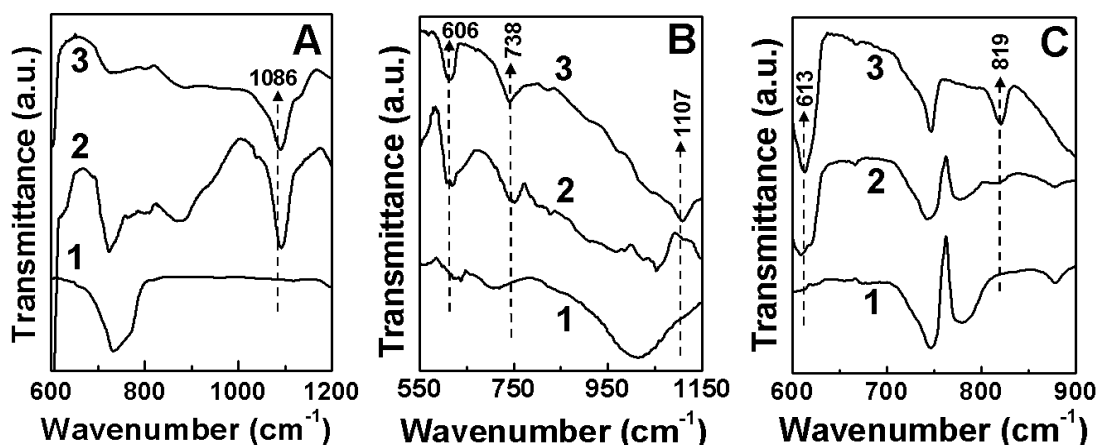


Figure 3.10 FTIR spectra recorded from powders of [A] K_2SiF_6 (curve 1), silica synthesized using fungal crude extract (curve 2) and silica synthesized using column purified cationic protein fraction (curve 3); [B] K_2TiF_6 (curve 1), titania synthesized using fungal crude extract (curve 2) and titania synthesized using column purified cationic protein fraction (curve 3); [C] K_2ZrF_6 (curve 1), zirconia synthesized using fungal crude extract (curve 2) and zirconia synthesized using CM sephadex–purified cationic protein fraction (curve 3).

It is evident that total extracellular fungal proteins as well as column-purified extracellular cationic proteins are capable of synthesizing oxides nanoparticles under *in vitro* conditions. However, FTIR spectroscopy results (Figure 3.10) suggest that when the proteins secreted by the fungus in the absence of anionic complexes were used for the hydrolysis of anionic complexes, the percentage hydrolysis of the anionic complexes was considerably lower than that observed when the reactions of the

anionic complexes were carried out directly in the presence of the fungus. This is evident in the form of significantly intense oxide precursors signals even after reacting precursors with extracellular proteins (compare FTIR spectra of respective precursors *i.e.* curve 1 with curve 2 and 3 in Figure 3.10). The incomplete hydrolysis by the proteins, which were secreted by the fungus in the absence of anionic complexes, indicates that the anionic complexes might induce the secretion of the hydrolyzing proteins from the fungus. Therefore, though we were able to detect the hydrolytic activity in column purified proteins, we could not analyze these proteins by SDS-PAGE, since the yield of proteins of our interest in the purified fractions was significantly low.

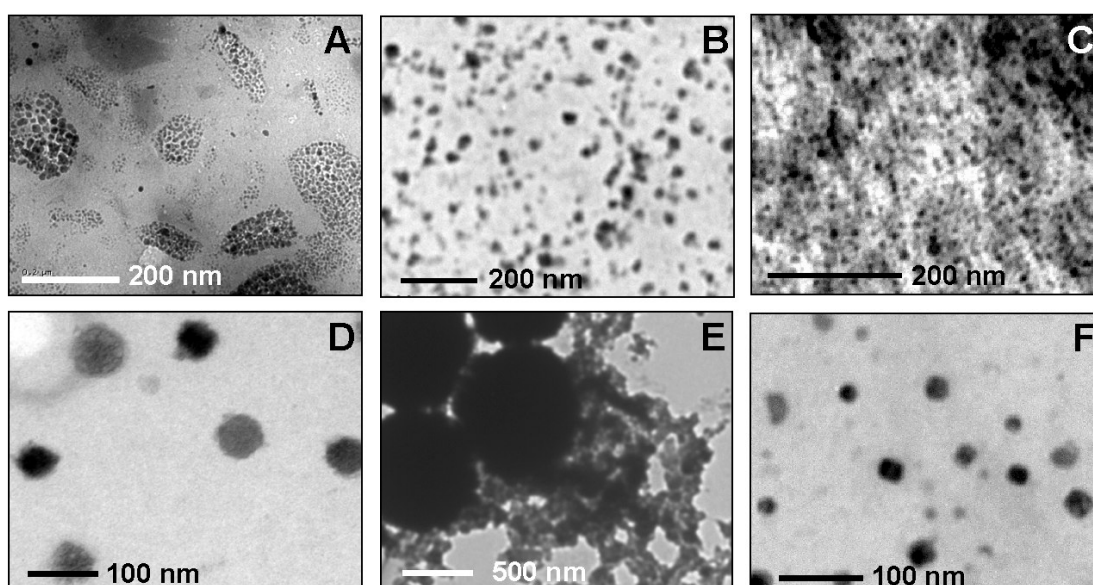


Figure 3.11 TEM micrographs of silica (A and D), titania (B and E) and zirconia (C and F) nanoparticles synthesized using the total extracellular fungal proteins (A, B and C) and the CM sephadex-purified active cationic proteins (D, E and F).

In order to validate the inducible nature of proteins in response to anionic precursor complexes, the differential expression profiles of extracellular proteins secreted by *F. oxysporum* in the absence (lane 1 and 4, Figure 3.12) and presence of ZrF_6^{2-} ions (lane 2 and 5, Figure 3.12) were analyzed using native PAGE (Figure 3.12 A) as well as SDS-PAGE (Figure 3.12 B). Native PAGE (non-denaturing gel) differential expression analysis clearly shows the induction of two extracellular proteins in the presence of ZrF_6^{2-} ions (bands highlighted by arrows in Figure 3.12 A). Similarly, SDS-PAGE (denaturing gel) differential expression analysis also shows the presence of two major proteins *ca.* 24 and 28 kDa (bands highlighted by arrows in

Figure 3.12 B). This, in turn suggests that exposure of the fungus *F. oxysporum* to ZrF_6^{2-} ions results in inducible secretion of two extracellular proteins of M_w ca. 24 and 28 kDa.

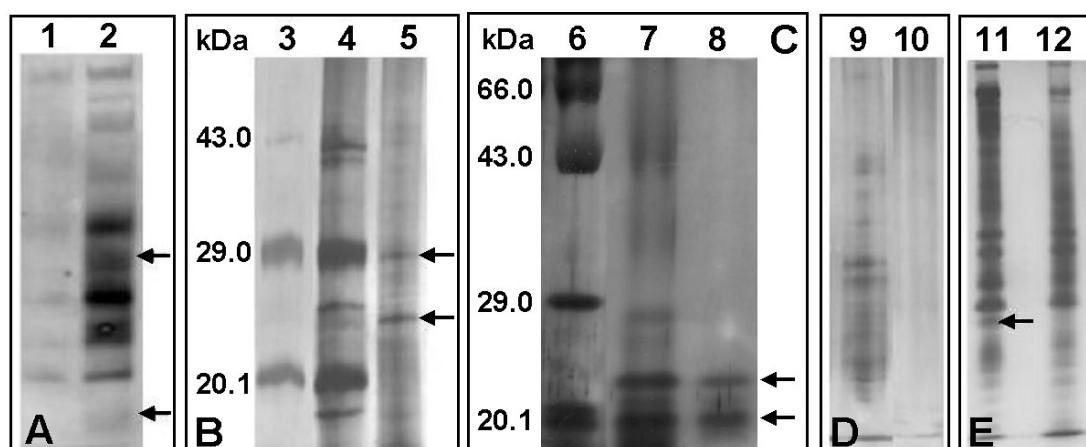


Figure 3.12 (A & B) Native (A) and SDS-PAGE (B) data showing the differential expression profile of extracellular proteins secreted by the fungus *F. oxysporum* in the absence (lane 1 and 4) and presence (lane 2 and 5) of aqueous ZrF_6^{2-} ions. (C) SDS-PAGE data showing the extracellular fungal proteins obtained by 80% ammonium sulfate precipitation of filtrate in the presence of aqueous SiF_6^{2-} ions (lane 7) and active protein fraction purified from CM sephadex column (lane 8). (D) SDS-PAGE data showing the profile of zirconia-bound *F. oxysporum* proteins before (lane 10) and after (lane 9) boiling zirconia particles in SDS solution. (E) Native PAGE data showing the extracellular protein profile of *Trichothecium* sp. obtained in the absence (lane 11) and presence (lane 12) of ZrF_6^{2-} ions. Lane 3 and 6 show the standard protein molecular weight markers with the corresponding molecular weights indicated. The arrows highlighting the bands in (A), (B) and (C) indicate the *F. oxysporum* extracellular proteins responsible for hydrolysis of metal complexes into oxide nanoparticles, while the arrow in (E) indicates the protein, whose expression is inhibited in *Trichothecium* sp. due to ZrF_6^{2-} ions.

Once the inducible nature of these proteins was established, the fungus *F. oxysporum* was exposed to 10^{-3} M aqueous solution of K_2SiF_6 and the proteins secreted by the fungus in the presence of SiF_6^{2-} ions were sequentially purified from extracellular fungal extract using 80% ammonium sulphate precipitation and CM sephadex column purification. The protein fraction obtained by ammonium sulfate precipitation (lane 7, Figure 3.12 C) and the column-purified protein fraction that tested positive for hydrolysis of SiF_6^{2-} ions (lane 8, Figure 3.12 C) were analyzed along with standard protein molecular weight markers (lane 6, Figure 3.12 C) by 10% SDS-PAGE carried out at pH 8.2. The protein fraction obtained by ammonium sulfate precipitation shows few proteins in the form of well-separated bands along with two intense bands of ca. 21 and 24 kDa (lane 7, Figure 3.12 C). The column-purified cationic protein fraction also shows only those two proteins

(lane 8, Figure 3.12 C), which appear at the same level as that of the intense bands in lane 7. The presence of these two cationic proteins in the same fraction, when eluted from CM sephadex column, suggests that the pI of these two proteins should be very close. Further efforts are required to characterize these two proteins separately and to establish the individual role of these proteins in hydrolysis of anionic precursor complexes. However with the results obtained so far, it can be suggested that the fungus inducibly secrete two low molecular weight cationic proteins in response to anionic complexes and either one or both of these cationic proteins play a crucial role in the hydrolytic conversion of anionic complexes into respective oxide nanoparticles.

The slight difference in molecular weights of the proteins involved in case of zirconia (24 and 28 kDa; lane 5, Figure 3.12 B) and silica (21 and 24 kDa; lane 8, Figure 3.12 C) suggests the involvement of similar proteins in the hydrolysis process and this difference might be mapped to various levels of post-translational modification of proteins involved in the hydrolysis of various oxide precursors. In future, it would be worthwhile to fully characterize these two proteins in terms of their amino acid sequence and nature of their interaction with silica, titania and zirconia particles. Since the proteins identified by various groups in diatoms and sponges for silica biosynthesis are also low molecular weight cationic proteins/polypeptides [6, 8], it would also be interesting to understand the role of these inducible, low molecular weight cationic proteins in the evolutionary biology of fungi, considering the fact that *F. oxysporum* is not commonly known to be exposed to these anionic complexes in its natural habitats. Furthermore, the role of these proteins in the fungal metabolism has to be determined.

The proteins bound to the surface of the biogenic zirconia nanoparticles were also analyzed on 10% SDS-PAGE (Figure 3.12 D). The protein profile of SDS-treated ZrO₂ nanoparticles show a large number of polypeptides/proteins (lane 9, Figure 3.12 D) while the profile of the untreated ZrO₂ nanoparticles did not show any protein, apart from some smearing at the top of the gel (lane 10, Figure 3.12 D). The smearing might be due to the restricted entry of ZrO₂-bound proteins in the gel because of the large size of nanoparticles. This suggests that the proteins bound to oxide nanoparticles might be different from those that are responsible for the hydrolytic conversion of anionic precursor complexes to respective oxide nanoparticles.

The anionic precursor complexes used in this study (SiF_6^{2-} , TiF_6^{2-} and ZrF_6^{2-} anions) are not toxic to the fungus *F. oxysporum*, which can be extracted from the anion complex–fungus reaction medium and re-cultivated in culture media. A number of other genera of fungi were also tested for extracellular hydrolytic activity (*Trichothecium* sp., *Phomopsis* sp., *Curvularia lunata*, *Colletotrichum gloeosporioides* and *Aspergillus niger*), but did not yield positive results. In an attempt to increase our understanding behind the process, the differential expression extracellular protein profile of *Trichothecium* sp. was studied by 10% native PAGE (Figure 3.12 E), both in the absence (lane 11, Figure 3.12 E) and presence of ZrF_6^{2-} ions (lane 12, Figure 3.12 E). The differential expression profile of the extracellular proteins secreted by *Trichothecium* sp. does not show induction of any additional extracellular protein on its exposure to ZrF_6^{2-} ions (lane 12, Figure 3.12 E). Moreover, it shows the inhibition of at least one extracellular protein that is secreted by *Trichothecium* sp. in the absence of ZrF_6^{2-} ions (band highlighted by arrow in lane 11, Figure 3.12 E). This suggests that ZrF_6^{2-} ions might be inhibitory for the metabolism of *Trichothecium* sp. and some other similar fungi, which do not show hydrolytic activity for the conversion of metal oxide precursors to metal oxides.

3.2.10 Summary

We have shown here that the fungus *Fusarium oxysporum* secretes at least two low molecular weight cationic proteins capable of hydrolyzing aqueous anionic complexes (SiF_6^{2-} , TiF_6^{2-} and ZrF_6^{2-} ions) to form respective oxide nanoparticles (silica, titania and zirconia) extracellularly at room temperature. Particularly gratifying is the fact that the fungus is capable of hydrolyzing tough metal halide precursors under acidic conditions. While the hydrolytic proteins secreted by *F. oxysporum* are yet to be sequenced and studied for their role in the fungus metabolic and evolutionary pathways, our studies indicate that they are cationic proteins of molecular weight centered around 20–30 kDa and thus, similar to silicatein [5c]. The regenerative capability of biological systems coupled with our finding that fungi such as *F. oxysporum* are capable of hydrolyzing metal complexes that they never encounter during their growth cycle shows enormous promise for development, particularly in large-scale synthesis of metal oxides.

3.3 Biosynthesis of complex oxide nanoparticles *i.e.* barium titanate using the fungus *Fusarium oxysporum*

3.3.1 Experimental details

The plant pathogenic fungus *Fusarium oxysporum* was cultured in MGYB medium as described in section 3.2.1 of this chapter. Twenty grams (wet weight) of the fungal biomass was suspended in 100 mL aqueous solution containing a mixture of 10^{-3} M $(\text{CH}_3\text{COO})_2\text{Ba}$ and 10^{-3} M K_2TiF_6 in 500 mL Erlenmeyer flasks and kept on a shaker (200 rpm) at 25–28 °C. Barium acetate was chosen as a source for Ba^{2+} ions, since the acetate ions will act as an energy source for the growth of fungus and will be utilized during the fungal metabolism. Potassium hexafluorotitanate was chosen as a source for TiF_6^{2-} ions, which has been demonstrated in section 3.2 of this chapter, to be hydrolyzed into TiO_2 nanoparticles by the fungus *F. oxysporum*. The reaction between the fungal biomass and the Ba^{2+} and TiF_6^{2-} ions was carried out for a period of 24 hours. The biotransformed product was collected at the end of the reaction by separating the fungal mycelia from the aqueous extract through filtration. The barium titanate ('BT'– BaTiO_3) particles were precipitated by centrifugation (10000 rpm) for 30 min and the BT-unbound extracellular fungal proteins were removed by repeated washings with deionized water, followed by centrifugation. The BT particles were dried under vacuum to form powder and the powder was calcined at 400 °C for 2 h in order to degrade the proteins occluded within the particles ensembles during their synthesis. Further characterization of the BT particles before and after calcination was carried out by TEM, high resolution TEM (HR–TEM), SAED, XRD, high–temperature XRD (HT–XRD), TGA, XPS and FTIR spectroscopy. HT–XRD measurement of BT powder was performed at 150 °C. Differential scanning calorimetry (DSC) measurements of powders of as-synthesized and calcined BT nanoparticles were carried out on DSC–Q10 V9.0–275 instrument under nitrogen environment from 25 °C–250 °C.

Biogenic BT particles, calcined at 400 °C for 2 h were embedded in polymethylmethacrylate (PMMA) for dielectric measurements. For embedding BT particles in PMMA matrix, various percentages (w/w) of BT nanoparticles (0%, 2%, 10% and 33%) were added to known amount of PMMA, solubilized in chlorobenzene. BT–PMMA–chlorobenzene mixtures were subjected to

ultrasonication for 30 min and drop-casted on glass substrates in the form of films. The solvent (chlorobenzene) was evaporated under vacuum and the dried films were peeled off the glass substrate, and were later cut into dimension of 1 cm x 1 cm. The frequency and temperature dependent dielectric response of these films were measured using a computer-controlled Solartron 1260 impedance analyser. The BT–PMMA nanocomposite films were characterized by FTIR, optical microscopy and tapping mode atomic force microscopy (AFM). For optical microscopy, the PMMA film containing 10% BT was microtomed into 5 μm thick sections using Shandon cryotome and sections were observed under Olympus optical microscope fitted with Nikon CCD camera. Frequency–dependent dielectric measurements on BT–PMMA nanocomposite films were performed at room temperature for a frequency sweep from 1 MHz–1 Hz. Temperature–dependent dielectric measurements on BT–PMMA films were performed between $-35\text{ }^{\circ}\text{C}$ to $100\text{ }^{\circ}\text{C}$ at fixed frequencies of 10 kHz and 1 kHz.

Tapping mode AFM and surface potential microscopy (SPM) imaging of BT particles as well as BT–PMMA sections was performed using a NanoScope IV Multimode scanning probe microscope by VEECO Inc. For AFM imaging of BT–PMMA sections, sections were stuck to AFM metallic discs using double sided conducting tape and height (topography) as well as phase images were recorded. For SPM imaging of BT particles, calcined BT nanoparticles dispersed in water were drop coated directly onto AFM metallic discs mounted on a 6399E–piezoscanner (10 μm) and scanned using 125 μm long metal-coated etched silicon probes. Height, phase and potential (voltage) images were collected in the electric force microscopy (EFM)–tapping mode at a scanning frequency of 1 Hz.

3.3.2 TEM and HR–TEM measurements

A representative TEM image of the BT nanoparticles obtained from the fungus *F. oxysporum* is shown in Figure 3.13 A. The particles are of irregular quasi-spherical morphology with an average size $4 \pm 1\text{ nm}$. The SAED analysis of the particle assemblies (inset, Figure 3.13 A) clearly indicates that they are crystalline and the SAED pattern could be indexed based on the tetragonal phase of barium titanate [30]. Figure 3.13 B shows a representative TEM image of the BT nanoparticles after calcination at $400\text{ }^{\circ}\text{C}$ for 2 h. After calcination, the BT nanoparticles become fairly

regular in shape, with a slight increase in size ranging from 4–8 nm (Figure 3.13 B). The SAED pattern of these particles indicated that they were also of the tetragonal phase (inset, Figure 3.13.B) [30].

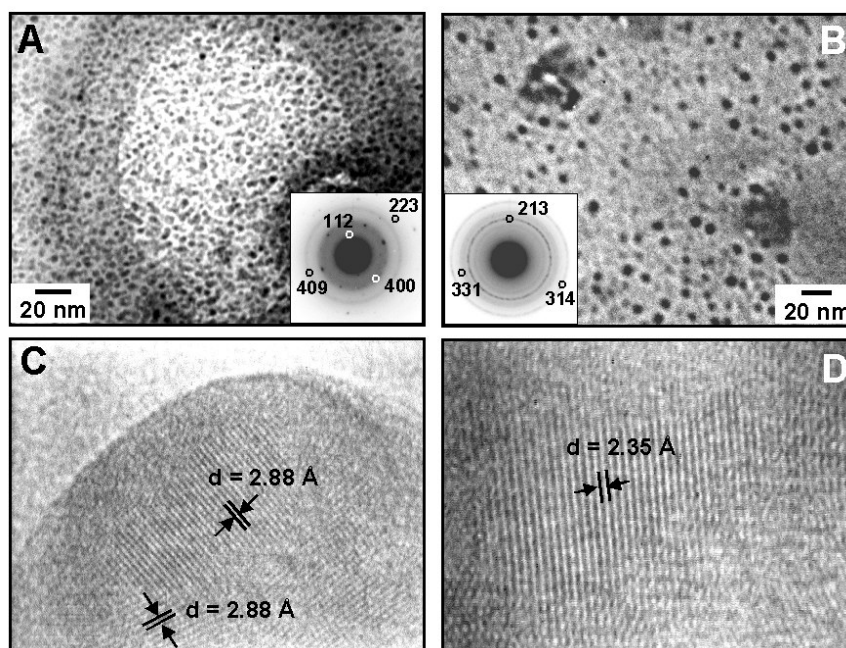


Figure 3.13 (A and B) TEM micrographs of BT nanoparticles synthesized using *F. oxysporum* before (A) and after calcination at 400 °C for 2 h (B). The insets in A and B are SAED patterns recorded from representative BT particles. (C and D) HR-TEM images of BT nanoparticles after calcination.

Figure 3.13 C and D show HR-TEM images of calcined BT nanoparticles; the lattice planes exhibit d -spacings of ~ 2.88 Å (Figure 3.13 C, (110) lattice planes) and ~ 2.35 Å (Figure 3.13 D, (111) lattice planes) of tetragonal BT. The previously reported lattice spacings for (110) and (111) lattice planes of bulk tetragonal BT correspond to 2.83 Å and 2.31 Å respectively. The slight increase in d -spacings in the biologically synthesized BT nanoparticles may be due to the lattice expansion of BT lattices [31]. We note that the particle shown in Figure 3.13 C consists of a narrow twin boundary region. The fact that the capacitance of such a structure can be large has been put to use in boundary-layer capacitors made of polycrystalline BT. Hence, biogenic BT might be useful for high-capacitance value applications where circuit element size is an important consideration [32].

3.3.3 XRD and HT-XRD measurements

To further verify the deviation in lattice parameters for BT nanoparticles, XRD analysis of as-synthesized (curve 1, Figure 3.14 A) as well as calcined BT

nanoparticles (curve 2, Figure 3.14 A) was performed. The diffraction pattern obtained from the calcined BT nanoparticles (curve 2, Figure 3.14 A) was subjected to Pauley's refinement (MS Modeling 3.0 software) assuming a c/a ratio of 1 (curve 3, Figure 3.14 A). The lattice constants obtained were $a = b = 4.0810(7)$ Å and $c = 4.0992(6)$ Å and could be assigned to the $P4mm$ crystal structure of tetragonal symmetry with an R factor of 7.09%. The lattice spacings obtained from the simulated diffraction pattern for the (110) and (111) lattice planes are 2.88 Å and 2.35 Å respectively (curve 3, Figure 3.13 A) that match exactly with the lattice spacings observed in the HR-TEM images (Figure 3.13 C and D). In general, line broadening in X-ray powder diffraction measurements occurs in very small crystallites, which is generally a result of combined effects of the crystallite size, nonuniform strain and instrumental broadening. Such a phenomenon acts as an obstacle for the structural characterization, particularly for BaTiO_3 with small tetragonality ($c/a = 1.004$).

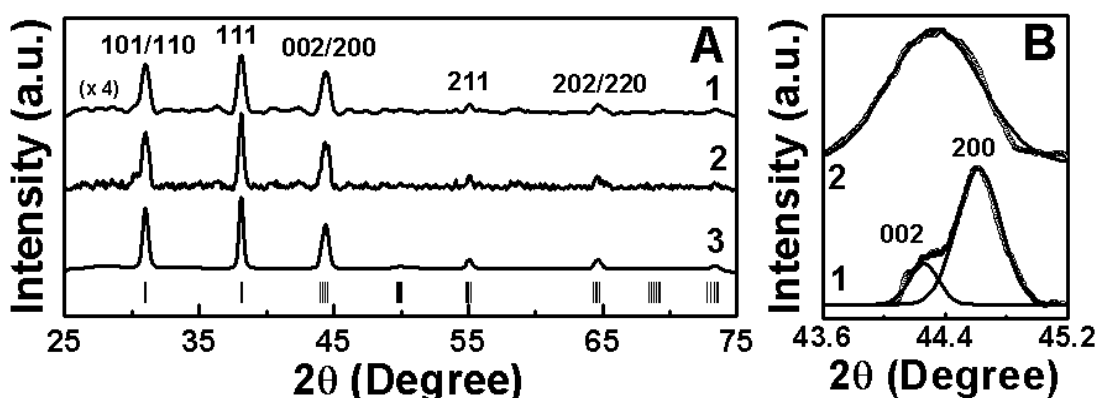


Figure 3.14 (A) XRD patterns of as-synthesized BT nanoparticles (curve 1), after calcination at 400 °C for 2 h (curve 2) and simulated diffraction pattern from calcined sample (curve 3). The intensity of curve 1 in (A) has been multiplied by a factor of 4 for the reasons of clarity. (B) XRD patterns of calcined BT nanoparticles in the region of 002/200 diffraction planes at room temperature (curve 1) and at 150 °C (curve 2). The raw data in (B) have been shown as dotted lines while the Lorentzian fit of the curves have been shown as solid lines.

Hence, in order to provide definite evidence for tetragonal/cubic transformation of BT particles, room-temperature as well as high-temperature XRD measurements in the region of the (002)/(200) Bragg reflections was performed at a slower scan rate of 0.25 deg/min (Figure 3.14 B). The XRD peak profiles in the two cases were fitted with Lorentzian curves in order to separate the (002) and (200) components. The XRD pattern obtained at room temperature (curve 1, Figure 3.14 B) showed the presence of an asymmetric peak [(002)/(200)] at around $2\theta = 45^\circ$ which confirms tetragonal distortion in BT particles at room temperature. However, at

150 °C (above the Curie point of bulk BT), the XRD pattern obtained (curve 2, Figure 3.14 B) could only be fitted to a single Lorentzian component, thus indicating the presence of cubic phase above the Curie temperature (T_C). Hence temperature-dependent XRD measurements provide clear evidence for tetragonal/cubic transformation in sub-10 nm BT particles.

3.3.4 TGA measurements

TGA measurements of as-synthesized BT particles (curve 1, Figure 3.15) as well as after calcination at 400 °C for 2 h (curve 2, Figure 3.15) were performed to find out the weight contribution of biomolecules/proteins in biogenic BT nanoparticles. It is evident from curve 1 that there is almost 70% weight loss during the heating up to 700 °C that can be accounted for the loss of moisture and due to the loss of biomolecules/proteins intercalated in the BT nanoparticles.

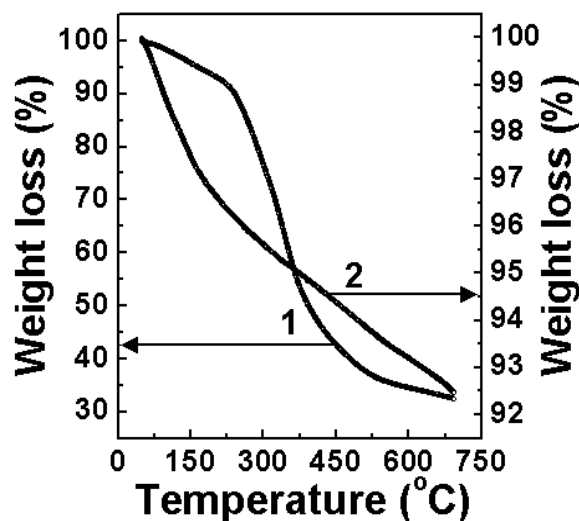


Figure 3.15 TGA spectra recorded from BT nanoparticles synthesized using *F. oxysporum* before (curve 1) and after calcination at 400 °C for 2 h (curve 2).

TGA of BT sample precalcined at 400 °C for 2 h (curve 2, Figure 3.15) also shows up to 8% weight loss on heating up to 700 °C. It is evident from curve 2 that ~ 4% of initial weight loss on precalcined sample occurs within 250 °C that can be attributed to moisture while the remaining ~ 4% weight loss between 250 °C–700 °C can be accounted due to loss of undecomposed biomolecules after the first calcination cycle at 400 °C. The presence of small amount of undecomposed biomolecules in precalcined sample (400 °C for 2 h) might play an important role in preventing aggregation of BT nanoparticles even after calcination, as is evident in the form of well separated BT nanoparticles in TEM image of calcined BT (Figure 3.13 B).

3.3.5 XPS measurements

A chemical analysis of as-synthesized and calcined BT nanoparticles was performed by XPS (Figure 3.16). The Ba 3d, Ti 2p, O 1s, C 1s and N 1s core level spectra were recorded, background corrected using the Shirley algorithm [24] and their core level binding energies (BEs) were aligned with the adventitious carbon binding energy of 285 eV.

The Ba 3d (Figure 3.16 A and B) core level spectra from as-synthesized (Figure 3.16 A) as well as calcined BT (Figure 3.16 B) could be fitted into single spin orbit pairs (spin-orbit splitting 15.4 eV) [25] with Ba 3d_{5/2} BEs of 779.7 eV (Figure 3.16 A) and 779.6 eV (Figure 3.16 B) respectively. These values match closely with that of previously reported nanocrystalline BT system [31]. Notably, the observed Ba 3d_{5/2} BEs in biogenic BT nanoparticles are smaller than that in BaO bulk crystals (780.05 eV) [25]. This can be explained on the basis of the fact that Ba in BaO bulk crystals has a nearly ideal ionic valence of Ba⁺² ion [33], however one would expect a minor change in the ideal ionicity of Ba while shifting from BaO bulk crystals to BaTiO₃ nanocrystals. This in turn, would lead to reduction in Ba 3d_{5/2} BE in BaTiO₃ nanoparticles from that in BaO bulk crystals. In addition, appearance of asymmetry towards the lower BE side of Ba 3d core level spectra (Figure 3.16 A and B) is not anomalous and can be explained on the basis of differential sample charging as previously noticed in barium and strontium titanate systems [34].

The Ti 2p (Figure 3.16 C and D) core level spectra from as-synthesized (Figure 3.16 C) as well as calcined BT (Figure 3.16 D) could be fitted into single spin orbit pairs (spin-orbit splitting 5.7 eV) [25] with Ti 2p_{3/2} BEs of 458.4 (Figure 3.16 C) and 458.5 eV (Figure 3.16 D) respectively, which are slightly lower than previously reported value of 458.9 eV for bulk BT crystals [31]. It has been observed previously that the Ti 2p_{3/2} BE depicts a decreasing trend with decreasing BT nanocrystallite size below the critical size, though, it is same as in bulk BT crystals above the critical size (458.9 eV) [31]. However, the slightly lower Ti 2p_{3/2} BEs of 458.4 eV in case of 4 ± 1 nm as-synthesized BT particles (Figure 3.16 C) and 458.5 eV in case of 4–8 nm calcined BT particles (Figure 3.16 D) correlate well with Ti 2p_{3/2} BE of 458.6 eV observed previously in 19 ± 3 nm BT [31]. It is possible that the reduced Ti 2p BE observed in our studies might be due to size dependent behaviour of BT nanocrystallites and the Ti 2p_{3/2} BEs of 458.4 eV and 458.5 eV most likely

correspond to 4 nm and 8 nm BT particles respectively. However, considering the XPS resolution limit of ~ 1 eV in our study, high resolution XPS studies might provide a better insight in this matter. It is further interesting to note that this reduction in BE below the critical size is in spite of no change in Ti–O bond distance from that of bulk system and hence, this decrease in BE can be accounted due to the change in Ti–O bond character from covalent to ionic below the critical size [31, 35–36]. The O 1s (Figure 3.16 E and F) core level spectra were also recorded from as-synthesized (Figure 3.16 E) as well as calcined BT (Figure 3.16 F), both of which could be fitted into single BE component of 531.9 eV, which matches exactly with O 1s BE in barium titanate environment [37].

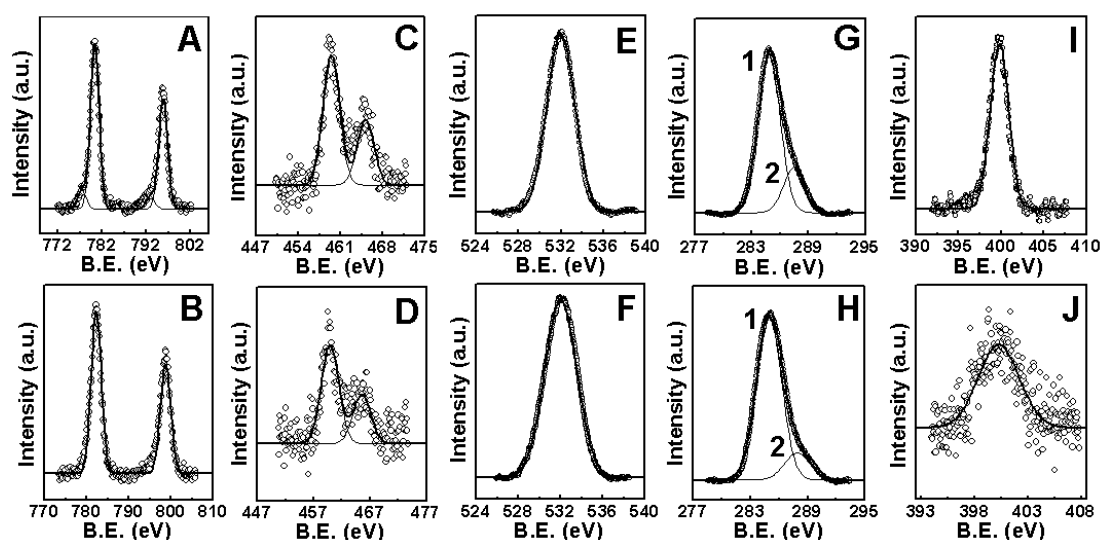


Figure 3.16 XPS data showing the Ba 3d (A and B), Ti 2p (C and D), O 1s (E and F), C 1s (G and H) and N 1s (I and J) core level spectra recorded from as-synthesized (upper row) and calcined BT nanoparticles (lower row). The raw data are shown as symbols, while the chemically resolved components are shown as solid lines in the figure and are discussed in the text.

In order to trace the proteins bound to BT nanoparticles, C 1s (Figure 3.16 G and H) and N 1s (Figure 3.16 I and J) core level spectra were recorded from BT nanoparticles. The C 1s core level spectra from as-synthesized (Figure 3.16 G) as well as calcined BT (Figure 3.16 H) could be resolved into two BE components of 285 eV (curve 1, Figure 3.16 G and H) and 287.7 eV (curve 2, Figure 3.16 G and H). The lower BE C 1s component of 285 eV can be assigned to core levels originating from the hydrocarbon chains while the broad higher BE components of 287.7 eV can be attributed collectively to $-\text{COOH}$ groups and α -carbon bound to $-\text{COOH}$ and $-\text{NH}_2$ groups of the proteins that are present in the protein–BT nanobiocomposite structures

[25]. In addition, N 1s core level spectra in as-synthesized (Figure 3.16 I) and calcined BT (Figure 3.16. J) could be fitted into single BE component of 400.3 eV, which matches closely with values reported for –NH amide linkage [28], indicating the complexation of proteins with the BT nanocrystallites. Notably, the presence of N 1s signal (Figure 3.16 J) and higher BE C 1s component (curve 2, Figure 3.16 H) in calcined BT sample, though in lower intensity than in as-synthesized BT (Figure 3.16 I and curve 2, Figure 3.16 G), indicate the presence of capping proteins even in calcined BT nanocrystallites. This precludes the possibility of nanoparticles aggregation after calcinations, as is evident from the TEM image of calcined sample (Figure 3.13 B) and from TGA of calcined BT particles which indicates the presence of ~ 4% proteins in BT particles even after calcination at 400 °C for 2 h (curve 2, Figure 3.15). Thus, XPS data further support our belief that surface-bound proteins play an important role as capping agents to restrict the growth of oxide particles in nanometer regime.

It is noteworthy that signatures of BaCO₃ were not observed in the XPS spectra, which is particularly significant considering the fact that BaCO₃ is the commonest impurity in BT synthesis system. In C 1s, O 1s and Ba 3d_{5/2} XPS spectra, BaCO₃ signatures are generally observed respectively towards +3.9 eV, +1.6 eV and +1.4 eV higher BE side as compared to signatures corresponding to BT [38].

3.3.6 Synthesis of BT–PMMA nanocomposite and its characterization

Various percentages *viz.* 0%, 2%, 10% and 33% (w/w) of the biogenic BT nanoparticles after calcination (400 °C for 2 h), were embedded in polymethylmethacrylate (PMMA) polymer in order to create BT–PMMA nanocomposites. The biogenic BT nanoparticles synthesized using the fungus *F. oxysporum* as well as the BT–PMMA nanocomposites were analyzed by FTIR spectroscopy. FTIR analysis of the as-synthesized BT nanoparticles showed the presence of resonance at *ca.* 600 cm⁻¹ and 1080 cm⁻¹ (curve 1, Figure 3.17 A) which are due to BaTiO₃ framework vibrations and can be assigned to the BT surface modes [39–40]. Two absorption bands centered at *ca.* 1658 cm⁻¹ and 1535 cm⁻¹ (amide I and II signatures respectively; curve 1, Figure 3.17 A) attest to the presence of proteins in the quasi-spherical particles, as is also evident from TGA (curve 1, Figure 3.15) and XPS analysis (Figure 3.16).

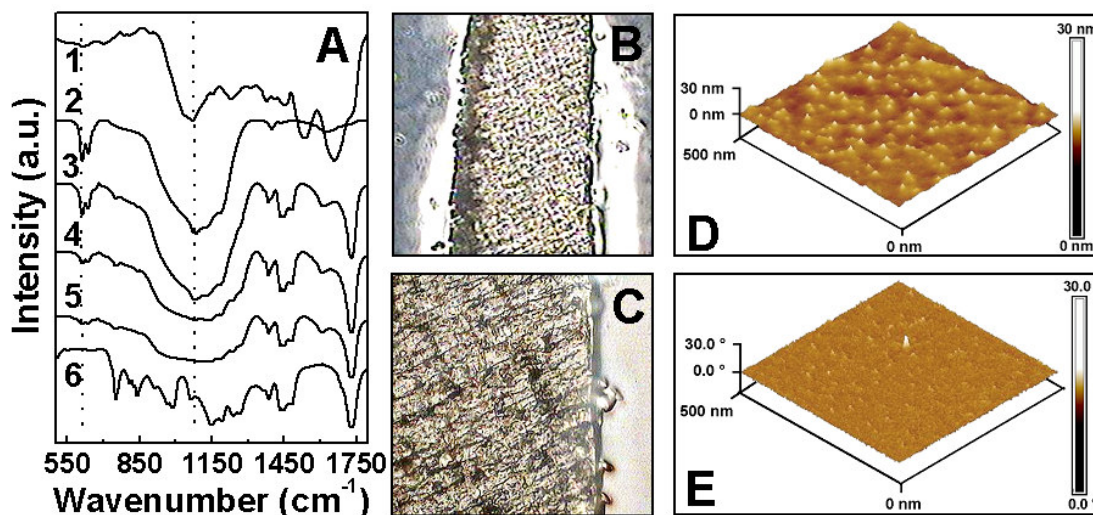


Figure 3.17 (A) FTIR spectra recorded from BT nanoparticles synthesized using *F. oxysporum* before (curve 1) and after calcination at 400 °C for 2 h (curve 2). Curves 3–5 correspond to various percentage of calcined BT embedded in PMMA matrix viz. 33% (curve 3), 10% (curve 4) and 2% (curve 5). Curve 6 correspond to FTIR spectrum of pure PMMA without any BT. (B and C) Optical microscopy image of 5 μm thick sections of BT–PMMA films in lower (B) and higher magnifications (C) respectively. (D and E) AFM images of 5 μm thick sections of BT–PMMA in topography (D) and phase mode (E).

Calcination of BT particles at 400 °C for 2 h results in denaturation of proteins as is evident from almost complete loss of 1658 cm⁻¹ and 1535 cm⁻¹ amide signatures in calcined BT sample (curve 2, Figure 3.17 A). Moreover an increase in resonance at *ca.* 600 and 1080 cm⁻¹ is observed in calcined BT particles, which again suggests an increase of BT particle density in calcined sample due to the removal of proteins. The FTIR analysis of the BT–PMMA nanocomposites formed by embedding various percentages of calcined BT nanoparticles in PMMA (Curves 3–5, Figure 3.17 A) was also performed. Curve 6 in Figure 3.17 A corresponds to the FTIR spectrum obtained from PMMA without any BT doping, while those in curves 3–5 correspond to the FTIR spectra obtained from BT–PMMA nanocomposite after embedment of 33% (curve 3), 10% (curve 4) and 2% (curve 5) of BT in PMMA. It is evident from curves 2–6 that with the reduction in amount of BT blended in the BT–PMMA nanocomposite, the intensity and sharpness of FTIR signatures, arising due to BT framework vibrations at *ca.* 600 cm⁻¹ and 1080 cm⁻¹ successively go down and as expected these signatures are completely absent in FTIR spectrum of pure PMMA without any BT (curve 6).

Proper dispersion of nanomaterials in the polymer matrix is extremely important as far as their application and device fabrication is concerned, however, it is

quite challenging to achieve uniform nanoparticles dispersion by conventional techniques. In order to comprehend the dispersion of BT particles in PMMA polymer, 5 μm thick sections were microtomed from the PMMA film containing 10% BT. The optical micrographs of cross-section of BT–PMMA nanocomposite film show uniform dispersion of BT particles in PMMA matrix throughout the composite film (Figure 3.17 B and C). Tapping mode AFM images of sections further facilitate the understanding of dispersion of BT particles in PMMA (Figure 3.17 D and E), in the form of fairly dispersed BT particles embedded in PMMA matrix, as clearly observed under height (Figure 3.17 D) and phase image (Figure 3.17 E). We have been able to achieve a fairly uniform dispersion of BT nanoparticles in PMMA matrix due to the fact that biomolecules get entrapped on to the surface of nanoparticles during biological synthesis of BT and these biomolecules being amphoteric in nature, have a greater probability of uniform dispersion in any media, and hence minimizing the aggregation of nanoparticles in polymer matrices. Biological synthesis of nanomaterials is thus, an added advantage to maintain the stability of nanoparticles in various matrices and can further be explored for various applications including device fabrication [41]. It is noteworthy that calcination at 400 $^{\circ}\text{C}$ for 2 h, though results in degradation of biomolecules, it does not remove the biomolecules completely (TGA: Figure 3.15) and hence dispersity of BT particles is maintained even after calcination, as observed under optical microscopy and AFM imaging (Figure 3.17 B–E).

3.3.7 DSC and dielectric measurements

DSC measurements in the temperature range 25–250 $^{\circ}\text{C}$ were performed on as-synthesized and calcined BT powders (curve 1 and 2 respectively, Figure 3.18 A). The as-synthesized BT nanoparticles show a broad exothermic–endothermic transition at 114 $^{\circ}\text{C}$ (curve 1, Figure 3.18 A), while the calcined sample shows a similar broad transition at 98 $^{\circ}\text{C}$, which is a signature of tetragonal to cubic transition. To our knowledge, such a transition has been observed for the first time for sub–10 nm BT particles. The marginally lower phase transition temperature in comparison with bulk BT (~ 128 $^{\circ}\text{C}$) is due to reduction in BT particle size; this is known to reduce the transition temperature, which is associated with ferroelectric to paraelectric phase transition [39].

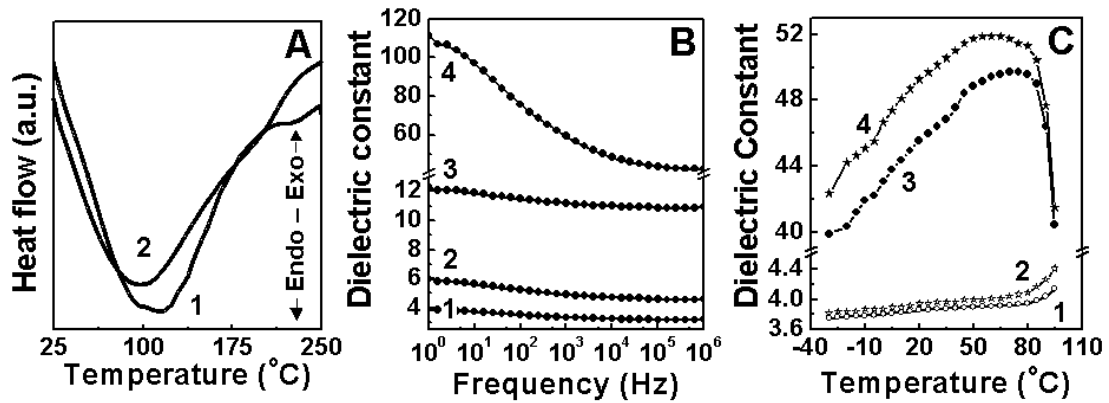


Figure 3.18 (A) DSC spectra recorded from BT nanoparticles synthesized using *F. oxysporum* before (curve 1) and after calcination at 400 °C for 2 h (curve 2). (B) Frequency–dependent dielectric spectra recorded from PMMA (curve 1) and from PMMA embedded with 2% (curve 2), 10% (curve 3) and 33% (curve 4) of calcined BT nanoparticles. (C) Temperature–dependent dielectric spectra recorded from PMMA (curves 1 and 2) and 33% BT–PMMA nanocomposite (curves 3 and 4) at 10 kHz (curves 1 and 3) and 1 kHz (curves 2 and 4) respectively.

The observation of ferroelectric/paraelectric phase transition phenomenon in DSC measurements motivated us to study the frequency and temperature dependent dielectric properties of BT nanoparticles. For this purpose, various percentages (w/w) of BT nanoparticles (calcined at 400 °C for 2 h) were embedded in PMMA polymer and casted in the form of free-standing films. Frequency–dependent dielectric measurements of BT–PMMA composite films (Figure 3.18 B) show a gradual increase in permittivity of BT–PMMA composites corresponding to an increase in BT content in BT–PMMA films from 0% to 33% (curves 1–4, Figure 3.18 B). The dielectric value obtained from pure PMMA, without any BT doping (curve 1, Figure 3.18 B) matches closely with literature reports (~2.6 at 1 MHz frequency) [42]. The dielectric values of BT in BT–PMMA composite was calculated using Inverse Maxwell Garnett (MG) equation (Equation 1) [43], which is the most commonly used mixing formula explaining dielectric permittivities of composites, wherein ϵ_{eff} is the permittivity of BT–PMMA composite, ϵ_i is the permittivity of BT particles, ϵ_e is the permittivity of PMMA matrix and f is the fraction of BT in PMMA particles.

$$\epsilon_{eff} = \epsilon_i + 3(1-f)\epsilon_i \frac{\epsilon_e - \epsilon_i}{\epsilon_e + 2\epsilon_i - (1-f)(\epsilon_e - \epsilon_i)} \dots\dots\dots \text{(Equation 1)}$$

The dielectric values calculated for BT using the MG effective medium formula at 1 MHz frequency were found to be 350–400. Though the dielectric values obtained on BT nanoparticles are much lower in comparison with that of

bulk BT [44], this is consistent with the fact that one will expect a reduction of dielectric values on size reduction [45]. These results correlate well with the HR-TEM (Figure 3.13 C and D) and HT-XRD studies (Figure 3.14 B) that also exhibit the tetragonality in BT nanoparticles at room temperature, which is responsible for this ferroelectric behaviour.

Temperature-dependent dielectric measurements were also performed on pure PMMA films (curves 1–2, Figure 3.18 C) as well as on PMMA films containing 33% BT (curves 3–4, Figure 3.18 C) between $-35\text{ }^{\circ}\text{C}$ and $100\text{ }^{\circ}\text{C}$ at fixed frequencies of 10 kHz (curves 1 and 3, Figure 3.18 C) and 1 kHz (curves 2 and 4, Figure 3.18 C). Higher dielectric values are observed at 1 kHz in comparison with those at 10 kHz (compare curves 2 and 4 with curves 1 and 3 respectively). In BT samples (curves 3 and 4, Figure 3.18 C), we also observe a broad diversion in the dielectric constant with a maximum around $75\text{ }^{\circ}\text{C}$ at 10 kHz (curve 3, Figure 3.18 C) and a maximum around $65\text{ }^{\circ}\text{C}$ at 1 kHz (curve 4, Figure 3.18 C). It appears as if there is a reduction in Curie transition temperature (T_C) with a reduction in the applied frequency. Moreover, a disparity in the T_C values obtained from temperature-dependent dielectric measurements at various frequencies ($75\text{ }^{\circ}\text{C}$ and $65\text{ }^{\circ}\text{C}$ at 10 kHz and 1 kHz respectively) and those from DSC measurements ($98\text{ }^{\circ}\text{C}$) (curve 2, Figure 3.18 A) is also observed. Though broadening of peaks in DSC and dielectric measurements can be explained on the basis of size reduction of BT nanocrystallite [46], difference in T_C values under varying experimental conditions cannot be explained solely on the basis of size effect. We believe that biologically synthesized BT particles are behaving as “ferroelectric relaxor” materials, since a broadening in the maxima of the temperature-dependent dielectric response as well as DSC maximum at ferroelectric transition is typical of “relaxor” materials, which are known to exhibit a diffused phase transition (DPT) [47]. In addition, DPT is also characterized by frequency-dependent dispersion of dielectric constant implying a frequency dependence of apparent T_C and hence, a difference in the value of T_C obtained from different physical measurements [47]. Though pure BT, without any cationic doping, is not an excellent ferroelectric relaxor, a few reports exist wherein piezoelectric response of single crystal tetragonal BT has been demonstrated either due to the formation of engineered domain walls [48] or due to Ti–O bond oscillations [49]. Since we observe

the occurrence of all the characteristic relaxor phenomena from DSC and dielectric measurements, it supports the ferroelectric relaxor behaviour of BT nanoparticles.

3.3.8 Kelvin probe (surface potential) microscopy

To further demonstrate the ability to polarize the BT nanoparticles in the ferroelectric phase (ability to electrically write and read), Kelvin probe/surface potential microscopy (SPM) was used (Figure 3.19–3.21) [50]. Initially, the sample was scanned under AFM using a conductive AFM tip without application of any external DC bias voltage and the corresponding height (Figure 3.19 A) and phase (Figure 3.19 B) images were obtained. Further, a DC bias voltage of +1 V (V_{write}) was applied between the conductive AFM tip and the BT particles that results in orientation of local electric dipoles of BT particles, following which, spontaneous polarization of BT particles was recorded (V_{read}) in the form of potential/voltage signals using SPM. This electrical information is evident in the form of brighter-contrasting elevations in Figure 3.19 C. Similarly, when a DC bias voltage $V_{\text{write}} = -1$ V was applied between the conductive tip and the particles, it results in orientation of local electric dipoles of BT particles in direction opposite to that of +1 V bias, following which spontaneous polarization (V_{read}) of BT particles is evident in the form of darker-contrasting depressions observed in Figure 3.19 D. This change in image contrast due to reversal of electrical polarization of BT particles, on reversal of external DC bias voltage suggests the ferroelectric nature of biogenic BT nanoparticles.

In order to understand the effect of externally applied DC bias voltage on the electrical signals arising from BT particles, the same region was also scanned after sequential application of +4 V, +7 V and +10 V positive DC bias voltage (Figure 3.19 E, G and I respectively) as well as after sequential application of -4 V, -7 V and -10 V negative DC bias voltage (Figure 3.19 F, H and J respectively) to the conductive tip. It is clearly evident from Figure 3.19 that while increasing the applied DC bias voltage (either positive or negative bias), there is an increase in the voltage signal arising from BT particles. These electrical signals are evident in the form of increasing brighter-contrasting elevations when the applied bias voltage was increasingly positive (Figure 3.19 C, E, G and I) and it was in the form of increasing darker-contrasting depressions when the applied bias voltage was increasingly

negative (Figure 3.19 D, F, H and J). It is also evident from the SPM imaging of BT particles (Figure 3.19) that when a DC bias voltage of < 4 V is applied, electrical dipoles of only few BT particle could be oriented by application of external DC bias

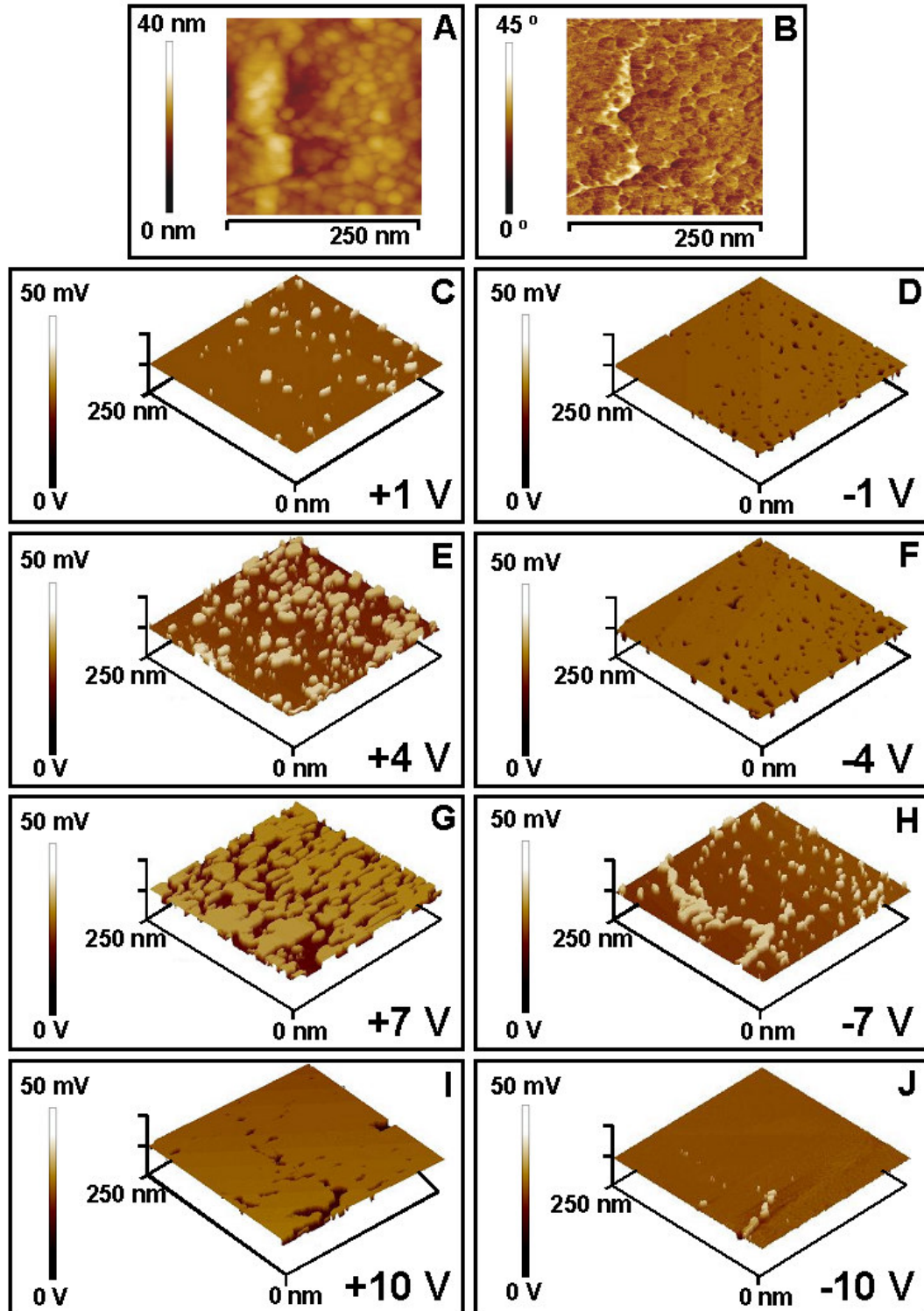


Figure 3.19 SPM images of BT particles obtained in Height (A) and Phase mode (B) without application of any external bias voltage and in Potential mode (C–J) after application of +1 V (C), -1 V (D), +4 V (E), -4 V (F), +7 V (G), -7 V (H), +10 V (I) and -10 V (J) external DC bias voltage to the conductive AFM tip.

voltage (Figure 3.19 C and D), however administration of > 4 V DC bias voltage results in increasing contrast in voltage images and hence resulting in fusion of electrical signals arising from individual BT particles (Figure 3.19 G–J). Therefore, in the case of biogenic 4–8 nm BT particles, 4 V DC bias voltage appears to be most appropriate for electrically writing and thereafter reading the electrical information from these particles. Notably, no change in the respective height and phase images is observed (Figure 3.19A and B), when potential mode images are collected at various DC bias voltages.

To validate the results obtained in the previous experiment, lower (Figure 3.20 A–C) as well as higher magnification (Figure 3.20 D–F) SPM imaging of BT particles was performed after application of ± 4 V DC bias voltage. Figure 3.20 A and D show the respective lower and higher magnification height images. Well-separated BT particles of opposing contrast can be clearly seen in lower magnification voltage images after application of +4 V (Figure 3.20 B) and -4 V (Figure 3.20 C) DC bias. Similarly, BT particles in the form of elevations and depressions can be clearly seen in higher magnification 3–D voltage images after application of +4 V (Figure 3.20 E) and -4 V (Figure 3.20 F) DC bias voltage.

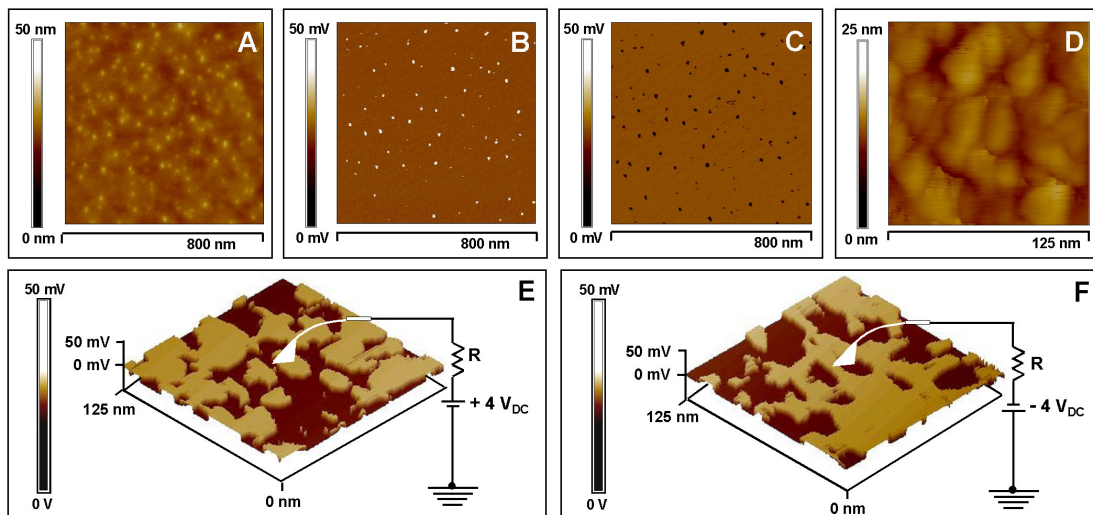


Figure 3.20 Lower (A–C) and higher magnification (D–F) SPM images from BT-particles obtained in height mode without application of any external bias (A and D), and in voltage mode after application of +4 V (B and E) and -4 V (C and F) external DC bias voltage to the conductive AFM tip.

In another experiment, to demonstrate the selective polarizability of BT particles in various regions of a single substrate, DC bias voltages (V_{write}) of +4 V, 0 V and -4 V were sequentially applied between the conductive AFM tip and

BT particles in a single scan. This results in polarization of electric dipoles in various directions in different regions of the substrate in response to diverse applied voltages (Figure 3.21). While reading the electric information (V_{read}) using SPM, it is evident that application of +4 V bias results in brighter contrast signals from BT particles, 0 V bias does not show any potential signals and -4 V bias results in darker contrast signals from BT particles (Figure 3.21 B), which suggest that the BT particles can be selectively written and read on a single substrate. Height image of BT particles was also recorded for the same region as is evident from Figure 3.21 A. Thus, SPM imaging clearly demonstrates that the room-temperature synthesized biogenic BT nanoparticles possess ferroelectric property in response to the applied external electric field and the various particles can be selectively written and read using SPM.

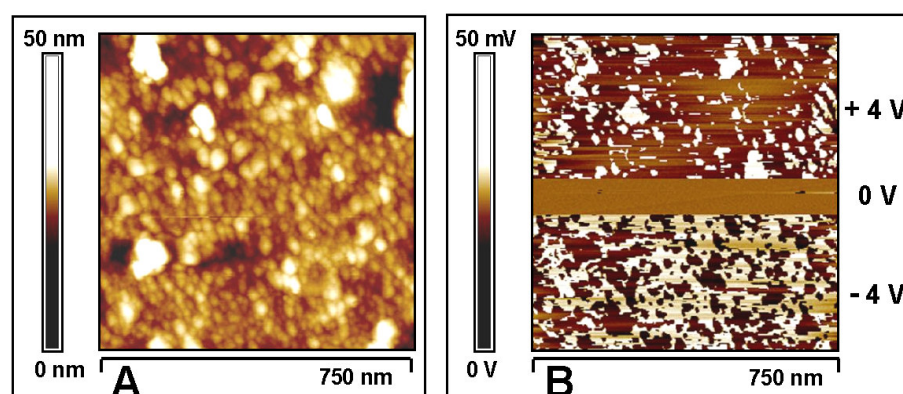


Figure 3.21 SPM images of BT particles obtained in height mode without application of any external bias voltage (A) and in voltage mode after sequential application of +4 V, 0 V and -4 V external DC bias voltages to the conductive AFM tip (B).

3.3.9 Discussion

The presence of room temperature tetragonal phase in sub-10 nm BT particles, responsible for their ferroelectric behaviour is quite interesting and at least to our knowledge, has not been reported previously. However, there are considerable discrepancies in the reported boundary size between the cubic and tetragonal phase, which vary from 190 nm [46] to about 30 nm [51]. According to a surface effect model proposed by Yen and co-workers [51] in terms of crystallite size effect, excess surface energy associated with ultrafine particles has been found to be responsible for the stabilization of the high-temperature cubic phase at room temperature for particles about or below 30 nm in size. Conversely, in our study, we do not observe stabilization of high-temperature cubic phase even in sub-10 nm particles and these particles exhibit tetragonality at room temperature. We believe that the charged

biomolecules associated with sub–10 nm BT particles might be playing an important role in avoiding the stabilization of cubic phase by balancing for excess surface energy in ultrafine particles and hence resulting in room-temperature tetragonal phase. This appears to be appealing considering the fact that various groups, including ours (Sections 3.2.8 and 3.2.9 of this chapter) have found cationic peptides/proteins to be associated with oxide nanoparticles synthesized using biological routes [12–13]. The presence of room temperature ferroelectric phase in the BT particles below 10 nm has significant importance as it opens up new opportunities such as ultra-high density non-volatile ferroelectric memories, ultra small capacitors etc. While reduction in the bit-size in the traditional ferromagnetic memories by reducing the particle size below 10 nm shows unstable behavior due to the superparamagnetism, we believe that the demonstration of the ferroelectricity in such a small size may revolutionize the electronics industries.

3.3.10 Summary

We have shown here a fungus-mediated biological route towards the synthesis of tetragonal barium titanate nanoparticles of sub–10 nm dimensions under ambient conditions. The extracellular proteins synthesized by the fungus are believed to provide a hydrolyzing as well as confining template for the synthesis of nanoscale BT particles, as reported previously for binary oxide nanoparticles (section 3.2). The Curie transition behaviour and ferroelectric response of 4–8 nm BT nanoparticles has also been demonstrated for the first time. Moreover the ferroelectric–relaxor behaviour observed in these particles implies that biogenic BT nanoparticles might also have interesting piezoelectric properties. The demonstration of capability to electrically write and thereafter read the information on individual BT particles paves a way towards application of biogenic complex oxide nanomaterials in memory devices.

3.4. Conclusions

In conclusion, in this chapter, we have shown a fungus–based biological approach towards the synthesis of oxide nanoparticles (silica, titania, zirconia and barium titanate) under ambient conditions. We believe that this approach can be generalized and extended to other oxide nanomaterials by using the appropriate

chemical precursors. The room-temperature synthesis of binary as well as complex oxide nanomaterials using microorganisms is an exciting possibility and could lead to ecologically benign and economically viable methods towards the synthesis of oxide nanomaterials of technological interests. The eco-friendly and energy-conserving nature of the fungus-based biological process for oxide synthesis in comparison with chemical processes such as the sol–gel method cannot be over-emphasized.

3.5 References

- [1] a) Lovley, D. R.; Stolz, J. F.; Nord, G. L.; Phillips, E. J. P. *Nature* **1987**, 330, 252. b) Philse, A. P.; Maas, D. *Langmuir* **2002**, 18, 9977.
- [2] Young, J. R.; Davis, S. A.; Bown, P. R.; Mann S. J. *Struct. Biol.* **1999**, 126, 195.
- [3] a) Pum, D.; Sleytr, U. B. *Trends Biotechnol.* **1999**, 17, 8. b) Sleytr, U. B.; Messner, P.; Pum, D.; Sara, M. *Angew. Chem. Int. Ed.* **1999**, 38, 1034.
- [4] Perry, C. C.; Tucker, T. K. *J. Biol. Inorg. Chem.* **2000**, 5, 537.
- [5] a) Mann, S. *Nature* **1993**, 365, 499. b) Oliver, S.; Kupermann, A.; Coombs, N.; Lough, A.; Ozin, G. A. *Nature* **1995**, 378, 47.
- [6] a) Kroger, N.; Bergsdorf, C.; Sumper, M. *EMBO J.* **1994**, 13, 4676. b) Shimizu, K.; Cha, J.; Stucky, G. D.; Morse, D. E. *Proc. Natl. Acad. Sci. USA* **1998**, 95, 6234.
- [7] Sumerel, J. L. *et al.*, *Chem.Mater.* **2003**, 15, 4804.
- [8] a) Kroger, N.; Deutzmann, R.; Sumper, M. *Science* **1999**, 286, 1129. b) Kroger, N.; Deutzmann, R.; Bersdorf, C.; Sumper, M. *Proc. Natl. Acad. Sci. USA* **2000**, 97, 14133.
- [9] Milligan, A. J.; Morel, F. M. M. *Science* **2002**, 297, 1848.
- [10] a) Hartmann, W. D. *Silicon and siliceous structures in biological systems*, Volcani, B. E.; Simpson, T. L. (eds.) Springer, Berlin Heidelberg New York pp. 453–493. b) Garrone, R.; Simpson, T. L.; Pottu–Boumendil J. *Silicon and Siliceous Structures in Biological Systems*, Volcani, B. E.; Simpson, E. L. (eds.) Springer, Berlin Heidelberg New York **1981**, pp. 495–525. c) Schwab, D. W.; Shore, R. E. *Nature* **1971**, 232, 501. d) Shore, R. E. *Biol. Bull.* **1972**, 143, 689.

- [11] Riedel, W. R.; Sanfilippo, A. *Silicon and Siliceous Structures in Biological Systems*, Volcani, B. E.; Simpson, T. L. (eds.) Springer, Berlin Heidelberg New York **1981**, pp. 323–346.
- [12] Mann, S.; Williams, R. J. P. *Proc. R. Soc. London Ser B* **1982**, *216*, 137.
- [13] a) Perry, C. C.; Tucker, T. K. *J. Biol. Inorg. Chem.* **2000**, *5*, 537. b) Volcani, B. E. *Biochemistry of Silicon and Related Problems*, Bendz, G.; Lindqvist I. (eds.) Plenum, New York pp 174–204.
- [14] a) Cha, J. N.; Stucky, G. D.; Morse, D. E.; Deming, T. J. *Nature* **2000**, *403*, 289. b) Patwardhan, S. V.; Mukherjee, N.; Steinitz–Kannan, M.; Clarson, S. J. *Chem. Commun.* **2003**, 1122.
- [15] Pomogailo, A. D. *Rus. Chem. Rev.* **2000**, *1*, 53–80.
- [16] a) Brumfiel G. *Nature*, **2003**, *424*, 246. b) *The big down*, available at the link <http://www.etcgroup.org/documents/TheBigDown.pdf>
- [17] a) Mukherjee, P. *et al.*, *ChemBioChem* **2002**, *3*, 461. b) Sastry, M.; Ahmad, A.; Khan, M. I.; Kumar, R. *Curr. Sci.* **2003**, 162.
- [18] Innocenzi, P.; Falcaro, P.; Grosso D.; Babonneau, F. *J. Phys. Chem. B* **2003**, *107*, 4711.
- [19] a) Shafi, K. V. P. M. *et al.*, *Langmuir* **2001**, *17*, 1726. b) Lee L. H.; Chen, W. C. *Chem. Mater.* **2001**, *13*, 1137.
- [20] Nakamura, R.; Imanishi, A.; Murakoshi K.; Nakato, Y. *J. Am. Chem. Soc.* **2003**, *125*, 7443.
- [21] Lopez, E. F.; Escribano, V. S.; Panniza, M.; Carnasciali M. M.; Busca, G. *J. Mater. Chem.* **2001**, *11*, 1891.
- [22] The SAED patterns were indexed with reference to the crystal structures from the ASTM charts: Silica [ASTM chart card no. 5–0490 (Tridynite)], Titania [ASTM chart card no. 3–0380 (Brookite) and Zirconia [ASTM chart card no. 2–0464 (Monoclinic) and 2–0733 (Tetragonal)].
- [23] Pottier, A.; Chaneac, C.; Tronc, E.; Mazerolles L.; Jolivet, J. P. *J. Mater. Chem.* **2001**, *11*, 1116.
- [24] Shirley, D. A. *Phys. Rev. B* **1972**, *5*, 4709.

- [25] Wagner, C. D.; Riggs, W. M.; Davis, L. E.; Moulder J. F.; Muilenberg, G. E. *Handbook of X-ray Photoelectron Spectroscopy*, Perkin Elmer Corp. Publishers, Eden Prairie, MN **1979**.
- [26] Verpoort, F.; Bossuyt A. R.; Verdonck, L. *J. Electron Spectrosc. Relat. Phenom.* **1996**, 82, 259.
- [27] Nocun, M.; Siwulski, S.; Leja, E.; Jedlinski, J. *Optical Materials*, **2005**, 27, 1523.
- [28] Bureau, C.; Valin, F.; Lecayon, G.; Charlier, J.; Detalle, V. *J. Vac. Sci. Technol. A* **1997**, 2, 353.
- [29] Briggs, D.; Seah, M. P. *Practical Surface Analysis*, Vol. 1, 2nd edition, John Wiley & Sons **1993**.
- [30] Takeuchi, T. *et al.*, *J. Mater. Sci.* **1997**, 32, 4053.
- [31] Tsunekawa, S.; Ito, S.; Mori, T.; Ishikawa, K.; Li, Z. Q.; Kawazoe, Y. *Phys. Rev. B.* **2000**, 62, 3065.
- [32] Bauer, C. L.; Seager, C. H. *Solid State Physics Source Book*, 6th edition, Parker, S. P. (ed.) McGraw–Hill Book Co., New York **1988**.
- [33] Shannon R. D.; Prewitt, C. T. *Acta Cryst. B* **1969**, 25, 925.
- [34] Vasquez, R. P. *J. Electron Spectrosc. Relat. Phenom.* **1991**, 56, 217.
- [35] Cohen R. E.; Krakauer, H. *Phys. Rev. B* **1990**, 42, 6416.
- [36] Cohen, R. E. *Nature* **1992**, 358, 136.
- [37] Girigharan, N. V.; Jayavel, R.; Ramasamy, P. *Cryst. Res. Technol.* **2001**, 36, 65.
- [38] Viviani, M. *et al.*, *J. Euro. Ceram. Soc.* **1999**, 19, 1047.
- [39] Ma, Y.; Vileno, E.; Suib, S. L.; Dutta, P. K. *Chem. Mater.* **1997**, 9, 3023.
- [40] Gao, Y.; Masuda, Y.; Yonezawa, T.; Koumota, K. *Chem. Mater.* **2002**, 14, 5006.
- [41] Gass, J.; Poddar, P.; Almand, J.; Srinath, S.; Srikanth, H. *Adv. Funct. Mater.* **2006**, 16, 71.
- [42] Neal, T. D.; Okamoto, K.; Scherer, A. *Optics Express* **2005**, 13, 5522.

- [43] Sihvola, A. *Subsurface Sensing Technologies and Applications* **2000**, 1, 393.
- [44] Frey, M. H.; Payne, D. A. *Chem. Mater.* **1995**, 7, 123.
- [45] Yashima, M. *et al.*, *J. Appl. Phys.* **2005**, 98, 014313.
- [46] Begg, B. D.; Vance, E. R.; Nowotny, J. *J. Am. Ceram. Soc.* **1994**, 77, 3186.
- [47] Chattopadhyay, S.; Ayyub, P.; Palkar, V. R.; Multani, M. *Phys. Rev. B* **1995**, 52, 13177.
- [48] Wada, S. *et al.*, *Jpn. J. Appl. Phys.* **1999**, 38, 5505.
- [49] Simon, A.; Ravez, J.; Maglione, M. *J. Phys.: Condens. Matter* **2004**, 16, 963.
- [50] Urban, J. J.; Spanier, J. E.; Lian, O. Y.; Yun, W. S.; Park, H. *Adv. Mater.* **2003**, 15, 423.
- [51] Yen, F.S., Chang, C. T.; Chang, Y.H. *J. Am. Ceram. Soc.* **1990**, 73, 3422.

CHAPTER IV

Fungus-mediated Bioleaching of Silica Nanoparticles from Naturally Available Materials and Agro-industrial By-products

This chapter discusses the use of the fungus *Fusarium oxysporum* in bioleaching of silica nanoparticles of diverse morphologies from naturally available materials such as white sand and zircon sand as well as from the agro-industrial by-product rice husk. The fungus is able to bioleach hollow silica nanoparticles from white sand. In addition, the fungus is also capable of bioleaching amorphous silica present in rice husk in aqueous solution and its further room-temperature biotransformation into crystalline silica particles of cubic morphology. The importance of cationic proteins secreted extracellularly by the fungus has been demonstrated in terms of its capability towards selectively leaching out silica from zircon sand and in turn, enhancing the high dielectric zirconia component in zircon sand.

Part of the work presented in this chapter has been published/communicated:

1) Bansal, V.; Sanyal, A.; Rautaray, D.; Ahmad, A.; Sastry, M. *Adv. Mater.* **2005**, *17*, 889–892. 2) Bansal, V.; Ahmad, A.; Sastry, M. *J. Am. Chem. Soc.* **2006**, *148*, 14059–14066. 3) Bansal, V.; Bhargava, S. K.; Ahmad, A.; Sastry, M. *Langmuir* (communicated).

4.1 Introduction

Bioleaching has become a potential tool for eco-friendly, low-cost synthesis of various metals from their precursors. Bioleaching is promoted in natural habitats by algae, mosses, lichens, plants, animals, actinomycetes, a variety of bacteria, and a few fungi [1–3]. Inorganic materials produced by organisms *via* bioleaching at commercial level include various metals like copper, iron and gold. Use of bacteria has been a prominent method for metal recovery [4]. The iron-oxidizer *Gallionella* sp. was found to be present in copper mines and *Bacillus coagulans* was reported from the waste dunes of bauxite mines in India [2]. Fungi such as *Aspergillus niger* and *Penicillium* sp. have also been found to be among the most effective organisms for metal recovery [5, 6].

Silicon, which is ubiquitous and quantitatively the second most prominent element in the earth crust after oxygen [7], is released in soil by chemical and biological processes [8, 9]. Plants contribute significantly to the biogeochemical cycle of silicon [9]. They take up silicon from soil water in the form of water-soluble silicic acid (H_4SiO_4) [10], polymerize it and accumulate it in the form of amorphous silica, which after plant death, again returns back to the soil. Biocycling of silica in soil occurs through microbial activities that involve fungi, bacteria and actinomycetes. Fungal activity has been reported previously to release an appreciable amount of silicate ions from minerals and rocks [3]. Thus, plants and microbes, through their intricate interplay with soil minerals, contribute appreciably to the global silicon cycle. Apart from plants and microbes in terrestrial environments, marine organisms like diatoms and sponges also play a crucial role in the global silica cycle.

Biomacromolecules (polyamines, carbohydrates, proteins, and glycoproteins) are involved in biosilicification and are capable of polymerizing silicic acid at neutral to acidic pH [11–15]. Since these biomolecules are incorporated into biogenic silica during biosilicification process [13], they may be isolated by selective dissolution of biosilica and can be further studied. The amino acid primary sequences of proteins and polycationic peptides that were isolated in this way from diatoms (silaffins) [16], grasses [17] and sponges (silicateins) [14] have been determined. Tacke [18] has proposed that the silaffin and silicatein proteins fulfill multiple roles by acting as catalysts/templates/scaffolds for the formation of silica *in vivo*. A few details of silica metabolic pathways in diatoms and other silicifying organisms have been discovered

recently, including hitherto unknown classes of enzymes (silicateins [14, 15]) as well as peptides (silaffins [16, 19], frustulins [20], pleuralins/HEPs [21] and SP41 [22]) being either associated with silicic acid polycondensation, precipitation or shell development.

From a material scientist's point of view, silica is by far among the most important inorganic matrices, both for mesoporous solids and hollow microspheres [23, 24]. In general, hollow/porous inorganic microstructures are of interest as low density and thermally stable particles, and also as mechanically resistant encapsulation structures. Hollow silica microspheres have been obtained by various chemical means [25]. However, the chemical syntheses of silica-based materials like resins, molecular sieves and catalysts are not only relatively expensive and eco-hazardous, but also often require extremes of temperature, pressure and pH. In contrast, biosilicification by living organisms such as diatoms, sponges and grasses proceeds under mild physiological conditions, producing an amazing diversity of complex and hierarchical biogenic silica nanostructural frameworks [23].

Despite the vast scientific literature on crystalline and amorphous silica synthesis by biological methods, which involve use of some chemical precursors, to our knowledge there have been no previous attempts at developing a bioleaching process for the synthesis of silica nanoparticles. In this chapter, we address this issue and describe our efforts to set up a biological model system for the extracellular bioleaching of silica nanoparticles from naturally available raw materials like white sand and zircon sand as well as from agro-industrial by-product like rice husk. The replacement of chemical precursors with naturally available materials, in turn, makes the process completely biogenic, economical and eco-friendly.

We show that the fungus *F. oxysporum*, when exposed to white sand, is capable of leaching out silica nanoparticles of quasi-spherical, hollow morphology within 24 h of reaction. In another experiment, *F. oxysporum*, when exposed to rice husk, is not only capable of leaching out huge amount of amorphous silica present in rice husk, in the form of flat, porous silica nanostructures; more interestingly, the fungus also biotransforms this amorphous silica into crystalline silica particles at room temperature. It is interesting to note that despite the *in vitro* studies of various proteins or synthetic macromolecules in this context [12, 13, 15, 25], only the *F. oxysporum* based system was able to produce the aforesaid silica structures for the

conditions studied to date. Moreover, high level of specificity of fungal enzymes towards the silica component in zircon sand has been shown in terms of their capability to selectively leach out silica from zircon sand and hence, simultaneous enhancement in the high dielectric zirconia component in zircon sand. This, in turn imparts value-addition to the zircon sand, which has been used as a raw material in this study. The results presented in this chapter add considerably to the potential for application of this versatile fungus to nanotechnology, particularly in the development of cheap, eco-friendly methods for large-scale synthesis of nanomaterials.

This chapter describes:

- 1) *Fungus-mediated bioleaching of white sand as a means of producing extracellular silica nanoparticles.*
- 2) *Fungus-mediated bioleaching and biotransformation of amorphous silica present in rice husk into nanocrystalline silica.*
- 3) *Fungus-mediated approach for selective bioleaching of silica and simultaneous enrichment of zirconia in zircon sand.*

4.2 Fungus-mediated bioleaching of white sand as a means of producing extracellular silica nanoparticles

4.2.1 Experimental details

The plant pathogenic fungus, *Fusarium oxysporum* was cultured as described in the experimental section of the previous chapter (Section 3.2.1, Chapter 3). Twenty grams (wet weight) of the harvested fungal biomass was suspended in 100 mL of sterile distilled water containing 10 g of white sand (obtained from the river Gomati at Lucknow, Uttar Pradesh, India) in 500 mL Erlenmeyer flasks and incubated on a shaker (200 rpm) at 25–28 °C. The reaction between the fungal biomass and white sand was carried out for a period of 24 hours. The various fractions of bioleached products were collected during the course of reaction, by separating the fungal mycelia as well as white sand from the aqueous component by filtration. The bioleached products thus obtained were treated with phenol/chloroform (1:1; v/v) to remove the free extracellular proteins in the aqueous solution. The purified silica nanoparticles were collected from the aqueous phase and the unbound extracellular proteins were obtained at the interface of the water and phenol/chloroform mixture.

The silica nanoparticle solutions were rotary evaporated to obtain a powder. Further characterization of these powders before and after calcination at 400 °C for 2 h were performed by Fourier transform infrared (FTIR) spectroscopy, transmission electron microscopy (TEM), selected area electron diffraction (SAED) analysis, X-ray diffraction (XRD) analysis and electron dispersive X-rays (EDX) analysis.

The reaction of the fungal biomass with the sand was monitored as a function of time by FTIR spectroscopy. This was accomplished both on the extracellular products formed in the reaction as well as fungal biomass. The extracellular proteins secreted by the fungus, but unbound to silica nanoparticles were also examined by FTIR spectroscopy. XRD measurements were performed on extracellularly synthesized biogenic silica as well as on the fungal biomass after 1 h and 24 h of reaction.

For scanning electron microscopy (SEM) analysis of sand grains, a single sand grain was fixed on a piece of double-sided tape and exposed to *F. oxysporum* for 24 hours. SEM analysis of the sand grain was performed before and after its reaction with the fungus.

4.2.2 Control experiments

In order to preclude the possibility of leaching out of silica due to the acidic nature of the reaction environment, a control experiment was performed wherein the sand was kept in distilled water maintained at pH 3.5 for 24 h, and then the filtrate was characterized by FTIR spectroscopy and TEM. We observed that characteristic Si–O–Si vibrational modes of silica as well as signatures from silicic acid (Si–OH vibrational modes) [27, 28] were absent and that no particles could be detected in the TEM analysis.

4.2.3 FTIR spectroscopy measurements

FTIR spectroscopy measurements of both the biomass (Figure 4.1 A) as well as the extracellular product (Figure 4.1 B) formed during reaction of white sand with *F. oxysporum* were carried out in order to understand the mechanism of bioleaching of silica from white sand. Curve 1 in Figure 4.1 A and B corresponds to the FTIR spectra recorded at early stages of the reaction (after 1 h). The spectrum recorded from the biomass (curve 1, Figure 4.1 A) shows a peak at *ca.* 896 cm⁻¹, which is

completely absent in that of the filtrate (curve 1, Figure 4.1 B). This peak is assigned to the Si–OH [27] stretching vibration and is believed to arise from silicic acid, which is formed during the initial stages of interaction of the fungal biomass with the sand. At the initial stage of reaction, it appears most likely that the proteins present in the fungal biomass interact with the complex silicates present in white sand, hydrolyze these silicates in the form of silicic acid and adsorb this silicic acid during the hydrolysis process, thus revealing Si–OH peak in the FTIR spectrum of the biomass (curve 1, Figure 4.1 A).

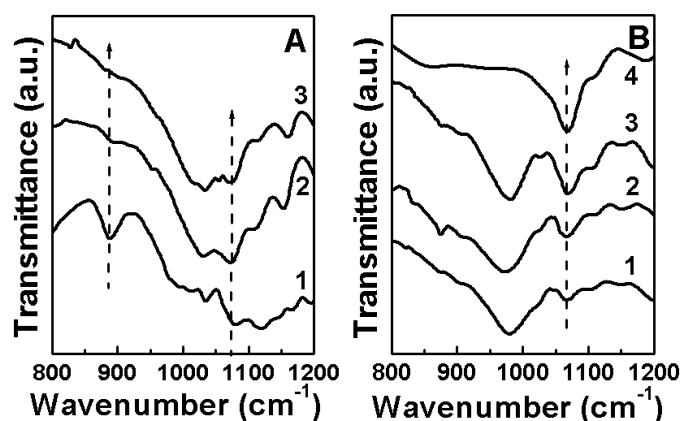


Figure 4.1 FTIR kinetics recorded from the fungal biomass (A) and the filtrate (B) after exposing sand to *F. oxysporum* at 1 h (curve 1), 12 h (curve 2) and 24 h (curve 3) after the reaction. Curve 4 in (B) corresponds to the FTIR spectrum recorded from the silica particles in the filtrate after calcination at 400 °C for 2 h.

Another interesting feature is the presence of a rather broad peak in the region 1060–1100 cm⁻¹ in the case of the biomass (curve 1, Figure 4.1 A) as well as in the filtrate (curve 1, Figure 4.1 B). This peak can be assigned to the Si–O–Si antisymmetric stretching mode of silica [28]. We believe that the silicic acid present in the fungal biomass undergo a condensation process by the action of fungal proteins to form silica particles, thus revealing Si–O–Si peak in the FTIR spectrum of biomass (curve 1, Figure 4.1 A). The simultaneous presence of Si–O–Si peak in the FTIR spectrum of filtrate (curve 1, Figure 4.1 B) suggests that silica particles are then released from biomass into solution. That the Si–OH vibrational band is absent in the filtrate even at early stages of reaction (curve 1, Figure 4.1 B) suggests that the hydrolysis of the silicate complexes occurs mainly within the fungal biomass, which then release the hydrolyzed product as silica particles into solution. As the reaction proceeds with time, the intensity of the Si–OH vibration decreases in the biomass, and this process is accompanied by a concomitant increase in intensity of the Si–O–Si

vibrational peak at *ca.* 1090 cm^{-1} (curves 2 and 3, Figure 4.1 A). This increase in the Si–O–Si vibrational band is much more pronounced in the filtrate (curves 2 and 3, Figure 4.1 B), clearly indicating that a large fraction of silica particles produced within the biomass by hydrolysis of the silicate complexes are released into solution.

The presence of strong amide I and II signatures in the FTIR spectrum of the bioleached silica at *ca.* 1645 cm^{-1} and 1530 cm^{-1} before (curve 1, Figure 4.2 B) and after (curve 3, Figure 4.2 B) removal of free proteins in the extracellular product by phenol/chloroform treatment suggests that these biomolecules are proteins that play an important role in leaching out the silica particles and stabilizing them in solution. The presence of a weak Si–O–Si vibration band in the free proteins removed by phenol/chloroform treatment (curve 2, Figure 4.2 A) might be due to trapping of some silica particles in free proteins (curve 2, Figure 4.2 B) that aggregates at the interface between water and the phenol/chloroform mixture. The FTIR spectrum of phenol/chloroform purified silica particles clearly show the strengthening of Si–O–Si vibration band (curve 3, Figure 4.2 A) along with reduced amide I and II signatures (curve 3, Figure 4.2 B), indicating the increase in density of silica particles after removal of free proteins.

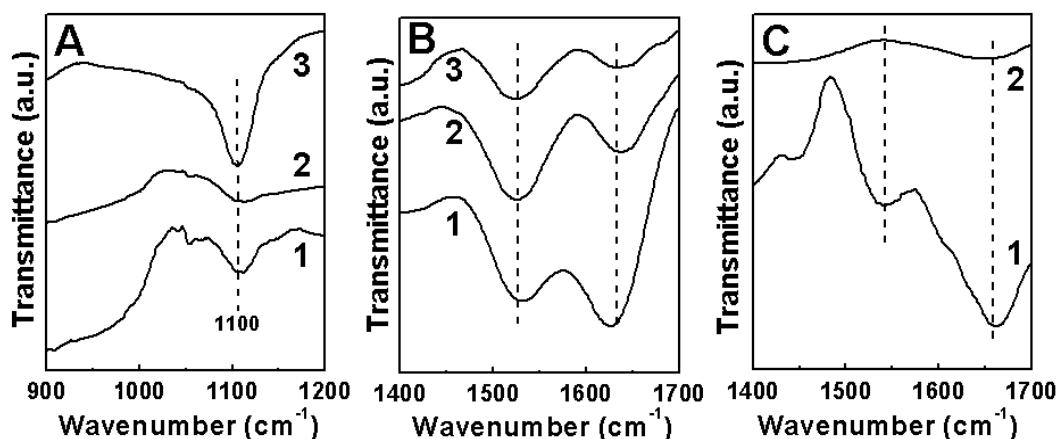


Figure 4.2 (A and B) FTIR spectra recorded from bioleached silica nanoparticles (curve 1), from unbound proteins obtained at phenol/chloroform interface during silica purification (curve 2) and from silica nanoparticles purified using phenol/chloroform in the aqueous phase (curve 3) in the region of Si–O–Si vibration (A) and amide bands (B). (C) FTIR spectra of the bioleached silica particles before (curve 1) and after calcination (curve 2) in the region of amide bands.

The FTIR results clearly show the presence of proteins in the bioleached silica powder. In order to remove the proteins that are occluded/intercalated within the silica structures, calcination of the bioleached silica powder was performed at 400 $^{\circ}\text{C}$ for

2 hours. The calcination process leads to sharpening of the Si–O–Si vibration band (curve 4, Figure 4.1 B). That the proteins are removed during calcination is shown by the complete disappearance of the amide I and II bands in the FTIR spectrum of the calcined silica (curve 2, Figure 4.2 C) that were present in bioleached silica before calcination (curve 1, Figure 4.2 C).

4.2.4 TEM and SAED measurements

The bioleaching of silica particles in the nanometer regime can be easily monitored using TEM. Figure 4.3 A shows a representative TEM image recorded from film of the extracellular product obtained by the reaction of *F. oxysporum* with the sand for 24 h (pH of the reaction medium ~ 3.5). The particles are small, ranging in size from 2 to 5 nm and tend to cluster. Figure 4.3 B shows a representative TEM image recorded from the silica nanoparticles after removal of free proteins in solution by phenol/chloroform treatment of the reaction medium. Removal of unbound proteins clearly enhances the quality of the TEM image of the nanoparticles (Figure 4.3 B). The aggregates of particles have become spherical and at higher magnification (upper inset, Figure 4.3 B), these clusters appear porous. The aggregates of particles have become spherical and at higher magnification (upper inset, Figure 4.3 B), these clusters appear porous.

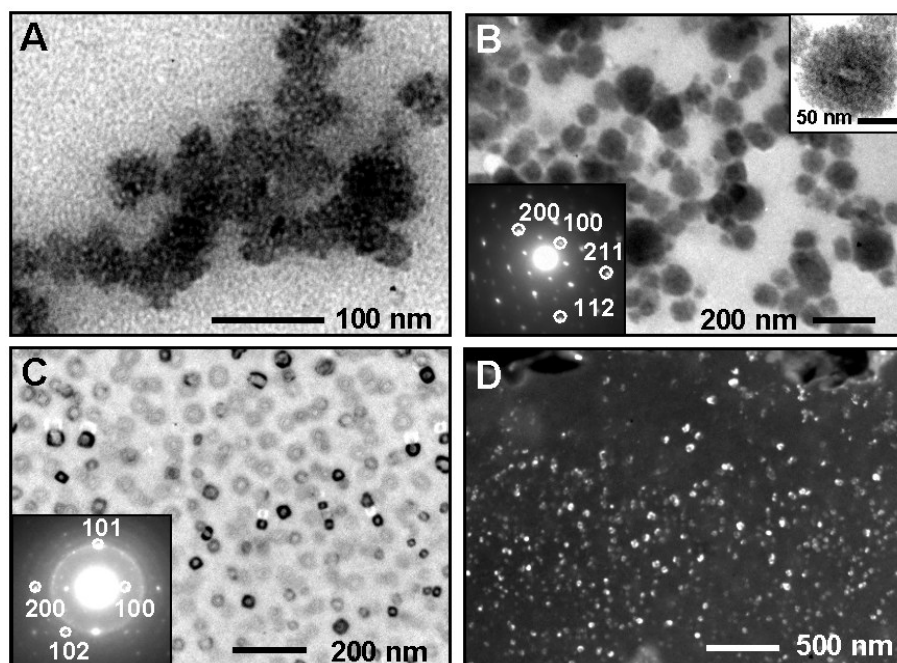


Figure 4.3 TEM micrographs of silica nanoparticles bioleached from sand after 24 h of its exposure to *F. oxysporum* before (A), after purification with phenol/chloroform (B) and after calcination at 400° C for 2 h (C and D). The lower insets in (B) and (C) are SAED patterns recorded from representative silica nanoparticles. The higher inset in (B) is the high magnification image of one of the particles shown in main figure. (D) shows the dark field image of the particles shown in (C).

SAED analysis of particle assemblies (lower inset, Figure 4.3 B) clearly indicates that they are crystalline. The diffraction spots in the SAED pattern could be indexed based on the silica structure [29]. The TEM and SAED results clearly show that silica nanoparticles are leached out from the sand by the fungus *F. oxysporum*. The calcined silica nanoparticle powder (400 °C for 2 h) after redispersion in chloroform was analyzed by TEM (Figure 4.3 C and D). It is observed that the process of calcination results in the formation of hollow, quasi-spherical structures of silica. The SAED pattern recorded from the hollow silica structures (inset, Figure 4.3 C) clearly shows the crystalline nature of the silica particles. Figure 4.3 D shows a dark field image of the hollow silica nanoparticles obtained after calcination. It thus appears that the proteins, which were occluded in the silica mosaic structures (Figure 4.3 A and B), after removal during calcination, create voids in the mosaic structures and hence result in formation of hollow silica nanoparticles. These results correlate well with the FTIR spectroscopy data, which also show the loss of amide signatures after calcination at 400 °C for 2 h (Figure 4.2 C).

4.2.5 XRD measurements

The crystallinity of bioleached silica nanoparticles was further established by XRD analysis of the biomass (curves 1 and 2, Figure 4.4) as well as the filtrate (curves 3 and 4, Figure 4.4). Even at very early stages of reaction (after 1 h), both the biomass (curve 1, Figure 4.4) and the filtrate (curve 3, Figure 4.4) show the presence

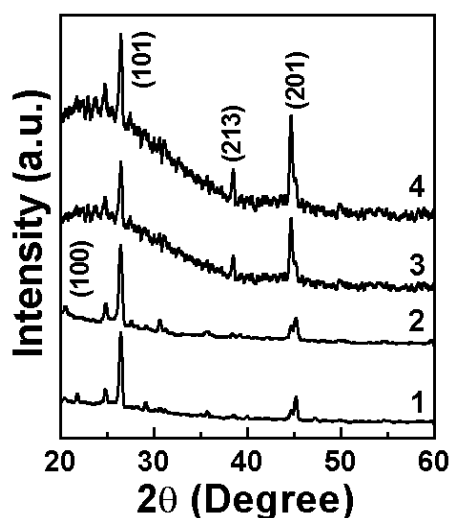


Figure 4.4 XRD patterns recorded from the silica particles synthesized by the exposure of sand to *F. oxysporum*. XRD patterns correspond to the silica particles formed in the biomass (curves 1 and 2) and in the filtrate (curves 3 and 4) after 1 h (curves 1 and 3) and 24 h (curves 2 and 4) of reaction.

of crystalline silica nanoparticles. Even after 24 h of reaction, no significant change in the crystallinity of silica particles was observed either in the biomass (curve 2, Figure 4.4) or in the filtrate (curve 4, Figure 4.4). The observation that the widths of the Bragg reflections do not change with time of reaction (compare curves 1 and 3 with curves 2 and 4 respectively) indicate that the reaction of the fungus with the sand results in a steady bioleaching process, leading to the formation of fairly uniformly-sized silica nanoparticles. The uniformity in size of the silica nanoparticles is possibly due to stabilization of the particles by capping proteins that prevent their aggregation both within the biomass and solution.

4.2.6 EDX measurements

Chemical analysis of the bioleached product was performed by EDX measurements (Figure 4.5). EDX analysis of the leached-out product clearly shows the strong signals arising from Si (1.741 keV) and O (0.517 keV), indicating the bioleaching of silica in the filtrate. In addition to Si and O signals, fairly intense C (0.266 keV), N (0.381 keV) and S (2.307 keV) signals are also observed, which indicate the presence of proteins in the silica nanoparticle powder.

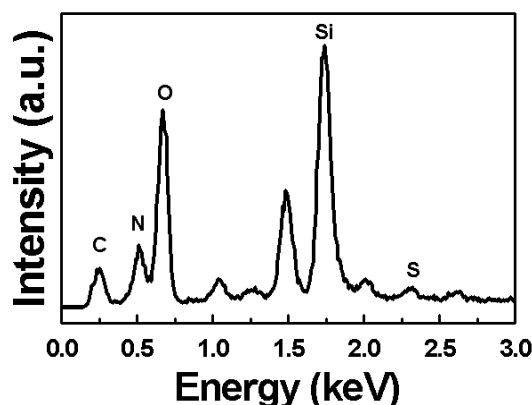


Figure 4.5 EDX spectrum recorded from the silica particles formed in the filtrate after 24 h of exposure of white sand to *F. oxysporum*.

4.2.7 SEM measurements

Important information on the bioleaching process can be obtained by imaging the texture of the sand particles before and after reaction with the fungus. Figure 4.6 A and B shows SEM images of a single sand grain before (Figure 4.6 A) and after (Figure 4.6 A) its exposure to the fungus *F. oxysporum*. It can be clearly seen from the SEM images that the surface of the sand grain is relatively smooth before

exposure (more clearly seen in the inset, Figure 4.6 A), which then becomes rough after exposure to the fungus (inset, Figure 4.6 B). The roughening of the surface of the sand grain after reaction with the fungus can be attributed to the fungus-mediated leaching out of silicate complexes present in the sand in the form of silica particles.

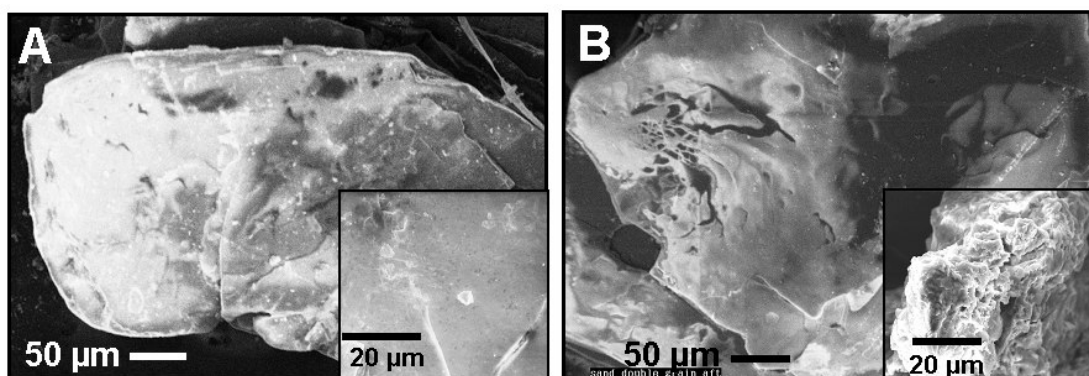


Figure 4.6 SEM micrographs of a single grain of sand before (A) and after (B) its exposure to *F. oxysporum* for 24 hours. The insets in A and B show magnified views of a selected area from the respective grains.

4.2.8 Summary

We have demonstrated that the fungus *Fusarium oxysporum* may be used in the bioleaching of silica nanoparticles from white sand. The formation of silica nanoparticles is believed to proceed *via* a two-step process. The first step involves the fungal biomass-mediated hydrolysis and leaching of silicate complexes present in the sand, in the form of silicic acid; in the second step, the condensation of silicic acid into silica most likely takes place by some specific fungal enzymes. The silica is in the form of nanoparticles capped by stabilizing proteins in the size range 2 to 5 nm and is released into solution by the fungus. Removal of the silica occluded proteins by calcination results in hollow silica particles. The room temperature bioleaching of silica nanoparticles from cheap materials like white sand is an exciting possibility and could potentially lead to large-scale synthesis of oxide nanomaterials.

4.3 Fungus-mediated bioleaching and biotransformation of amorphous silica present in rice husk into nanocrystalline silica

4.3.1 Experimental details

The plant pathogenic fungus, *Fusarium oxysporum* was cultured as described in the experimental section of the previous chapter (Section 3.2.1, Chapter 3). Twenty grams (wet weight) of the harvested fungal biomass was suspended in 100 mL of

sterile distilled water containing 10 g of rice husk (obtained from a rice milling plant at Lucknow, Uttar Pradesh, India) in 500 mL Erlenmeyer flasks and incubated on a shaker (200 rpm) at 25–28 °C. The reaction between the fungal biomass and rice husk was carried out for a period of 24 h and the reaction products were collected during various time intervals, upto 24 h, by separating the fungal mycelia and rice husk from the aqueous component by filtration. The filtrate thus obtained was treated with phenol/chloroform (1:1; v/v) and centrifuged (6000 rpm) for 10 min to remove the free extracellular fungal proteins from the aqueous solution. The purified silica nanoparticles were collected from the aqueous phase and the unbound extracellular proteins were obtained at the interface of the water and phenol/chloroform mixture. The silica nanoparticle solution was rotary evaporated to obtain powder. Further characterization of these powders before and after calcination at 400 °C for 2 h were performed by transmission electron microscopy (TEM), selected area electron diffraction (SAED) analysis, Fourier transform infrared (FTIR) spectroscopy, X-ray diffraction (XRD) analysis, electron dispersive X-rays (EDX) analysis and X-ray photoemission spectroscopy (XPS). Rice husk used in this study was characterized using scanning electron microscopy (SEM), EDX, FTIR, XRD, XPS and high resolution TEM (HRTEM). For SEM analysis, fragments of rice husk before and after its reaction with the fungus as well as after hydrofluoric acid (HF) treatment for 24 h were fixed onto Al substrate holder with silver paste.

In XPS, the C 1s, Si 2p and O 1s core level spectra were recorded with un-monochromatized Mg K α radiation (photon energy = 1253.6 eV) at a pass energy of 50 eV and electron takeoff angle (angle between electron emission direction and surface plane) of 60°. The overall resolution was 1 eV for the XPS measurements. The core level spectra were background corrected using the Shirley algorithm [30] and the chemically distinct species were resolved using a nonlinear least squares fitting procedure. The core level binding energies (BEs) were aligned with the adventitious carbon binding energy of 285 eV.

The effect of the fungus *F. oxysporum* was also studied on commercially available standard amorphous (silica gel) and crystalline silica (quartz) and the reaction products obtained were analyzed using FTIR, TEM and XRD. The biomolecules occluded in the silica nanostructures were analyzed using 12% sodium dodecyl sulphate polyacrylamide gel electrophoresis (SDS–PAGE). For protein

analysis, the bioleached silica particles were obtained by centrifugation (10000 rpm) for 30 min at 4 °C and the free proteins were removed by repeated washing and centrifugation. Silica nanoparticles along with the occluded proteins were treated with 3 M ammonium fluoride (NH₄F) for 48 h at 4 °C with constant stirring to dissolve silica from the proteins. Following dissolution, sample was dialyzed against seven changes of deionized water over 7 days and lyophilized before being analyzed by SDS–PAGE. In order to understand the nature of silica-bound proteins, the lyophilized protein fraction was loaded onto cationic (CM–sephadex) and anionic (DEAE–sephadex) ion exchange matrices respectively. The unbound fractions obtained from both these columns were also lyophilized and checked on SDS–PAGE.

The extracellular fungal proteins obtained by inoculating 20 g of fungal biomass in sterile deionized water for 24 h were also checked for their capability to synthesize silica particles from rice husk *in vitro*. Briefly, 0.1 g of rice husk was suspended in 10 mL of extracellular fungal extract and the reaction was carried out at 4 °C for 72 h. The extracellular fungal extract was concentrated by lyophilization and loaded separately onto CM–sephadex and DEAE–sephadex matrices. The unbound fractions obtained from both these columns were checked for their activity to synthesize silica particles *in vitro*. The reaction products formed were analyzed by FTIR, XRD and TEM studies.

4.3.2 SEM and EDX analysis of rice husk

In order to understand the morphology of amorphous silica present in the rice husk, a fragment of rice husk was imaged by SEM. Figure 4.7 A1 and A2 show the lower and higher magnification SEM images recorded from the upper surface of rice husk while Figure 4.7 B1 and B2 show the similar images recorded from the lower surface of rice husk before its exposure to the fungus *F. oxysporum*. The SEM images exhibit the presence of heterogeneously distributed silica on upper as well as lower surface of rice husk which was further confirmed by EDX analysis as shown in Figure 4.7 A3 and B3 for upper and lower surfaces respectively. From these SEM images one concludes that the silica present on the surface of rice husk is of micron dimensions with the particles being of variable morphology. Further confirmation of the presence of silica in rice husk was done by treating rice husk with HF which selectively dissolves silica particles.

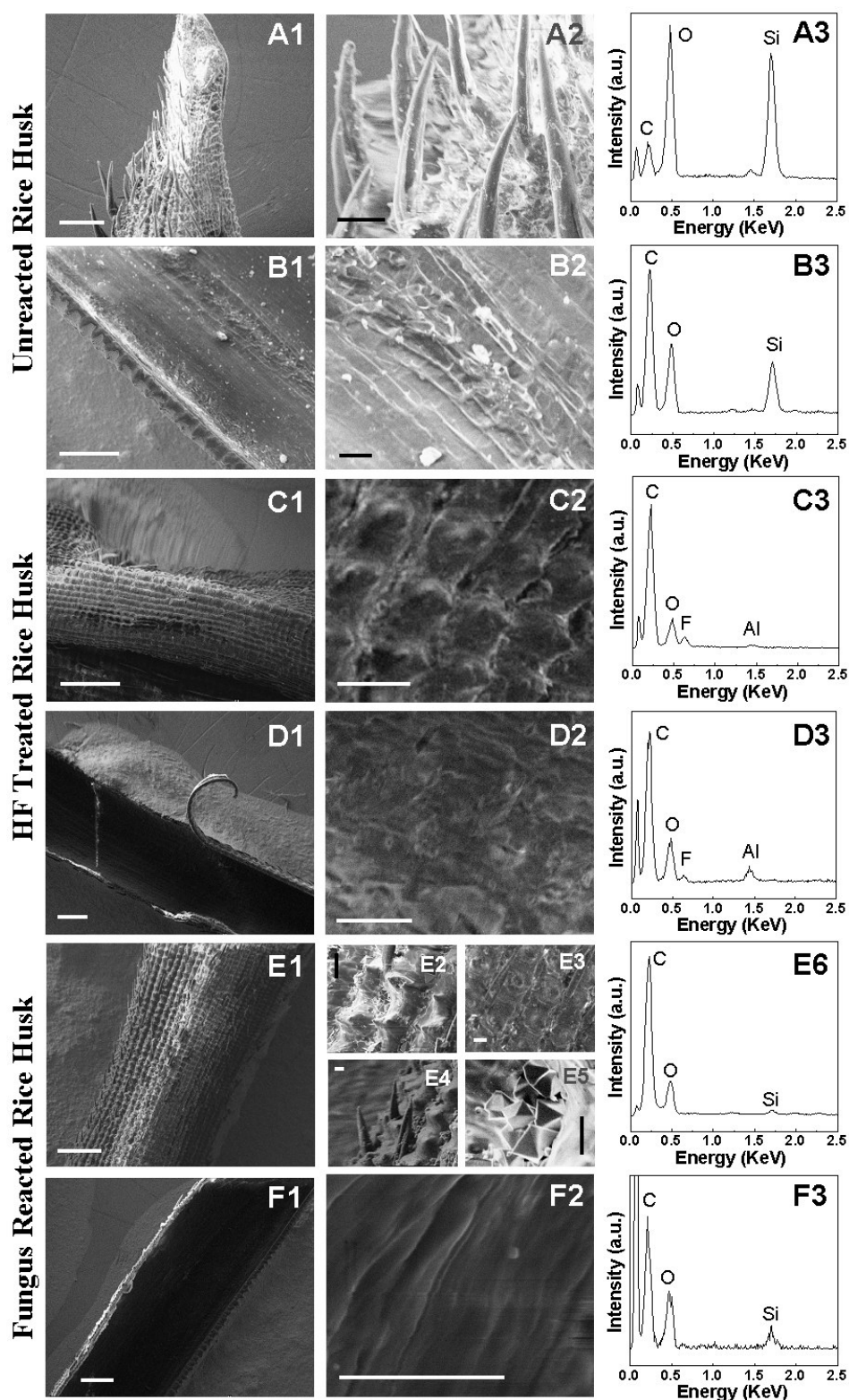


Figure 4.7 SEM micrographs (columns 1 and 2) and corresponding EDX spectra (column 3) of upper (A, C and E) and lower (B, D and F) surface of rice husk before (A1–A3 and B1–B3) and after (E1–E6 and F1–F3) its reaction with the fungus *F. oxysporum* as well as after its treatment with hydrofluoric acid (C1–C3 and D1–D3). Column 1 and 2 show the low and high magnification SEM images of single rice husk flake while column 3 shows the EDX spectra from their respective high magnification field views shown in column 2. Scale bars in the images shown in first column (A1–FI) correspond to 500 μm while those in second column (A2–F2) correspond to 50 μm.

Figure 4.7 C1–C2 and Figure 4.7 D1–D2 show the SEM images obtained from upper and lower surfaces of rice husk respectively after HF treatment. No silica particles are visible in SEM images of Figure 4.7 C and D that correlate well with the corresponding EDX spectra shown in Figure 4.7 C3 and D3 from upper and lower rice husk surfaces after HF treatment, which do not show any Si signal (1.741 keV). We observe a weak fluoride signal in these EDX spectra due to residual fluoride ions from HF even after repeated washing of rice husk with deionized water. The presence of aluminium signal is from the substrate holder.

The change in morphology of silica present in rice husk after its reaction with the fungus *F. oxysporum* for 24 h was also studied as is shown in Figure 4.7 E1–E5 (upper surface) and Figure 4.7 F1–F2 (lower surface). Figure 4.7 E2–E5 show the higher magnification images of the various regions of upper surface of rice husk after fungal reaction as that shown in Figure 4.7 E1. We observe the formation of some pyramidal/triangular silica structures in some regions of rice husk (Figure 4.7 E5), which give a strong Si signal in EDX (data not shown). However, the EDX profiles from large regions of rice husk show very small Si signal as shown in Figure 4.7 E6 and F3 from respective upper and lower surfaces of rice husk after fungal reaction. This suggests that most of the silica present in rice husk has leached out within 24 h of its reaction with *F. oxysporum*.

4.3.3 Quantification of silica bioleached from rice husk by EDX and XPS

In order to quantitate the amount of silica leached out from rice husk during its course of reaction with the fungus, the husk obtained after reaction with fungus at various time intervals (0 h, 8 h, 16 h and 24 h) was finely ground and EDX kinetics of

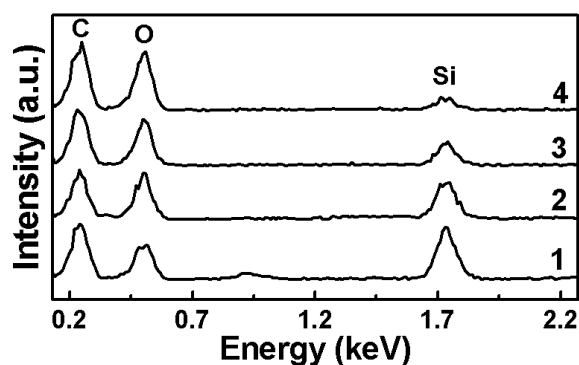


Figure 4.8 EDX spectra recorded from rice husk during the course of its reaction with the fungus *F. oxysporum* at 0 h (curve 1), 8 h (curve 2), 16 h (curve 3) and 24 h (curve 4) respectively.

ground husk was performed (curves 1–4, Figure 4.8). Based on the change in Si:C ratio in rice husk during the reaction, it was established using EDX analysis that interestingly, 90% and 95% of silicon is leached out within 8 h and 16 h of reaction respectively, while it takes 24 h to leach out 97% of silica from rice husk.

Since EDX is a semi-quantitative technique, a more precise approach to quantitate silica bioleaching was followed using XPS analysis. Figure 4.9 shows the Si 2p (Figure 4.9 A and C) and C 1s (Figure 4.9 B and D) core level XPS spectra obtained from finely ground rice husk before (Figure 4.9 A and B) and after (Figure 4.9 C and D) its reaction with *F. oxysporum* for 24 hours. The Si:C ratios (ratios of integrated areas under the respective curves) in the rice husk before and after reaction with the fungus were used to quantitate the amount of silica bioleached from rice husk; it was observed that the reaction of fungus with rice husk results in leaching out 96% of silica from rice husk in aqueous solution within 24 h of reaction. The XPS results thus correlate well with EDX analysis, which also shows that the fungus is capable of leaching out 97% of silica from rice husk within 24 h of reaction.

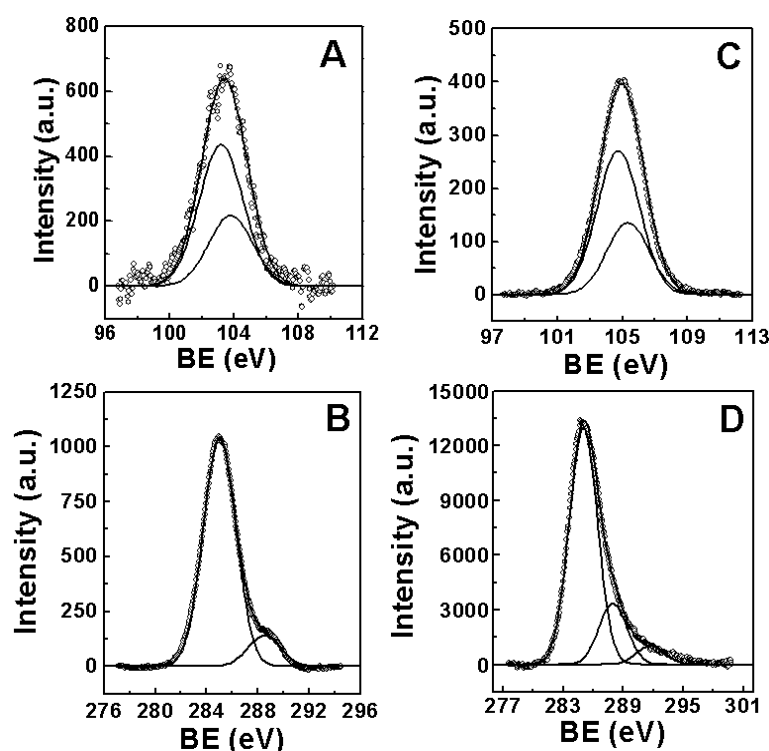


Figure 4.9 Si 2p (A and C) and C 1s (B and D) core level XPS spectra recorded from rice husk before (A and B) and after (C and D) its reaction with the fungus *F. oxysporum*. The Si 2p spectra (A and B) have been deconvoluted into Si 2p_{3/2} and 2p_{1/2} spin orbit pairs with spin orbit splitting ~ 0.6 eV. The chemically resolved components in C 1s spectra (B and D) have been shown as solid lines in the figure.

4.3.4 TEM and SAED measurements of bioleached silica

Figure 4.10 A shows a representative TEM image recorded from the extracellular product obtained by the reaction of *F. oxysporum* with the rice husk for 24 h (pH of the reaction medium \sim 4.5). A number of particles of irregular morphology are observed in the extracellular reaction medium; the particles are small, ranging in size from 2 nm to 6 nm and tend to cluster. SAED analysis of the particle assemblies (inset, Figure 4.10 A) clearly indicates that the particles are crystalline. The diffraction spots in the SAED pattern could be indexed based on the quartz polymorph of silica [31]. Figure 4.10 B shows a representative TEM image recorded from silica nanoparticles after removal of free proteins in solution by phenol/chloroform treatment. Removal of unbound proteins clearly enhances the quality of the TEM image of the nanoparticles (Figure 4.10 B). The particles embedded in the biomolecular matrix are fairly regular in shape and depicts an overall quasi-spherical morphology (Figure 4.10 B).

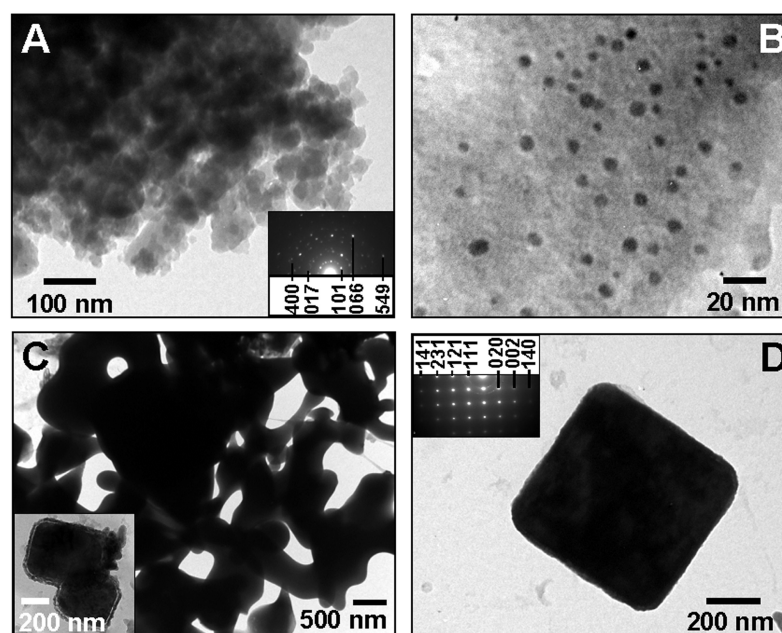


Figure 4.10 TEM micrographs at different magnifications of silica nanoparticles synthesized by the exposure of rice husk to *F. oxysporum* before (A and B; see text for details) and after calcination at 400° C for 2 h (C and D). The inset in C corresponds to a high magnification image of silica particles shown in the main figure. The insets in A and D are SAED patterns recorded from representative silica nanoparticles in the corresponding images.

In order to remove the biomolecules bound to silica particles, the phenol/chloroform-purified particles were subjected to calcination at 400 °C for 2 h. TEM analysis of calcined silica powder clearly shows that the breakdown of entrapped biomolecules by calcination leads to sintering of the silica nanoparticles

and results into formation of large, apparently porous silica structures of flat morphology (Figure 4.10 C and D). Higher magnification images of these particles indicate that these structures might be porous and encompass several silica particles of nanometric dimensions (inset, Figure 4.10 C). Apart from the entangled network of these flat structures (Figure 4.10 C), we also notice a large number of cubic (Figure 4.10 D) and cuboid (inset, Figure 4.10 C) silica structures in the calcined sample. It thus appears that the proteins occluded in the silica mosaic structures (Figure 4.10 A and B) leave behind a porous network after their degradation during calcination (Figure 4.10 C and D). The SAED pattern recorded from calcined silica structures (inset, Figure 4.10 D) also indicates the highly crystalline nature of the silica particles.

4.3.5 FTIR spectroscopy measurements of bioleached silica

To understand the mechanism of bioleaching of silica from rice husk, a time dependent FTIR analysis of leached out product from the fungus–rice husk reaction medium was carried out after 4 h, 8 h, 12 h, 16 h, 20 h and 24 h of reaction (curves 2–7 respectively, Figure 4.11 A). Curve 2 in Figure 4.11 A corresponds to the FTIR spectrum of bioleached product recorded during early stage of reaction (after 4 h) wherein, we observe a shoulder at *ca.* 900 cm^{-1} . We also observe a concomitant reduction in the peak at 900 cm^{-1} as the reaction proceeds from 4 h to 24 h (curves 2–7 respectively, Figure 4.11 A).

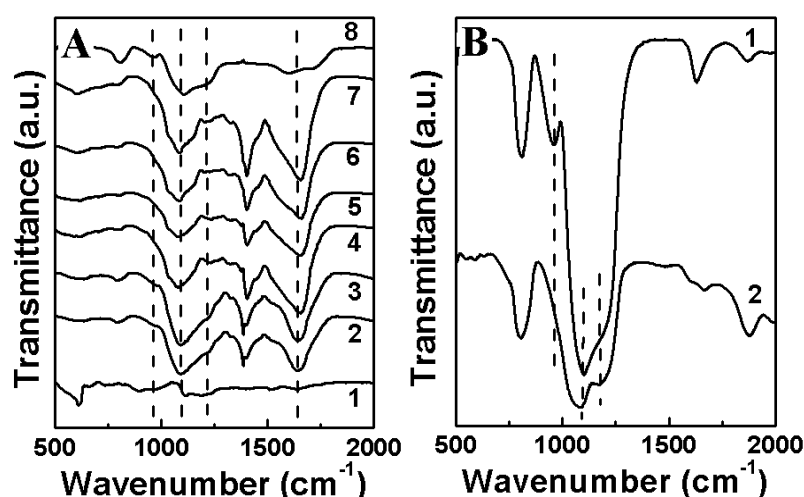


Figure 4.11 (A) FTIR spectra recorded from the filtrates containing silica particles synthesized by exposing rice husk to *F. oxysporum* for 4 h, 8 h, 12 h, 16 h, 20 h and 24 h (curves 2–7 respectively); from silica nanoparticles calcined at 400 °C for 2 h (curve 8) and from the filtrate obtained by exposing rice husk to water of pH 4.5 for 15 days (curve 1). (B) FTIR spectra recorded from standard silica gel (curve 1) and quartz particles (curve 2).

Another interesting feature is the presence of a rather broad peak at *ca.* 1050–1250 cm^{-1} upto 8 h of reaction (curves 2–3, Figure 4.11 A) with a maximum at 1070 cm^{-1} . This peak can be assigned to the Si–O–Si antisymmetric stretching mode (TO_3 mode) present in the leached out product [28]. A shoulder towards higher frequency side generally accompanies the TO_3 mode. Interestingly, during initial course of reaction, we do not observe any such shoulder (curves 2–3, Figure 4.11 A), however, after 8 h of reaction (curves 4–7, Figure 4.11 A), the broad feature at *ca.* 1050–1250 cm^{-1} starts resolving into smaller components and we observe a shoulder developing at *ca.* 1150 cm^{-1} that becomes very clear after 24 h of reaction (curve 7, Figure 4.11 A).

In order to understand the gradual loss in intensity of the shoulder towards lower wavenumbers ($\sim 900 \text{ cm}^{-1}$) and a gradual growth of the peak towards higher wavenumber ($\sim 1150 \text{ cm}^{-1}$), FTIR analysis of standard silica samples *viz.* amorphous silica (silica gel) and crystalline silica (quartz) were also performed (Figure 4.11 B). Interestingly, the standard amorphous silica sample (curve 1, Figure 4.11 B) shows similar FTIR spectrum as that from the reaction product obtained during beginning of reaction (a broad peak around 1100 cm^{-1} with a shoulder at around 900 cm^{-1}) (compare curve 2, Figure 4.11 A and curve 1, Figure 4.11 B). However, standard crystalline quartz sample (curve 2, Figure 4.11 B) shows an FTIR spectrum similar to that obtained from the reaction product obtained towards the end point of reaction (a prominent peak around 1100 cm^{-1} with a shoulder at around 1150 cm^{-1} and shoulder around 900 cm^{-1} missing) (compare curve 7, Figure 4.11 A and curve 2, Figure 4.11 B). At the initial stages of reaction (4 h), it is most likely that the hydrolyzing enzyme(s) secreted by *F. oxysporum* act on silica present in rice husk and bioleach amorphous silica in the aqueous solution, thus revealing a shoulder towards lower wavenumber (900 cm^{-1}) at initial stages of reaction (curves 2–3, Figure 4.11 A). The disappearance of lower wavenumber shoulder at the later stages of reaction (curves 4–7, Figure 4.11 A) with concomitant sharpening of the Si–O–Si peak (1100 cm^{-1}) and intensification of the shoulder towards higher wavenumber (1150 cm^{-1}) indicate that some biomolecules/proteins might form a complex with amorphous silica bioleached from rice husk and crystallize it to form crystalline silica nanoparticles. This is in good agreement with TEM results that reveal a high concentration of bioleached silica nanoparticles embedded in protein matrix

(Figure 4.10 A and B). Therefore, FTIR kinetics of silica bioleaching indicates that silica is initially leached in amorphous form from rice husk, which is later biotransformed into crystalline form at room temperature, as the reaction proceeds. Presence of a broad and intense amide band between 1500 cm^{-1} and 1700 cm^{-1} further reaffirms the entrapment of proteins released by the fungus in the quasi-spherical silica particles (curves 2–7, Figure 4.11 A). When the bioleached silica is calcined at $400\text{ }^{\circ}\text{C}$ for 2 h in order to remove silica-entrapped proteins, the amide signatures (between 1500 cm^{-1} and 1700 cm^{-1}) as well as the signatures from organic molecules around *ca.* 1400 cm^{-1} in FTIR spectra fade away, indicating the removal of most of the biomolecules during calcination (curve 8, Figure 4.11 A).

4.3.6 XRD measurements of bioleached silica

The crystallization progression of silica particles was studied by XRD analysis of the bioleached product formed in the fungus-rice husk reaction medium at 0 h, 4 h, 8 h, 12 h, 16 h, 20 h and 24 h of reaction (curves 2–8, Figure 4.12 A). When XRD analysis of finely powdered rice husk (curve 2, Figure 4.12 A) was performed, no Bragg reflections could be observed from rice husk, indicating the absence of crystalline silica in rice husk. It is evident from curves 2–8 in Figure 4.12 A that as the fungus–rice husk reaction proceeds from 0 h to 24 h, the crystallinity of silica particles increase and after 24 h of reaction (curve 8, Figure 4.12 A), the silica nanoparticles show well-defined Bragg reflections characteristics of quartz polymorph of crystalline silica [31].

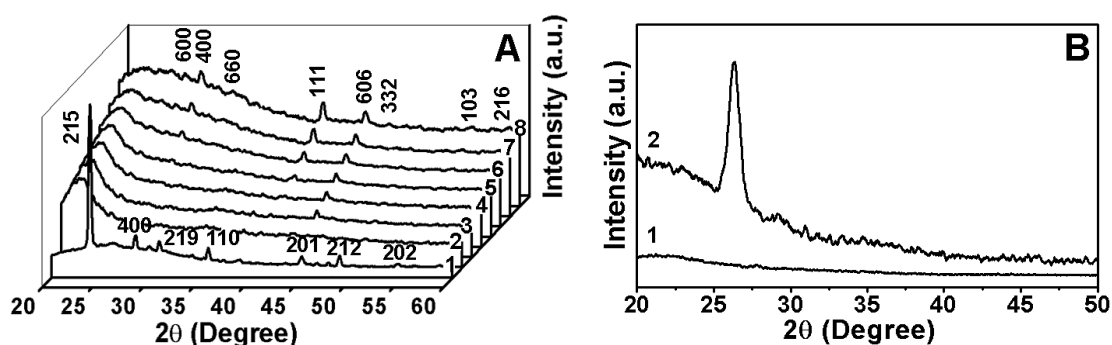


Figure 4.12 (A) XRD patterns recorded from silica particles synthesized by the exposure of rice husk to *F. oxysporum* before (curves 2–8) and after calcination at $400\text{ }^{\circ}\text{C}$ for 2 h (curve 1). Curve 2 correspond to XRD pattern obtained from rice husk while curves 3–8 correspond to silica particles formed at 4 h, 8 h, 12 h, 16 h, 20 h and 24 h respectively. (B) XRD patterns recorded from standard silica gel (curve 1) and quartz particles (curve 2).

The XRD analysis, when performed on silica powder calcined at 400 °C for 2 h (curve 1, Figure 4.12 A), also showed well-defined intense Bragg reflections characteristic of quartz polymorph of silica nanoparticles [31]. It is obvious that calcination and the consequent degradation of proteins from the silica matrix results in increased crystallinity of the silica particles (curve 1, Figure 4.12 A) when compared with the as-synthesized silica nanoparticles (curve 8, Figure 4.12 A). The XRD measurements of standard amorphous silica *i.e.* silica gel (curve 1, Figure 4.12 B) as well as crystalline silica *i.e.* quartz (curve 2, Figure 4.12 B) were also performed for the sake of comparison (Figure 4.12 B).

4.3.7 Control experiments

It is observed that the XRD analysis of the rice husk, which has been used as a precursor in this study, does not show presence of crystalline silica (curve 2, Figure 4.12 A). Moreover, in order to validate the absence of crystalline silica in rice husk, SAED and HRTEM analysis of finely ground rice husk were also attempted along with HRTEM–coupled EDX measurement (Figure 4.13 A). We could neither observe any lattice planes in HRTEM image of silica in rice husk (Figure 4.13 A), nor could we obtain any electron diffraction from the same (inset, Figure 4.13 A). However, at the same time, we could record the Si signal in EDX spectrum arising from silica particles in rice husk (Figure 4.13 B). These experiments completely abolish the possibility of presence of any crystalline silica in the starting material (rice husk).

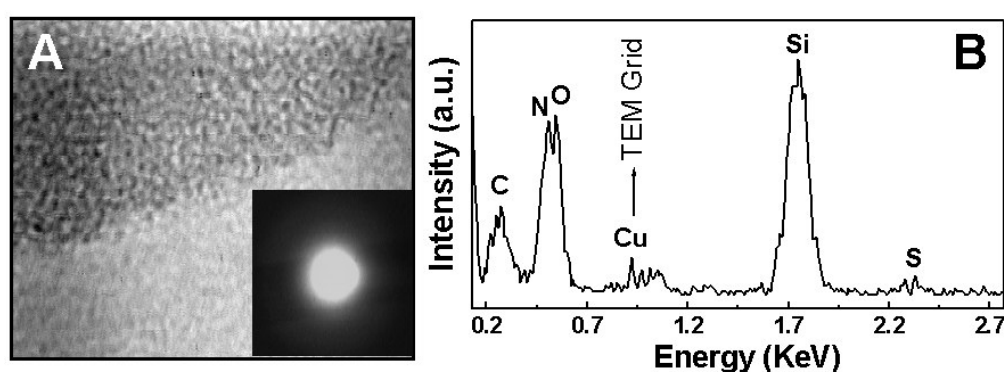


Figure 4.13 (A) HRTEM image of silica present in finely ground rice husk from which the EDX spectrum shown in (B) has been obtained. Inset in (A) shows the electron diffraction obtained from the region shown in main figure (A).

In order to preclude the possibility of leaching out of silica due to the acidic nature of the reaction medium, another control experiment was performed wherein the rice husk was kept in distilled water maintained at an acidic pH of 4.5 for 15 days and

the filtrate obtained was thereafter characterized by FTIR spectroscopy and TEM. We observed that characteristic Si–O–Si vibrational modes [28] of silica as well as signatures from silicic acid (Si–OH vibrational modes) [27] were clearly missing in the control rice husk sample not exposed to the fungus (curve 1, Figure 4.11 A). In addition, the amide signatures arising from the extracellular fungal proteins were also missing from the fungus-deficient control sample (curve 1, Figure 4.11 A). No particles could be detected in the TEM micrographs of drop cast films from the control experiment.

4.3.8 Additional evidence for fungus-mediated biotransformation of amorphous silica into crystalline silica

In order to establish the universality in fungus-mediated room temperature biotransformation of amorphous silica into crystalline silica, commercially available standard amorphous silica (silica gel) was exposed to *F. oxysporum* and the reaction product obtained after 24 h of reaction was analyzed by FTIR and XRD (Figure 4.14). FTIR analysis of silica gel (Figure 4.14 A) shows that the previously discussed smaller peak *ca.* 950 cm^{-1} , which is generally observed only in amorphous silica (curve 1, Figure 4.14 A), is clearly missing after exposure of silica gel to the fungus (curve 2, Figure 4.14 A). In addition, after reacting with fungus, there is development of a shoulder towards the high wavenumber side of the 1100 cm^{-1} peak (curve 2, Figure 4.14 A). These results are similar to that observed in the case of rice husk when exposed to the fungus (curves 1–7, Figure 4.11 A), which clearly suggests that the fungus is capable of transforming amorphous silica gel into crystalline silica.

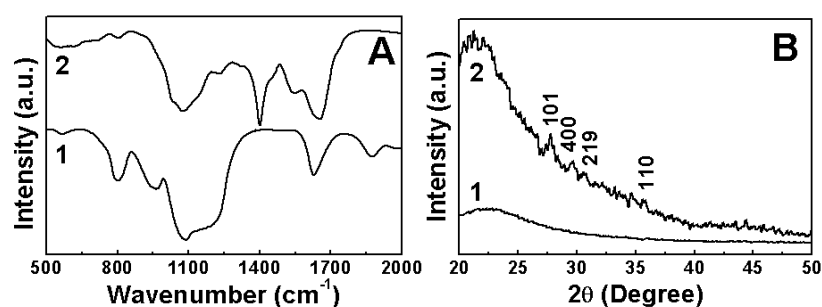


Figure 4.14 FTIR (A) and XRD (B) spectra recorded from standard amorphous silica (silica gel) before (curve 1) and after (curve 2) its exposure to *F. oxysporum* for 24 hours.

The proof of crystallinity is more evident by XRD analysis of silica gel (Figure 4.14 B), wherein amorphous silica gels do not show any Bragg reflections

before its exposure to the fungus (curve 1, Figure 4.14 B), while after exposure to the fungus, we observe the development of few diffraction planes in the form of Bragg reflections, which correspond to the quartz polymorph of silica (curve 2, Figure 4.14 B).

Thus, the control experiments and the TEM, FTIR and XRD results of the fungus–rice husk reaction medium clearly establish that specific biomolecules/proteins released by the fungus initially bioleach the amorphous silica from the rice husk and then biotransform this amorphous silica into crystalline silica particles.

4.3.9 Chemical analysis of bioleached silica

The chemical analysis of the biotransformed crystalline silica nanoparticles was performed by EDX (Figure 4.15 A) and XPS (Figure 4.15 B and C). Curve 1 in Figure 4.15 A shows the EDX spectrum from as-synthesized silica particles after 24 h of reaction. Curve 1a in the inset of the main figure shows the higher magnification region of the curve shown in main figure. The presence of the C signal along with Si and O signal suggests the presence of biomolecules occluded in the silica nanostructures (curves 1 and 1a, Figure 4.15 A). However EDX spectrum of calcined silica particles (curve 2, Figure 4.15 B) shows only Si and O signals, while C 1s signal is missing from silica particles after calcination, suggesting that most of the carbon is removed from the silica matrix after calcination at 400 °C for 2 h [compare curves 2a (calcined sample) with curve 1a (uncalcined sample)]. These results correlate well with the TEM results that show aggregation of silica particles after calcination due to removal of capping biomolecules from these structures (Figure 4.10 C).

A detailed chemical analysis of biotransformed silica particles was also performed by XPS, which is known to be a highly surface sensitive technique. Figure 4.15 B shows the Si 2p core level spectrum from the bioleached product, which could be resolved into two spin-orbit pairs (spin-orbit splitting ~ 0.6 eV) with 2p_{3/2} BEs of 100.5 eV (curve 1, Figure 4.15 B) and 103.3 eV (curve 2, Figure 4.15 C) respectively. The higher BE component at 103.3 eV agrees excellently with values reported for SiO₂ [32], while the lower BE component at 100.5 eV [33] can be assigned collectively to the signals arising from sub-oxidation states of silicon.

It is known that silicon suboxides (and hydroxides) show Si 2p_{3/2} binding energies in the region 100.5–102.5 eV [33]; attempts to resolve these suboxides failed due to small BE shifts between them. From the peak intensities of curve 2 (SiO₂) and curve 1 (silicon suboxides), it is observed that the amount of suboxides formed is extremely small indicating that most of the bioleached silica is in the form of SiO₂ nanoparticles. In addition to the Si 2p spectrum, the O 1s signal was also recorded in the sample (Figure 4.15 C) that shows a single relatively broad peak with a BE of 532.1 eV. Oxygen in the Si–O–Si environment has been reported to possess an O 1s BE of 532.3 eV [34] while oxygen in Si(OH)₄ has an O 1s BE of 531.9 eV [35]. We believe that both these components contribute to the XPS spectra shown in Figure 4.15 C.

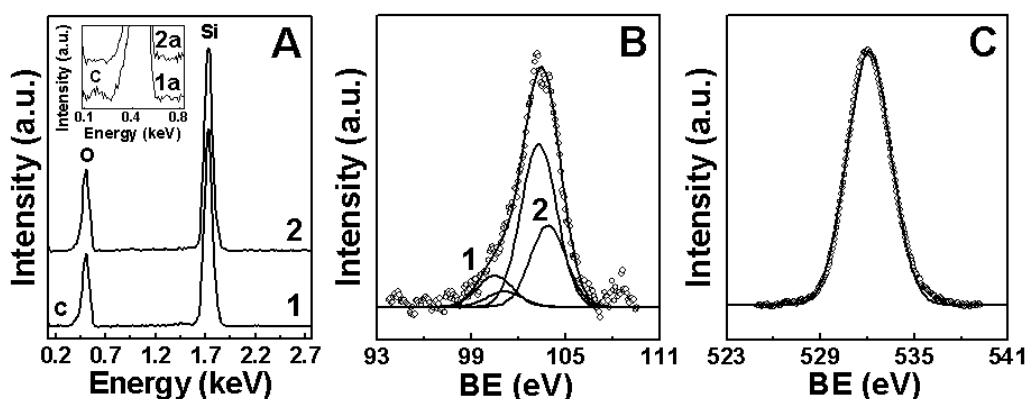


Figure 4.15 (A) EDX spectra recorded from silica particles synthesized by the exposure of rice husk to *F. oxysporum* for 24 h before (curves 1 and 1a) and after calcination at 400 °C for 2 h (curves 2 and 2a). Spectra 1a and 2a demonstrate the higher magnification of the spectra shown in spectra 1 and 2 respectively, showing the presence of C in uncalcined as-synthesized silica particles. (B and C) Si 2p (B) and O 1s (C) core level XPS spectra recorded from bioleached silica nanoparticles from fungus–rice husk after 24 h of reaction.

4.3.10 Protein analysis and *in vitro* silica bioleaching

In order to identify the biomolecules bound to silica nanoparticles, the purified silica particles were treated with ammonium fluoride, which selectively dissolves silica without causing significant harm to non-glycosylated proteins. The proteins occluded within the silica matrix, when analyzed using 12% SDS–PAGE, showed two low molecular weight proteins of around 15–20 kDa and a very high molecular weight protein of more than 200 kDa (Figure 4.16 A). It is likely that the low molecular weight proteins might be acting as hydrolyzing/capping proteins and that the high molecular weight proteins could be acting as a template for nanosilica synthesis. In order to understand the nature of these silica-bound proteins, the proteins obtained by ammonium fluoride treatment of bioleached silica were loaded

separately on DEAE–sephadex and CM–sephadex ion-exchange matrices. The unbound cationic and anionic protein fractions obtained respectively from DEAE–sephadex and CM–sephadex columns were loaded onto SDS–PAGE. Interestingly, the SDS–PAGE analysis showed that all the three protein bands were obtained in cationic fraction, whereas there was no protein band present in the anionic fraction. This indicates that the proteins involved in bioleaching process are cationic in nature. This result correlates well with our previous observations that when *F. oxysporum* is exposed to anionic oxide precursors, the fungus inducibly secretes low molecular weight cationic proteins, which are responsible for hydrolysis of oxide precursors (Section 3.2.8, Chapter 3). Other groups have also shown involvement of cationic proteins and peptides in the biosilicification process [11b, 14, 16a]. The new results obtained in this study further reaffirms our view that most of the proteins involved in the biosilicification process are cationic in nature.

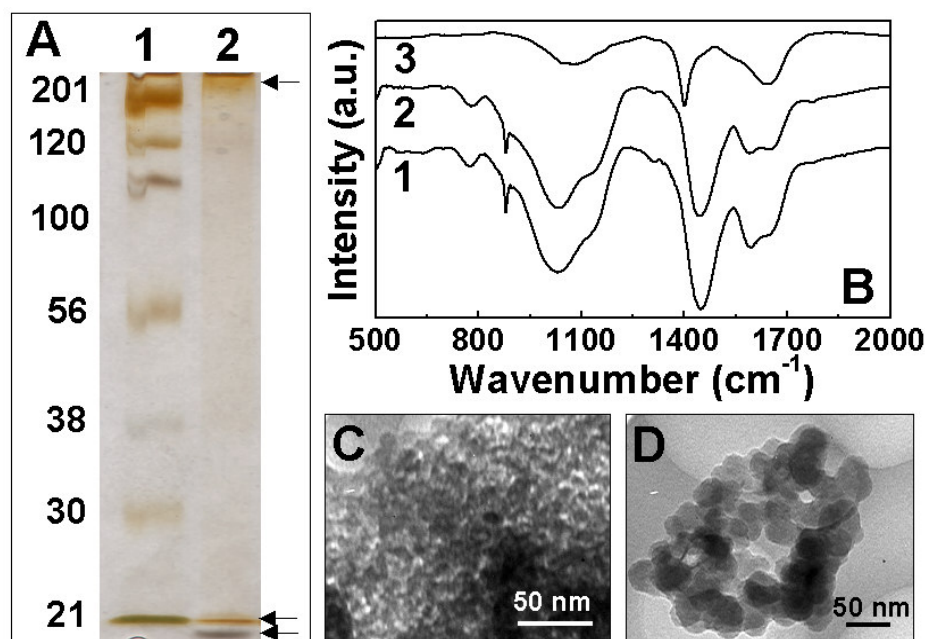


Figure 4.16 (A) 12% SDS–PAGE data showing extracellular fungal proteins bound onto the surface of silica particles, bioleached from rice husk using *F. oxysporum*. Lane 1 corresponds to the standard protein molecular weight markers with their molecular weights indicated in kDa. Lane 2 corresponds to the proteins bound to silica particles, obtained by mild dissolution of silica particles by ammonium fluoride treatment. (B) FTIR spectra of the reaction products from *in vitro* exposure of rice husk to total extracellular proteins (curve 1), cationic extracellular proteins (curve 2) and anionic extracellular proteins (curve 3) of *F. oxysporum*. (C and D) TEM images of silica particles formed under *in vitro* conditions using total extracellular proteins (C) and cationic extracellular proteins (D) from *F. oxysporum*.

To appreciate the role of extracellular fungal proteins in the silica bioleaching and biotransformation process, *in vitro* synthesis of silica particles from total

extracellular fungal proteins as well as from cationic and anionic fractions obtained was also monitored using FTIR, XRD and TEM analysis (Figure 4.16 B–D). FTIR spectra of silica particles synthesized using total extracellular fungal proteins (curve 1, Figure 4.16 B) and cationic extracellular protein fraction (curve 2, Figure 4.16 B) clearly indicate the bioleaching of silica from rice husk, as is evident from a peak at *ca.* 1050 cm⁻¹. Figure 4.16 C and D show the corresponding TEM images of silica particles synthesized using total extracellular protein fraction and cationic protein fraction respectively. It is worth mentioning that the reaction of rice husk with anionic fraction though depicted a low intensity broad signature close to 1100 cm⁻¹, no particles could be observed in TEM measurements. XRD measurements of these three *in vitro* reaction products were also performed, however XRD analyses of these samples revealed absence of any crystallinity in the material (data not shown). Absence of crystallinity in silica nanoparticles synthesized under *in vitro* conditions suggest that metabolic energy considerations in silica biotransformation process cannot be neglected and in addition to extracellular fungal proteins, fungal metabolism might also be playing some interesting role in imparting crystallinity to amorphous silica. The understanding of role of fungal metabolism would definitely be an issue of great interest in future investigations.

4.3.11 Summary

We have demonstrated that the fungus *Fusarium oxysporum* may be used to biotransform amorphous silica present in rice husk into highly crystalline silica nanoparticles. The silica synthesized is in the form of nanoparticles capped by stabilizing proteins in the size range 2 nm to 6 nm; that the nanoparticles are released into solution is an advantage of this process with significant application and commercial potential. Calcination of the silica nanoparticles leads to loss of occluded protein and eventually results in apparently porous structures often of cubic morphology. The amorphous silica particles can also be bioleached from rice husk under *in vitro* conditions using cationic extracellular proteins, however these proteins, stand alone, do not lead to biotransformation of amorphous silica into silica nanocrystallites. The room temperature synthesis of oxide nanomaterials using microorganisms starting from potential cheap agro-industrial waste materials like rice husk is an exciting possibility towards the large-scale synthesis of oxide nanomaterials.

4.4 Fungus-mediated two fold approach for selective bioleaching of silica and simultaneous enrichment of zirconia in zircon sand

4.4.1 Experimental details

The plant pathogenic fungus, *Fusarium oxysporum* was cultured as described in the experimental section of the previous chapter (Section 3.2.1, Chapter 3). Twenty grams (wet weight) of the harvested fungal biomass was suspended in 100 mL of sterile distilled water containing 10 g of zircon sand (zirconium silicate: $ZrSiO_4$) in 500 mL Erlenmeyer flasks and incubated on a shaker (200 rpm) at 25–28 °C. The reaction between the fungal biomass and zircon sand was carried out for a period of 24 h and the bioleached product was collected by separating the fungal mycelia and zircon sand from the aqueous component by filtration. The nanoparticle solution was rotary evaporated to obtain powder. Further characterization of these powders before and after calcination at 400 °C for 2 h were performed by Fourier transform infrared (FTIR) spectroscopy, X-ray diffraction (XRD) analysis, transmission electron microscopy (TEM), selected area electron diffraction (SAED) analysis and X-ray photoemission spectroscopy (XPS). Zircon sand used in this study was characterized using scanning electron microscopy (SEM), XRD and XPS.

XPS measurements of the bioleached product as well as zircon sand before and after its exposure to the fungus were performed. The Si 2p, Zr 3d and O 1s core level spectra for all the samples were recorded with an overall resolution of ~1 eV. The core level spectra were background corrected using the Shirley algorithm [30] and the chemically distinct species were resolved using a nonlinear least squares fitting procedure. The core level binding energies (BEs) were aligned with the adventitious carbon binding energy of 285 eV.

4.4.2 FTIR spectroscopy measurements

FTIR analysis of the bioleached product obtained from the fungus–zircon sand reaction medium showed the presence of bands at *ca.* 1100 cm^{-1} and 611 cm^{-1} (curve 1, Figure 4.17). The prominent 1100 cm^{-1} band can be assigned to the Si–O–Si [28] antisymmetric stretching mode present in the leached out product. Another distinct vibrational mode detected around 600 cm^{-1} is generally observed in sol-gel silica materials and can be assigned to some cyclic structures present in the silica

network. Yoshino *et al.* [36] have assigned this IR vibration to cyclic tetrameric siloxane species by referring to different types of cyclic siloxanes and silicate minerals, and this attribution has also been supported by molecular orbital calculations [37]. Two absorption bands at *ca.* 1650 cm^{-1} and 1540 cm^{-1} (amide I and II bands respectively; curve 1, Figure 4.17) attest to the presence of proteins in the quasi-spherical silica particles that have been released by the fungus during reaction with zircon sand.

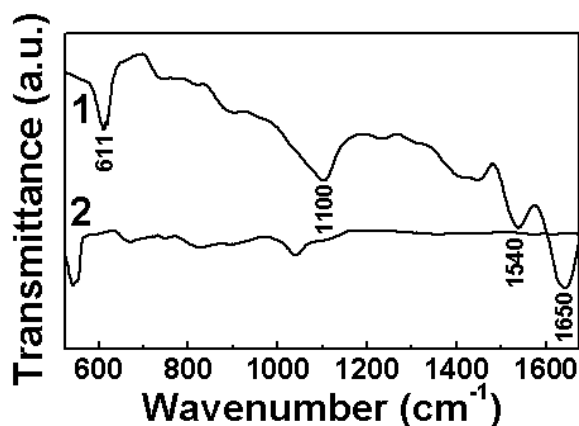


Figure 4.17 (A) FTIR spectra recorded from the filtrate containing silica particles synthesized by exposing zircon sand to *F. oxysporum* for 24 h (curve 1) and from the filtrate obtained by exposing zircon sand to water of pH 3.5 for 24 h (curve 2).

4.4.3 TEM and SAED measurements

The bioleached product obtained from the fungus-zircon sand reaction medium was analyzed by TEM. Figure 4.18 A and B show the representative TEM images recorded from the film of extracellular product obtained by the reaction of *F. oxysporum* with the zircon sand for 24 h (pH of the reaction medium ~ 3.5). The particles embedded in the biomolecular matrix are fairly regular in shape and depicts an overall quasi-spherical morphology, ranging in size from 2 nm to 10 nm. SAED analysis of the particle assemblies (inset, Figure 4.18 A) clearly indicates that they are crystalline in nature. The diffraction spots in the SAED pattern could be indexed based on the cristobalite polymorph of silica structure [38].

The FTIR results show the presence of proteins in the silica nanoparticle powders (curve 1, Figure 4.17). In order to remove the proteins that are intercalated/incarcerated into the silica structures, calcination of the silica powder was performed at $400\text{ }^{\circ}\text{C}$ for 2 hours. The calcined silica nanoparticle powder after redispersion in water was analyzed by TEM (Figure 4.18 C and D). It is observed that

the removal of incarcerated biomolecules by calcination leads to sintering of silica nanoparticles and consequently results in the formation of larger silica nanoparticles of average size 50–100 nm (Figure 4.18 C and D). The SAED pattern recorded from calcined silica nanoparticles (inset, Figure 4.18 D) clearly shows the crystalline nature of silica particles formed and could be indexed based on cristobalite polymorph of silica [38].

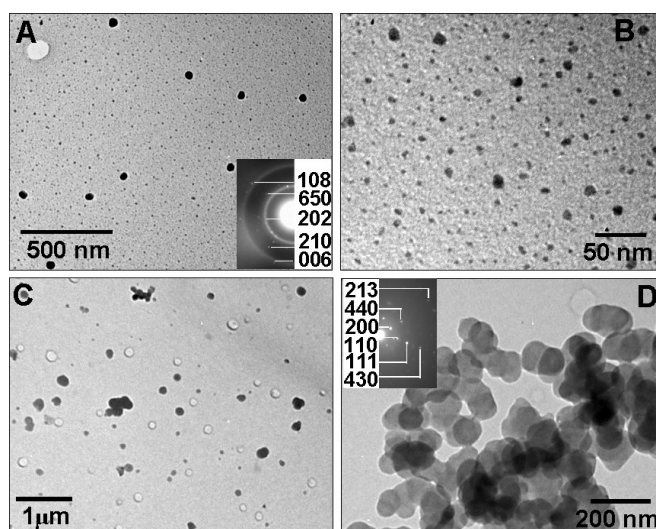


Figure 4.18 TEM micrographs of silica nanoparticles synthesized by the exposure of zircon sand to *F. oxysporum* before (A and B) and after calcination at 400 °C for 2 h (C and D). The insets in A and D are the SAED patterns recorded from representative silica nanoparticles.

4.4.4 XRD measurements

Additional evidence for the crystalline nature of the bioleached silica nanoparticles is provided by XRD analysis of the bioleached product formed by the fungus–zircon sand reaction medium (curve 1, Figure 4.19 A). The XRD pattern of as-formed silica nanoparticles shows well-defined Bragg reflections characteristics of cristobalite polymorph of crystalline silica [38]. The crystalline nature of bioleached silica nanoparticles indicates that the presence of entrapped proteins in the silica particles does not interfere much with their crystallinity. In addition, the bioleached silica nanoparticles, calcined at 400 °C for 2 h were also characterized by XRD (curve 2, Figure 4.19 A). The XRD analysis of the calcined powder further shows well-defined Bragg reflections characteristic of the cristobalite polymorph of silica nanoparticles (curve 2, Figure 4.19 A) [38]. It is obvious that calcination leads to removal of proteins from the silica matrix and hence results in increased crystallinity (curve 2, Figure 4.19 A) of silica particles in comparison with the as-synthesized silica nanoparticles (curve 1, Figure 4.19 A). Moreover, XRD pattern for zircon sand

used as a precursor in this study was also recorded as a control that exactly matches with zirconium silicate (ZrSiO_4) (Figure 4.19 B).

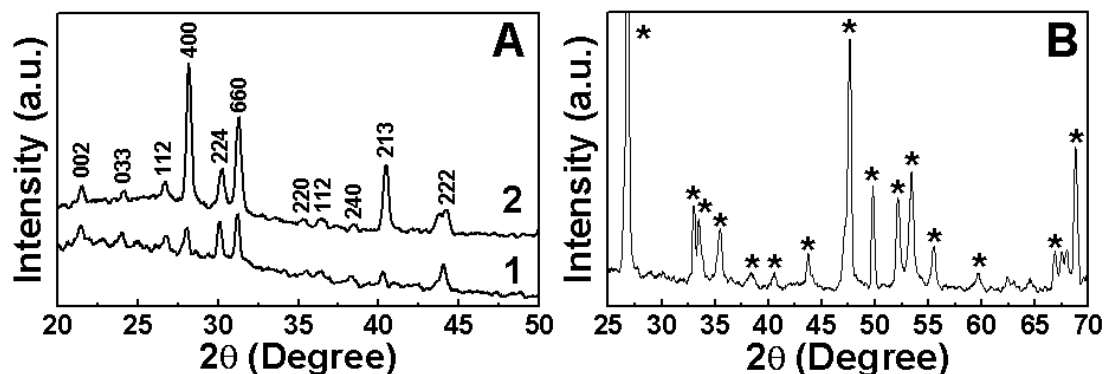


Figure 4.19 (A) XRD patterns recorded from silica particles synthesized by the exposure of zircon sand to *F. oxysporum* before (curve 1) and after calcination (curve 2) of particles at 400 °C for 2h. (B) XRD pattern recorded from zircon sand used as a precursor material in the bioleaching process. (*) represent the diffraction peaks that correspond to zircon (ZrSiO_4).

4.4.5 Control experiment

In order to preclude the possibility of leaching out of silica due to the acidic nature of the reaction environment, a control experiment was performed wherein the zircon sand was kept in distilled water maintained at an acidic pH of 3.5 for 24 h and the filtrate obtained was characterized by FTIR spectroscopy and TEM. We observe that the characteristic Si–O–Si vibrational modes [28] of silica as well as signatures from silicic acid (Si–OH vibrational modes) [27] were clearly missing in the control zircon sand sample not exposed to the fungus (curve 2, Figure 4.17). In addition, the amide I and II signatures arising from the extracellular fungal proteins in the zircon sand, exposed to the fungus (curve 1, Figure 4.17) were also missing from the fungus-deficient control sample (curve 2, Figure 4.17). No particles could be detected in TEM analysis of the control experiment.

The control experiment and the FTIR, TEM, SAED and XRD results of the fungus–zircon sand reaction medium clearly suggest that *F. oxysporum* selectively leaches out silicon component of zircon sand in the form of extracellular crystalline silica nanoparticles and does not cause the leaching of zirconium counterpart of zircon sand.

4.4.6 XPS analysis of bioleached product

A chemical analysis of the nanoparticles bioleached from zircon sand was performed by XPS (Figure 4.20). Figure 4.20 shows the Si 2p spectrum which could

be fitted into a single spin-orbit pair (spin-orbit splitting ~ 0.6 eV) [39] with a $2p_{3/2}$ BE of 103.5 eV (Figure 4.20 A). The BE component at 103.5 eV agrees excellently with values reported for SiO_2 [40].

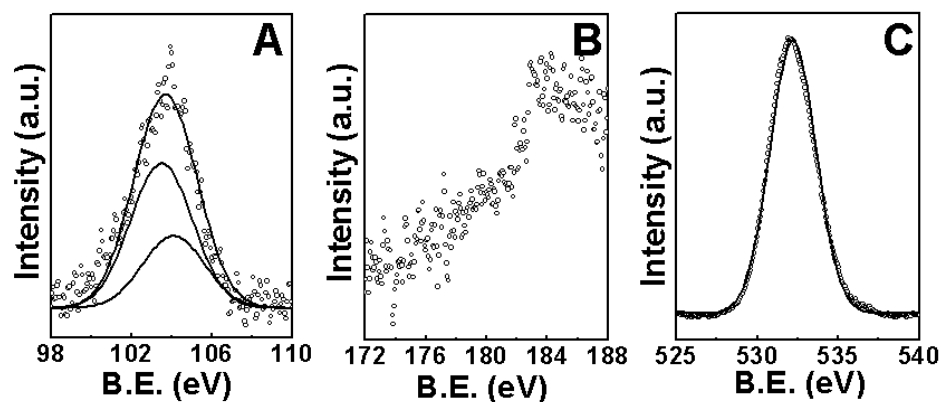


Figure 4.20 XPS data showing the Si 2p (A), Zr 3d (B) and O 1s (C) core level spectra recorded from silica nanoparticle bioleached from zircon sand. The raw data are shown in the form of symbols, while the chemically resolved components are shown as solid lines in the figure and are discussed in the text.

In addition to the Si 2p spectrum, the sample was also scanned for Zr 3d signal, however we could not detect the Zr 3d signal arising from the sample (Figure 4.20 B). Besides, the O 1s signal was also recorded in the sample (Figure 4.20 C) that shows a single BE component at 532.2 eV. Oxygen in the Si–O–Si environment is known to show O 1s BE component at 532.5 eV [39]. Similarly, oxygen in Si(OH)_4 shows O 1s BE component at 531.9 eV [23b]. We believe that both these components contribute to the XPS spectra shown in Figure 4.20 C and hence illustrating an O 1s BE component at *ca.* 532.2 eV. Notably, we do not observe any lower BE component at *ca.* 530.1 eV arising from ZrO_2 [39]. The absence of Zr 3d signal and O 1s signal corresponding to Zr–O further supports the selective bioleaching of silica nanoparticles from zircon sand.

4.4.7 XPS analysis of zircon sand

A chemical analysis of zircon sand before and after exposure to the fungus *F. oxysporum* was also performed by XPS (Figure 4.21). The Si 2p and Zr 3d core level spectra from finely ground zircon sand before (Figure 4.21 A and C) and after its reaction with the fungus (Figure 4.20 B and D) were recorded. Figure 4.21 A shows the Si 2p spectrum from zircon sand before its reaction with the fungus, which could be fitted into a single spin-orbit pair (spin-orbit splitting ~ 0.6 eV) [39] with $2p_{3/2}$ BE of 102.2 eV (Figure 4.21 A) which matches excellently with Si $2p_{3/2}$ BE in Zr–O–Si

phase as reported previously [39]. The Si 2p XPS analysis of zircon sand after its reaction with the fungus (Figure 4.21 B) leads to attribution of two distinct chemical species of Si atoms by resolving the Si 2p spectra into two spin-orbit pairs with $2p_{3/2}$ BEs of 98.4 and 102.1 eV respectively (curves 1 and 2 respectively, Figure 4.21 B). The higher BE component at 102.1 eV (curve 1, Figure 4.21 B), which is slightly lower than that observed in zircon sand before reaction with fungus (Figure 4.21 A) is predominant in the spectra and again can be assigned to Si $2p_{3/2}$ BE of Si present in silica–zirconia network [39], whereas an extremely feeble BE component at 98.4 eV (curve 2, Figure 4.21 B) can be assigned to non-network bonded Si atoms that apparently precipitate in the zirconium silicate network [41].

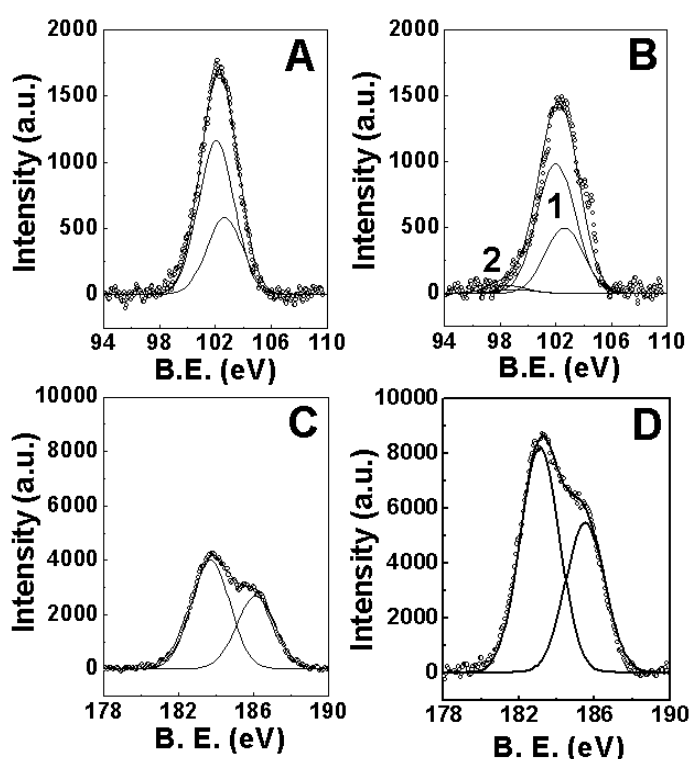


Figure 4.21 XPS data showing the Si 2p (A and B) and Zr 3d (C and D) core level spectra recorded from zircon sand before (A and C) and after its exposure to *F. oxysporum* (B and D). The raw data are shown in the form of symbols, while the chemically resolved components are shown as solid lines in the figure and are discussed in the text.

Zircon sand was also analyzed for the Zr 3d signal before and after reaction with the fungus. Figure 4.21 C shows the Zr 3d spectrum from zircon sand before reaction with the fungus, which could be fitted into a single spin-orbit pair (spin-orbit splitting ~ 2.4 eV) [39] with $3d_{5/2}$ BE of 183.7 eV (Figure 4.21 C). The 183.7 eV BE component can be assigned to Zr $3d_{5/2}$ BE of Zr present in silica–zirconia network [23b]. The Zr 3d spectrum from zircon sand after reaction with the fungus was also

analyzed and could be fitted to a single spin-orbit pair with $3d_{5/2}$ BE of 183.1 eV (Figure 4.21 D). It is apparent that reaction of zircon sand with the fungus results in a 0.6 eV reduction in Zr $3d_{5/2}$ BE in the zircon sand (183.7 eV in Figure 4.21 C vs. 183.1 eV in Figure 4.21 D). Our results match well with the previous reports where Zr $3d_{5/2}$ in ZrO_2 has been shown to be more than 0.5 eV lower than in $ZrSiO_4$ [42]. In addition, it has also been shown previously that successive reduction in silica content in SiO_2 - ZrO_2 alloys results in consecutive reduction of Si 2p and Zr 3d binding energies [23b]. The reduction of Si 2p and Zr 3d BEs by 0.1 eV and 0.6 eV respectively after reaction of zircon sand with the fungus, thus can be explained on the basis of reduction in silica content in zircon sand, as a consequence of silica bioleaching. The difference in the drop of Si 2p and Zr 3d BEs after reaction (0.1 and 0.6 eV respectively) is consistent with the principle of electronegativity equalization, *i.e.* the charge transfer out of Zr is larger in $ZrSiO_4$ than in ZrO_2 because electronegativities of Si and O are each larger than that of Zr [43].

The XPS analysis of zircon sand before and after reaction with the fungal biomass clearly suggests the enrichment of zirconia component in zircon sand. In order to quantitatively comprehend the enrichment of zirconium component in zircon sand, the Zr:Si ratios in zircon sand before (Figure 4.21 A and C) and after reaction with the fungal biomass (Figure 4.21 B and D) were calculated taking the integrated values of the respective fitted curves into account. The Zr:Si ratios in zircon sand before and after exposure to the fungus were found to be *ca.* 3.06 and 6.52 respectively. We therefore estimate that selective bioleaching of silica nanoparticles from zircon sand results in about 110% increase in zirconium component in zircon sand.

4.4.8 SEM analysis of zircon sand

Important information on the bioleaching process could be obtained by imaging the texture of the zircon sand particles before and after its reaction with the fungus *F. oxysporum*. Few sand grains were fixed on a double-sided conducting tape and were imaged by SEM. Figure 4.22 A and B show SEM images of the zircon sand grains before and after exposure to the fungus respectively. It is evident from the SEM images that the sand grains surface is relatively smooth before exposure (Figure 4.22 A), which then becomes rough after exposure to the fungus (Figure 4.22 B).

The roughening of the surface of the grain of sand after reaction with the fungus can be attributed to the leaching out of silica from zircon sand in the form of nanoparticles by the fungus.

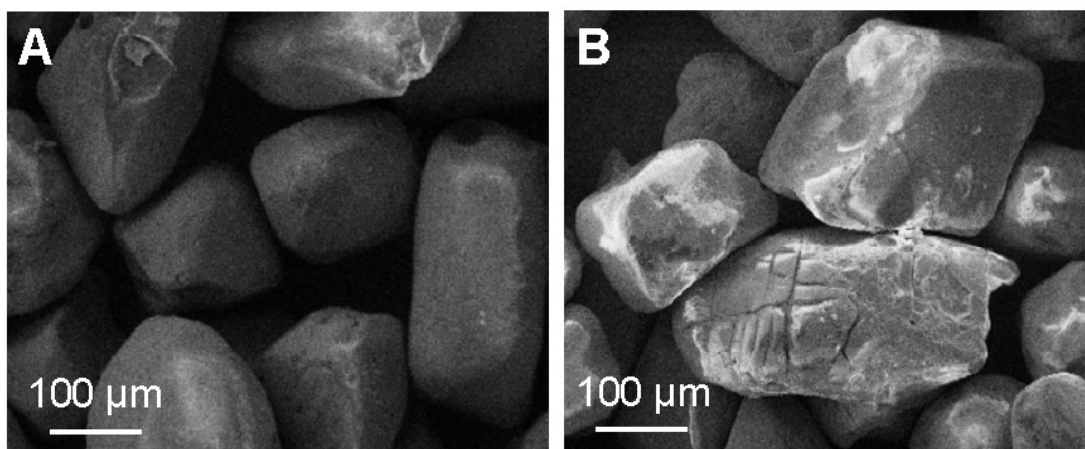


Figure 4.22 SEM micrograph of zircon sand grains before (A) and after (B) their exposure to *F. oxysporum* for 24 hours.

4.4.8 Summary

In summary, we have demonstrated that the fungus *Fusarium oxysporum* may be used for selective bioleaching of silica present in zircon sand. The silica synthesized is in the form of crystalline nanoparticles capped by stabilizing proteins in the size range 2 nm to 10 nm and is released into solution by the fungus. It appears that the fungal enzymes involved in the silica bioleaching act specifically on silica precursors present in zircon sand and they do not act on zirconium component of the precursor. We have shown previously in section 4.2 of this chapter that the proteins secreted by the fungus *F. oxysporum* act on silicates to convert them into silicic acid; and then silicic acid, on further condensation by fungal proteins, gets converted into silica nanoparticles. We believe that silica nanoparticles from the zirconium silicate present in zircon sand are being leached out by a similar mechanism, which provides selectivity and specificity to this reaction. In addition, the observation that the selective bioleaching of silica from zircon sand results in significant enhancement of zirconium component in zircon sand within 24 h of reaction is very interesting and has potential commercial implications. Therefore, this two-fold approach, which results into silica nanoparticles at room temperature as well as quality enhancement of raw material used in terms of enrichment of zirconia in zircon sand is an exciting possibility towards the large-scale synthesis of nanomaterials.

4.5 Conclusions

In conclusion, in this chapter, we have shown a fungus-based bioleaching approach towards the room-temperature synthesis of oxide nanoparticles using cheap naturally available raw materials (white sand and zircon sand) as well as agro-industrial by-products (rice husk). We believe that this approach can be extended towards extracting nanomaterials from other minerals present in large quantity in natural environments. The room-temperature bioleaching of oxide nanomaterials using microorganisms is an exciting possibility and could lead to eco-friendly and economically viable methods towards the large-scale synthesis of oxide nanomaterials of technological interests.

4.6 References

- [1] a) Ehrlich, H. I. *Chem. Geol.* **1996**, *132*, 5. b) Munch, J. C.; Ottow, J. C. G. *J. Soil. Sci.* **1980**, *129*, 15. c) Wierzchos, J.; Ascaso, C. *Clays Clay Miner.* **1996**, *44*, 652.
- [2] Natarajan, K. A. *Biogeochemistry of Rivers in Tropical South and South East Asia*, Ittekkot, V.; Subramanian, V.; Annadurai, S. (eds.) SCOPE, Sonder band, Heft **1999**, *82*, 55.
- [3] Henderson, M. E. K; Duff, R. B. *J. Soil. Sci.* **1963**, *14*, 237.
- [4] Rawlings, D. E. *J. Ind. Microbiol. Biotechnol.* **1998**, *20*, 268.
- [5] Mulligan, N.; Kamali, M. *J. Chem. Tech. Biotechnol.* **2003**, *78*, 497.
- [6] Valix, M.; Usai, F.; Malik, R. *Mater. Engg.* **2001**, *14*, 197.
- [7] a) Epstein, E. *Proc. Natl. Acad. Sci. USA* **1994**, *91*, 11. (b) Patwardhan, S. V.; Clarson, S. J.; Perry, C. C. *Chem. Commun.* **2005**, 1113.
- [8] Lucas, Y.; Luizao, F. J.; Rouiller, J.; Nahon, D. *Science* **1993**, *260*, 521.
- [9] a) Treguer, P.; Nelson, D. M.; Van Benkom, A. J.; DeMaster, D. J.; Leynaert, A.; Queguiner, B. *Science* **1995**, *268*, 375. b) Alexandre, A.; Meunier, J. D.; Colin, F.; Koud, J. M. *Geochim. Cosmochim. Acta* **1997**, *61*, 677. c) Derry, L. A.; Kurtz, A. C.; Ziegler K.; Chadwick, O. A. *Nature* **2005**, *433*, 728.
- [10] Barber, D. A.; Shone, G. T. *J. Exp. Bot.* **1966**, *17*, 569.

- [11] a) Mitzutani, A. J.; Nagase, H.; Fujiwara, N.; Ogoshi, H. *Chem. Soc. Jpn.* **1998**, *71*, 2017. b) Kroger, N.; Deutzmann, R.; Bergsdorf, C.; Sumper, M. *Proc. Natl. Acad. Sci. USA* **2000**, *97*, 14133. c) Sumper, M.; Kroger, N. *J. Mater. Chem.* **2004**, *14*, 2059.
- [12] a) Pohnert, G. *Angew. Chem. Int. Ed.* **2002**, *41*, 3167. b) Swift, D. M.; Wheeler, A. P. *J. Phycol.* **1992**, *28*, 202.
- [13] Hecky, R. E.; Mopper, K.; Kilham, P.; Degans, E. T. *Mar. Biol.* **1973**, *19*, 323.
- [14] Shimizu, K.; Cha, J.; Stucky, G. D.; Morse, D. E. *Proc. Natl. Acad. Sci. USA* **1998**, *95*, 6234.
- [15] Cha, J. N. *et al.*, *Proc. Natl. Acad. Sci. USA* **1999**, *96*, 361.
- [16] a) Kroger, N.; Deutzmann, R.; Sumper, M. *Science* **1999**, *286*, 1129. b) Kroger, N.; Lorenz, S.; Brunner, E.; Sumper, M. *Science* **2002**, *298*, 584.
- [17] Harrison, C. C. *Phytochemistry* **1996**, *41*, 37.
- [18] Tacke, R. *Angew. Chem. Int. Ed.* **1999**, *38*, 3015.
- [19] a) Kroger, N.; Deutzmann, R.; Sumper, M. *J. Biol. Chem.* **2001**, *276*, 26066. b) Kroger, N.; Deutzmann, R.; Bergsdorf, C.; Sumper, M. *Proc. Natl. Acad. Sci. USA* **2001**, *97*, 14133.
- [20] Kroger, N.; Bergsdorf, C.; Sumper, M. *Eur. J. Biochem.* **1996**, *239*, 259.
- [21] a) Kroger, N.; Wetherbee, R. *Protist* **2000**, *151*, 263. b) Kroger, N.; Lehmann, G.; Rachel, R.; Sumper, M. *Eur. J. Biochem.* **1997**, *250*, 99.
- [22] Schultz, T. F.; Egerton-Warburton, L.; Crawford, S. A.; Wetherbee, R. *Protist* **2001**, *152*, 315.
- [23] a) Mann, S. *Nature* **1993**, *365*, 499. b) Oliver, S.; Kupermann, A.; Coombs, N.; Lough, A.; Ozin, G. A. *Nature* **1995**, *378*, 47. c) Mann, S.; Ozin, G. A. *Nature* **1996**, *382*, 313. d) Mann, S.; Webb, J.; Williams, R. J. P. (eds.) *Biom mineralization: Chemical and Biochemical Perspectives*, Wiley VCH, Weinheim, Germany **1998**. e) Lowenstam, H. **1981**, *Science* *211*, 1126.
- [24] a) Simpson, T. L.; Volcani, B. E. (eds.) *Silicon and Siliceous Structures in Biological Systems*, Springer-Verlag, New York **1981**. b) Levi, C.; Barton, J. L.;

- Guillemet, C.; Bras, E. Le; Lehuède, P. *J. Mater. Sci. Lett.* **1989**, *8*, 337. c)
Westall, F.; Boni, L.; Guerzoni, E. *Palaeontology* **1995**, *38*, 495.
- [25] a) Lootens, D.; Vautrin, C.; Damme, H. V.; Zemb, T. *J. Mater. Chem.* **2003**, *13*, 2072. b) Hubert, D. H. W.; Jung, M.; Fredrik, P. M.; Bomans, P. H. H.; Meuldijk, J.; German, A. L. *Adv. Mater.* **2000**, *12*, 1286. c) Pevzner, S.; Regev, O.; Lind, A.; Linden, M. *J. Am. Chem. Soc.* **2003**, *125*, 652. d) Lind, A.; Spliethoff, B.; Linden, M. *Chem. Mater.* **2003**, *125*, 652. e) Hentze, H. P.; Raghavan, S. R.; McKelvey, C. A.; Kaler, E. W. *Langmuir* **2003**, *19*, 1069.
- [26] a) Cha, J. N.; Stucky, G. D.; Morse, D. E.; Deming, T. J. *Nature* **2002**, *403*, 289.
b) Patwardhan, S. V.; Clarson, S. J. *Silicon Chemistry* **2002**, *413*, 291.
- [27] Silverstein, R. M. *Spectrometric Identification of Organic Compounds*, 2nd edition, John Wiley & Sons **1967**.
- [28] Innocenzi, P.; Falcaro, P.; Grosso, D.; Babonneau, F. *J. Phys. Chem B.* **2003**, *107*, 4711.
- [29] The XRD patterns were indexed with reference to the crystal structures from the *ASTM* charts: silica (*ASTM* chart card no. 5–0490).
- [30] Shirley, D. A. *Phys. Rev. B* **1972**, *5*, 4709.
- [31] The XRD patterns were indexed with reference to the crystal structures from the *PCPDF* charts: silica (*PCPDF* card nos. 46–1045 and 40–1498).
- [32] Oya, A.; Beguin, F.; Fujita K.; Benoit, R. *J. Mater. Sci.* **1996**, *31*, 4609.
- [33] Graham, M. J. *Corrosion Sci.* **1995**, *37*, 1377.
- [34] Barr, T. L. *J. Phys. Chem.* **1978**, *82*, 1801.
- [35] Mink, G. *et al.*, *Surface Interface Analysis* **1988**, *12*, 527.
- [36] Yoshino, H.; Kamiya, K.; Nasu, H. *J. Non-Cryst. Solids* **1990**, *126*, 68.
- [37] Hayakawa, S.; Hench, L. L. *J. Non-Cryst. Solids* **2000**, *262*, 264.
- [38] The XRD and SAED patterns were indexed with reference to the crystal structures from the *PCPDF* charts: silica (*PCPDF* card nos. 03–0272, 32–0993, 45–0112 and 45–0131).

- [39] Seo, K. I.; McIntyre, P. C.; Kim, H.; Saraswat, K. C. *Appl. Phys. Lett.* **2005**, *86*, 082904.
- [40] Wagner, C. D. *J. Vac. Sci. Technol.* **1978**, *15*, 518.
- [41] Carriere, B.; Brion, D.; Escard, J.; Deville, J. P. *J. Electron. Spectrosc. Relat. Phenom.* **1977**, *10*, 85.
- [42] Guittet, M. J.; Crocombette, J. P.; Gautier-Soyer, M. *Phys. Rev. B* **2001**, *63*, 125117.
- [43] Sanderson, R. T. *Chemical Bonds and Bond Energy*, Chapter 2, Academic Press, New York **1971**.

CHAPTER V

Visible Light Induced Photo-oxidative Dye Degradation and Antimicrobial Applications of Non-metals Doped Biogenic Titania Nanoparticles

This chapter discusses the diffused indoor light and solar light excited photo-oxidative and antimicrobial activity of a new class of biogenic anatase titania, which is considerably modified with nitrogen, carbon and fluorine simultaneously (NCF-TiO₂). NCF-TiO₂ nanoparticles are capable of photodegrading the environmentally toxic azo dye Congo Red as well as arylmethane dyes, Malachite Green and Basic Fuchsin, under indoor and solar light conditions. NCF-TiO₂ nanoparticles have been shown to possess antimicrobial and antisporulation activity under indoor light conditions. In addition, the mechanism of photo-oxidative action of NCF-TiO₂ on fungal spores has also been explored by atomic force microscopy (AFM).

Part of the work presented in this chapter has been published/communicated:

1) Bansal, V.; Ahmad, A.; Sastry, M. *Nat. Nanotechnol.* **2006** (communicated).

5.1 Introduction

Titania, one of the most popular photocatalysts, has long been investigated for photocatalytic degradation of organic pollutants [1], antimicrobial activity [2], photocatalytic dissociation of water [3], and solar energy conversion [4] *etc.* Among brookite, rutile and anatase phases of TiO_2 , anatase is considered to be the most efficient phase for carrying out photocatalytic reactions [5]. However, the efficiency of TiO_2 based photocatalytic reactions for daylight-induced applications like degradation of organic pollutants is hampered by the fact that due to its band gap of around 3.1 eV, TiO_2 has a photothreshold that extends from the ultraviolet region into the solar spectrum to only about 400 nm, which comprises of < 10% of the solar spectrum [5]. Moreover artificial UV light sources are somewhat expensive. TiO_2 also has potential indoor applications like degradation of microorganism in clinical surroundings and inhibiting microbial growth in damp areas. This is important, since the widespread use of antibiotics have led to the emergence of more resistant and virulent strains of microorganisms, which poses an urgent need to develop alternative sterilization technologies [6, 7]. The TiO_2 photocatalytic process is a conceptually feasible technology, however, most of the studies on antimicrobial applications of TiO_2 indicate that TiO_2 photocatalyst is effective only upon excitation with UV light [8–14] at levels that would induce serious damage to plants, animals and human cells, which greatly restricts its potential applications in our living environments [12, 15]. Therefore, the increasing demand for such applications, coupled with the fact that TiO_2 has inherent large band gap characteristics, have fueled a great deal of research in lowering the threshold energy for TiO_2 excitation – to utilize a larger fraction of solar spectra.

Earlier investigations have dealt with doping of TiO_2 with transition metals and in very few cases, the resulting materials were active under visible light irradiation [16]. Also, surface modification with transition metal halide complexes afforded a type of hybrid semiconductor that was active in diffused indoor daylight [17–21]. Asahi *et al.*, first presented the idea of reducing band gap edge of anatase TiO_2 by doping with anionic species based on density of states (DOS) calculations [22]. Later, substitutional doping or modification of TiO_2 with nonmetals such as nitrogen [23–29], carbon [30–31], sulfur [32–34] or fluorine [35–37] was found to

degrade the organic molecules on excitation with visible light [38]. Very recently, N-doped TiO₂ has been shown to exhibit visible light induced bactericidal activity [15].

Despite the numerous efforts towards the development of visible light-active, single nonmetal-doped TiO₂ involving use of some well-planned and complicated syntheses procedures, to the best of our knowledge, there are no previous reports of visible light-induced photoactivity in biogenic TiO₂ nanoparticles, wherein nonmetals like nitrogen, carbon and fluorine are simultaneously doped in TiO₂ during its synthesis. We had previously shown that titania nanoparticles can be synthesized under ambient conditions using hexafluoro precursors in the presence of fungus *Fusarium oxysporum*, wherein hydrolyzing proteins get entrapped in biogenic oxides during their synthesis (discussed in Chapter 3) [39]. In this chapter, we address above discussed issues and show by detailed surface studies of biogenic titania that nitrogen and carbon from proteins get substitutionally doped into TiO₂ lattices during calcination. Additionally, fluoride ions from the precursor solution also bind to the surface of TiO₂ particles. This, in turn, results in a new class of anatase TiO₂ based nanomaterial, which is considerably modified with N, C and F simultaneously (hereafter referred as NCF-TiO₂), and hence exhibit a combined effect of these nonmetals in the form of enhanced photoactivity with a reduction in band gap edge to 2.2 eV, that extends photoabsorption of NCF-TiO₂ throughout the visible region and well into the near-infrared (NIR) region.

The enhanced photoactivity of NCF-TiO₂ has been explored for indoor and solar-light photocatalysis applications, in terms of degradation of organic dyes like Congo Red, Malachite Green and Basic Fuchsin, which represent a group of extensively used organic pollutants, posing an increasing environmental threat [40]. In addition, antimicrobial and antispore effect of NCF-TiO₂ is also shown against a range of microorganisms including Gram-negative and Gram-positive bacteria, fungi, actinomycetes, alkalothermophiles and plant as well as human pathogens. A plausible mechanism of NCF-TiO₂ action for destruction of fungal spores has been explored by AFM studies. The body of data suggests a possible and effective approach towards the degradation of toxic organic pollutants in wastewaters and degradation of a range of harmful microbes in the environment. This chapter describes “*Photo-oxidative and antimicrobial activity of biogenic NCF-TiO₂ nanoparticles under indoor and solar light conditions.*”

5.2 Photo-oxidative and antimicrobial activity of biogenic NCF-TiO₂ nanoparticles under indoor and solar light conditions

5.2.1 Experimental details

The titania nanoparticles were synthesized by reaction of 1 mM K₂TiF₆ with the fungus *Fusarium oxysporum* for 24 h and characterized by Fourier transform infrared (FTIR) spectroscopy, transmission electron microscopy (TEM) analysis, selected area electron diffraction (SAED) analysis, X-ray diffraction (XRD) analysis, thermogravimetric analysis (TGA) and electron dispersive X-rays (EDX) analysis, as described in the section 3.2 of chapter 3. The biogenic TiO₂ particles, thus obtained were precipitated by centrifugation (15000 rpm for 30 min) and dried to powder. The TiO₂ powder was further calcined at 300 °C for 3 h as well as 500 °C for 2 h and characterized by XRD analysis, XPS and Ultraviolet-Visible-NIR (UV-Vis-NIR) spectroscopy. The TiO₂ powder obtained after calcination at 500 °C for 2 h has been referred to as NCF-TiO₂ throughout the text. Standard commercial anatase TiO₂ powder (May and Baker Ltd., England) was analyzed by XRD and used as a control in photoactivation studies.

In XPS analysis of NCF-TiO₂ particles, N 1s, C 1s, F 2p, Ti 2p and O 1s core level spectra were recorded with un-monochromatized Mg K_α radiation (photon energy = 1253.6 eV) at a pass energy of 50 eV and electron takeoff angle (angle between electron emission direction and surface plane) of 60°. The overall resolution was 1 eV for the XPS measurements. The core level spectra were background corrected using the Shirley algorithm [41] and the chemically distinct species were resolved using a nonlinear least square fitting procedure. The core level binding energies (BEs) were aligned with the adventitious carbon binding energy of 285 eV. For optical studies, as-synthesized biogenic TiO₂ as well as calcined TiO₂ nanoparticles were separately dispersed in water, followed by ultrasonication (30 min) and their absorbance spectra were recorded in the range 250–1250 nm using Jasco dual beam UV-vis-NIR spectrophotometer (model V-570).

For studying the photocatalytic effect of NCF-TiO₂ nanoparticles in terms of their ability to degrade azo dye Congo Red (CR), the aqueous solutions containing CR (100 mg/L), along with various concentrations of NCF-TiO₂ nanoparticles (0 µg/ml, 50 µg/ml, 125 µg/ml, 250 µg/ml and 500 µg/ml) were exposed to different

light conditions (UV light, indoor light and solar light). All the reactions were performed in quartz tubes. For UV light exposure, reactions were performed in the home-made photocatalytic reactor and illuminated with a UV lamp source (400 Watts, emission maxima 280 nm, Hanovia, USA) at a distance of 1 m; for diffused indoor daylight, the tubes were placed near to window in the laboratory; and for solar light exposure, experiments were performed on a bright sunny day in an open space from 09:00 to 16:00 hours. After 16:00 hours, white light illumination from 40 W sources at a distance of 4 m was used as a source of indoor light. The CR degradation during the course of reaction (1 h, 3 h, 5 h, 7 h) was followed by recording its optical absorbance maxima at 510 nm, while establishing a baseline data set with CR solutions exposed directly to various light conditions without addition of any TiO₂. The baseline correction was followed in order to account for some possible degradation of CR under direct effect of light. The optical absorbance of dye during the reaction was monitored using Jasco dual beam UV–Vis–NIR spectrophotometer. Similarly, photo-oxidative effect of NCF–TiO₂ nanoparticles (50 µg/ml) on aqueous solutions of arylmethane dyes Malachite Green (100 mg/L) and Basic Fuchsin (100 mg/L) after excitation with solar light for 3 h was also studied.

For studying the antimicrobial potential of NCF–TiO₂ nanoparticles, the particles were dispersed in sterile water upto a final concentration of 1 mg/ml. The commercially available anatase TiO₂ particles (May and Baker Ltd., England) dispersed in sterile water to a final concentration of 10 mg/ml were used as control. The Gram–negative bacterial strains *viz.* *Escherichia coli* and *Pseudomonas sp.*; the Gram–positive bacterial strains *viz.* *Bacillus sp.* and *Staphylococcus sp.*; the fungal strains *viz.* *Trichoderma sp.* and *Aspergillus niger*; and alkalothermophilic actinomycete *Thermomonospora sp.* were obtained from the National Collection of Industrial Microorganisms (NCIM), National Chemical Laboratory (NCL), Pune, India. Petri dishes (10 cm diameter) containing Potato Dextrose Agar (PDA) media were used for zone inhibition studies and all the experiments were performed in triplicates. All the microbial strains except *Thermomonospora sp.* were grown in PDA media of pH 6.8 at 28 °C, however *Thermomonospora sp.* was grown in PDA media of pH 10 at 50 °C. A 2.5 cm x 2.5 cm sterile filter paper was placed in the center of each Petri dish and 100 µl of TiO₂ solutions (10 mg per mL commercial TiO₂ or 1 mg per mL NCF–TiO₂) was added on the filter paper after spread plating the

bacterial colonies/fungal spores on PDA media. Petri dishes were kept in the laboratory close to the window, under diffused indoor daylight conditions for a period of 8 hours. After 8 h, white light illumination from 40 W sources at a distance of 4 m was used as a source of indoor light. Pictures of microbial growth were taken using a Nikon 4600 digital camera at an image resolution of 4 megapixels.

Atomic force microscopy (AFM) imaging of *Aspergillus* spores was performed using a VEECO Digital Instruments multimode scanning probe microscope equipped with a NanoScope IV controller. For sample preparation, fungal spores were dispersed in deionized water as well as in deionized water containing 50 $\mu\text{g/ml}$ NCF-TiO₂ in quartz tubes and kept under indoor light conditions. Samples were drop-cast on the Si (100) wafers at various time intervals after dispersion. The Si wafers containing fungal spores were attached to AFM metallic packs mounted on a 6399e-piezoscanner (10 μm) with conducting double-sided tape. For AFM imaging, 125 μm long etched silicon probes were used. Topography and phase images were collected in the tapping mode at a scanning frequency of 1 Hz.

5.2.2 XRD measurements

Since the photocatalytic response of TiO₂ strongly depends on its crystalline phase, the as-synthesized biogenic TiO₂ nanoparticles as well as TiO₂ powders calcined at 300 °C for 3 h and 500 °C for 2 h respectively were subjected to XRD measurements (Figure 5.1). A number of Bragg reflections characteristic of the brookite phase of TiO₂ (peaks marked with 'b') with a small percentage of the rutile phase of TiO₂ (peak marked with 'r') are evident in the XRD pattern obtained from the as-synthesized particles (curve 1, Figure 5.1 A). XRD analysis of the titania powder after calcination at 300 °C for 3 h indicates complete conversion of the rutile phase to brookite (peaks marked with 'b') as is evident from an increase in intensity of all the brookite peaks, along with disappearance of Bragg reflection corresponding to the rutile phase (curve 2, Figure 5.1 A). However, calcination of biogenic titania at 500 °C for 2 h (NCF-TiO₂; curve 3, Figure 5.1 A) results in transformation of most of the brookite and rutile phases to anatase (peaks marked as 'a'). An XRD pattern was also recorded from commercially available standard anatase for the sake of comparison (curve 4, Figure 5.1 A). It is evident from curves 3 and 4 that NCF-TiO₂

(curve 3, Figure 5.1 A) consists mainly of the anatase phase, which is considered to be most active phase for photocatalytic applications [5].

Since a few of the most intense Bragg's reflections in various phases of TiO₂ have very similar d-spacings, the XRD patterns plotted in Figure 5.1 A were finely resolved in the 2θ range of 25°–26° (Figure 5.1 B) and 53°–57° (Figure 5.1 C). The finely resolved spectra clearly establish the transformation of brookite phase into anatase after calcination at 500 °C for 2 h (curve 3, Figure 5.1 B and C). The d values obtained in the XRD patterns of titania particles match well with the standard d values of the brookite, rutile and anatase phases of TiO₂ [42].

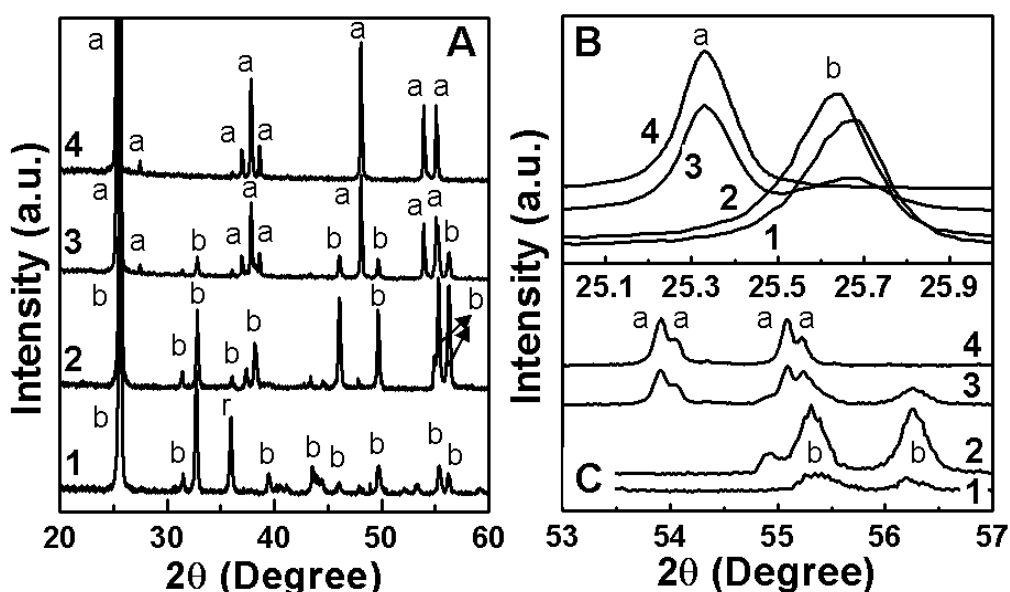


Figure 5.1 (A) XRD patterns recorded from as-synthesized biogenic titania nanoparticles (curve 1), titania nanoparticles after calcination at 300 °C for 3 h (curve 2), titania nanoparticles after calcination at 500 °C for 2 h (curve 3) and commercial anatase (curve 4). (B and C) Finely resolved XRD patterns in the region of 25°–26° 2θ (B) and 53°–57° 2θ (C). The peaks marked with 'r', 'b' and 'a' correspond to rutile, brookite and anatase phases of TiO₂ respectively.

When TEM measurements were performed on various titania particles, we observed that calcination leads to aggregation of TiO₂ particles and hence it was difficult to obtain the particle size by TEM. However, properties at nanoscale are determined by crystallite size, rather than virtual size of the particles. The crystallite size of as-synthesized as well as calcined titania samples were determined by the Debye–Scherrer's equation [43]:

$$D = 0.89 \lambda / \beta \cos \theta$$

where D is the crystal size (nm), λ is the wavelength of the X-ray radiation (nm), β is the full width at half maximum of the Bragg's peak (radian), and θ is the diffraction

angle. From the XRD analysis, the average crystallite size of as-synthesized biogenic TiO_2 (curve 1), titania calcined at 300 °C for 3 h (curve 2), titania calcined at 500 °C for 2 h (curve 3), and commercial anatase TiO_2 (curve 4, Figure 5.1) were calculated to be 12 nm, 35 nm, 40 nm and 75 nm respectively.

5.2.3 XPS measurements

Our previous studies have indicated that proteins get embedded in TiO_2 nanoparticles during their synthesis (discussed in Chapter 3) [39]. Calcination of TiO_2 nanoparticles at 500 °C for 2 h results in degradation of most of these proteins and it is highly possible that C and N from proteins might dope into TiO_2 lattices during calcination. A detailed chemical analysis of the calcined titania nanoparticles (NCF- TiO_2) was performed by XPS, which is considered to be a highly surface sensitive technique (Figure 5.2).

To investigate the N states in NCF- TiO_2 nanoparticles, N 1s core levels were measured using XPS, which indicated a weak and broad N 1s signal (Figure 5.2 A) that could be fitted into a single binding energy (BE) component at 398.2 eV. The N 1s core level BE of 398.2 eV in our study is greater than the typical N 1s core level BE of 397.2 eV in TiN [44], and therefore can be attributed to the N 1s BE in the O-Ti-N environment. This high BE shift in N 1s core levels can be understood by the fact that higher electronegative O atoms in Ti-N surrounding would reduce the local electron density on N atoms, and hence, would lead to an increase in N 1s BE in O-Ti-N. When N substitutes for O in the initial O-Ti-O structure in TiO_2 crystal, the electron density around N is reduced, compared to that in TiN, because of the presence of an O atom in close proximity of Ti atom. These observations suggest that N substitutes partially for O in the TiO_2 lattices to form O-Ti-N linkages, since any direct interaction between N and O within the lattice would significantly increase the BE of the N 1s core level and hence, any such direct interaction between N and O within the TiO_2 lattice is ruled out. Moreover, the observed N 1s BE component at 398.2 eV matches excellently with the recently observed N 1s core level in N doped TiO_2 , which was previously assigned to the anionic N^- in O-Ti-N linkages [45–46]. It is worth mentioning that the presence of N in the form of O-Ti-N linkages in TiO_2 lattice is extremely important considering the classic theoretical predictions as well as experimental studies conducted by Asahi *et al.*, wherein they emphasized

the importance of substitutional site N doping in significant increase in photocatalytic activity [22].

Although the N 1s core level XPS spectrum suggests the incorporation of N in the TiO₂ lattices, in a form favorable for photoactivity, we cannot rule out the incorporation of some carbon from the biomolecules involved in the titania formation process. To investigate the C states in calcined biogenic titania, C 1s core levels were measured using XPS, which could be fitted into two BE components at 283 eV and 285 eV respectively (Figure 5.2 B). The lower BE C 1s component at 283 eV (curve 1, Figure 5.2 B) is greater than the typical C 1s BE of 282.3 eV in TiC [47], and hence can be attributed to the C 1s BE in the O–Ti–C environment in the TiO₂ lattice, since one would expect the C 1s BE to be shifted towards higher BE in the presence of highly electronegative O atoms. The higher BE C 1s component at 285 eV (curve 2, Figure 5.2 B) may be assigned to the contribution from adventitious C [31]. These observations suggest that C also substitutes partially for O in the TiO₂ lattices to form O–Ti–C linkages.

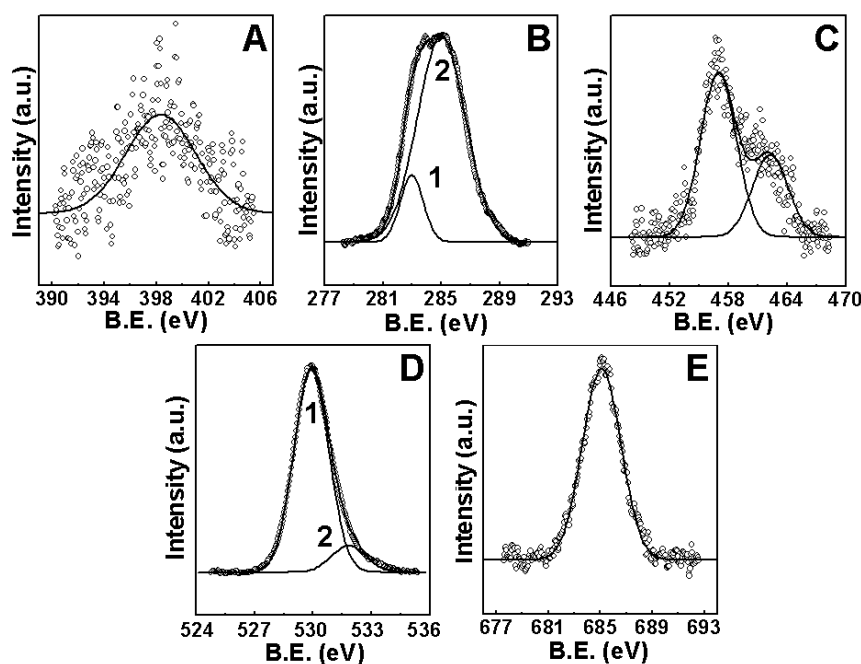


Figure 5.2 XPS data showing the N 1s (A), C 1s (B), Ti 2p (C), O 1s (D) and F 2p (E) core level spectra recorded from NCF–TiO₂ nanoparticles. The raw data is shown in the form of symbols, while the chemically resolved components are shown as solid lines and are discussed in the text.

The Ti 2p core level spectrum obtained from calcined biogenic titania could be fitted into a single spin–orbit pair (spin–orbit splitting ~ 5.3 eV) with 2p_{3/2} BE of 457 eV (Figure 5.2 C), which is lower than that previously reported for undoped

titania (459.3 eV) [45]; however the observed value (457 eV) lies in between the values reported for N-doped titania (458.5 eV) [45] and C-doped titania (455.5 eV) [47]. Lower BEs of Ti 2p core levels in C- and N-doped TiO₂ can be attributed due to significant increase in covalency of Ti in O–Ti–C and O–Ti–N bonds, in comparison with O–Ti–O bonds in undoped TiO₂ (Electronegativities: O > N > C). This implies that the substitution of O atom in O–Ti–O structure of TiO₂ lattice by N and C atoms would cause an increase in electron density around the Ti atom, and hence, would result in a lower Ti 2p BE in N-doped TiO₂, which will further reduce in C-doped TiO₂. The Ti 2p core level BE also supports the information obtained from N 1s and C 1s core levels, which also indicate the partial substitution of O in TiO₂ lattices by N and C to yield O–Ti–N and O–Ti–C linkages respectively.

The O 1s core level spectrum from calcined biogenic titania could be fitted to two BE components at 529.9 eV and 532.6 eV (Figure 5.2 D). The intense low BE O 1s component at 529.9 eV (curve 1) can be attributed to the core levels originating from O–Ti–O in TiO₂ lattice, while the higher BE O 1s component at 532.6 eV (curve 2) can be assigned to oxygen in the Ti–O–N structure in TiO₂ lattice, which has been found to be a consistent feature for N substitution in TiO₂ lattices [45, 48–49].

Since F⁻ doping/surface complexation can also significantly affect the photocatalytic properties of TiO₂ by altering the electron transfer paths at the water–semiconductor interface [22, 35–37], and in view of the fact that a fluorine based precursor (K₂TiF₆) was employed for the synthesis of NCF–TiO₂ nanoparticles [39], the F 1s core levels from NCF–TiO₂ were also investigated (Figure 5.2 E). The F 1s BE at 685.1 eV matches well with that previously observed for F⁻ ions adsorbed on TiO₂ surface, and no signature of F⁻ ions in the TiO₂ lattice (BE ≥ 688.5 eV) was observed [36–37]. The surface fluorination of TiO₂ is expected in view of previous pH dependent studies wherein the surface coverage of TiO₂ by F⁻ ions was found to be highest at pH 3.6 (pH of precursor solution in our study ~ 3.5) [36].

Hence, the detailed XPS analysis of NCF–TiO₂ nanoparticles (Figure 2) not only establishes the partial substitutional doping of N and C in anatase TiO₂ lattices (in the form of O–Ti–N and O–Ti–C structures), it also demonstrate TiO₂ surface complexation with F⁻ ions. Previous efforts on modulating the electronic and photocatalytic properties of TiO₂ with anions have dealt with using a single anionic species at a time, wherein doping with C, N, or F individually has been seen to shift

the photoactivity of TiO₂ in visible region [22–31,35–37]. However, we, for the first time observe the modification of anatase TiO₂ nanoparticles by the simultaneous association of N, C and F (hence referred as NCF–TiO₂), which might have important implications in photocatalysis.

5.2.4 UV–Vis–NIR absorbance spectroscopy measurements

The presence of C, N and F in TiO₂ can significantly affect the photoabsorption characteristics of TiO₂ nanoparticles, as shown in Figure 5.3. The UV–Vis–NIR absorption spectrum of as-synthesized TiO₂ particles shows significant absorption at wavelengths shorter than 400 nm, which correspond to band gap edge at 3.2 eV (curve 1, Figure 5.3) and can be assigned due to the collective intrinsic absorption from brookite (>3.2 eV) and rutile titania (~3.0 eV) [50]. This is supported by XRD data, which shows a mixture of brookite and rutile phases in the as-synthesized titania powders (curve 1, Figure 5.1 A). The absorption of as-synthesized particles extends well upto 500 nm, which might be due to the complexation of biomolecules with TiO₂ particles that can extend the absorption of TiO₂ particles in the visible region. After calcination at 300 °C for 3 h, the absorption spectrum of TiO₂ particles shows a strong absorption throughout the visible range, and a red shift of 0.4 eV in the band gap transition is observed with a band gap edge at 2.8 eV (curve 2, Figure 5.3). Further calcination of biogenic TiO₂ particles at 500 °C for 2 h (NCF–TiO₂) results in enhancement of absorption in UV as well as visible region, accompanied with a significant red shift of 1.0 eV in the band gap transition,

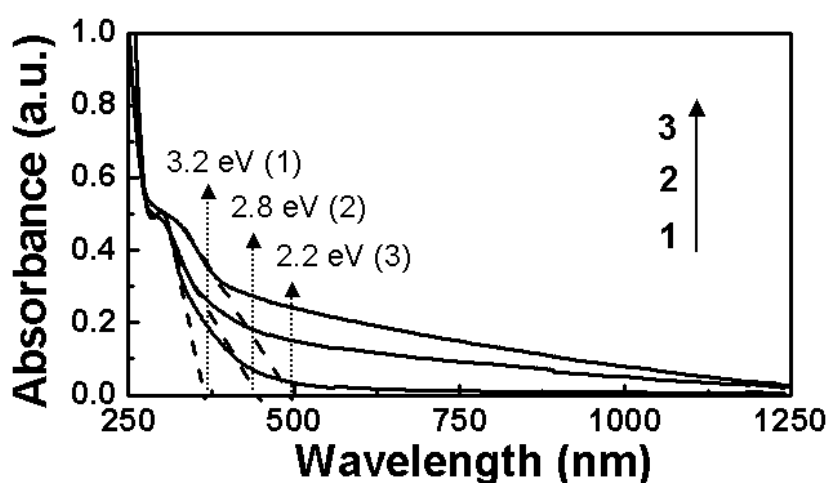


Figure 5.3 UV–Vis–NIR absorbance spectra recorded from as-synthesized biogenic TiO₂ nanoparticles (curve 1), and after their calcination at 300 °C for 3 h (curve 2) and 500 °C for 2 h (curve 3) respectively. The solid lines show the main spectra, the dashed lines represent the tangent drawn to find out band edges of respective spectra, as indicated by the dotted lines.

which leads to a band gap edge at 2.2 eV (curve 3, Figure 5.3). In addition, a very strong absorption throughout the visible region, extending upto the NIR region is observed in calcined titania samples (curves 2 and 3, Figure 5.3), which can be assigned to the contribution of lower energy states arising due to the simultaneous presence of C and N in TiO₂ lattices, as well as surface complexation of TiO₂ with F⁻ ions, as is evident from XPS studies (Figure 5.2). It is observed that as-synthesized biogenic titania does not show considerable absorption in visible region, however, calcination at increasing temperatures leads to significant enhancement in visible region absorbance (compare curves 1–3, Figure 5.3), which can be attributed to the increase in doping levels in calcined samples [33]. The increase in doping levels after calcination may be explained on the basis of the fact that calcination would lead to degradation of biomolecules entrapped in TiO₂ structures, and hence would result in doping of C and N from degraded biomolecules into TiO₂ lattices. The broad absorbance of biogenic NCF–TiO₂ nanoparticles throughout the solar spectra is a significant advance over previous studies on single anionic species–doped TiO₂, where, even though modification of TiO₂ particles with either of these anionic impurities (C, N or F) has helped in red shift of band gap edge, it could not extend the absorption beyond 735 nm [22–31, 35–37].

As observed, the long-range absorbance of biogenic NCF–TiO₂ nanoparticles is an important result, which will enable the use of biogenic titania nanoparticles in visible light photocatalytic applications and to compete favorably with chemical methods that require immense efforts to shift the band gap of titania in the visible region for similar applications.

5.2.5 Photo-oxidative degradation of organic pollutants

Organic dyes represent an important class of organic pollutants, among which azo (Congo Red) and arylmethane (Malachite Green and Basic Fuchsin) class of dyes are highly toxic to the environment. For instance, Malachite Green has been classified as Class II health hazard in developed countries like Canada, because of its potential lung tumor hazard [51]. However due to low manufacturing cost, these dyes are still used in textile and paper industries in certain countries with less restrictive laws, and hence polluting the aquatic ecosystem [52]. Although several physico-chemical methods have been used to eliminate the colored effluents in

wastewater, they are generally expensive, have limited applicability and produce large amounts of sludge [53]. Therefore, interest is now focused on devising an efficient technology for degradation of these toxic dyes. We have used photodegradation of organic dyes as an index reaction for evaluating the efficiency of NCF-TiO₂ photocatalyst. The chemical structures of Congo Red (CR), Malachite Green (MG) and Basic Fuchsin (BF) dyes used in our study have been shown in Figure 5.4.

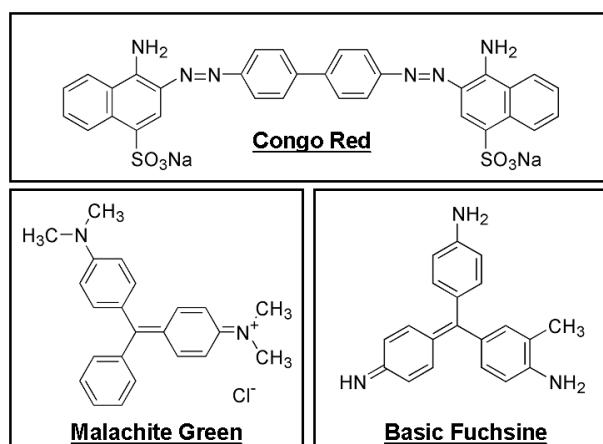


Figure 5.4 Chemical structures of Congo Red, Malachite Green and Basic Fuchsin dyes drawn using ChemDraw software.

Among many factors, the photocatalytic response of TiO₂ also depends on excitation wavelength, excitation duration and on the concentration of photocatalyst. In order to study the excitation wavelength-dependent response of NCF-TiO₂ photocatalyst (Figure 5.5), the aqueous solutions of CR (100 mg/L) containing NCF-TiO₂ (50 µg per ml of CR) were exposed to same intensity (400 Watts) source at wavelengths of 500 nm, 350 nm and 280 nm for 30 min, and the absorbance spectra of the CR solutions were recorded. It is clear from Figure 5.5 that excitation at 280 nm results in maximum degradation of CR dye (curve 4) as compared to control CR solution, which was kept in dark (curve 1). Excitation at 350 nm (curve 3) results in reduced photodegradation of CR as compared to that at 280 nm (curve 4), which further reduces on excitation at 500 nm (curve 2). These results are in accordance with the absorbance spectrum of NCF-TiO₂ photocatalyst (curve 3, Figure 5.3), which indicates that the photocatalyst shows maximum absorbance at around 280 nm, which consecutively reduces towards the higher wavelength side and hence leads to reduced activity of the photocatalyst on excitation with higher wavelength light. However, the observation that the excitation at any of these wavelengths (curves 2–4, Figure 5.5) results in significant photodegradation of CR solutions is interesting and

may lead to more efficient utilization of solar irradiation for photocatalytic applications.

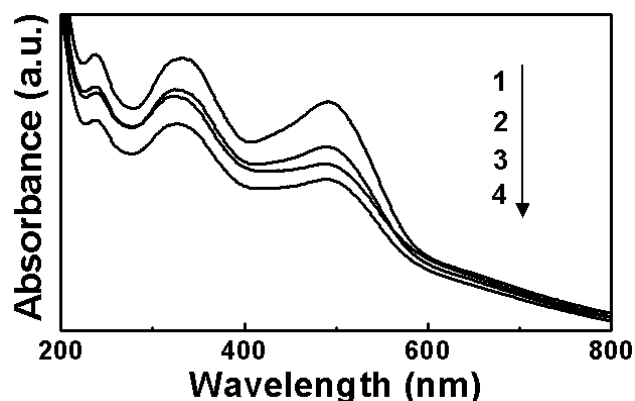


Figure 5.5 Photoabsorption of aqueous solutions of Congo Red dye (100 mg/L) in the presence of 50 µg/ml NCF-TiO₂, kept in dark for 30 min (curve 1) and after 30 min exposure to lights of wavelength 500 nm (curve 2), 350 nm (curve 3) and 280 nm (curve 4) respectively.

In order to study the concentration-dependent photocatalytic response of NCF-TiO₂ photocatalyst, the aqueous solutions of CR (100 mg/L) containing varying concentrations of NCF-TiO₂ (0, 50, 125, 250 and 500 µg per ml of CR) were exposed to solar irradiation for 3 h, and the absorbance spectra of the CR solutions were recorded (Figure 5.6). It is evident from Figure 5.6 that an increase in the concentration of photocatalyst from 50 µg/ml to 500 µg/ml (curves 2–5, Figure 5.6) leads to a monotonous increase in CR photodegradation, as compared to control CR solution, which was exposed to solar irradiation for 3 h without addition of any photocatalyst (curve 1, Figure 5.6). This indicates that photocatalytic response of NCF-TiO₂ also depends on its concentration in the photocatalytic reactions.

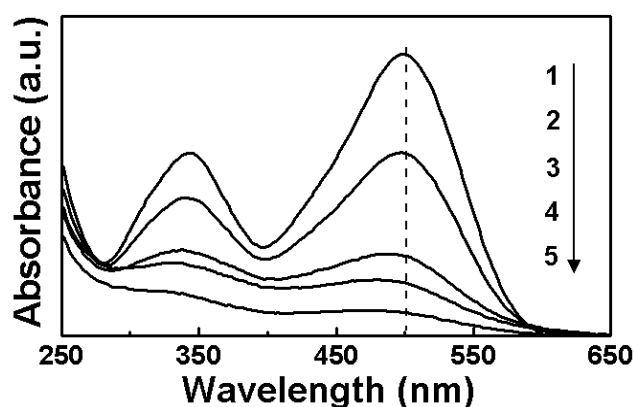


Figure 5.6 Photoabsorption of aqueous solutions of Congo Red dye (CR – 100 mg/L) in the presence of various concentrations of NCF-TiO₂ viz. 0 µg/ml (curve 1), 50 µg/ml (curve 2), 125 µg/ml (curve 3), 250 µg/ml (curve 4) and 500 µg/ml (curve 5) on exposure to solar light for 3 h.

In order to understand the combined effect of concentration of NCF-TiO₂ photocatalyst, photoexcitation source and photoexcitation time, the aqueous solutions of CR (100 mg/L) were exposed to UV light, sunlight as well as diffused indoor room light conditions with varying concentrations of NCF-TiO₂ (0, 50, 125, 250 and 500 µg per ml of CR) for varying time intervals (1, 3, 5 and 7 h), and the absorbance maxima of CR were recorded at 510 nm. The discoloration response of CR dye on exposure to NCF-TiO₂ nanoparticles was calculated using the following equation:

$$\% \text{Discoloration} = \frac{[(\text{Initial Absorbance}) - (\text{Absorbance After Treatment})]}{(\text{Initial Absorbance})} \times 100$$

During the photo-oxidative degradation of CR, it was observed that NCF-TiO₂ particles cause maximum degradation of CR in the presence of sunlight followed by diffused indoor light and UV light respectively (Figure 5.7). This result correlates well with our photoabsorbance studies of NCF-TiO₂ particles, which indicate that these particles absorb throughout the solar spectrum, and hence result in enhanced photoactivity in solar light (curve 3, Figure 5.7).

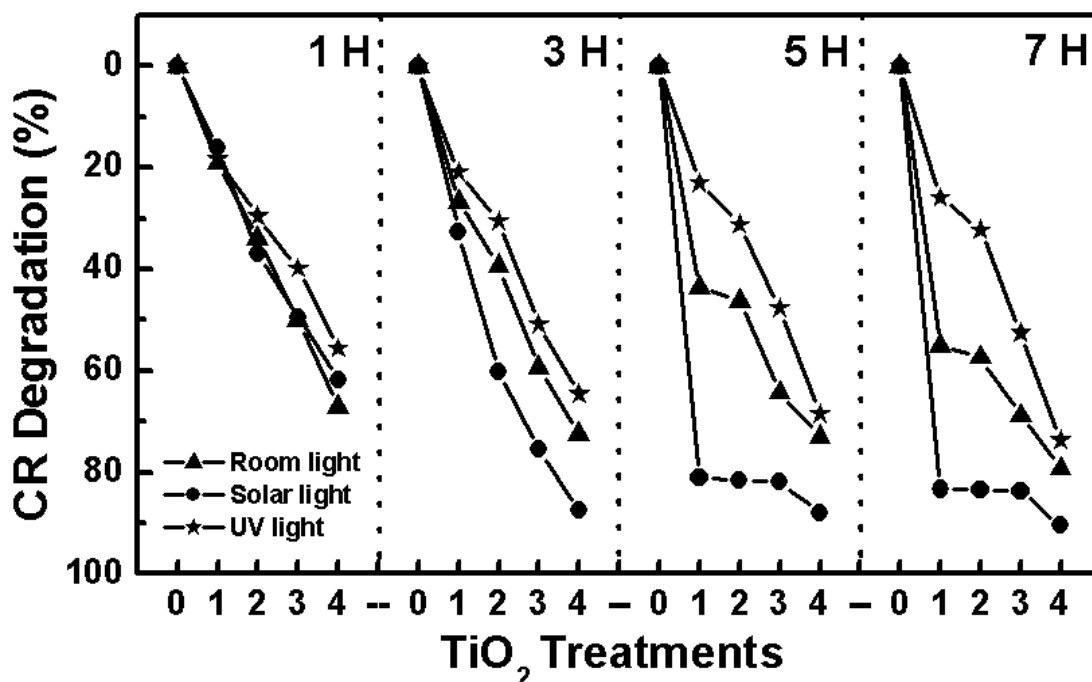


Figure 5.7 Photodegradation of aqueous solutions of Congo Red dye (100 mg/L) in the presence of various concentrations of NCF-TiO₂ treatments (indicated on x-axis) viz. 0 µg/ml (treatment 0), 50 µg/ml (treatment 1), 125 µg/ml (treatment 2), 250 µg/ml (treatment 3) and 500 µg/ml (treatment 4) on exposure to UV light (*), diffused room light (▲) and solar light (●). The % CR degradation has been shown in terms of % reduction in absorbance maxima of CR at 510 nm after various NCF-TiO₂ treatments.

It is also evident from photo-oxidation studies that exposure of CR to even lower concentration of TiO_2 (50 $\mu\text{g/ml}$) in the presence of solar light for 5 h results in more than 80% CR degradation, and a further increase in TiO_2 concentration upto 250 $\mu\text{g/ml}$ or its prolonged exposure to solar light upto 7 h does not significantly increase CR degradation; however, a higher concentration of TiO_2 (500 $\mu\text{g/ml}$) causes more than 90% photodegradation of CR within 3 h of its exposure to sunlight (Figure 5.7).

In order to understand the mechanism of photo-oxidation of CR by NCF- TiO_2 , CR was exposed to various concentrations of NCF- TiO_2 in dark, wherein we do not observe any detectable adsorption of CR to TiO_2 particles (data not shown). This can be explained based on the fact that anionic CR dye molecules (pH 4.5) will experience a electrostatic repulsion from the TiO_2 particles, which are known to be negatively charged at $\text{pH} > 3$, as determined by Zeta-potential measurements previously [54]. Moreover, surface complexation of titania particles with highly electronegative F^- is further expected to inhibit the adsorption of CR on TiO_2 surface [36]. Though, capability of F^- -modified NCF- TiO_2 to significantly photo-oxidize unadsorbed CR dye appears contrary to the previous studies wherein preadsorption of dye molecules to F^- -undoped TiO_2 was found to be an important parameter for enhanced photocatalytic activity [55], our results correlate well with a recent study on photocatalytic activity of F^- -doped TiO_2 where it was observed that photo-oxidative degradation of various substrates in F^- - TiO_2 suspensions is promoted within the solution (not on the surface) through the enhanced generation of free/mobile hydroxyl radicals, because direct hole trapping or the generation of surface-bound hydroxyl radicals is not allowed on the fluorinated surfaces [36]. Similar mechanism seems to operate in degradation of CR by NCF- TiO_2 particles with the involvement of free hydroxyl radicals.

The effect of NCF- TiO_2 photocatalyst was also studied on arylmethane dyes Malachite Green (Figure 5.8 A) and Basic Fuchsine (Figure 5.8 B). Similar to Congo Red, Malachite Green and Basic Fuchsine dyes also degrade in the presence of NCF- TiO_2 nanoparticles on exposure to solar light for 3 h. These results suggest that NCF- TiO_2 nanoparticles can be used for degradation of a wide range of environmentally toxic organic dyes, present in the industrial effluents.

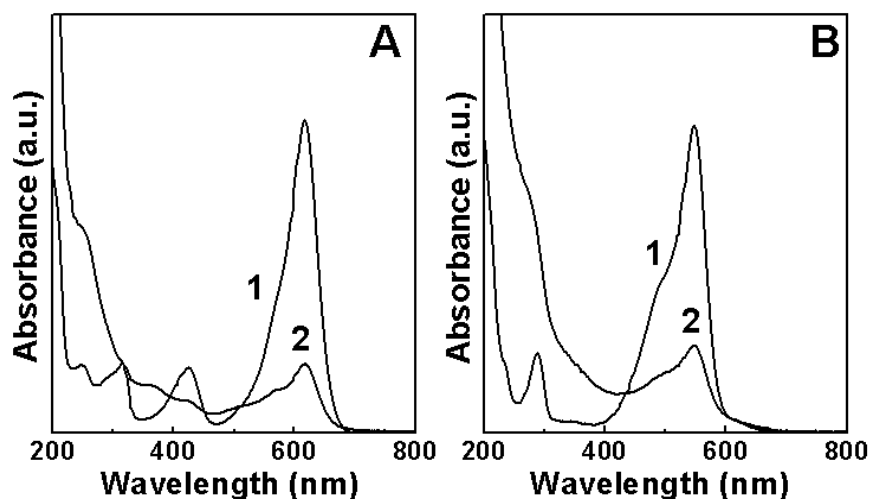


Figure 5.8 Photoabsorption of aqueous solutions of Malachite Green (A) and Basic Fuchsin (B) dyes exposed to solar light for 3 h in the absence (curves 1) and presence of 50 µg/ml NCF-TiO₂ nanoparticles (curves 2).

5.2.6 Antimicrobial activity by zone inhibition assays

Since we have observed a strong photo-oxidative efficiency of NCF-TiO₂ nanoparticles in terms of dye degradation even under diffused indoor light conditions, it is reasonable to believe that the NCF-TiO₂ photocatalyst might be applied for the control of various harmful microbes in our living environment. To investigate the antimicrobial activity of NCF-TiO₂ photocatalyst, zone inhibition assays were carried out on PDA plates under diffused indoor light conditions, for a range of microorganisms including Gram-negative and Gram-positive bacteria, fungi as well as extremophilic actinomycete (Figure 5.9–5.11). The microbial variants used in this study include *Escherichia coli* (a human pathovar responsible for colitis in human stomach); *Pseudomonas* sp. (responsible for spoilage of unpasteurized dairy products); *Bacillus* sp. (a sporulating spoilant of preserved foods); *Staphylococcus* sp. (a wound infecting agent); *Trichoderma* sp. (human skin pathogenic fungus); *Aspergillus niger* (an isolate from damp walls responsible for plant mildews and highly challenging to control) and *Thermomonospora* sp. (an extremophilic/alkalothermophilic isolate from hot sulfur springs). It is clear from Figure 5.9 that application of NCF-TiO₂ nanoparticles (100 µl of 1 mg/mL solution) does not allow microorganisms to grow in the surroundings, which is evident in the form of halo/clearance zones in the center of the Petri plates (Figure 5.9 A2–F2), however application of even 10 times higher doses of commercial anatase TiO₂ (100 µl of 10 mg/mL solution) does not lead to microbial inhibition under indoor light

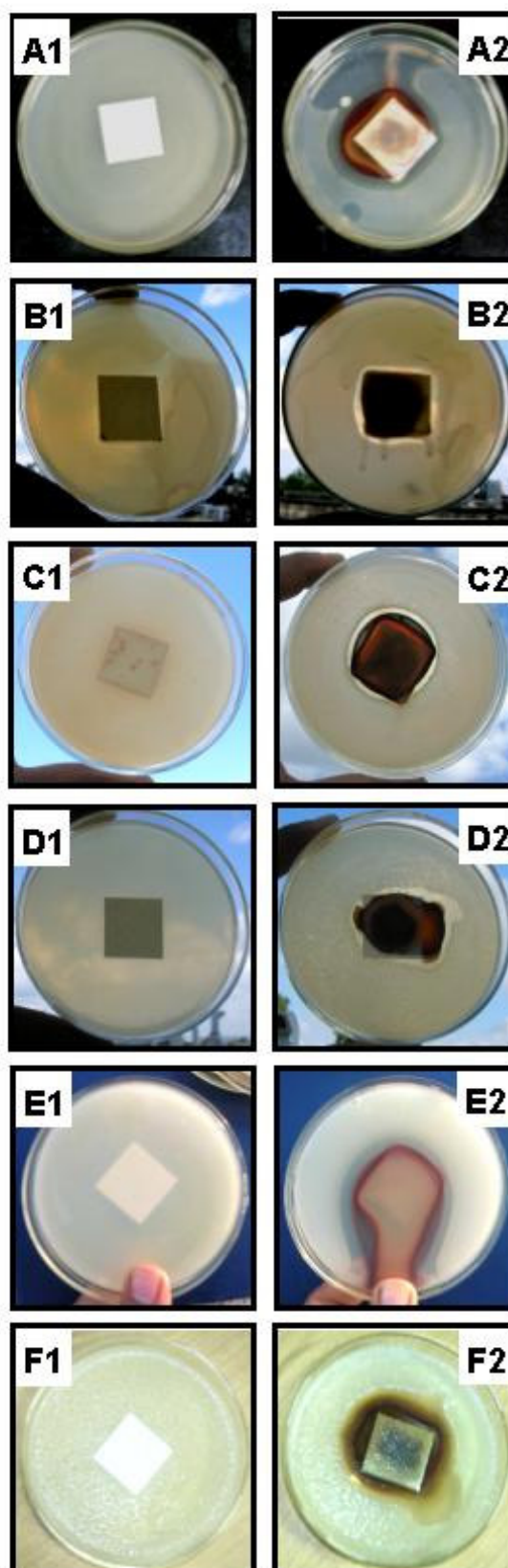


Figure 5.9 Antimicrobial activity of undoped commercial anatase TiO₂ (A1–F1) and NCF–TiO₂ nanoparticles (A2–F2) exhibited in terms of inhibition zones on exposure to *Escherichia coli* (A1–A2), *Pseudomonas* sp. (B1–B2), *Bacillus* sp. (C1–C2), *Staphylococcus* sp. (D1–D2), *Trichoderma* sp. (E1–E2) and *Thermomonospora* sp. (F1–F2) under indoor light conditions for 24 h.

conditions, showing a continuous growth of microbes (Figure 5.9 A1–F1). The broad-spectrum antimicrobial activity of NCF–TiO₂ nanoparticles in visible light is significant considering the huge potential of TiO₂ based materials for a variety of antimicrobial applications [2, 8–15].

Aspergillus niger consists of a very complex cell envelope structure and is extremely difficult to control even with strong antifungal agents. Previous efforts to control *A. niger* with undoped TiO₂ did not result in much success, even after prolonged exposure to UV light [12]. The effect of undoped TiO₂ (100 µl of 10 mg/mL solution) as well as NCF–TiO₂ (100 µl of 1 mg/mL solution) on the fungus *A. niger* was studied for a period of 3 months under indoor conditions (Figure 5.10). It was observed that high doses of commercial anatase does not inhibit *A. niger* (Figure 5.10 A1) and the fungus starts sporulation on the 3rd day (as is seen in the form of black dot like structures on the white mycelial mass in Figure 5.10 B1), which becomes more prominent on the 5th day (Figure 5.10 C1) and the 15th day (Figure 5.10 D1) respectively, resulting in complete coverage of white mycelial mass with black fungal spores after 3 months (Figure 5.10 E1). On the other hand, application of NCF–TiO₂ results in the inhibition of *A. niger* within 1 day, as is evident from a clearance zone (Figure 5.10 A2). The clearance zone becomes more prominent, without any apparent sign of fungal spores on the 3rd day (Figure 5.10 B2) and we do not observe any spore production until the 90th day of our observation (Figure 5.10 C2–E2). It is evident from Figure 5.10 that the NCF–TiO₂ nanoparticles not only possess antifungal activity, they also behave as antispore-producing agent. It is highly possible that the NCF–TiO₂ particles might be diffusing from the center towards the periphery in extremely small amounts and inhibiting the sporulation process in the fungus, however these small amounts are not sufficient enough to inhibit the mycelial growth. The antispore-producing activity of small doses of NCF–TiO₂ without inhibition of mycelial growth is a significant result with potential in fermentation technology, wherein sporulation leads to inhibition of mycelial growth in fermentors, and hence leading to reduced production of commercially important products.

In order to understand the effect of NCF–TiO₂ on fungal inhibition under varying light intervals, *Aspergillus niger*, treated with NCF–TiO₂ particles was exposed to indoor light for 0 h to 96 h, followed by exposure to dark until 30th day

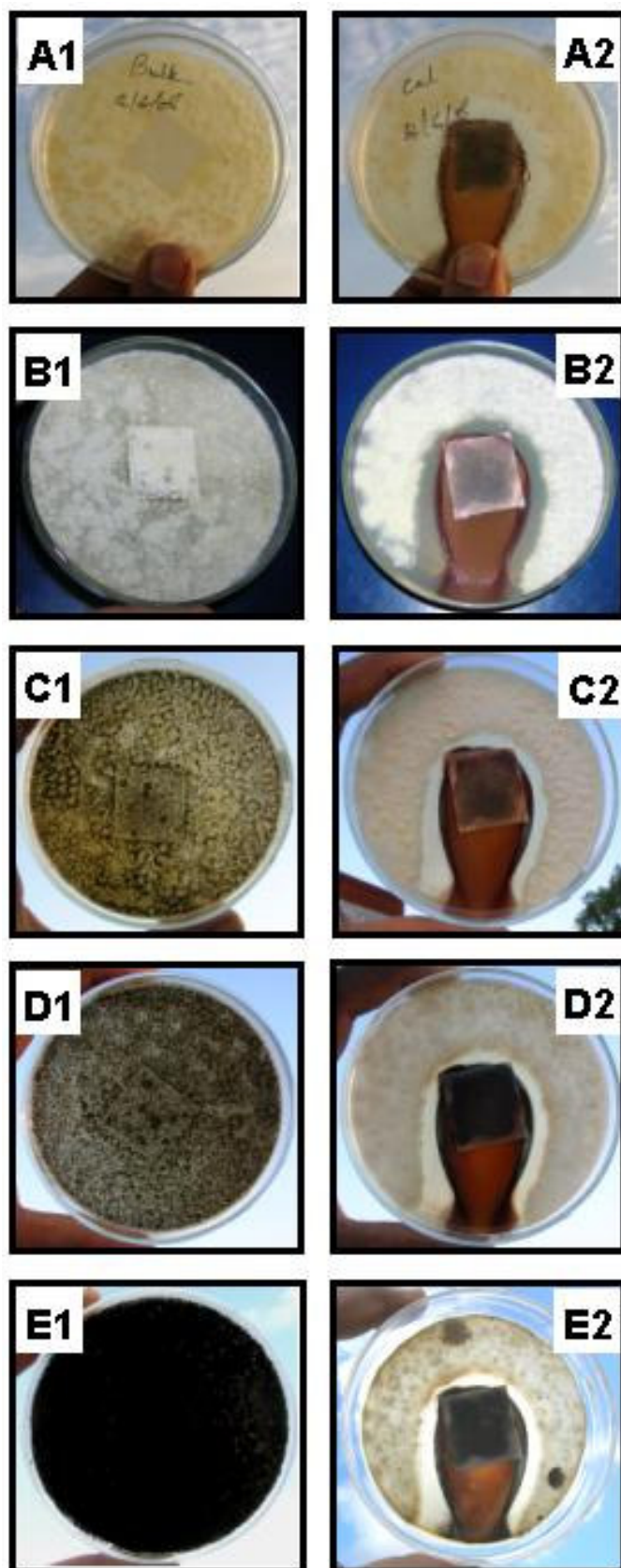


Figure 5.10 Antimicrobial activity of undoped commercial anatase TiO₂ (A1–E1) and NCF–TiO₂ nanoparticles (A2–E2) exhibited in terms of inhibition zones on exposure of fungus *Aspergillus niger* to indoor light conditions for various time intervals viz. 1 day (A1–A2), 3 days (B1–B2), 5 days (C1–C2), 15 days (D1–D2) and 90 days (E1–E2).

(Figure 5.11). Absence of light neither inhibits mycelial growth, nor affects sporulation (Figure 5.11 A). However, when the NCF-TiO₂ treated plates are pre-exposed to indoor light, before being kept in the dark, we observe that exposure for increasing amount of indoor light upto 48 h, though does not cause any mycelial inhibition, it results in subsequent inhibition of sporulation process (Figure 5.11 B–D). Further increase in the light pre-exposure time upto 72 h, followed by dark results in mycelial inhibition as well as partial inhibition of sporulation (Figure 5.11 E). Increase in the light pre-exposure time to 96 h results in complete inhibition of mycelial growth and sporulation, which does not allow fungus to grow even after being kept in dark for 30 days (Figure 5.11 F). These results suggest that NCF-TiO₂ particles might cause complete death of fungal mycelia after 96 h of light exposure. In order to verify this, a part of fungal mycelia were taken from Petri dish shown in Figure 5.11 F and reinoculated on a fresh media. No fungal growth was observed from the reinoculated mycelial mass, hence verifying that NCF-TiO₂ particles have fungicidal activity.

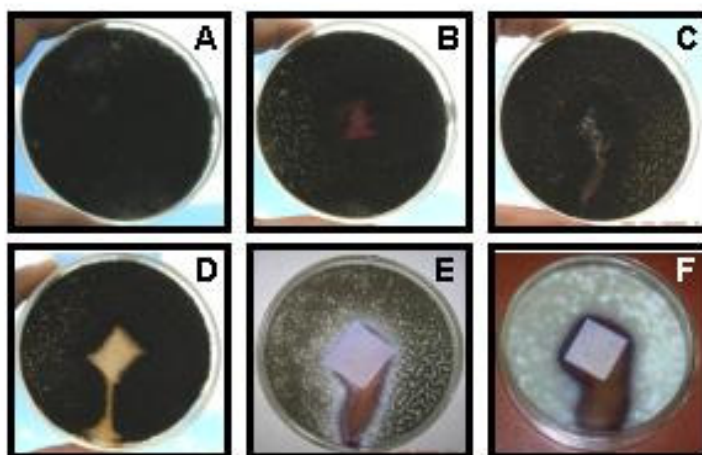


Figure 5.11 Antifungal activity of NCF-TiO₂ nanoparticles exhibited in terms of inhibition zones on exposure of fungus *Aspergillus niger* to indoor light conditions for various time intervals viz. 0 h (A), 8 h (B), 24 h (C), 48 h (D), 72 h (E) and 96 h (F), followed by exposure to dark until 30th day. Images shown have been recorded on the 30th day after inoculation.

5.2.7 AFM analysis of fungal spores

The effect of NCF-TiO₂ particles on *Aspergillus* spores was studied by tapping mode AFM (Figure 5.12). Height mode AFM images of fungal spores, without exposure to TiO₂ particles show spherical fungal spores (Figure 5.12 A), which become elongated after 1 day (Figure 5.12 B), leading to germ tube formation after 2 days (Figure 5.12 C), which clearly approaches mycelia formation

(Figure 5.12 D). Exposure of fungal spores to NCF-TiO₂ particles for 24 h in room light leads to degradation of fungal spores in the form of pores formation, and hence resulting in doughnut like spore structures, as seen in the tapping mode height image (Figure 5.12 E). The corresponding tapping mode phase image of NCF-TiO₂ treated spores indicate the presence of a material of varying contrast within the pore like structures (Figure 5.12 F). It appears that NCF-TiO₂ particles degrade the spore wall and get inside the fungal spores. This is evident from higher magnification height (Figure 5.12 G) and phase (Figure 5.12 H) images of NCF-TiO₂ treated spores, wherein degradation of cell wall structures is clearly visible.

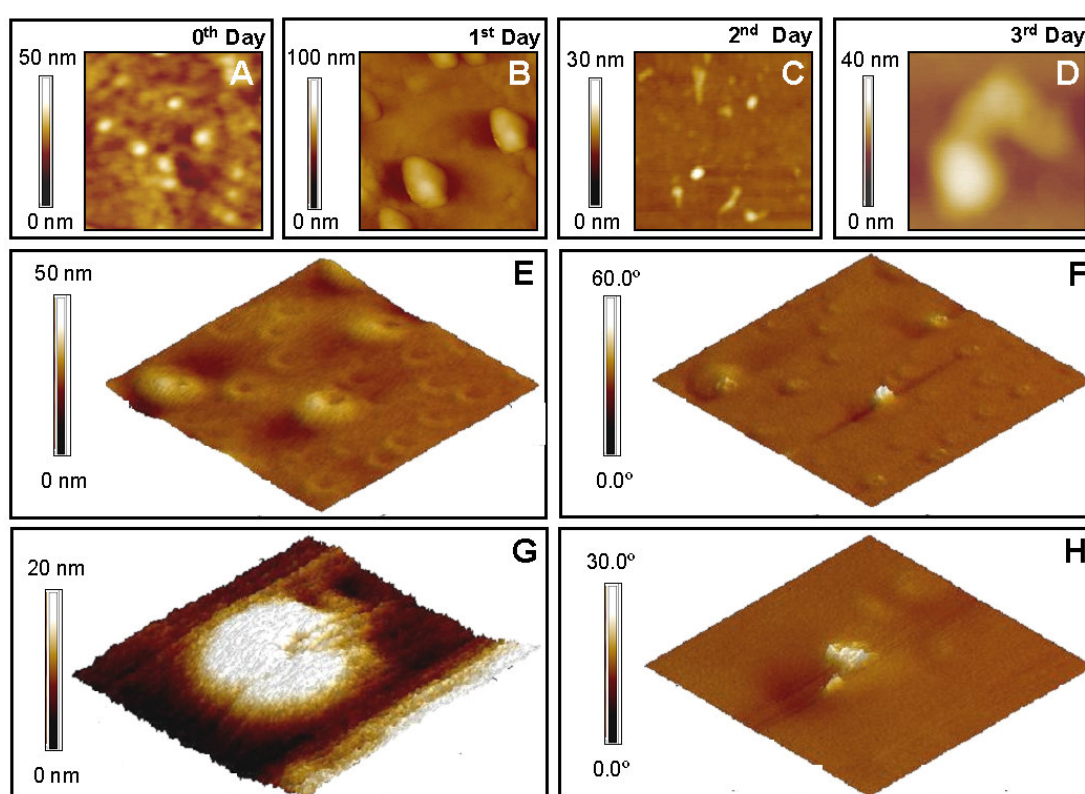


Figure 5.12 Tapping mode AFM images of *Aspergillus niger* spores before (A–D) and after (E–H) their exposure to NCF-TiO₂ nanoparticles for 0 h (A), 24 h (B, E–H), 48 h (C) and 72 h (D) under indoor light conditions. Images shown in panels (A–F) correspond to area 5 μm x 5 μm (A), 3 μm x 3 μm (B), 5 μm x 5 μm (C), 1 μm x 1 μm (D), 4 μm x 4 μm (E and F) and 1 μm x 1 μm (G and H) respectively. Panels (A–E, G) show height images of spores while panels (F and H) show the corresponding phase image of that shown in panel (E and G) respectively.

5.3 Conclusions

In this chapter, we have shown that a new class of anatase titania based nanomaterial (NCF-TiO₂) can be synthesized using a fungus-mediated approach. NCF-TiO₂ nanoparticles are considerably modified with nitrogen, carbon and

fluorine, which impart interesting visible light photoabsorption properties to this material. The visible light induced photo-oxidative properties of NCF–TiO₂ have been shown in terms of degradation of azo dye Congo Red as well as arylmethane dyes Malachite Green and Basic Fuchsin under indoor light and solar light conditions. We have also demonstrated the broad-spectrum antimicrobial activity of NCF–TiO₂ against Gram–negative and Gram–positive bacteria, fungi, actinomycetes, extremophiles and plant as well as human pathogens. NCF–TiO₂ nanoparticles show antispore activity in fungi and its mechanism of action on fungal spores has been explored by AFM. Titanium dioxide based similar nanomaterials might have diverse commercial implications.

5.4 References

- [1] Linsebigler, A. L.; Lu, G. Q.; Yates, J. T. Jr. *Chem. Rev.* **1995**, *95*, 735.
- [2] Fujishima, A.; Hashimoto, K.; Watanabe, T. *TiO₂ Photocatalysis: Fundamentals and Applications*, Best Knowledge Center (BKC), Tokyo, Japan **1999**.
- [3] Fujishima, A.; Honda, K. *Nature* **1972**, *238*, 37.
- [4] Gratzel, M. *Curr. Opin. Colloid Interface Sci.* **1999**, *4*, 314.
- [5] Thompson, T. L.; Yates, J. T. Jr. *Chem. Rev.* **2006**, *106*, 4428.
- [6] Aiello, A. E.; Larson, E. *Lancet Infet. Dis.* **2003**, *3*, 501.
- [7] Russell, A. D. *J. Hosp. Infect.* **2004**, *57*, 97.
- [8] Matsunaga, T.; Tomada, R.; Nakajima, T.; Wake, H. *FEMS Microbiol. Lett.* **1985**, *29*, 211.
- [9] Choi, Y.S.; Kim, B.W. *J. Chem. Technol. Biotechnol.* **2000**, *75*, 1145.
- [10] Wolfrum, E. J. *et al.*, *Environ. Sci. Technol.* **2002**, *36*, 3412.
- [11] Kuhn, K.P. *et al.*, *Chemosphere* **2003**, *53*, 71.
- [12] Seven, O. *et al.*, *J. Photochem. Photobiol. A* **2004**, *165*, 103.
- [13] Belapurkar, A. D.; Sherkhane, P.; Kale, S. P. *Curr. Sci.* **2006**, *91*, 73.
- [14] Song, M. *et al.*, *Biomaterials* **2006**, *27*, 4230.
- [15] Wong, M. S. *et al.*, *Appl. Environ. Microbiol.* **2006**, *72*, 6111.

- [16] Yamashita, H.; Ichihashi, Y.; Takeuchi, M.; Kishiguchi, S.; Anpo, M. *J. Synchrotron Radiat.* **1999**, *6*, 451.
- [17] Kisch, H. *et al.*, *Angew. Chem., Int. Ed.* **1998**, *37*, 3034.
- [18] Zang, L. *et al.*, *J. Phys. Chem. B* **1998**, *102*, 10765.
- [19] Zang, L. *et al.*, *Chem. Eur. J.* **2000**, *6*, 379.
- [20] Macyk, W.; Kisch, H. *Chem. Eur. J.* **2001**, *7*, 1862.
- [21] Burgeth, G.; Kisch, H. *Coord. Chem. Rev.* **2002**, *230*, 41.
- [22] Asahi, R.; Morikawa, T.; Ohwaki, T.; Aoki, A.; Taga, Y. *Science* **2001**, *293*, 269.
- [23] Sato, S. *Chem. Phys. Lett.* **1986**, *123*, 126.
- [24] Morikawa, T.; Asahi, R.; Ohwaki, T.; Aoki, A.; Taga, Y. *Jpn. J. Appl. Phys.* **2001**, *40*, 561.
- [25] Sakthivel, S.; Kisch, H. *ChemPhysChem* **2003**, *4*, 487.
- [26] Irie, H.; Watanabe, Y.; Hashimoto, K. *J. Phys. Chem. B* **2003**, *107*, 5483.
- [27] Lindgren, T. *et al.*, *J. Phys. Chem. B* **2003**, *107*, 5709.
- [28] Gole, J. L.; Stout, J. D.; Burda, C.; Lou, Y.; Chen, X. *J. Phys. Chem. B* **2004**, *108*, 1230.
- [29] Diwald, O. *et al.*, *J. Phys. Chem. B* **2004**, *108*, 6004.
- [30] Lettmann, C.; Hildenbrand, K.; Kisch, H.; Macyk, W.; Maier, W. F. *Appl. Catal. B* **2001**, *32*, 215.
- [31] Sakthivel, S.; Kisch, H. *Angew. Chem., Int. Ed. Engl.* **2003**, *42*, 4908.
- [32] Umebayashi, T.; Yamaki, T.; Itoh, H.; Asai, K. *Appl. Phys. Lett.* **2002**, *81*, 454.
- [33] Umebayashi, T.; Yamaki, T.; Tanaka, S.; Asai, K. *Chem. Lett.* **2003**, *32*, 330.
- [34] Ohno, T.; Mitsui, T.; Matsumura, M. *Chem. Lett.* **2003**, *32*, 364.
- [35] Wang, C. M.; Mallouk, T. E. *J. Phys. Chem.* **1990**, *94*, 4276.
- [36] Park, H.; Choi, W. *J. Phys. Chem. B* **2004**, *108*, 4086.
- [37] Yu, J. C.; Yu, J.; Ho, W.; Jiang, Z.; Zhang, L. *Chem. Mater.* **2002**, *14*, 3808.

- [38] Hoffmann, M. R.; Martin, S. T.; Choi, W.; Bahnemann, D. W. *Chem. Rev.* **1995**, *95*, 69.
- [39] Bansal, V. *et al.*, *J. Mater. Chem.* **2005**, *15*, 2583.
- [40] Martin, H. M. *Photodegradation of Water Pollutant*, CRC Press, Boca Raton **1996**.
- [41] Shirley, D. A. *Phys. Rev. B* **1972**, *5*, 4709.
- [42] The XRD patterns were indexed with reference to the crystal structures from the ASTM and PCPDF charts: Brookite (ASTM chart card no. 3–0380), Rutile (PCPDF chart card no. 34–0180) and Anatase (PCPDF chart card no. 21–1272).
- [43] Cullity, B.D. *Elements of X-ray Diffraction*, Addison–Wesley Publishing Co. Inc., Reading, MA, 294, **1987**.
- [44] Saha, N. C.; Tompkins, H. G. *J. Appl. Phys.* **1992**, *72*, 3072.
- [45] Satish, M.; Viswanathan, B.; Viswanath, R. P.; Gopinath, C. S. *Chem. Mater.* **2005**, *17*, 6349.
- [46] Gopinath, C. S. *J. Phys. Chem. B* **2006**, *110*, 7079.
- [47] Zhang, L.; Koka, R. V. *Mater. Chem. Phys.* **1998**, *57*, 23.
- [48] Gyorgy, E.; Pino, A.; Serra, P.; Morenza, J. L. *Surf. Coat. Technol.* **2003**, *173*, 265.
- [49] Chen, X.; Burda, C. *J. Phys. Chem. B* **2004**, *108*, 15446.
- [50] Mo, S. D.; Ching, W. Y. *Phys. Rev. B* **1995**, *51*, 13023.
- [51] Culp, S. J. *et al.*, *Food Chem. Toxicol.* **2006**, *44*, 1204.
- [52] http://en.wikipedia.org/wiki/Malachite_green
- [53] Gregory, P. *Encyclopedia Chem. Toxicol.* Kroschwitz, J. I. (ed.) John Wiley & Sons, New York **1993**, *8*, 544.
- [54] Hu, C.; Wang, Y.; Tang, H. *Appl. Catal. B.* **2001**, *30*, 277.
- [55] Vinodgopal, K.; Wynkoop, D.; Kamat, P. V. *Environ. Sci. Technol.* **1996**, *30*, 1660.

CHAPTER VI

Conclusions

This chapter details the salient features of the work presented in the thesis and emphasizes on potential avenues for future work.

6.1 Summary of the work

A promising avenue of research in materials science is to follow the strategies used by Nature in order to fabricate ornate hierarchical materials. Organisms have been engaged in on-the-job testing for ages to craft structural and functional materials and have evolved extensively in due course to create the best materials. Some of the strategies used by Nature may well have practical implications in the world of nanomaterials. Therefore, the strive towards exploiting Nature's ingenious work for designing strategies for nanomaterials synthesis has led to biological routes for materials synthesis.

In this thesis, we have described the use of a fungus-mediated biological approach towards the synthesis of oxide nanomaterials. We observe that the fungus *Fusarium oxysporum*, on exposure to hexafluoro chemical precursors such as SiF_6^{2-} , TiF_6^{2-} and ZrF_6^{2-} , is capable of synthesizing extracellular silica, titania and zirconia nanoparticles respectively, in aqueous media. In addition, ternary oxide nanoparticles like barium titanate could also be synthesized by the fungus in the presence of Ba^{2+} and TiF_6^{2-} ions. Interestingly, the sub-10 nm barium titanate nanoparticles were of tetragonal phase and exhibit well-defined dielectric and ferroelectric-relaxor behavior. Using Kelvin probe microscopy, we have shown that electrical information can be written/read on individual barium titanate nanoparticles and hence, these particle can, in principle, be used in fabricating electrical storage devices. An important observation that we recorded in fungus-mediated oxide synthesis was that all the oxide nanoparticles formed were of average size ≤ 10 nm, which poses the possibility of size confinement effects manifested by the biomolecules, bound to oxide nanoparticles during their biosynthesis. The biomolecules involved in the biosynthesis process were explored and the involvement of low molecular weight cationic proteins could be established. We also showed that these extracellular fungal proteins could conceptually be used for the *in vitro* synthesis of oxides nanoparticles.

In order to make the fungus-mediated oxide synthesis completely biogenic, we replaced the chemical precursors with naturally available materials and agro-industrial by-products. This extends the fungus-mediated biosynthesis approach to a bioleaching approach. We observe that the fungus *Fusarium oxysporum* is capable of bioleaching complex silicates present in white sand, in the form of extracellular silica nanoparticles, which on further calcination results in hollow silica. In addition,

Fusarium oxysporum also leaches out huge amount of amorphous silica present in rice husk extracellularly in the form of crystalline cubic silica particles. The most intriguing observation is that the fungus is capable of biotransforming amorphous silica in rice husk into silica nanocrystallites at room temperature. Additionally, we have also shown that *Fusarium oxysporum* selectively leaches out silica present in zircon sand (zirconium silicate) in the form of silica nanoparticles. This in turn results in enhancement of high dielectric zirconia component in zircon sand, which is an extremely important material for refractories.

The visible light excited photo-oxidative and antimicrobial activity of biogenic titania nanoparticles was also investigated. Biogenic anatase titania is found to be considerably modified with nitrogen, carbon and fluorine simultaneously (NCF-TiO₂), which extends the photocatalytic response of these particles throughout the visible region and well into the infrared region of the electromagnetic spectrum. NCF-TiO₂ particles are capable of photodegrading the environmentally toxic azo dye Congo Red as well as arylmethane dyes, Malachite Green and Basic Fuchsin, under indoor and solar light conditions. NCF-TiO₂ nanoparticles possess antimicrobial and anti-spore activity under indoor light conditions against a range of harmful microbes. In addition, the mechanism of photo-oxidative action of NCF-TiO₂ on fungal spores has also been explored by atomic force microscopy (AFM).

These results suggest that the biological route to oxides synthesis is not merely an addition to the existing list of synthesis routes. The biological synthesis provides an edge over other synthesis routes in terms of being eco-friendly, low energy intensive and low cost synthesis. Moreover, biological means of nanooxides synthesis exert interesting functionalities to these materials, as is observed in the form of visible light inducible photoactivity in titania and ferroelectricity in sub-10 nm barium titanate particles.

6.2 Scope for future work

The potential of biosynthesis routes described in this thesis is limited only by the imagination of the researcher. It is quite obvious that the fungus-mediated biosynthesis approach may be extended for the synthesis of other technologically important oxide nanomaterials. Additionally, there is a growing interest in the synthesis of multifunctional nanomaterials like metal-metal oxide core shells, metal

oxide–metal oxide core shells, mixed oxides, multiferroics, etc., which is difficult to achieve using conventional synthesis routes. It appears that these multifunctional materials can be synthesized using this fungus-mediated biological approach by utilizing the proteins bound on to the surface of already synthesized particles.

It is difficult to predict at this stage about the kind of applications, these intriguing and complex biocomposite structures might find, since it is just a beginning towards exploring the potential of an entirely new class of biomaterials. However, applications of these materials have started becoming evident in the form of unconventional properties of biogenic titania and barium titanate nanoparticles that we have observed in our study, thus leading to interesting applications.

In addition, there is a need for in-depth characterization of nanomaterials synthesized *via* biological routes. We could assign the interesting visible region photocatalytic activity of biogenic titania due to nitrogen, carbon and fluorine doping. This suggests the possible reasons of ferroelectricity in sub–10 nm biogenic barium titanate particles, which were found to be tetragonal in such a small dimension (this is unusual, since previous investigations in similar size regime report cubic phase). It is highly possible that there is a similar doping factor involved in case of barium titanate nanoparticles, which imparts unusual ferroelectric properties in small dimensions. One needs to revisit the biogenic barium titanate from detailed surface studies point of view, which might provide important insights and mechanism of action.

Moreover, the question remains how to determine which organism would yield a particular class of nanomaterial? Current microbial route of nanomaterials synthesis is more like a “hit or miss” strategy. Though, the choice of the fungus *Fusarium oxysporum* for oxides synthesis is a result of screening of more than 200 microorganisms, it is possible that there might be another microorganism, which could deliver a better size and shape control than *Fusarium oxysporum*. This poses an urgent need for a rational strategy for identifying the organisms, which could efficiently synthesize various nanomaterials of interest. Few other open questions are how the organic species (proteins/fungal biomass) interact with the oxide precursors to yield oxide nanoparticles, and why do these interactions result in formation of nanoparticles? What are the roles of these organic species in the physiology of organisms? A detailed investigation of the biochemical mechanism and the proteins involved in the biosynthesis process would pave a way towards application of genetic

engineering approaches in this field. Once the genes involved in the biosynthesis of nanomaterials are identified, we might be able to answer these open issues. This would, in turn help in significant development of this budding field of nanomaterials synthesis. This might further lead to the large-scale biosynthesis of oxide nanoparticles. The fungus-mediated biosynthesis approach therefore, might have important commercial implications in the future industrial processes.

List of Publications

- 1) **Bansal, V.**; Rautaray, D.; Ahmad A.; Sastry, M. Biosynthesis of zirconia nanoparticles using the fungus *Fusarium oxysporum*. *J. Mater. Chem.* (2004) *14*, 3303-3305.
 - 2) Joshi, H.; Shirude, P. S.; **Bansal, V.**; Ganesh, K. N.; Sastry, M. Isothermal titration calorimetry studies on the binding of amino acids to gold nanoparticles. *J. Phys. Chem. B* (2004) *108*, 11535-11540.
 - 3) **Bansal, V.**; Sanyal, A.; Rautaray, D.; Ahmad A.; Sastry, M. Bioleaching of sand by the fungus, *Fusarium oxysporum* as a means of producing extracellular silica nanoparticles. *Adv. Mater.* (2005) *17*, 889-892.
 - 4) **Bansal, V.**; Rautaray, D.; Bharde, A.; Ahire, K.; Sanyal, A.; Ahmad, A.; Sastry, M. Fungus-mediated biosynthesis of silica and titania particles. *J. Mater. Chem.* (2005) *15*, 2583-2589.
 - 5) Shukla, R.; **Bansal, V.**; Chaudhary, M.; Basu, A.; Bhonde R. R.; Sastry, M. Biocompatibility of gold nanoparticles and their endocytotic fate inside the cellular compartment: a microscopic overview. *Langmuir* (2005) *21*, 10644-10654.
 - 6) Sanyal, A.; Rautaray, D.; **Bansal, V.**; Ahmad, A.; Sastry, M. Heavy metal remediation by a fungus as a means of production of lead and cadmium carbonate crystals. *Langmuir* (2005) *21*, 7220-7224.
 - 7) Bharde, A.; Rautaray, D.; **Bansal, V.**; Ahmad, A.; Sarkar, I.; Yusuf, S. M.; Sanyal, M.; Sastry, M. Extracellular biosynthesis of magnetite using fungi. *Small* (2006) *2*, 135-141.
 - 8) **Bansal, V.**; Poddar, P.; Ahmad, A.; Sastry, M. Room-temperature biosynthesis of ferroelectric barium titanate nanoparticles. *J. Am. Chem. Soc.* (2006) *128*, 11958-11963.
 - 9) **Bansal, V.**; Ahmad, A.; Sastry, M. Fungus-mediated biotransformation of amorphous silica in rice husk to nanocrystalline silica. *J. Am. Chem. Soc.* (2006) *128*, 14059-14066.
 - 10) **Bansal, V.**; Bhargava, S. K.; A. Ahmad and M. Sastry. Zirconia enrichment in zircon sand by selective fungus-mediated bioleaching of silica. *Langmuir* (communicated).
 - 11) **Bansal, V.**; Ahmad, A.; Sastry, M. Visible light induced photocatalytic and broad-spectrum antimicrobial activity of N, C and F simultaneously doped biogenic titania nanoparticles. *Nat. Nanotechnol.* (communicated).
-